Philosophical Dissertation

Theoretical and Experimental Investigations on Silicon Single Crystal Resonant Structures

submitted to the Faculty of science of the University of Neuchâtel to obtain the degree of Doctor of science

by

Rudolf A. Buser
dipl. phys. ETHZ

Institute of Microtechnology
University of Neuchâtel
Breguet 2, 2000 Neuchâtel
Switzerland

Πάντα ῥεῖ

HERAKLIT

IMPRIMATUR POUR LA THÈSE

Theoretical and Experimental Investigations on Silicon Single Crystals resonant Structures

de Monsieur Rudolf Buser

UNIVERSITÉ DE NEUCHÂTEL

FACULTÉ DES SCIENCES

La Faculté des sciences de l'Université de Neuchâtel sur le rapport des membres du jury,

MM. N. de Rooij, R. Dändliker, H. Brändle (Baden), R. Kubli (Greifensee) et B. Hök (Uppsala)

autorise l'impression de la présente thèse.

Neuchâtel, le 14 juillet 1989

Le doyen:

F. Persoz

Vorwort

Die vorliegende Dissertation entstand in den Jahren 86-89 grösstenteils aus einem Industrieprojekt. Einzig der Tactile Sensor war ein gänzlich unabhängiges Projekt. Rhythmus und Stossrichtung der Arbeit waren damit weitgehend fremdbestimmt. Die meisten theoretischen Ansätze wurden erst im nachhinein entwickelt.

Von den vielen hundert Messungen, welche zur Überblickgewinnung, zur Abschätzung der Messmethode und zur Abrundung eines Eindruck dienten, wurden nur relativ wenige in dieser Arbeit explizit dargestellt. Die dabei jeweils gemachten Erfahrung äussern sich darin, dass die experimentellen Kapitel 5-10 mit Schlussfolgerungen enden, welche die generelle Tendenz und die offenstehenden Probleme aufzeigen.

War auch auf der einen Seite diese Arbeit eingebunden in einen Industrievertrag, war doch auf der andern Seite das Gebiet für die Gruppe völliges Neuland, was zwar auf der einen Seite interessante Studien ermöglichte, auf der anderen Seite eine Entwicklung für alles und jedes ab ovo erforderte. Eine Ausnahme bildete hier lediglich das Interferometer, konstruiert von F. Willemin, welches mir Prof. Dändliker in verdankerswerter Weise vollumfänglich zur Verfügung stellte.

All die aufwendigen Messprogramme sowie die Berechnungsprogramme wurden, ausser dem Ätzsimulationsprogramm, in der vorliegenden Arbeit nicht detailliert dargestellt. Dies ersparte etwa hundert Seiten Papier. Einige Programme wurden in einem internen Bericht abgelegt.

Danken möchte ich an dieser Stelle der Firma Mettler für die Zusammenarbeit sowie Herrn Prof. Dr. H. Beck für die Diskussion, die ich mit ihm über die theoretischen Kapitel führen konnte.

Ganz besonderen Dank schulde ich Herrn Prof. Dr. N. de Rooij dafür, dass ich die vorliegende Dissertation an seinem Institut durchführen konnte.

Preface

The present dissertation emerges mainly from an industrial project of the years 86 to 89. Only the Tactile sensor was a completely independent project. Rhythm and direction of the work were thus mostly heterogeneous. Most of the theoretical developments were done after design and measurements.

Of the hundreds of measurements, which were necessary to gain an overview, to appraise the measurement method and to round off an impression, only relatively few are presented in this work explicitly. The gained experience finds its expression in the discussion section of the experimental chapters, where the general tendency shows the unsolved problems.

Being on one hand embedded in an industrial contract this work was on the other hand completely new territory for the group, what allowed on one side to perform interesting studies but required on the other side the development of everything ab ovo. The only exception was the interferometer, developed by F. Willemin and kindly placed completely at my free disposal by Prof.Dr. R. Dändliker.

All the large scale measurement and calculation programs, excepting the etch simulation program, are not presented in detail in the present work. This saved about hundred pages of paper. Some of these programs are described in IMT internal reports.

I would like to acknowledge here the company Mettler for the collaboration as well as Prof. Dr. H. Beck for the discussion with him I could have about the theoretical subjects.

A very special thank I owe to Prof. Dr. N. de Rooij that I could perform the present Dissertation at his Institute.

Contents

Chapter 1
Introduction

1.1 Resonators and materials

The trend toward digital information and control systems, together with the need for more accurate sensors have encouraged the development of resonant structures as basic sensing elements, which give an intrinsically digital output. Thereby frequency is only one parameter of an oscillation: amplitude, phase angle and damping are also available as readout parameters. We are proposing two types of sensors with frequency output : one device with an electrical oscillation circuit and several others with a mechanical equivalent. In the latter case forces, torques, mass or a change of the modulus of elasticity influence the resonance frequency. Generally spoken, the higher the Q-factor, the better the measurement accuracy of the resonance frequency. A general overview over resonator principles may be found in the articles of Gast[1] and Langdon[2].

For mechanical resonators single crystals are best candidates. Braginsky[3] cites some publications on monocrystalline materials with very high Q-factors up to 10^6 at room temperature and up to 10^9 measured at 4 K for Al_2O_3 (sapphire). The performance of Si is somewhat lower. It has to be noted in this context, that there is a fundamental difference between mechanical resonators vibrating in a pure thickness or shear mode (as most piezoelectric resonators are designed for) and those vibrating in a transverse mode. Because in piezoelectric resonators the dipoles feel the electric field (compared to frequency and dimensions) almost immediately, the state of strain is distributed homogeneously in the volume and there are no thermodynamic losses by entropy flow. This is not the case in a flexural mode, where even over a cross section we have compression and dilatation and thus temperature variations. This is important to keep in mind when comparing Q-factors in vacuo of different devices not to speak about those in air or other damping media, where the amplitudes of the vibration have a significant influence.

So far especially quartz based resonators have been extensively investigated. But also GaAs[4], sapphire[5], lithiumniobate[6] and other[7,8] single crystal resonators are reported. Thickness monitoring by quartz resonators is a meanwhile widespread technique[9]. Also in chemical analysis resonators have potential applications. Hlavay[10] gives an overview how quartz resonators may be used for chemical analysis by covering them with appropriate absorbing materials. Tuning fork like devices are used to perform temperature[11,12], pressure[13] or force[14] measurements.

Silicon single crystal is a highly interesting material not only for microelectronics but also for micromechanics. Its elasticity is almost the same as that of steel whereas its strength performance even exceeds that of steel[15]. Moreover as being a single crystal there is theoretically no fatigue. In reality crystal defects limit this ideal behavior, but IC fabrication industry has pushed the purity and the perfectness of silicon to a high degree. However, silicon is not as is quartz piezoelelectric, and thus needs special driving forces (see chapter 4).

Silicon is easily available in a mass production fitted form, namely as wafers, with a well developed processing technology established. The possibility to form easily a highly homogeneous SiO_2 layer offers some important technological advantages for creating passivation layers. To fabricate the micromechanical structures the same photolithographic techniques can be applied as in the semiconductor fabrication. Miniaturization and mass production are therefore built-in profits of this technology. Moreover, the combination of silicon mechanics with silicon electronics may provide high performance sensing systems, with respect to sensitivity, compactness and output signal conditioning, a feature, that quartz doesn't offer.

The first approach of a micromachined resonator in the context of silicon wafer processing was published with Nathanson's *Resonant Gate Transistor*[16] in 1965. This group realized a thin metallic film as a mechanically resonating gate with a Q-factor of 500. The free standing cantilever was obtained by depositing it over a metallic spacer layer which was etched away afterwards by a selective etching.

It was but years later that microfabrication techniques have been introduced to realize resonators in silicon (monocrystalline as well as polycrystalline). Both membranes[17] and beam like structures[18,19,20] have been reported. The impetus came mainly from the optics, especially fiber optics. They are handling frequencies every day. More references for that "optical" branch of researchers can be found in chapter 10.

In this context we distinguish between static and dynamic operating mode of the elements, subsuming under *static* devices where the physical quantity to be measured causes a deflection (resulting e.g. in a change of resistivity or capacity) and under *dynamic* such where the eigenfrequency or the damping is changed by the quantity to be measured. Thus with static devices only forces, pressures, accelerations and at the limit temperatures can be measured, whereas by dynamic devices beyond that interactions with the surrounding medium like density and viscosity can be measured. Moreover, the eigenfrequency is more sensitive to a change of the internal state (change of mass, stress, temperature, e.g.) than a static deflection with an analog (amplitude modulated) output. The situation for static devices improves in case of a frequency modulated output signal as we have done with one device (see chapter 5).

This work is thought to present various possibilities for the fabrication of mechanical sensors, which emerges from the technique of anisotropic etching in monocrystalline silicon. Special emphasis will be laid on a certain optimization of vibrating structures. Starting from relatively simple lumped mass-beam system the structures have been improved with respect to the clamping. By modelling and extensive calculations optimal structures could be calculated.

Resonant structures of single crystal silicon are investigated in view of their potential use as basic elements for various sensor applications, like pressure, viscosity, temperature or adsorbed molecules, as is already well known with quartz resonators.

It is the purpose of this work to study wether resonant silicon devices can be realized with a frequency resolution in the order of ppm in order to develop sensors with a similar resolution. To this end high Q-factor resonators are needed. As stated above ultrasonic absorption measurements showed that the internal damping of the single crystal silicon might be very low. The relatively poor Q-factors reported in literature for realized resonant silicon devices originate therefore from external damping, i.e. clamping, medium and supplementary thin films and treatments. Some investigations on these external damping factors of silicon resonators will be presented in this work (see chapter 6).

The fundamental difference between vibration isolation in common mechanical problems and the conceiving of a high-Q system is that in the latter one the isolation may not be achieved by dissipation. The isolation has to be therefore infinitly rigid, mechanically not possible, or a high-Q system, too (dynamical absorbers). A single piece structure, the resonant structure with the isolation system integrated, is possible with the techniques described here. Proposals of such an integrated solution will be presented in the chapters 7 & 9.

1.2 State of the art

1.2.1 Static structures

Since classical structural element like beams, plates or rods can be fabricated in silicon quite directly according to the needs and the etching possibilities,- which can be checked with a simulation program, described in section 3.3.-, optimization is only a question of stiffness and yield strength or breaking in the case of single crystals. One of our first structure realized in silicon was thus a bending bearing. An overview of this large field of research on static devices can be found in a special issue of IEEE Electron Devices[21], the Proceedings of Eurosensors II, 1988[22], of the Hilton Head Conference 86[23] and 88[24] and Transducers '85 [25] and '87 [26].

1.2.2. Dynamic structures

Some experimental reports on resonating silicon structures were cited above. Typically these are simple structures as known from static cases (beams, paddles and membranes), where no special attention was paid to the very critical clamping. More specific references are given in the corresponding chapters.

On the theoretical side two new factors add in the case of dynamic structures namely first per definition the time (t) and secondly the dissipation of energy. Dynamic, non dissipative continuous as well as discrete structures are treated mathematically in a multitude of publications either in the field of physics, mechanical engineering or building construction and recently also in sensor technics. Less are then the number of publications when continuous systems have also discrete elements attached (typically mass beam systems, which have a special importance, as we will show later). The evolution of this subject is described in the appendix A. These mechanical engineering subjects (simulation of aircraft wing and similar) have not reached sensor engineers. Finite element methods (ANSYS) have been applied in this field recently by Barth *et al.*[27].

Publications on dissipative systems are rare (in physics such systems are considered not to be generally mechanical systems and therefore seldom mentioned. Only very recently an article was published, where dissipation is included in the Hamilton Jacobi theory[28]. Also papers describing dissipative continuous systems with discrete elements (dashpot, mass, spring), are treated only by a few authors. In engineering as well as in construction some interest in non-conservative systems raised in the last years although from a different point of view: Engineers are looking typically for strong damping in order to avoid unnecessary fatigue of material or destruction by resonance phenomena, while we are searching to reduce damping as much as possible. The mathematical treatment is in principle the same and only the optimizing process is opposite.

In the context of miniaturized sensors some trials were made, to include damping in the differential equations. In the case of simple continuous systems like beams, there is no special difficulty to do so. But in case of a mass beam system, accelerometers e.g., this has never been done in great detail. The fundamental difficulty arises that the solution of the partial differential equation can no longer be separated into a simple product of a space and a time function. Thus such an ansatz must fail and other methods must be developed.

Kokubun[29], who analyzed the nature of damping in air (and whose expression for the damping factors we are including in our analysis) solved for his string of beads model only an ordinary differential equation model (which may be considered as being the separated time part of a proportionally damped system). Others neglected the damping of the beam in an accelerometer type structure and solved just an ordinary differential equation, too.

We achieved on the basis of modal analysis to deduce an analytical solution of a mass-beam system vibrating in a damping medium in a first approximation. Thus, it was possible to derive the Q-factor with respect to any geometry or physical parameter and thus to localize the maximum value. Numerically any degree of approximation is possible with this model of course, too.

1.3. The structure of the present work

One type of static sensor and four different types of dynamic structures (resonators) are presented in this work. In order to avoid repetition we start with four general chapters, where theory, design tools, fabrications steps, mounting and experimental principles are treated. Then five sections follow where for each structure type the special design, calculations, mounting and other experimental aspects are discussed, each followed by a chapter of results and one with discussion.

---

1 Gast T.; Sensors with oscillating elements, J. Phys. E: Sci. Instrum. Vol 18, 1985, GB, p.783

2 Langdon, R.M.; Resonator sensors- a review. J. Phys. E: Sci. Instrum. Vol 18, 1985, GB, p.103

3 Braginsky V.B. Mitrofanov,V.P., Panov, V.I.; Systems with small dissipation . Chicago Press Chicago London 1985.

4 Hök,B., Ovren C., Gustafsson E.; "Batch fabrication of micromechanical elements in GaAS-AlxGa1-xAs". Sensors and Actuators, 4. (1983) p. 341.

5 Apal'kov, V.K., Mitrofanov, V.P., Shiyan, V.S.; Frequency stability of oscillator with sapphire resonator. Sov. Phys.-Dokl. (USA), vol23, no 9, pp 671-2 , Sept 1978.

6 Kojima, Y., Fujiwara, Y., Yamada,S., Wakatsuki, N.; Chip crystal resonator with load capacitors. Proceedings of the 38th Annual Frequency Control Symposium 1984 (Cat No 84CH2062-8) pp. 114-18, 1984.

7 Lefevre, R., Joly, C.; Laser processed miniature $LiTaO_3$ resonators and monolithic filters with integrated holders. Int. Conf. on Frequency Control and Synthesis (Publ. No 75) pp.37-43 1987. Publ. IERE, London England, ISBN 0 903748 71 1.
and
Lefevre, R., Jenselme, L., Servajean, D.; Laser processed miniature $LiTaO_3$ resonators and monolithic filters. Proceedings of the 39th Annual Frequency Control Symposium 1985 (Cat No 85CH2186-5) pp. 333 - 7, 1985.

8 Zelenka, J.; Piezoelectric Resonators and their Applications, Elsevier , 1986.

9 Sauerbrey., G.; Verwendung von Schwingquarzen zur Wägung dünner Schichten und zur Mikrowägung, Zeitschrift für Physik 155,1959, p. 206.

10 Hlavay J.Guilbault, G.G.; Applications of the Piezoelectric Crystal Detector in Analytical Chemistry, Analytical Chemistry, vol 49, no 13 november 1977, p. 1890.

11 EerNisse,E.P. and Wiggins, R.B.; A Resonator Temperature Transducer with no Activity Dips, 40th Annual Frequency Control Symposium, Philadelphia, May 1986, p.216.

12 Ueda,T. et al.; Temperatue Sensor using Quartz tuning Fork Resonator, 40th Annual Frequency Control Symposium, Philadelphia, May 1986, p.224.

13 Paros, J.M.; Precision Digital Pressure Transducer, ISA TRANSACTION, Vol 12, 1973,p173.
14 Langdon, R.M.; Resonator sensors - a review, J Phys.E: Sci. Instrumen., Vol 18,1985, p. 103.
15 Culshaw, B.; Silicon in Optics, SPIE Vol. 798 Fiber Optic Sensors II (1987) p. 346
16 Nathanson, H.C. and Wickstrom, R.A.; A Resonant Gate silicon surface Transistor with High-Q Bandpass Properties", Applied Phys. Lett. August, 1965., cited in Nathanson, H.C.Newell, W.E. and Wickstrom, R.A.Electronics " Tuning Forks' sound a hopeful note" September vol 20 p.84.
17 Smith, I.G. et al.; Resonant Diaphragm pressure measurement system with ZnO on Si Excitation, Sensor and Actuators, 4 (1983) p. 565.
18 Greenwood, J.C.; Etched Silicon Vibrating Sensor, J. Phys. E: Sci Instrum., Vol 17, 1984, p. 650.
19 Howe,R.T. and Muller,R.S.; Resonant-microbridge Vapor Sensor , IEEE TRANSACTIONS ON ELECTRON DEVICES, VOL ED-33, NO 4, April 1986 p.499.
20 Wölfelschneider, H., Kist, R., Knoll., G., Ramakrishnan, S., Höfflin, H., Benecke, W., Csepregi, L. Heuberger, A., Seidel, H..; Optically excited and interrogated micromechanical silicon cantilever structure., SPIE Vol. 798. Fiber optic sensors II (1987) p.61
21 IEEE Transactions on Electron Devices, Vol 35, Number 6, June 1988, Special issue on Microsensors and Microactuators.
22 Eurosensors II, 4th symposium on sensors & actuators , Twente, 1988.
23 IEEE Solid State Sensor and Actuator Workshop, Hilton Head Island, South Carolina , June2.-5- 1986,
24 IEEE Solid State Sensor and Actuator Workshop, Hilton Head Island, South Carolina June 6.-9- 1988 IEEE Cat No *88TH0215-4*
25 Transducers '85, The 4th Int. Conf. on Solid-State Sensors and Actuators, Philadelphia 1985, IEEE Cat Num. 85 CH2127-9,
26 Transducers '87, The 4th Int. Conf. on Solid-State Sensors and Actuators, Tokyo 1987, ISBN 4-88686-010-9.
27 Barth, Ph.W., Pourahmadi, F. Mayer, R., Poydock, J., Petersen K.; A Monolithic silicon accelerometer with integral air damping and overrange protection. 1988 SolidState Sensor and Actuator Workshop, Hilton Head Island, SC. June 6-9, 1988, IEEE Cat no 88TH 0215-4.pp. 35-38.
28 Vuijanovic, B., Strauss, A.M.; Application of the Hamilton-Jacobi method to linear non conservative vibration theory. Journal of Mathematical Physics, vol 29, no 7 july 1988. p. 1604.
29 Kokubun , K.et al.; Frequency dependendence of a quartz oscillator on gas pressure, J. Vac. Sci. Technol. A3 (6), Nov/Dec. 1985. p.2184.

Chapter 2
Theory and modelling

Underlined variables mean operators, bold letters vectors or tensors

2.1. Introduction

2.1.1. Statement of the problem

By a simple beam we mean in the following a beam with constant cross section and no discrete element on it. Moreover we are considering only weak bending of the beam. With such approximations the beam is called an Euler-Bernoulli beam. The vibration modes of such a beam can be calculated best analytically. This is described in any textbook on vibrations including different boundary conditions like clamped, free, pinned and combinations of them. Even when supplementary lumped masses are added, classical analytical method leads to a solution as long as the system stays conservative (see later). The analytical solution is typically based on the assumption, that the solution may be well separated in real functions of time and space, i.e. the points of the beam vibrate all in phase. This is still the case, when proportional damping is present on a uniform beam.

The availability of powerful numerical hard- and software intensifies the use of approximation methods where discretization or developing in series is the mathematical approach. On the other hand in large scale mechanics modal analysis is a well known technique to calculate the dynamic behaviour of structures. In micromechanics, however, little is seen in this direction. Rayleigh methods are used instead. Recently also finite element methods have been introduced[1].

A direct method however consists in solving the partial differential equation of the transverse vibration of a beam with appropriate boundary conditions. The boundary conditions constitute then a system of a linear homogeneous equations which has only a non trivial solution in the case that the determinant of its coefficient matrix equals zero. This condition gives a transcendental equation for λ, the eigenvalue, which determines finally the eigenfrequencies. Sandmaier[2] has solved this eigenvalue equation for a beam with a mass in the middle by an approximation and ends with the same equation for the resonance frequency as results from a simple static calculation with an equivalent spring constant. In section 2.3. we solve this eigenvalue equation numerically, which gives the correct value for λ.

When discrete dissipative elements are present, i. e. non-proportional damping (see below), things may change drastically, because energy has to be transported to the location of dissipation. To see this imagine a beam, fixed at both ends but with in the middle part a strong damper, vibrating freely. Obviously the whole beam damps out, not only the middle point. Energy therefore has to flow to that middle point. This means, that travelling waves are present (no fixed nodes) and a separation into space and time as above is no longer possible. This is the physical explication of the complications encountered with non-proportional damping present. This consideration shows that there are no solutions in the simple form of $X(x)\cdot T(t)$.The mathematical description and solution of the problem is given in the subsequent sections.

An important distinction has to be made between proportional damping and non-proportional damping.

Proportional damping means damping proportional to the mass and stiffness distribution. For continuous systems this is typically material damping, adding to the Newtionian Differential Equation (DE) of the undamped system a damping force per unit length. But also external damping of air can be described in that way in case of a beam with a constant cross section

Non- proportional damping means that the distribution of the damping in that case can no longer be represented as a linear combination of mass distribution and stiffness distribution. In terms of matrix calculus this means that the damping matrix cannot be diagonalized by the eigenvectors of the undamped system (coupling of damping).

In the appendix A an overview of the publications on that subject is given. The different approaches can be classified as follows.

- * discrete systems
- * modal analysis of continuous structures
  - ° without damping
    - - without lumped masses and springs
    - - with additional masses and springs
  - ° with damping
    - - proportional
    - - non-proportional
- * transfer matrix
- * integral transformations

Adkins[3] describes a modal analysis method for proportional and non-proportional damped systems with lumped masses by uncoupling the DE of the generalized coordinates. His calculations end with complex eigenvalues and complex eigenfunctions. The disadvantage of this method is, that an eigenvalue problem has to be solved in order to be able to perform the transformation which decouples the equations cited above. Because the eigenvalues are complex numbers, all the subsequent calculations (matrix transformations, solving of the differential equations, calculations of the functions) have to be done complex. As the number of considered modes exceeds three, this calculation has to be done numerically, with the result that any trace of the parameters (like damping, masses) is lost. He calculated therefore the specific example of a pinned beam (here the eigenfunction and eigenvalue of the undisturbed beam are simple) with additional mass and friction and he rearranged the different (complex) components, in order to get real function at the end. He assumes that the eigenvalues appear in conjugate complex pairs in order to get real functions at the end.

Another comprehensive work which includes non-proportional damping is done by Wahle[4]. Although actually looking for solutions of large forced structure with dynamic absorbers (response of TV-Towers subjected to random excitation (earthquake)), this work nevertheless cites an interesting method to calculate the eigenfrequencies of a mass beam system with non-proportional damping. This method based on the publication of Jacquot[5] avoids the problem of the coupled DE system by applying a Fourier transformation with respect to time to the initial DE, after having done the modal decomposition. Here only one large calculation has to be done at the end consisting however of a nonlinear equation whose complex zero's have to be found. Numerically this is not a very comfortable situation and moreover the solutions have to be found (for small damping) in the surroundings of singularities (poles). We developed however a computer program to find the numerical solution (see section 2.4.3.2.).

Because we are interested in transient cases we are proposing here to replace the Fourier transformation by a Laplace transformation. With this transformation, the initial conditions have to be included, so one might fear to get serious problems when they are not well posed. The analysis will show however that this problem can be solved with the developement of the initial condition in modes, too.

If one is looking for the lowest eigenfrequency of the system, a good initial condition would be for example the first undisturbed mode. But it has to be pointed out that any other initial condition may be used provided that it may be developed into the undisturbed modes.

2.1.2. Overview

In this chapter we concentrate ourselves on the calculation of the resonance frequency and the Q-factor of mass beam structures with damping. As stated in the introduction, only few attempts have been made in the field of sensors to treat this subject rigorously. This chapter summarizes also the theories about damping by gases and some remarks on internal damping.

---

1 see chapter 1 ref 23.

2 Sandmaier, H., Kühl, K., Obermeier, E.; A silicon based micromechanical accelerometer with cross acceleration sensitivity compensation, Transducers '87, 4th Int. Conf. on Solid-state Sensors and Actuators, Tokyo, 1987.

3 Adkins, R.L.; Modal Analysis of liner non-conservative system. Air Force Materials Lab. Report AFML-TR-75-2. 1975.

4 Wahle, Michael; Beitrag zur passiven Kontrolle schwach gedämpfter elastischer Strukturen mittels dynamischer Schwingungsdämpfer. Dissertation, TH Aachen, Aachen, 1984.

5 Jacquot, R.G.; The forced vibration of simply modified damped elastic surface systems. Journ. of Sound and Vibr. 48(2), 1976, pp. 195-201.

2.2. Calculation of the Mesamass

In order to be able to calculate the resonance frequencies of mass beam systems, one has to know precisely the value of the lumped mass. The calculation of the lumped mass (proof mass) is possible, because we are dealing with rather stereometrical bodies (mesas) due to the the corner compensation method (see chapter 3).

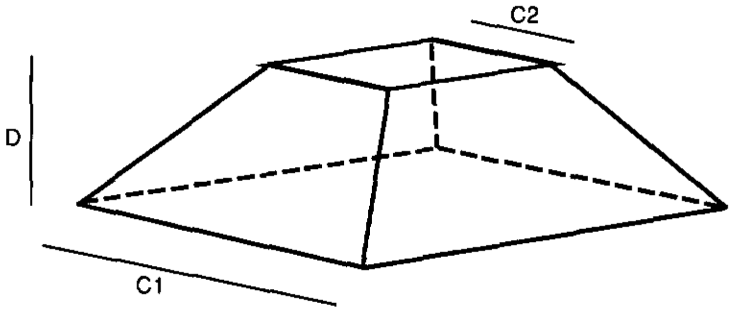

Fig.2.1. Sketch of the truncated pyramid (mesa)

The Volume of a truncated pyramid is (see Fig.2.1.):

$$V=\frac{D}{6}\left(C_1^2 + (C_1+ C_2)^2 + C_2^2\right) \qquad [2.1]$$

where D is the height, C_1 is the length of the bottom and C_2 is the length of the roof of the mesa.
When the side walls are (111)-planes C_1 is defined by D and C_2 and can be found by planimetric rules. The volume expressed by D and C_2 alone is then

$$V = D\left(\frac{2}{3} D^2 + \sqrt{2}\, D\, C_2 + C_2^2\right) \qquad [2.2]$$

The mass is then

$$M = \rho_{si} * V \qquad [2.3]$$

2.3. Calculation of the resonance frequency without damping

2.3.1. Introduction

The resonance frequency under vacuum conditions is calculated by solving the equations of the transverse vibration of a beam with the appropriate boundary conditions. This method is of cause more accurate than the approximation by the Rayleigh method. Moreover it allows to include different boundary conditions properly and also to calculate higher order eigenfrequencies. The boundary conditions constitute then a system of linear homogeneous equations which has only a non trivial solution in the case that the determinant of its coefficient matrix equals zero. This condition gives a transcendental equation for the eigenvalue of the space equation λ, which determines finally the eigenfrequencies.

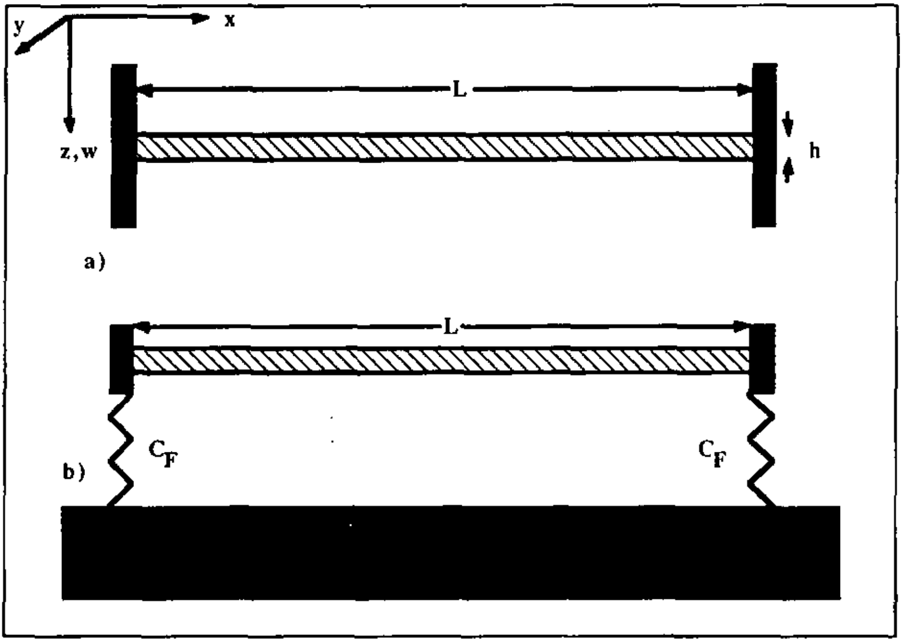

Fig.2.2. Simple clamped-clamped beam of length L with eigther a)rigid or b) elastic clamping

The weak bending of a simple beam is described by the Euler-Bernoulli[1] formula (see Fig. 2.2.a):

$$EJ_y \frac{\partial^4 w(x,t)}{\partial x^4} = -\mu \frac{\partial^2 w(x,t)}{\partial t^2} \qquad [2.3.]$$

where E is the modulus of elasticity (defined first by EULER, but entered as Young's modulus in literature), J_y= static moment of inertia and μ is the mass per unit length of the beam , w(x,t) is the elastic line.
Separation of the variables x and t with a separation constant named ω_o^2 results in a space equation:

$$\frac{EJ_y}{\mu} \frac{d^4X(x)}{dx^4} + \omega_o^2 X(x) = 0 \qquad [2.4]$$

and a time equation

$$\frac{d^2T(t)}{dt^2} + \omega_o^2 T(t) = 0 \qquad [2.5]$$

Introducing the abbreviation

$$\lambda^4 = \frac{\mu \omega_o^2}{E J_y} L^4 \qquad [2.6]$$

simplifies the expressions and the (angular) resonance frequency ω_o is then

$$\omega_o = \left(\frac{\lambda}{L}\right)^2 \sqrt{\frac{E J_y}{\mu}} \qquad [2.7]$$

Remark: λ is sometimes defined differently in literature, i.e. without the factor L^4 .

The solution of the space equation is then

$$X(x) = C_1 \cos\frac{\lambda}{L}x + C_2 \sin\frac{\lambda}{L}x + C_3 \sinh\frac{\lambda}{L}x + C_4 \cosh\frac{\lambda}{L}x \qquad [2.8a]$$

and that of the time equation

$$T(t) = A \cos(\omega t + \alpha) \qquad [2.8b]$$

The complete solution then can be presented in the form w(x,t) = X(x)· T(t).The coefficients C_i are determined by the boundary conditions.

We are giving here only the results of the calculations for various boundary conditions starting with those of a clamped-clamped beam. The detailed calculations can be found in the appendices B-E.

Each times the four boundary conditions form the 4x4 matrix **A** of a homogeneous system of linear equations for C_i which has only a non trivial solution in the case that the determinant of **A** is 0. A typical example of the value of the determinant in dependance of λ is represented in Fig.2.6. As can be seen from this figure this condition restricts λ to discrete values λ_i. Using equation [2.7] the corresponding eigenfrequencies ω_{oi} can be found.

2.3.2. Simple beam with rigid clamping

In this case we have the following boundary conditions:

$$\begin{aligned} &\text{I:} && w(0,t) = 0 \\ &\text{II:} && w'(0,t) = 0 \\ &\text{III:} && w(L,t) = 0 \\ &\text{IV:} && w'(L,t) = 0 \end{aligned} \qquad [2.9]$$

This system of equations can be witten as follows (see Appendix B):

$$\mathbf{A} \cdot \mathbf{C} = \mathbf{0} \qquad [2.10]$$

with

$$A = \begin{pmatrix} (\cos\lambda - \cosh\lambda) & (\sin\lambda - \sinh\lambda) \\ -(\sin\lambda + \sinh\lambda) & (\cos\lambda - \cosh\lambda) \end{pmatrix} \qquad [2.11]$$

and

$$\mathbf{C} = \begin{pmatrix} C_1 \\ C_2 \end{pmatrix} \qquad [2.12]$$

A nontrivial solution exists in case that det $\mathbf{A} = 0$ or equivalently

$(\cos\lambda - \cosh\lambda)^2 + (\sin\lambda - \sinh\lambda)(\sin\lambda + \sinh\lambda) = 0$

and finally the condition for the allowed (discrete) λ is as follows:

$$\boxed{\cos\lambda \cosh\lambda = 1} \qquad [2.13]$$

with the solutions $\lambda_1 = 4.730$, $\lambda_2 = 7.853, \ldots$

To complete the calculations we are writing now the space equation

$$X(x) = C_1\left((\cos\frac{\lambda}{L}x - \cosh\frac{\lambda}{L}x) + \Gamma\,(\sin\frac{\lambda}{L}x - \sinh\frac{\lambda}{L}x)\right) \qquad [2.14]$$

with the abbreviation

$$\frac{(\sin\lambda + \sinh\lambda)}{\cos\lambda - \cosh\lambda}) = \Gamma = 0.9825 \text{ for the first mode} \qquad [2.15]$$

which leaves one parameter, C_1, free. It is determined by the initial condition. The amplitude $X(x)$ is known (measured) in the middle of the beam. Thus the following equation determines the constant C_1

$$X(\frac{L}{2}) = C_1\left((\cos\frac{\lambda}{2} - \cosh\frac{\lambda}{2}) + \Gamma\,(\sin\frac{\lambda}{2} - \sinh\frac{\lambda}{2})\right) = C_1 \cdot (1.58815) \qquad [2.16]$$

for the first mode. The resulting space function is shown in Fig. 2.9.

2.3.3. Simple beam with elastic clamping

If the clamping is elastic, the four boundary conditions of a mass-beam system are as follows[2,13] (see Appendix C):

$$\begin{array}{llll} \text{I} & w(0,t) & = c_F\,|F(0)| = c_F\,EJ_y\,|w'''(0,t)| & \\ \text{II} & w'(0,t) & = c_M\,|M(0)| = c_M\,EJ_y\,|w''(0,t)| & [2.17] \\ \text{III} & w(L,t) & = c_F\,|F(L)| = c_F\,EJ_y\,|w'''(L,t)| & \\ \text{IV} & w'(L,t) & = c_M\,|M(L)| = c_M\,EJ_y\,|w''(L,t)| & \end{array}$$

Here F is the transverse force and M is the momentum . c_F and c_M are constants of the elastic resistance against F and M. c_F was calculated for a elastic beam with a linearly decreasing cross section as encountered at anisotropically etched silicon clamping[3] calculated for the symmetrical case (see Fig.2.3. and appendix C), $c_F = \frac{4.5\,\sqrt{2}}{Eb}$, E the modulus of elasticity and b the width of the clamped beam.

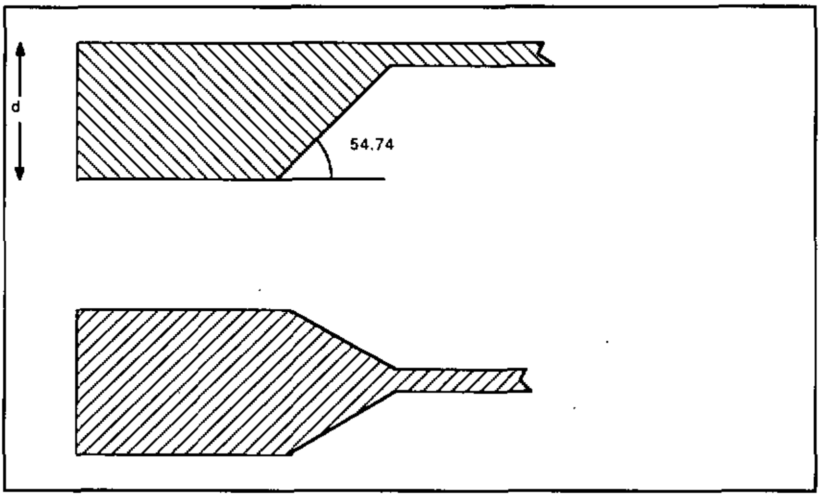

Fig.2.3. Scheme of the clamping part

whereas c_M was taken from the simulation program SENSIM[14] ($c_M = 1 \cdot 10^{-6}\ N^{-1}$). We can thus compare theoretically the influence of an elastic clamping on the eigenvalues as will be presented in the results section 6.5 (Table 6.II).

Now we introduce the following abbreviations:

$$\alpha = c_F\,EJ_y\left(\frac{\lambda}{L}\right)^3 \qquad [2.18]$$

$$\beta = c_M\,EJ_y\left(\frac{\lambda}{L}\right) \qquad [2.19]$$

As above the system [2.10] with :

$$A = \begin{pmatrix} 1 & \alpha & -\alpha & 1 \\ -\beta & 1 & 1 & -\beta \\ (\cos\lambda-\alpha\sin\lambda) & (\sin\lambda+\alpha\cos\lambda) & (\sinh\lambda-\alpha\cosh\lambda) & (\cosh\lambda-\alpha\sinh\lambda) \\ (-\sin\lambda+\beta\cos\lambda) & (\cos\lambda+\beta\sin\lambda) & (\cosh\lambda-\beta\sinh\lambda) & (\sinh\lambda-\beta\cosh\lambda) \end{pmatrix} \qquad [2.20]$$

and

$$C = \begin{pmatrix} C_1 \\ C_2 \\ C_3 \\ C_4 \end{pmatrix} \qquad [2.21]$$

has a solution in case that det **A** = 0.

This determinant is calculated numerically. Special care had to be taken to the numerical determination of the coefficient vector **C** for the singularity of **A** has first to be removed by transformation to a equivalent inhomogeneus system with 3 unknown. Then the system **A'C'** = **B** can be calculated by the well known matrix formalism $\mathbf{A'}^{-1}\mathbf{A'C'} = \mathbf{A'}^{-1}\mathbf{B} \Rightarrow \mathbf{C'} = \mathbf{A'}^{-1}\mathbf{B}$. One parameter (the amplitude) stays arbitrary.

2.3.4. Doubly supported mass

2.3.4.1. Introduction

A static calculation of the equivalent elastic constant of a double side clamped beam with a force applied in the middle ends with the following equation for the resonance frequency ω [11]:

$$\omega = \sqrt{\frac{24\ E'\ J_y}{M\ L^3}} \qquad [2.22]$$

Here $E' = \frac{E}{(1-\nu^2)}$ is the equivalent modulus of elasticity in the appropriate crystal direction corrected by a factor for thin but broad beams (boards),ν is the Poisson's ratio, M is the mass of the mesa, L is the beam length, $J_y = \frac{b\ h^3}{12}$ is the static moment of inertia, b is the beamwidth and h is the beam thickness (see Fig.2.4.)

2.3.4.2. Beam with the inertial mass as a boundary condition

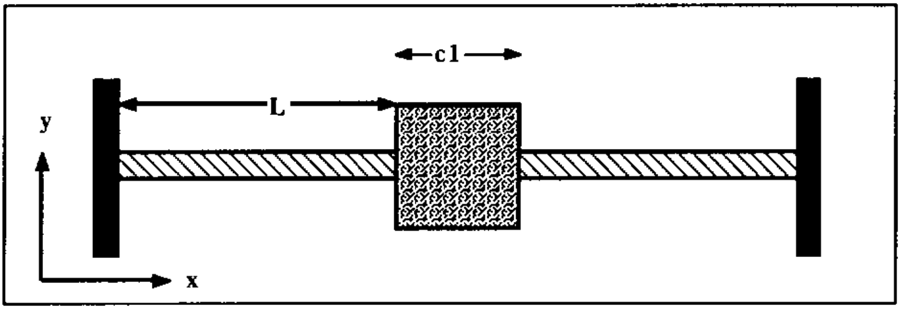

Fig.2.4. The inertial mass as a boundary condition (top view)

We are calculating half of the beam with half of the inertial mass M as the boundary condition. Sandmaier[4] has solved this eigenvalue equation for a similar structure by an approximation and ends with the same equation for the resonant frequency as above ([2.22]). The correct value, however, can be found by calculating the zero values of the determinant of the appropriate matrix **A** numerically as executed above for the other cases of boundary conditions.

The first two boundary conditions (at x=0) stay the same (either [2.9] I,II or [2.17] I,II), whereas at the side of the mass we have for the boundary condition III:

$$\text{III)} \qquad F(L) = EJ_y\ w'''(L,t) = -\frac{M}{2}\ddot{w} = -\frac{M}{2}\left(\frac{EJ_y}{\mu} w''''(L,t)\right) \qquad [2.23]$$

where M is the total mass of the mesa and for the boundary condition IV:

$$\text{IV)} \qquad w'(L,t) = 0$$

as in the simple case ([2.9] IV).

Again we can distinguish between rigid and elastic boundary conditions at the clamping side of the system, which is done in the following two paragraphs.

2.3.4.2.1. Rigid clamping

In this case the matrix **A** can be calculated to be (see appendix D) ([2.24]):

$$\mathbf{A} = \begin{pmatrix} (\sin\lambda-\sinh\lambda)-\frac{M\lambda}{2\mu L}(\cosh\lambda-\cos\lambda) & -(\cos\lambda+\cosh\lambda)-\frac{M\lambda}{2\mu L}(\sinh\lambda-\sin\lambda) \\ -(\sin\lambda+\sinh\lambda) & (\cos\lambda-\cosh\lambda) \end{pmatrix}$$

With again the condition that this matrix must be zero, we end with the following equation

$$\boxed{\frac{\mu L}{M} = \frac{\lambda}{2}\,\frac{\{1-\cos\lambda\cosh\lambda\}}{(\cos\lambda\sinh\lambda+\cosh\lambda\sin\lambda)}} \qquad [2.25]$$

Thus λ depends,- besides its discretization-, on the ratio of beam mass μL and supported mass M. This function is plotted in Fig. 2.8. for the first eigenvalue λ_1.

2.3.4.2.2. Elastic clamping

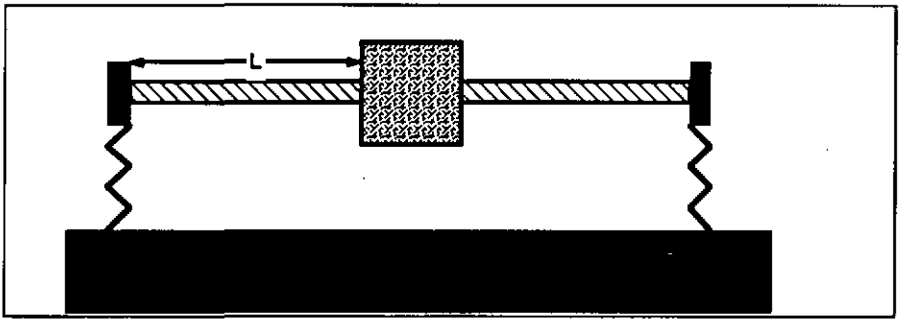

Fig.2.5. Doubly supported mass with elastic clamping

The complete set of the four boundary conditions is in this case now:

$$\begin{array}{llll}
\text{I} & w(0,t) & = c_F\,|F(0)| & = c_F\,EJ_y\,|w'''(0,t)| \\
\text{II} & w'(0,t) & = c_M\,|M(0)| & = c_M\,EJ_y\,|w''(0,t)| \\
\text{III} & F(L) & = EJ_y\;w'''(L,t) & = -\frac{M}{2}\,\ddot{w} = -\frac{M}{2}\left(\frac{EJ_y}{\mu}\,w''''(L,t)\right) \\
\text{IV} & w'(a,t) & = 0 &
\end{array} \qquad [2.26]$$

where M is again the total mass of the supported mesa. From the boundary conditions [2.26] follows:

$$\begin{array}{ll}
\textbf{I} & C_1 + \alpha C_2 - \alpha C_3 + C_4 = 0 \\
\textbf{II} & -\beta C_1 + C_2 + C_3 - \beta C_4 = 0 \\
\textbf{III} & C_1\sin\lambda - C_2\cos\lambda + C_3\cosh\lambda + C_4\sinh\lambda \\
 & +\frac{M\lambda}{2\mu L}\{C_1\cos\lambda + C_2\sin\lambda + C_3\sinh\lambda + C_4\cosh\lambda\} = 0 \\
\textbf{IV} & -C_1\sin\lambda + C_2\cos\lambda + C_3\cosh\lambda + C_4\sinh\lambda = 0
\end{array} \qquad [2.27]$$

Again we can write this system of equation in a matrix form as [2.10] with ([2.28]):

$$A = \begin{pmatrix} 1 & \alpha & -\alpha & 1 \\ -\beta & 1 & 1 & -\beta \\ (\sin\lambda+\frac{M\lambda}{2\mu L}\cos\lambda) & -(\cos\lambda+\frac{M\lambda}{2\mu L}\sin\lambda) & (\cosh\lambda+\frac{M\lambda}{2\mu L}\sinh\lambda) & (\sinh\lambda+\frac{M\lambda}{2\mu L}\cosh\lambda) \\ -\sin\lambda & \cos\lambda & \cosh\lambda & \sinh\lambda \end{pmatrix}$$

and **C** as [2.21].The zeros of this determinant A are calculated numerically. Γ is formally the same as in the simple beam case [2.15]. Thus X(x) is determined (cf. Fig.2.9.). The higher zero points follow periodically as shown in Fig. 2.6.

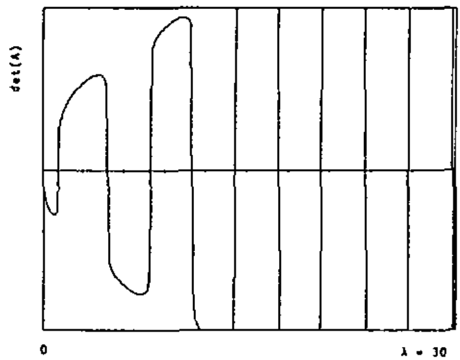

Fig.2.6. The periodicity of the zeros of the determinant in dependance of λ for a double supported mass. In case of a simple beam without mass in the middle the first zero disappears and the one at 4.73 becomes the relevant for the lowest frequency.

2.3.5. Simply supported mass

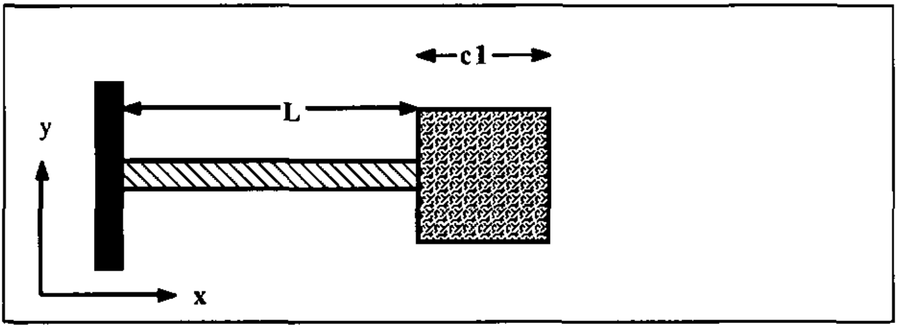

Fig.2.7. Simply supported mass (top view).

In the case of a simply supported mass, the mass rotates and we have instead of equation [2.26] IV (see Appendix E):

$$\text{IV:}\quad M(L) = EJ_y\, w''(L,t) = \Theta_o \frac{\partial^2 w'(L,t)}{\partial t^2} \Leftrightarrow X''(L) = \gamma X'(L) \qquad [2.29]$$

with the abbreviation :

$$\gamma = \frac{\Theta_o\, \omega^2}{EJ_y} \qquad [2.30]$$

and

Θ_o = the inertial moment of the proof mass.

Thus by replacing the last row in the matrix for the doubly supported mass with elastic clamping we have [2.31]:

$$A := \begin{pmatrix} 1 & \alpha & -\alpha & 1 \\ -\beta & 1 & 1 & -\beta \\ (\sin\lambda + \frac{M\lambda}{\mu L}\cos\lambda) & -(\cos\lambda + \frac{M\lambda}{\mu L}\sin\lambda) & (\cosh\lambda + \frac{M\lambda}{\mu L}\sinh\lambda) & (\sinh\lambda + \frac{M\lambda}{\mu L}\cosh\lambda) \\ \left(\gamma\sin\lambda - \frac{\lambda}{L}\cos\lambda\right) & \left(\gamma\cos\lambda - \frac{\lambda}{L}\sin\lambda\right) & -\left(\gamma\cosh\lambda + \frac{\lambda}{L}\sinh\lambda\right) & \left(\frac{\lambda}{L}\cosh\lambda - \gamma\sinh\lambda\right) \end{pmatrix}$$

We calculated for an accelerometer type structure (simply clamped short beam, see Chapter 6) the resonance frequency to compare different methods (see Table 2.1).

Table 2.I. Comparision between different methods for the calculation of the resonance frequency of an accelerometer with one beam (beam length 1.2mm, beam thickness 39 μm, beam width 1mm, mass of the proof mass 5.3 μg).

	f [Hz]
Rayleigh method (Roylance[5], Szabo[6])	901.23
calculation with equivalent spring constant	1084.95
eigenvaluemethod with inelastic clamping[7]	900.793
eigenvaluemethod with elastic clamping	900.790
measured frequency in air	898.

The Rayleigh method gives an upper bound and lies therefore above the value of the direct method. The static calculation neglects the influence of the time dependence of the boundary conditions. As can be seen the admission of elastic clamping has a relatively small effect on the resonance frequency.

Fig.2.8. shows λ as a function of the mass ratio of beam and proof mass for a simply and a doubly clamped proof mass. The upper straight line a) represents λ for the simple clamped clamped beam (not mass dependent). Elastic clamping changes λ little and wouldn't be distiguishable in this representation.

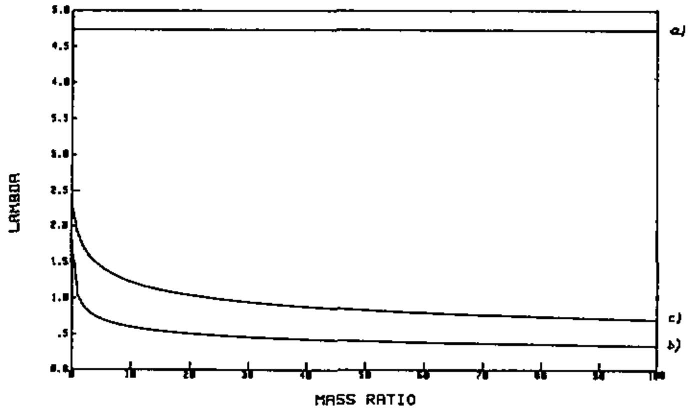

Fig.2.8. λ as a function of the mass ratio of beam and proof mass for a) a clamped-clamped beam without a discrete mass , b) a simply and c) a doubly clamped proof mass.

When the mass ratio is zero (i.e. the proof mass is infinite) the doubly clamped structure has exactly the same boundary conditions as a simple clamped-clamped beam with half the length. Thus λ of curve c) is then half the value of curve a) at mass ratio zero.

Fig 2.9. shows the displacement function X(x) for a simple clamped-clamped beam with and without a proof mass for the condition of the structures of chapter 6. One can see that the beam with the supplementary proof mass is bent a little more than the simple beam for the same amplitude. On has the consider only the left part because by assumption we calculated the curve for the mass beam system for one side only and the rigth side is therefore out of range. It is left for illustration in the plot stressing thus on the fact that we have two different calculation methods. The proof mass distorts the undisturbed beam towards a triangular shape, but the difference is actually small.

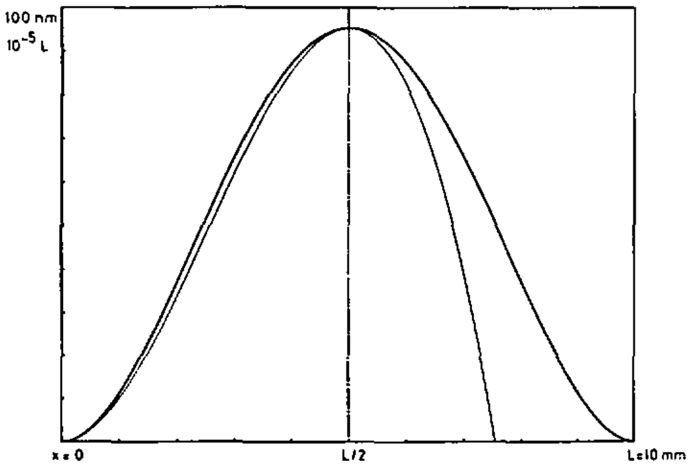

Fig. 2.9. The function X(x) for a simple clamped-clamped beam and a beom with a proof mass with a mass ratio of about ten, a length of the beam of L=10mm and a maximal amplitude of 100nm or 10^{-5}L. The thickness of the beam was assumed to be 60 μm and the proof mass 5.5mg (structure from chapter 6).

2.3.6. Structures with compensated forces and moments at the boundary

The eigenfrequencies of this type of structure are calculated the same manner as for the doubly supported mass. The ideas and the calculations of the compensation itself are treated in chapter 7.

2.3.7. Torsion

The equation for a torsional motion with $\theta(x,t)$ as the angle of torsion is as follows:[8]

$$\frac{\partial^2\theta(x,t)}{\partial t^2} = \frac{G\,J_t}{\Theta}\frac{\partial^2\theta(x,t)}{\partial x^2} = c^2\,\frac{\partial^2\theta(x,t)}{\partial x^2} \qquad [2.32]$$

with

$c = \sqrt{\frac{G\,J_t}{\Theta}}$, the velocity of the torsional motion

$\Theta_{bar} = \Theta L$ inertial moment of the bar

L= length of the torsional bar

J_t = Static moment of inertia

G = Shear modulus

The boundary conditions (only two, because of the second derivative) are:

I: $\theta(0,t) = 0$ clamping

$$\text{II:}\quad Mt(L,t) = G\,J_t\frac{\partial\theta(L,t)}{\partial x} = -\,\Theta_o\frac{\partial^2\theta(L,t)}{\partial t^2} \qquad [2.33]$$

Θ_o = Moment of inertia of the end mass

A factorial ansatz and $-\omega^2$ as the separation constant results in the following solution:

$$\theta(x,t) = (A\cos\omega t + B\sin\omega t)(C\cos\frac{\omega}{c}x + D\,\text{sind}\,\frac{\omega}{c}x) \qquad [2.34]$$

The boundary and initial conditions define now the constants A,B,C and D. The boundary condition I leads to C=0 and thus D = 1 without lost of generality.The boundary condition II presents then as follows:

$$\text{II}\qquad \frac{\partial\theta(L,t)}{\partial x} = -\,\frac{\Theta_o}{G\,J_t}\frac{\partial^2\theta(L,t)}{\partial t^2} = -\,\frac{\Theta_o}{\Theta c^2}\frac{\partial^2\theta(L,t)}{\partial t^2} \qquad [2.35]$$

This results in

$$(A\cos\omega t + B\sin\omega t)\,\frac{\omega}{c}\cos\frac{\omega}{c}L = +\,\frac{\Theta_o}{\Theta c^2}\,(A\;\omega^2\cos\omega t + B\,\omega^2\;\sin\omega t)\sin\frac{\omega}{c}L$$

$$\Rightarrow \frac{\omega}{c}\cos\frac{\omega}{c}L = +\frac{\Theta_o}{\Theta c^2}\ \omega^2 \sin\frac{\omega}{c}L$$

$$\Rightarrow \cos\frac{\omega}{c}L = +\frac{\Theta_o}{L\Theta}\frac{L\omega}{c}\ \sin\frac{\omega}{c}L \qquad [2.36]$$

with the abbreviations

$$\zeta = \frac{\omega}{c}L \qquad [2.37]$$

and

$$\kappa = \frac{\Theta_{bar}}{\Theta_o} \qquad [2.38]$$

we can rewrite [2.36] as

$$\zeta \operatorname{tg} \zeta = \kappa, \qquad [2.39]$$

which is a transcendental equation for ζ having discrete solutions ζ_i and thus by [2.37] we find for the resonance frequencies:

$$\omega_i = \frac{\zeta_i\, c}{L} \qquad [2.40]$$

For small κ's (i.e. thin beams and large endmass), equation [2.39] can be approximated by the following formula[9]:

$$\zeta_1 = \sqrt{\frac{3\kappa}{3+\kappa}} \qquad [2.41]$$

The first resonance frequency of a bar with a relatively large end mass can be thus written as

$$\boxed{f_1 = \frac{1}{2\pi}\sqrt{\frac{J_t}{\Theta_{bar}\, L}\left(\frac{3\kappa}{3+\kappa}\right)}} \qquad [2.42]$$

J_t depends on the dimensions and the shape of the cross section of the bar. For an elliptical cross section (including circular) J_t is $J_t = \frac{\pi\, a^3 b^3}{a^2 + b^2}$, a and b the major and minor axis of the ellipse respectively. Other cross sections (like rectangular) have to be approximated. For a thin rectangular cross section (b » h), as we have with the structures in chapter 6, Szabo[10] gives the following approximation for J_t:

$$J_t = \frac{5}{18} h b^3 \qquad [2.43]$$

In appendix F, we did the calculation for a mass beam system.

2.3.8. Beam covered by a layer

The following section develops a theory of a beam covered with a supplementary layer by starting with the combined beam theory of Timoshenko[11]. We are first calculating the position h_1 of the neutral axis of such a beam

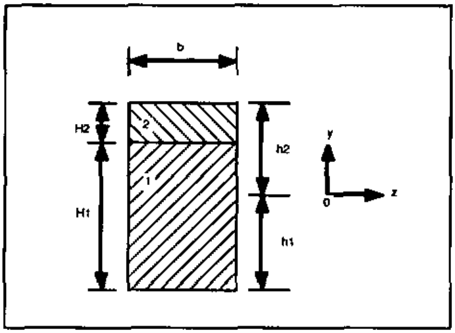

Fig.2.10. Cross section of a combined beam with the neutral axes at the heigth h_1.

The total force on the cross section contributed by the region 1 , defined by $H_1 \times b$ (see Fig.2.10.), and the region 2, defined by $H_2 \times b$, with $H_1 > H_2$ are calculated as follows:

region 1:

$$E_1 \int_1 y\, dA = E_1 \int_{-b/2}^{b/2} dx \int_{-h_1}^{H_1-h_1} y\, dy = E_1 b \int_{-h_1}^{H_1-h_1} y\, dy = E_1 b \left[\frac{y^2}{2}\right]_{-h_1}^{H_1-h_1} =$$

$$= E_1 b \left\{\frac{(H_1-h_1)^2 - (h_1)^2}{2}\right\} = E_1 b H_1 \left\{\frac{H_1}{2} - h_1\right\} \qquad [2.44]$$

region 2:

$$E_2 \int_2 y\, dA = E_2 \int_{-b/2}^{b/2} dx \int_{H_2-h_2}^{-h_2} y\, dy = E_2 b \int_{H_2-h_2}^{-h_2} y\, dy = E_2 b \left[\frac{y^2}{2}\right]_{H_2-h_2}^{-h_2} =$$

$$= -E_2 b \left\{\frac{(H_2-h_2)^2 - (h_2)^2}{2}\right\} = -E_2 b H_2 \left\{\frac{H_2}{2} - h_2\right\} \qquad [2.45]$$

By definition we have

$H_1 + H_2 = h_1 + h_2 \Rightarrow h_2 = H_1 + H_2 - h_1$

Substituting h_2 in [2.45] we obtain

$$E_2 \int_2 y\, dA = E_2 b H_2 \left\{\frac{H_2}{2} + H_1 - h_1\right\} \qquad [2.46]$$

Because the total force on the cross section has to be zero,

$E_1 \int_1 y\, dA + E_2 \int_2 y\, dA = 0$, we can calculate h_1 from [2.44] and [2.46].

We are transforming the resulting equation

$$E_1 b H_1\left\{\frac{H_1}{2} - h_1\right\} + E_2 b H_2\left\{\frac{H_2}{2} + H_1 - h_1\right\} = 0$$

to an explicit form for h_1:

$$\frac{E_1 H_1}{E_2 H_2}\left\{\frac{H_1}{2} - h_1\right\} + \left\{\frac{H_2}{2} + H_1 - h_1\right\} = 0$$

or

$$\frac{E_1 H_1}{E_2 H_2}\left(\frac{H_1}{2}\right) + \frac{H_2}{2} + H_1 = h_1\left(1 + \frac{E_1 H_1}{E_2 H_2}\right)$$

and that

$$\frac{\frac{E_1 H_1}{E_2 H_2}\left(\frac{H_1}{2}\right) + \frac{H_2}{2} + H_1}{\left(1 + \frac{E_1 H_1}{E_2 H_2}\right)} = h_1$$

$$\Rightarrow \boxed{h_1 = \frac{E_1 H_1\left(\frac{H_1}{2}\right) + E_2 H_2\left(\frac{H_2}{2} + H_1\right)}{(E_2 H_2 + E_1 H_1)}} \qquad [2.47]$$

The statical moment J_1 for the region 1 with respect to the neutral axis is with the theorem of Steiner (EULER):

$$J_1 = J_o + F a^2 = \frac{b H_1^3}{12} + H_1 b\left(h_1 - \frac{H_1}{2}\right)^2 \qquad [2.48]$$

and simularly the static moment for the region 2:

$$J_2 = \frac{b H_2^3}{12} + H_2 b\left(h_2 - \frac{H_2}{2}\right)^2 = \frac{b H_2^3}{12} + H_2 b\left(H_1 + \frac{H_2}{2} - h_1\right)^2 \qquad [2.49]$$

We are going now to develop the DE for the combined beam. The relation of the elastical line w(x) of a beam with the applied momentum is with the usual simplification $w'' = \frac{1}{r}$, r the bending radius, as follows [12]

$$w''(x) = \frac{M(x)}{E_1 J_1 + E_2 J_2} \qquad [2.50]$$

with [13]

$$\frac{d^2 M(x)}{dx^2} = - q(x)$$

and

$q(x) = \mu(x)\,\ddot{w}(x)$

$\mu(x) = \rho_1 A_1 + \rho_2 A_2$ the total mass per unit length, ρ and A the density and the area of the two materials respectively, we obtain the following equation of motion :

$$\boxed{(E_1J_1 + E_2J_2)w''''(x) = -\mu\,\ddot{w}(x)} \qquad [2.51]$$

Thus the equation of motion is the same as for an simple beam [2.3.] with the exception that λ is now defined by

$$\lambda^4 = \frac{\mu\,\omega^2}{(E_1J_{y1}+E_2J_{y2})}L^4 \qquad [2.52a]$$

and thus the resonance frequency of the covered beam

$$\boxed{\omega_{cov} = \left(\frac{\lambda}{L}\right)^2 \sqrt{\frac{(E_1J_{y1}+E_2J_{y2})}{\mu}}} \qquad [2.52b]$$

2.3.9. Elastic energy of a beam under dynamical deformation

In order to estimate the energy loss per cycle one has to know the total energy stored in the system. This is for an elastic beam[14]

$$U = \frac{EJ}{2}\int_0^L X''^2 dx \qquad [2.53]$$

In the case of a pinned pinned beam the space equation is as follows

$$X(x) = C_1 \sin\left(\frac{\pi}{L}x\right) \qquad [2.54]$$

C_1 the amplitude in the middle of the beam and thus the second derivative of [2.54]

$$X''(x) = -C_1\left(\frac{\pi}{L}\right)^2 \sin\left(\frac{\pi}{L}x\right) \qquad [2.55]$$

The energy [2.53] for a pinned-pinned beam becomes then

$$U_{pp} = \frac{EJ}{2}C_1^2\left(\frac{\pi}{L}\right)^4 \int_0^L \left[\sin\left(\frac{\pi}{L}x\right)\right]^2 dx = \frac{EJ}{2}C_1^2\left(\frac{\pi}{L}\right)^4\left[\frac{x}{2} - \frac{L}{4\pi}\sin\left(\frac{2\pi}{L}x\right)\right]_{x=0}^{x=L} =$$

$$\boxed{U_{pp} = \frac{EJ}{2}C_1^2\left(\frac{\pi}{L}\right)^4 \frac{L}{2}} \qquad [2.55]$$

For the clamped clamped beam the direct calculation would become somewhat more extensive. But it can be shown by partial integration and using the homogeneus boundary conditions that the functions X_i'' are orthonormal[15], moreover

$$\int_0^L X''^2 dx = \int_0^L X^2 dx = L \qquad [2.56]$$

thus

$$\boxed{U_{cc} = \frac{EJ}{2}\left(\frac{\lambda}{L}\right)^4 C_1^2 \quad L} \qquad [2.57]$$

C_1 is here no longer the amplitude A_o at the middle of the beam but
$C_1 = 0.6297 \cdot A_o$

We can thus calculate the ratio of the energies between a clamped-clamped beam U_{cc} and a pinned-pinned one U_{pp} for the same amplitude in the middle of the beam to be

$$\frac{U_{cc}}{U_{pp}} = 3.983$$

with the same dimensions but its natural frequency 2.266 times higher than the pinned one. Corrected by this factor we have for the ratio

$$\frac{U_{cc}}{U_{pp}} = 1.758$$

This is natural from the fact that the curvature (a measure for the strain) is more pronounced in the clamped beam than in the pinned one.

For a mass beam system, the simple orthogonality [2.56] no longer holds. The integrated term of the partial integration disappears only in the case of homogeneous boundary conditions. We have to execute then the full integration of the square of the second derivative which is given in the appendix G with the result shown below.

The integral [2.56] without the factor $\left(\frac{\lambda}{L}\right)^4 C_1^2$ and Γ as defined in [2.15] becomes

then ([2.58])

$$\boxed{L\left(1+\frac{\Gamma}{\lambda}\{\sin\lambda+\sinh\lambda\}^2+\frac{1}{\lambda}\{[\frac{\sin\lambda}{2}+\sinh\lambda]\cos\lambda(1-\Gamma^2)+(1+\Gamma^2)\cosh\lambda[(\sin\lambda+\frac{\sinh\lambda}{2}]\}\right)}$$

Both the simple beam and the mass-beam can be brougth to an equal formal expression for X(x), when we use the singularity of the systems to eliminate this equation (or row in A) which originates from the changed boundary condition (nr. III). Only λ is different of course. Thus, expression [2.58] should hold for both cases, what we checked numerically by finding that it equals L in the case of a simple beam.

In the case of a simply supported mass (accelerometer) two boundary conditions have to be changed and one has to replace then Γ by

$$\Gamma = \frac{A_{11}}{A_{12}} = \frac{A_{21}}{A_{22}} = \frac{\left(\sin\lambda + \frac{M\lambda}{\mu l}\cos\lambda - \sinh\lambda - \frac{M\lambda}{\mu l}\cosh\lambda\right)}{\left(-\cos\lambda - \frac{M\lambda}{\mu l}\sin\lambda - \cosh\lambda - \frac{M\lambda}{\mu l}\sinh\lambda\right)}$$

$$= \frac{\left(\gamma \sin\lambda - \frac{\lambda}{l}\cos\lambda - \frac{\lambda}{l}\cosh\lambda + \gamma \sinh\lambda\right)}{\left(\gamma \cos\lambda - \frac{\lambda}{l}\sin\lambda + \gamma \cosh\lambda + \frac{\lambda}{l}\sinh\lambda\right)} \qquad [2.59]$$

(see appendix E.)

1 Szabo I.; Höhere Technische Mechanik, Springer Verlag Berlin, 1977, 5 th ed. p. 79
2 Timoshenko, S., Young, D.H., Weaver, W Jr.: Vibration problems in Engineering, 4th ed.John Wiley & Sons, New York.1974 p.455
3 Szabo, I.; Einführung in die Technische Mechanik, Springer, Berlin, 8th ed.,1984, p.173
4 Sandmaier, H., Kühl, K., Obermeier, E.: A silicon based micromechanical accelerometer with cross acceleration sensitivity compensation, Transducers '87, 4th Int. Conf. on Solid-state Sensors and Actuators, Tokyo, 1987.
5 Roylance, L.M.; A Miniature integrated circuit accelerometer for biomedical applications. Integrated circuits laboratory, Atansford University, Standford, CA 94305, Technical Report No 4603-2,November 1977.
6 Szabo I.; Höhere Technische Mechanik, Springer Verlag Berlin, 1977, 5 th ed. p. 85
7 Present work
and
Seidel, H., Csepregi, L.; Design Optimization for Cantilever-Type Accelerometers, Sensors and actuators 6(1984) 81-92.
8 Szabo I.; Höhere Technische Mechanik, Springer Verlag, Berlin, 1977, 5 th ed. p. 78
9 ibid., p. 77
10 ibid., p.283
11 Timoshenko, S.; Mechanics of materials, Nostrand, 1972.
12 ibid., p 145.
13 Szabo, I.; Einführung in die Technische Mechanik, Springer, Berlin, 8th ed.,1984, p. 73
14 Bishop, R.E.D., Johnson D.C.: The Mechanics of Vibration, Cambridge University press, Cambridge, 1979.
15 ibid.

2.4. Damping

2.4.1. Introduction

On damped structures we have to distinguish between

i) damping of the elastic element (beam or membrane).
This includes energy loss into gas (external damping) either by viscous or turbulent flow, acoustic radiation, exchange of momentum and internal damping by thermoelastic coupling (entropy flow) and defects of the crystal (internal friction) or also by supplementary layers or surface texture

ii) the damping of rigid elements like paddles.
Here we have the same external damping mechanism as for the beam. Such a damping can be replaced by a discrete damping element (e.g. a dashpot, see Fig.2.11.). In that case a term weighted by a Dirac function has to be added to the DE instead of just a simple damping term per unit length as in case i).

iii) the damping of the clamping.
Here the damping of the medium is very small because of the small amplitude of the clamping and we have to consider only the radiation of elastic waves into to frame (the fraction of the elastic wave not rejected)

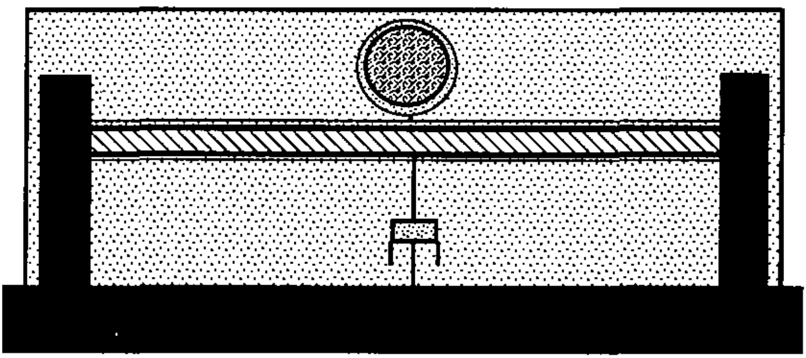

Fig.2.11. Complete model of a mass beam system with proportional and discrete damping as well as added inertial mass to the beam and the mass.

Baker[1] includes for macroscopic beams the air damping at atmospheric pressure (1 bar) for calculating the logarithmic decrement (only energy expressions). His formalisms for distinguished damping proportional to velocity for small amplitudes and proportional to the square of the velocity for large amplitudes as well as that for including internal damping of different types are quite helpful. But he gives no physical explanation for the constants he used. Direct comparison of the air damping is thus difficult, because we have quite different dimensions (100 times smaller)

Blake[2] gives a theoretical treatment of acoustic radiation from free free beams in air and water. Here, too, the application is prohibited because of the assumptions of the same large structures.

Jeyapalan[3]. works out a little bit more the limitations but the assumption are tacitly large structures and atmospheric pressure, too.

Drawin[4] derives the damping for the molecular region, but recommends empirical factors for the other regions.

Coolidge[5] has obviously measured objects with similar dimensions as ours also in the higher pressure range, but he uses an empirical constant to caracterize the viscous damping, too

Christian[6] gives a somewhat more precise derivation for the damping force at low densities by applying the Maxwell-Boltzmann distributed velocities instead of just a mean velocity resulting in the same dependency of pressure and temperature but with somewhat different constants. We are going to use this approach for the low pressure range.

Tough[7] describes for the viscous region on the model of a oscillating cylinder the damping forces and the hydrodynamic effective mass. We are going to use this approach for the high pressure range.

In the following paragraphs we are developing first the mathematical tools for damped mass beam systems (beams with discrete elements, see Fig.2.11.), analyzing then the nature of the damping to find physical expressions for the damping constants and ending with the complete modeling of the damped system.

2.4.2. Proportional damping (constant cross section beam)

2.4.2.1. General equations

When damping proportional to speed (and a constant cross section of the beam is assumed) is included the DE [2.3] extends to:

$$E\,J_y \frac{\partial^4 w(x,t)}{\partial x^4} = -\mu \frac{\partial^2 w(x,t)}{\partial t^2} - \xi \frac{\partial w(x,t)}{\partial t} \qquad [2.60]$$

where ξ is the damping per unit length.

The same procedure of separation as described in section 2.3. leads to the same space equation [2.4], and to the following time equation:

$$\frac{d^2T(t)}{dt^2} + \frac{\xi}{\mu}\frac{dT(t)}{dt} + \omega_o^2\, T(t) = 0 \qquad [2.61]$$

This equation is formally equal to a simple damped harmonic oscillator. In standard textbooks on mechanics (Lifschitz[8]) the following abbreviation for a simple hamonic oscillator is introduced:

$$\beta = \xi/2\mu \qquad [2.62]$$

Then the solution of the time equation reads as follows:

$$T(t) = A\, e^{-\beta t} \cos(\omega t + \alpha) \qquad [2.63]$$

where

$$\omega^2 = \omega_o^2 - \beta^2 \qquad [2.64]$$

α = the phase

The quality-factor Q as beeing the ratio of the stored energy in the resonator to the energy lost in the time $1/\omega$ writes as follows[9]

$$Q = \frac{\omega}{2\beta} \qquad [2.65]$$

and thus

$$\beta = \frac{\pi f}{Q} \qquad [2.66]$$

where f is the frequency $\omega/2\pi$

In case of a beam with constant cross section and a high Q-factor we may write also:

$$\xi = 2f\pi\rho \cdot bh/Q \qquad [2.67]$$

b the beam width

h the beam heigth

ρ the density

2.4.2.2. Resonance frequency in an atmosphere of gas

In an atmosphere of gas, several forces act on the resonator, which have to be taken into account in the DE. Not the damping itselself causes the observed strong dependance of the frequency on pressure, but the additional mass χ of the gas molecules to be accelerated. Thus the DE for the vibrating beam has to be extended to:

$$EJ_y \frac{\partial^4 w(x,t)}{\partial x^4} = (\mu+\chi)\, \frac{\partial^2 w(x,t)}{\partial t^2} - \xi \frac{\partial w(x,t)}{\partial t} \qquad [2.68]$$

Formally this is equal to [2.60] we have just to replace [2.62] by

$$\beta = \xi/(\mu + \chi) \qquad [2.69]$$

2.4.2.3. Additional layer

Apart from the additional mass and the changed modulus of elasticity (both will affect the frequency, cf. section 2.3.8) additional internal friction is added i.e. a supplementary term in ξ. In the case of proportional damping, it follows from the definitions [2.62] and [2.65] that ξ is inversionally proportional to Q, which means that in such a model the inverse of the Qs are additive:

$$1/Q_{tot} = 1/Q_1 + 1/Q_2 + \ldots \qquad [2.70]$$

This is experimentally proved in chapter 6.

2.4.3. Non-proportional damping and modal analysis

2.4.3.1. Introduction

Taking the same system as described in section 2.3.4. in the case with no damping and extending the DE as in equation [2.60] to take into account the damping of the beam, the boundary condition [2.23] has to be changed as follows: With $\frac{\Xi}{2}\dot{w}$ (L,t) as the damping force of the proof mass M the corresponding boundary condition III becomes

$$\text{III:} \qquad F(L) = EJ_y\ w'''(L,t) = -\frac{M}{2}\ddot{w}(L,t) + \frac{\Xi}{2}\dot{w}(L,t) \qquad [2.71]$$

whereas the other ones stay as [2.9] I,II,IV. The method, we used in section 2.3.4. by setting the DE [2.3] respectively [2.60] into the boundary condition [2.23] to eliminate the time derivative, can no longer be applied, since only either $\ddot{w}(L,t)$ or $\dot{w}$ (L,t) can be eliminated.

The method of modal analysis is more appropriate in the case of non-proportional damping. However, these calculations make typically extended use of matrix calculations and thus numerical methods. As stated in the introduction to this chapter a method was developed by Jacquot[10] to avoid for simple cases these numerical approaches by using symbolic functions and integraltransformations. The singular behaviour (see next paragraph), that prohibits a representation in the Fourier space and even more the back transformation, is cancelled in the case of Laplace transformation by the initial function, which has to be included. Moreover our calculations end with a symbolic equation in the Laplace space. Even the back transformation may be performed by noting that the end formula is actually a ratio of two ploynomials in s multiplied by a function of the space. To execute the back transformation we have to know the zeros of the denominator's polynomial p(s). Because all the coefficients are real values (this can be guaranteed here because they are still the original physical parameters) these zeros are real or complex conjugates. When they are real, the polynomials are real, too, and there is no problem of interpretation. If they appear in pairs of conjugate numbers, the polynomials are conjugate, too, and the real periodical functions (sin and cos) may be formed, which have an evident interpretation (see Adkins[11]). Thus the decision of the degree of the approximation, the values of the parameters and the kind of the modes of the undisturbed system (the boundary conditions e.g.) is taken but just before the back transformation, which ends in the solution in time and space.

In a first order approximation we can even represent the solution symbolically which gives a direct insight in the main dependence of the solution on the physical parameters. This first approximation shows an amazing simplicity for the interpretation. In the exponential factor the mass of the beam and that of the damping system are added together with a weighting factor for the concentrated mass. The same holds for the damping coefficients. The frequency (Ω) takes into account the ratio of the beam mass to the total mass.

2.4.3.2. Modal analysis with Fourier transformation

The problem of this method is the singular behavior of the equation (Wahle[12])

$$W(r,\lambda) = - Z(\lambda)\, W(r_M, \lambda) \sum_{k=1}^{\infty} Y_k(\lambda)\, \phi_k(r_M)\, \phi_k(r) \qquad [2.72]$$

with W the deflection

λ the eigenvalue

Z the impedance of the descrete system

Y a function $Y(\omega) \sim \dfrac{1}{\omega_i^2 - \omega^2}$ cf. section 2.4.3.3.

r the position on the beam

r_M the position of the discrete system

ϕ_k the eigenfunctions of the undisturbed system.

which can not be solved for $W(r_M,\lambda)$. This prevents a representation in the Fourier space and even more the backtransformation for this our free decay case, which is natural because the Fourier transformation is fitted to find response to periodic excitations (steady state), not transient cases. Therefore we are left with complex frequencies which are rather hard to interpret.

We developed however a computer program to find numerically the complex and real parts of the eigenfrequency ω. Hereby the following , numerical problem arises: Since we have a complex function of a complex variable of which we have to find the zero : $\mathbb{C} \rightarrow \mathbb{C}$,$W(\omega)$, we have to scan in the hole complex plane and checking for each point real and imaginary part of W to be zero[13]. One can simplify this procedure a little bit by checking only the magnitude of the complex vector.

Moreover, one can consider the additional mass and damping as a disturbance of the simple clamped clamped beam, who's eigenvalues have to be calculated anyway. Thus the real part should be somewhere in the surrounding of the undisturbed eigenvalue and the imaginary part somewhere around zero (small damping). This implies, that we have to find zeros in the vincinity of a pole (because of the function $Y(\omega) \sim \frac{1}{\omega_i^2 - \omega^2}$, cf. next section) numerically a rather uncomfortable situation, which even fails in the case of $Z(\omega) \approx 0$ (zero mechanical impedance)

As an example we are presenting in Table II the calculations of the structure described in chapter 6. We limited the sum of the above formula to 100 and neglected the damping.

Table 2.II. Theoretical eigenvalues of different methods for a mass beam system with abeam thickness of 60μm and a thickness of the proof mass 380μm and a beam length of 4mm

eigenfrequency of the beam without proof mass: $\omega_1/2\pi$	3620.47 Hz
eigenfrequency calculated with the formula [2.22]	2372.36 Hz
eigenfrequency calculated with the method developed in the section 2.3.	2286.12 Hz
real part with the method from above	2456.92 Hz

This shows, that this method gives a too high resonance frequency, which is compared to the expense (a sum of 100 for each iteration step in the complex plane) quite disappointing. The advantage is however the possibility to include the damping. This may be helpfull when the character of the damping is investigated. This situation (for the frequency calculations) is similar to that developed in the next section.

2.4.3.3. Modal analysis with Laplace transformation

This analysis follows the description of Jacquot[14] for the Fourier transformation quite closely. The general equation of a beam vibrating transversally with damping and forces is

$$\underline{L}[w(\mathbf{r},t)] + c(\mathbf{r})\,\dot{w}(\mathbf{r},t) + m(\mathbf{r})\,\ddot{w}(\mathbf{r},t) = g(\mathbf{r},t) + \sum_{k=1}^{n} f_k(t)\,\delta(\mathbf{r}-\mathbf{r}_k) \qquad [2.73]$$

with

$\underline{L} : \nabla\,(E\,J\,(\mathbf{r}))\nabla$

m: effective mass per unit length of the beam $m = \mu + \chi + \ldots$

g : distributed force

f_k: point force

E : Modul of Elasticity

J : static moment of inertia

In our case we confine us to a homogeneous Euler-Bernoulli beam with one external point force, introduced in the DE by a the delta function δ:

$$\underline{L}[w(r,t)] + c\,\dot{w}(r,t) + m\,\ddot{w}(r,t) = f_1(t)\,\delta(r-r_1) \quad [2.74]$$

$$\underline{L} : E\,J\,\frac{\partial^4}{\partial r^4}$$

First we are developing the eigenfuntions ϕ_i of the undisturbed (homogeneous) system. This problem was actually solved in section 2.3. for various boundary conditions. We repeat here the results in a concise notation.

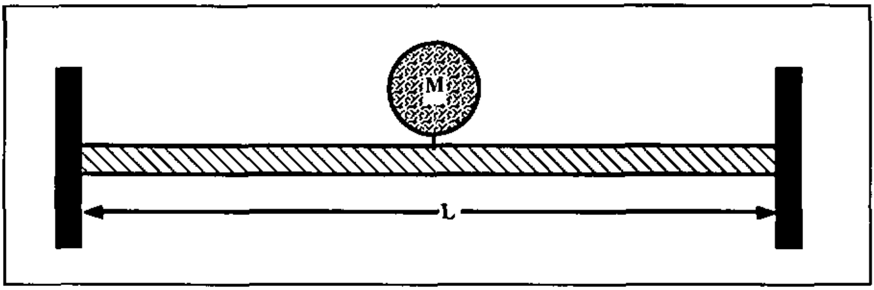

Fig.2.12. A simple beam with a discrete element attached to it in the middle.

The homogeneous equation

$$\underline{L}[w(r,t)] + m\,\ddot{w}(r,t) = 0 \quad [2.75]$$

with appropriate boundary conditions:

$$\underline{B}_i\,[w(r_o,t)] = 0 \quad [2.76]$$

can be separated in space and time with the separation constant ω^2 resulting in a eigenvalue problem such that

$$\underline{L}[\,\phi_i(r)] = m\,\omega_i^2\,\phi_i(r) \quad [2.77]$$

The eigenfunction $\phi_i(r)$ are orthogonal :

$$<\phi_i(r),\phi_j(r)> = \int_0^L \phi_i(r)\,\phi_j(r)\,dr \quad \begin{matrix} = 0 \ (i \neq j) \\ = a \ (i = j) \end{matrix} \quad [2.78]$$

for a clamped clamped beam e.g. $a = L$

Further on we are denoting by ϕ_i the orthonormalized functions:

$$\frac{1}{\sqrt{a}}\phi_i \rightarrow \phi_i$$

After a Laplace transformation of [2.74] with respect to time, assuming that it commutes with the operator $\underline{L}$, we obtain ([2.79]):

$$\underline{L}\,[W(r,s)] + c\{sW(r,s) - w(r,+0)\} + m\{s^2W(r,s) - sw(r,+0) - w'(r,+0)\} = F(s)\,\delta(r-r_1)$$

where

$$F(s) = -Z(s)\,W(r_1,s) \qquad [2.80]$$

is the force at point r_1 (cf. Fig.2.12.) and $w(r,+0)$ is the initial condition (it has to be written as a limit).

Assuming now, that the solution of the transformed problem can be expanded in eigenfunctions (modal analysis)

$$\boxed{W(r,s)= \sum_{i=1}^{\infty} Q_i(s)\,\phi_i(r)} \qquad [2.81]$$

where the $Q_i(s)$ are unknown, we can with the help of [2.77] replace the operator $\underline{L}$ applied to W by

$$\underline{L}\,[W(r,s)] = m \sum_{i=1}^{\infty} \omega_i^2\, Q_i(s)\,\phi_i(r) \qquad [2.82]$$

Expanding the Dirac function in terms of the eigenfunctions [14]

$$\delta(r-r_1) = \sum_{i=1}^{\infty} a_1^i \phi_i(r) \qquad [2.83]$$

with

$$a_1^i = \frac{\phi_i(r_1)}{\int_0^L \phi_i^2(r)\,dr} = \phi_i(r_1)$$

and because the ϕ_i are orthonormalized, [2.83] becomes

$$\delta(r-r_1) = \sum_{i=1}^{\infty} \phi_i(r_1)\phi_i(r) \qquad [2.84]$$

the DE becomes an algebraic equation with the $Q_i(s)$ unknown ([2.85]):

$$m \sum_{i=1}^{\infty} \omega_i^2\, Q_i(s)\, \phi_i(r) + c\,\{s \sum_{i=1}^{\infty} Q_i(s)\, \phi_i(r) - w(r,+0)\} +$$

$$+ m\,\{s^2 \sum_{i=1}^{\infty} Q_i(s)\, \phi_i(r) - sw(r,+0) - w'(r,+0)\} = -Z(s)\, W(r_1,s) \sum_{i=1}^{\infty} \phi_i(r_1)\, \phi_i(r)$$

$$\Rightarrow \sum_{i=1}^{\infty} \{m\, \omega_i^2 + c\, s + m\, s^2\}\, Q_i(s)\, \phi_i(r) + c\, \{-\, w(r,+0)\} +$$

$$+ m\, \{-\, sw(r,+0) - w'(r,+0)\} = -Z(s)\, W(r_1,s) \sum_{i=1}^{\infty} \phi_i(r_1)\, \phi_i(r) \qquad [2.85]$$

This implicit equation for the Q_i has to be worked out to give them explicitetly. We are now expanding the initial amplitude in term of the eigenfunctions, too.

$$w(r,+0) = \sum_{i=1}^{\infty} P_i\, \phi_i(r) \qquad [2.86]$$

and its derivative

$$w'(r,+0) = \sum_{i=1}^{\infty} R_i\, \phi_i(r) \qquad [2.87]$$

Thus those terms of equation [2.85] containing the initial conditions can be written as:

$$c\, \{-\, w(r,+0)\} + m\, \{-\, sw(r,+0) - w'(r,+0)\} =$$

$$c\, \{-\sum_{i=1}^{\infty} P_i\, \phi_i(r)\} + m\, \{-\, s \sum_{i=1}^{\infty} P_i\, \phi_i(r) - \sum_{i=1}^{\infty} R_i\, \phi_i(r)\} = \sum_{i=1}^{\infty} \{-cP_i - msP_i - mR_i\}\, \phi_i(r)$$

With the abbreviations

$$\psi_i(s) := m\omega_i^2 + c\, s + \mu\, s^2 \qquad [2.88]$$

and

$$\chi_i(s) = -\{cP_i + msP_i + mR_i\} \qquad [2.89]$$

the algebraic equation [2.85] to be solved for Q_i is thus as follows

$$\sum_{i=1}^{\infty} \{\psi_i(s)\, Q_i(s) + Z(s)\, W(r_1,s)\, \phi_i(r_1) + \chi_i(s)\}\, \phi_i(r) = 0 \qquad [2.90]$$

Because the $\phi_i(r)$ are orthogonal and not zero everywhere we have thus

$$\psi_i(s)\, Q_i(s) + Z(s)\, W(r_1,s)\, \phi_i(r_1) + \chi_i(s) = 0 \qquad \forall\, i \qquad [2.91]$$

and the Q_i becomes in a simplified notation, ommiting some dependencies on s and introducing the abbreviation:

$$Y_i := \frac{1}{\psi_i(s)} \qquad [2.92]$$

$$Q_i(s) = -\frac{Z(s)\, W(r_1,s)\, \phi_i(r_1) + \chi_i(s)}{\psi_i(s)} = -\{Z(s)\, W(r_1,s)\, \phi_i(r_1) + \chi_i\}\, Y_i$$

and thus

$$W(r,s) = -\sum_{i=1}^{\infty} \{Z(s)\, W(r_1,s)\, \phi_i(r_1) + \chi_i\}\, Y_i\, \phi_i(r)$$

or

$$\boxed{W(r,s) = -Z(s)\, W(r_1,s) \sum_{i=1}^{\infty} \phi_i(r_1) Y_i\, \phi_i(r) - \sum_{i=1}^{\infty} \chi_i Y_i\, \phi_i(r)} \qquad [2.93]$$

The problem arises now, that we have in [2.93] the function W on both sides. But because this equation most hold for every r including r_1 we can find an expression for $W(r_1,s)$:

$$W(r_1,s) + Z(s)\, W(r_1,s) \sum_{i=1}^{\infty} \phi_i(r_1) Y_i\, \phi_i(r_1) = -\sum_{i=1}^{\infty} \chi_i Y_i\, \phi_i(r_1)$$

$$W(r_1,s)\left(1 + Z(s) \sum_{i=1}^{\infty} \phi_i(r_1) Y_i\, \phi_i(r_1)\right) = -\sum_{i=1}^{\infty} \chi_i Y_i\, \phi_i(r_1)$$

and thus

$$W(r_1,s) = -\frac{\sum_{i=1}^{\infty} \chi_i Y_i\, \phi_i(r_1)}{\left(1 + Z(s) \sum_{i=1}^{\infty} \phi_i(r_1) Y_i\, \phi_i(r_1)\right)} \qquad [2.94]$$

Substituting [2.94] in [2.93] we find

$$\boxed{W(r,s) = -\sum_{i}^{\infty} Y_i\, \chi_i\, \phi_i(r) + Z(s) \frac{\sum_{i}^{\infty} Y_i\, \chi_i\, \phi_i(r_1)}{1 + Z(s) \sum_{i}^{\infty} Y_i\, \phi_i^2(r_1)} \sum_{k}^{\infty} Y_k\, \phi_k(r_1)\, \phi_k(r)} \qquad [2.95]$$

This is an explicit solution in the Laplace space (variable s) of the DE [2.74].

For the back transformation we have to bring it into a form of a fraction of two polynoms, because then standard transfromations are known. This is done in the appendix H.

2.4.3.3.1. Movement of point r_1 (the point of the middle mass)

To find the movement of the discrete mass (our main interest, we are not using the general formula from above but rather [2.94], written somewhat more explicitely:

$$W(r_1,s) = \frac{-\sum_{i=1}^{\infty}\left(\frac{\chi_i(s)}{\psi_i(s)}\right)\phi_i(r_1)}{\left(1+Z(s)\sum_{i=1}^{\infty}\left(\frac{\phi_i(r_1)}{\psi_i(s)}\right)\phi_i(r_1)\right)} \qquad [2.96]$$

This expression , too, can be brougth into a form of a fraction of two polynoms:

$$W(r_1,s) = \frac{-\sum_{i=1}^{\infty}\left(\frac{\chi_i(s)}{\psi_i(s)}\right)\phi_i(r_1)\frac{\prod_k^{\infty}\psi_k}{\prod_k^{\infty}\psi_k}}{\left(1+Z(s)\sum_{i=1}^{\infty}\left(\frac{\phi_i(r_1)}{\psi_i(s)}\right)\phi_i(r_1)\frac{\prod_k^{\infty}\psi_k}{\prod_k^{\infty}\psi_k}\right)}$$

$$W(r_1,s) = -\frac{\sum_{i=1}^{\infty}\frac{\chi_i\phi_i(r_1)}{\psi_i}\prod_k^{\infty}\psi_k}{\prod_k^{\infty}\psi_k+Z(s)\sum_{i=1}^{\infty}\frac{\phi_i^2(r_1)}{\psi_i}\prod_k^{\infty}\psi_k}$$

$$W(r_1,s) = -\frac{\displaystyle\sum_{i=1}^{\infty} \chi_i \phi_i(r_1) \prod_{k \neq i}^{\infty} \psi_k}{\displaystyle\prod_{k}^{\infty} \psi_k + Z(s) \sum_{i=1}^{\infty} \phi_i^2(r_1) \prod_{k \neq i}^{\infty} \psi_k} \qquad [2.97]$$

2.4.3.3.2..Backtransformation at point r_1 by analytical development of the first term

Retaining of [2.96] only the first term we have

$$W(r_1,s) = \frac{-\left(\dfrac{\chi_1(s)}{\psi_1(s)}\right)\phi_1(r_1)}{\left(1 + Z(s)\ \left(\dfrac{\phi_1(r_1)}{\psi_1(s)}\right)\phi_1(r_1)\right)} \qquad [2.98]$$

The impedence (discrete mass m_d and discrete damping c_d) at point r_1 can be written as

$$Z(s) = m_d\, s^2 + c_d\, s \qquad [2.99]$$

and remembering [2.88] and [2.89]we obtain an expression as follows

$$W(r_1,s) = \frac{-\left(-\{cP_1 + msP_1 + mR_1\}\right)\phi_1(r_1)}{\left(\psi_1(s) + \ (m_d\, s^2 + c_d\, s)\ \phi_1(r_1)\ \phi_1(r_1)\right)}$$

or

$$W(r_1,s) = \frac{-\left(-\{cP_1 + msP_1 + mR_1\}\right)\phi_1(r_1)}{\left(m\ \omega_1^2 + c\ s + m\ s^2 + \ (m_d\, s^2 + c_d\, s)\ \phi_1(r_1)\ \phi_1(r_1)\right)} \qquad [2.100]$$

with the following definitions

$$\phi_o := \phi_1(r_1)$$
$$a := \left(m + m_d\, \phi_o^2\right)$$
$$b := \left(c + c_d\, \phi_o^2\right)$$

$$c' := m\omega_1^2 \quad \text{(in this context not the damping)}$$

we can rewrite [2.100] as:

$$W(r_1,s) = \frac{\{cP_1 + msP_1 + mR_1\}\ \phi_o}{as^2 + bs + c'} \qquad [2.101]$$

which is a fraction of two polynoms p(s) and g(s). The backtransformation of Laplace of such a fraction is generally[15]

$$f(t) = \sum_{i=1}^{n} \frac{g(s_i)}{p'(s_i)} e^{s_i t} \qquad [2.102]$$

with the s_i the zeros of the denominator polynom $p(s) = as^2 + bs + c'$ which are

$$s_{1,2} = \frac{-b \pm \sqrt{b^2 - 4\ a\ c'}}{2\ a}$$

$$= \frac{-\left(c + c_d\ \phi_o^2\right) \pm \sqrt{\left(c + c_d\ \phi_o^2\right)^2 - 4\left(m + m_d\ \phi_o^2\right)\left(m\ \omega_1^2\right)}}{2\left(m + m_d\ \phi_o^2\right)} \qquad [2.103]$$

By defining the following terms

$$D := \frac{-\left(c + c_d\ \phi_o^2\right)}{2\left(m + m_d\ \phi_o^2\right)} \qquad [2.104]$$

$$\Omega := \sqrt{\frac{4\left(m + m_d\ \phi_o^2\right)\left(m\ \omega_1^2\right) - \left(c + c_d\ \phi_o^2\right)^2}{4\left(m + m_d\ \phi_o^2\right)^2}} > 0 \qquad [2.105]$$

we can write the solutions as:

$$\boxed{s_{(1,2)} = D \pm i\ \Omega} \qquad [2.105]$$

In the following lines we are doing the backtransformation of this first approximation for the movement of the point r_1, where we have attached our impedence.

We have two complex conjugate poles $s_{(1,2)}$ and the function to be calculated is of the form

$$w(r_1,t) = \frac{g(s_1)}{p'(s_1)} e^{s_1 t} + \frac{g(\bar{s}_1)}{p'(\bar{s}_1)} e^{\bar{s}_1 t} \qquad [2.106]$$

with

$$s_1 = D + i\,\Omega$$

The coeficient of the first term of [2.106] is

$$\frac{g(s_1)}{p'(s_1)} = \frac{\{cP_1 + ms_1P_1 + mR_1\}\,\phi_o}{as_1 + b}$$

$$= \frac{\{cP_1 + mP_1(D + i\,\Omega) + mR_1\}\,\phi_o}{a(D + i\,\Omega) + b}$$

$$= \frac{\{cP_1 + mP_1D + mR_1\}\,\phi_o + imP_1\phi_o\,\Omega}{aD+b + ia\Omega}$$

splitting into real and imaginary part results in

$$\frac{g(s_1)}{p'(s_1)} = \frac{(\{cP_1 + mP_1D + mR_1\}\,\phi_o + imP_1\phi_o\,\Omega\,)\,(aD+b - ia\Omega)}{(aD+b)^2 + (a\Omega)^2}$$

$$\Re := \frac{\{cP_1 + mP_1D + mR_1\}\,\phi_o(aD+b) + (mP_1\phi_o\,\Omega\,)(a\Omega)}{(aD+b)^2 + (a\Omega)^2} \qquad [2.107]$$

$$\Im := \frac{+\,(mP_1\phi_o\Omega)\,(aD+b) - \{cP_1 + mP_1D + mR_1\}\,\phi_o(a\Omega)}{(aD+b)^2 + (a\Omega)^2} \qquad [2.108]$$

and thus

$$\frac{g(s_1)}{p'(s_1)} = \Re + i\,\Im \qquad [2.109]$$

Since $s_2=\bar{s}_1$ and because of the real coefficients and the rules of complex conjugate numbers $g(\bar{s}_1) = \overline{g(s_1)}$ we have imediately for the coefficient of the second term of [2.106]

$$\frac{g(\bar{s}_1)}{p'(\bar{s}_1)} = \Re - i\,\Im \qquad [2.110]$$

Thus [2.106] becomes with [2.109] and [2.110]

$w(r_1,t) = (\,\Re + i\,\Im)\,e^{s_1 t} + (\Re - i\,\Im)\,e^{\bar{s}_1 t}$

$\Rightarrow\ w(r_1,t) = \Re\,e^{s_1 t} + i\,\Im\,e^{s_1 t} + \Re\,e^{\bar{s}_1 t} - i\,\Im\,e^{\bar{s}_1 t}$

$\Rightarrow\ w(r_1,t) = \Re\,e^{Dt}\,e^{i\Omega t} + i\,\Im\,e^{Dt}\,e^{i\Omega t} + \Re\,e^{Dt}\ e^{-i\Omega t} - i\,\Im\,e^{Dt}\,e^{-i\,\Omega t}$

$\Rightarrow\ w(r_1,t) = \Re\,e^{Dt}\,(e^{i\Omega t} + e^{-i\Omega t}) + i\,\Im\,e^{Dt}\,(e^{i\Omega t} - e^{-i\,\Omega t})$

$\Rightarrow$

$$\boxed{w(r_1,t) = 2\Re\ e^{Dt}\cos\Omega t + 2\,\Im\ e^{Dt}\sin\Omega t} \qquad [2.111]$$

Thus the backtransformation shows that the complex conjugate pair $s_{1,2}$ can be rearranged in order that D determines the damping and Ω the frequency. Remember however, that this is only the very first approximation.

2.4.4.The Q-factor of the first mode in the first approximation

The interpretation from above allows now to define a Q-factor for this rather complex system in a similar way as done for the simple beam by identifying D ([2.104])with $-\beta$ ([2.62]) and Ω ([2.105]) with the eigenfrequency ω.

This can be verified to make sense by setting the discrete values m_d and c_d to zero. The result is then just the unmodified beam frequency and damping. The discrete elements are thus introduced into the equation by a weighting factor ϕ_o^2, the normalized amplitude of the undisturbed beam at point r_1, which has the dimension $[\ L^{-1}]$. One can interprete this also as a smearing out of the discrete elements over the whole beam .

From [2.65] we have $\beta = \frac{\omega}{2Q}$, thus $D=\frac{\Omega}{2Q}$ and

$$Q = \frac{\Omega}{2D} \qquad [2.112]$$

With the definitions for Ω and D ([2.104]&[2.105]) the Q-factor of our system can be written as

$$Q = \frac{\sqrt{4\left(m + m_d\,\phi_o^2\right)\left(m\,\omega_1^2\right) - \left(c + c_d\,\phi_o^2\right)^2}}{2\left(c + c_d\,\phi_o^2\right)}$$

or

$$\boxed{Q = \sqrt{\frac{2\left(m + m_d\,\phi_o^2\right)\left(m\,\omega_1^2\right)}{\left(c + c_d\,\phi_o^2\right)^2} - \frac{1}{4}}} \qquad [2.113]$$

Explicit expresssions for c, the damping per unit length of the beam, c_d damping of the discrete proof mass, m the total mass of the beam and m_d the total mass of the proof mass are calculated in the next section. Examples can be found in chapter 6, where these calculation are compared to experimental results.

Thus we have shown with the above calculations, that we can give an analytical expression for the Q-factor and the frequency for continous systems with nonproportional damping. To derive directly the influence of parameters like dimension or mass distribution on the Q-factor we have to develop first physical models for the nature of the damping coefficients. This will be done in the following section, but one can say already now that obviously adding mass without adding friction increases the Q-factor. One can achieve this e.g. by·increasing the thickness (this is done with the mesa mass in chapter 6), because this parameter will not appear in the denominator.

2.4.5. The nature of damping

2.4.5.1. External damping

2.4.5.1.1. Low pressure range

For the region, where the mean free path length of the molecules is substantially larger than the maximal amplitude of the resonator (Knudsen-region) the change of momentum by the moleculs exerted on a beam per unit length can be calculated by taking the Maxwell- Boltzmann distribution of the velocities[16] :

$$dn = n\left(\frac{m'}{2\pi kT}\right)^{\frac{3}{2}} e^{-\frac{m'v^2}{2kT}} dv \qquad [2.114]$$

with

m' : Mass of the molecule = $1.66 \cdot 10^{-24}$ M

M : In this context the mass of a mole

n : Particle density

Integration of [2.114] over dv_y and dv_z from - ∞ till + ∞ gives the number of particles per unit volume of velocity in x-direction (see Christian[4])

$$dn_x = n\sqrt{\frac{m'}{2\pi kT}}\, e^{-\frac{m'v^2}{2kT}} dv \qquad [2.115]$$

The pressure difference Δp_x between front and backside of a plate moving with the velocity u_x is twice the rate of change of momentum.

$$\Delta p_x = 4\sqrt{\frac{2}{\pi}}u_x p\sqrt{\frac{M}{R_oT}} \qquad [2.116]$$

The force exerted on the moving surface with an area A is then

$$f = \Delta p_x A = 4\sqrt{\frac{2}{\pi}}u_x p\sqrt{\frac{M}{R_oT}}A = 4\sqrt{\frac{2}{\pi}}\sqrt{\frac{M}{R_oT}}\, p\, bL\, u_x \qquad [2.117]$$

with b the width of the beam

Thus the damping coefficient per unit length is

$$\boxed{\xi = 4b\sqrt{\frac{2}{\pi}}\sqrt{\frac{M}{R_oT}}\, p} \qquad [2.118]$$

This is four times the coefficient given by Kokubun for a sphere, when his factor πR^2 is interpreted as the projected surface of the sphere:

$$f_{Kok} = R^2\sqrt{\frac{2\pi M}{R_oT}}\, p\, u_x = \sqrt{\frac{2\pi}{\pi^2}}\pi R^2\sqrt{\frac{2\pi M}{R_oT}}\, p\, u_x = \sqrt{\frac{2}{\pi}}\sqrt{\frac{M}{R_oT}}\, p\, \pi R^2 u_x$$

It has been pointed out by Chrsitian[4], who compared to earlier work, that one has to take half of the exposed area for a cylinder instead of the projected area.This means for a sphere, that ($2\pi R^2$) would have to be taken. Thus, the formula of Kokubun, who wants finnaly explain the damping of a beam of rectangular cross section, underestimates the damping by a factor 2.

We can thus summarize the expression needed to calculate the Q-factor as follows

$m = \mu = \rho\, b\, h$: Mass per unit legth of the beam

$m_d = \rho\, d\, c_1^2$: Mass of the mesa

where c_1 is the side length of the mesa (correct formula or the mass see section 2.2)

$c = \xi_o + \xi$: Damping per unit length of the beam

where ξ_o is the simulated damping in vacuum (internal, clamping)

$c_d = \frac{\xi}{b} c_1^2$: air damping of the mesa ($\frac{\xi}{b}$ is the pressure of the air damping)

2.4.5.1.2. High pressure range

In the high pressure range Tough[5] finds for a cylinder moving with constant velocity at NTP through air the following approach (see Appendix).

$$\xi = +\pi\rho\, a^2\omega\, k' = +\pi\rho\, a^2\omega \left\{\frac{2}{a}\sqrt{\frac{2\eta}{\omega\rho}} + \frac{2\eta}{a^2\omega\rho}\right\} \qquad [2.119]$$

Thus

$$\boxed{c = \xi_o + 2\pi\, a\sqrt{2\eta\omega\rho} + 2\pi\eta} \qquad [2.120]$$

a: the radius of the cylinder

$\eta = 17.2\ 10^{-6}$ Pa s viscosity

$\rho = 1.293\ \mathrm{kg/m^3}$ air density

ω is the actual frequency of the oscillating cylinder (see chapter 6)

In the case now of higher pressure the masses have to be corrected for the additional inertial mass of the gas accelerated during the oscillation. For the added mass per unit length of a beam Christen[17] proposes the simple formula

$$\chi = \frac{\pi\, \rho\, b^2}{2} \qquad [2.121]$$

with b the width of the beam.

For the damping of the proof mass we are taking the approximation Kokubun[18], who proposes for a sphere of radius R moving in a viscous fluid:

$$c_d = c_o + 6\pi\eta R + 3\pi R^2\sqrt{2\eta\rho\omega} \qquad [2.122]$$

and for the total mass of the proof mass

$$m_d = m_o + \left(3\pi R^2\sqrt{\frac{2\eta\rho}{\omega}} + \frac{2}{3}\pi R^3\rho\right) \qquad [2.123]$$

with

m_o the mass of the proof mass

We can summarize the expressions for the damping as follows

$$c = \xi_o + \pi b\sqrt{2\eta\omega\rho} + 2\pi\eta, \qquad [2.124]$$

ξ_o the intrinsic damping

$$c_d = 6\pi\eta R + 3\pi R^2\sqrt{2\eta\rho\omega} = 3\pi\eta c_1 + \frac{3}{4}\pi c_1^2\sqrt{2\eta\rho\omega} \qquad [2.125]$$

with c_1 the side length of the proof mass

and those for the masses as:

$$m = \mu + \chi = \rho_{Si} bh + \frac{\pi\rho b^2}{2} \qquad [2.126]$$

$$m_d = \rho_{Si} dc_1^2 + \left(\frac{3}{4}\pi c_1^2\sqrt{\frac{2\eta\rho}{\omega}} + \frac{1}{12}\pi c_1^3\rho\right) \qquad [2.127]$$

Together with the formula $\rho = \frac{p}{RT}$ and the formula [2.112] or [2.113] we have thus derived the dependence of the Q-factor of a mass beam system on the pressure (high pressure range).

2.4.5.2. Internal damping

The calculation done by Braginsky[19] for quartz and aluminum shows, that the thermoelastic dissipation, the dissipation due to phonon-phonon interactions and to phonon-electron interactions (in metals) are some order of magnitude smaller than the lowest dissipation we measured. It is therefore not these fundamental (intrisic) processes which limit the Q-factor but rather, besides clamping, point defects like lattice vacancies, impurities and interstitial atoms and dislocations jumping from one site to another. The relaxation time $(\tau^*)^{-1}$ of these internal processes can often be described by an Arrhenius formula[19]

$$(\tau^*)^{-1} = \tau_o^{-1} e^{-\Delta E/kT}$$

where τ_o^{-1} is the rate factor, k the Boltzmann constant and ΔE an activation energy and are thus strongly temperature dependent. This is confirmed by the experiments (see chapters 6 and 9), if one assumes, that the radiation into the clamping is not temperature dependent.

On beams covered by thin films besides the films itself also the interfaces may contribute to damping although our RBS measurements showed[20], that the interdiffusion is very low.

---

1 Baker, Wilfried,E. Woolam,W.E. Young,D.; Air and internal damping of thin cantilever beams. Int J. Mech Sci, Pergamon Press Ltd. 1967, vol9, pp 743-766.

2 Blake, W.T. ; The radiation from free-free beams in air and water. J. of Sound and vibration, 33(1974) 427-450.

3 Jeyapalan, R.K. and Richards, E.J.; Radiation efficiencies af beams in flexural vibration, J. Sound Vibration, 67 (1979) 55-67

4 Drawin. H.W.; Vakuum Technik 11-2, 45-49,1962.

5 Coolidge, A.S.; The upper range of the quarz-fiber manometer. J. Amer. Chem. Soc., 45, 1923, p. 1637

6 Christian, R.G.; The Theory of oscillating-vane vacuum gauges.Vacuum 16, 175 (1966)

7 Tough, J.T. McCormick, W.D. and Dash, J.G.; Vibrating wire viscosimeter, Rev. Sci. Instr. 35 (1964) 1345-48.

8 Landau Lifshitz; Mechanics, 3rd Ed. Pergamon press, 1987

9 Braginsky, V.B. Mitrofanov, V.P. Panov.V.I.; Systems with Small Dissipation, University of Chicago Press, Chicago and London 1985.

10 see section 2.1. ref 5.

11 Adkins, R.L.; Modal Analysis of liner non-conservative system.Air Force Materials Lab. Report AFML-TR-75-2. 1975.

12 Wahle, Michael; Beitrag zur passiven Kontrolle schwach gedämpfter elastischer Strukturen mittels dynamischer *Schwingungsdämpfer. Dissertation, TH Aachen, Aachen, 1984, p.31*

13 Press, W.; Flannery, B. Teukolsky, S. Vetterling, W. Numerical Recipes. Cambridge University Press, 1987.

14 Jacquot, R.G. and Gibson, J.D. 1972. Journal of sound and vibration. 23, p. 237-244. The effects of dicrete masses and elastic supports on continous beam natural frequencies.

15 Abramowitz M, and Stegun, A.; Handbook of mathematical functions. Dover Publications , NY,1965

16 Adam, Gerhard, Hittmair, Otto; Wärmetheorie, Vieweg. 1978

17 Christen,M.; Air and gas damping of quartz tuning forks, Sensors and Actuators, 4(1983) p.555.

18 Kokubun , K.et al.; Frequency dependendence of a quartz oscillator on gas pressure, J. Vac.Sci Technol. A3 (6), Nov/Dec. 1985. p.2184.

19 Braginsky V.B. et al.; Systems with small dissipation . Chicago Press Chicago London 1985

20 Dr. J. Weber from the Inst. of Physiscs of the University of Neuchâtel was so kind to do the RBS measurements of our samples.

2.5. Discussion

We have done is this chapter quite extensive calculation to be able to characterize the damping behaviour of our structures theoretically, allowing thus to optimize structures. This was found necessary since published approaches seemed to us rather qualitatively than quantitative. The justification will be given in the experimental chapters, where we compare the theory to experimental results (with an astonishingly good agreement).

Chapter 3
Fabrication of microstructures

3.1. Introduction

3.1.1. Anisotropy

As explained in the general introduction chapter 1 microfabrication using silicon anisotropic wet etching (i.e. chemical etching compared to plasma etching, where the etching is rather machine than crystal dependent) is a main concern of this work and all the structures described hereafter are fabricated by this technique.

Silicon, having a diamond crystal structure, (i.e. a fcc lattice with a double base), shows in a (100) oriented wafer the fourfold symmetry of a cubic crystal (see Fig. 3.1.)

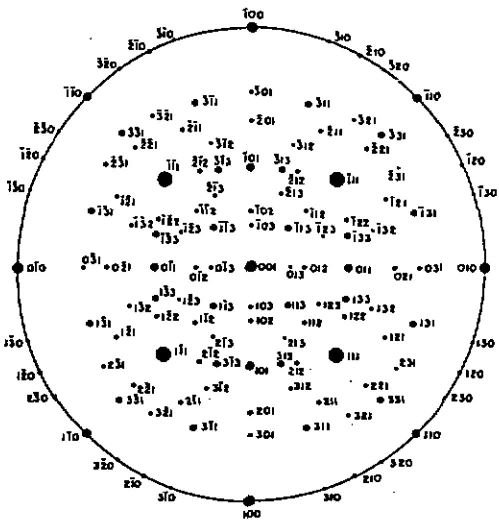

Fig.3.1. Stereographic projection of the (001) oriented silicon crystal

Potassium hydroxide solution (KOH), hydrazine as well as Ethylene Diamine Pyrocathecol (EDP) etch the (111) planes up to 500 times slower than the (100) planes. This means that the (111) planes might be considered as etch stop planes during the etching of the (100) planes. There are also some fast etching planes with etch rates larger than the (100) planes. Thus monocrystalline silicon can be etched anisotropically.

3.1.2. State of the art

Greenwood[1] pubished as one of the first on anisotropic etching of silicon using EDP and in the same year Lee[2], but using a hydrazine/isopropanol/water mixture. He had still electronic applications like separation of two active circuits in mind, thus no mechanical application. Weirauch[3] related in his article the phenomenologically observed anisotropical etching behaviour of circular mesas in silicon wafers with that of etched spheres and thus with the crystalline structure. Bean[4] has written a quite comprehensive article including data on etch rates of EDP and KOH. He also describes a comer compensation method for the surface. A treatment of hydrazine etching can be found in the recently published article of Mehregany[5]. The tedious work of the German group (Csepregi)[6] which summarized different possibilities and limitation of this technique has to be mentioned here.Petersen[7] describes in his review article various mechanical application of silicon micromachining.

Since then several groups in the world have recognized silicon micromachining as a very interesting technology. They are cited in the appropriate chapters because no fundamentally new ideas on etching were brought in .

Various technological innovations are published for the first time by the author:

i. Section 3.3. describes a CAD program to simulate the anisotropic etching of silicon.
ii. Section 3.4. describes a comer compensation method to obtain mesa structures which are perfect in three-dimensions.
iii. In section 8.3.2 we describe for the first time a method to do a photolithographic process on a completely etched through wafer.
iv. In chapter 7 structures etched in 100 silicon with vertical walls are described (tuning forks).

3.2. Silicon etching techniques

Heavily doped regions show a lower etch rate than ligthly silicon, especially in a EDP etchant[8]. Thus underetching of beams and cantilevers may be performed.

A (110) orientation shows a lower symmetry, but here two (111) planes stand perpendicularly to the surface and allow therefore to etch deep trenches with no lateral underetching.

Dry etching is another possibility to etch anisotropically, but deep etching becomes difficult because of low etch rates (respectively low selectivity) and vertical walls are difficult to etch properly.

We did not want to use EDP because of its large expenditure for security and the therefore resulting troublesome handling and selected thus KOH as etchant. The disadvantage of possible pollution and the higher etchrate for silicondioxid is by far evened out by its simply handling. Moreover KOH of 40 % (b. w.) at 60° C allows to etch perfectly polished surfaces and, by appropriate aligning, one can realize vertical walls[9] allowing some interesting constructions (see chapter 8).

When starting this work we had first to find a masking layer for long etch time in KOH, because the silicondioxide, nearest at hand, is somewhat etched in KOH (this is the reason why a lot of peoples prefer EDP). Aluminiumoxid seemed to be an material inert enough to withstand KOH. Long series of experiments showed however, that the used CVD Al_2O_3 had a high density of pinholes. Moreover it needed for the photolithographic process, because we did have plasma etching at our disposition, a CVD oxide which itself was not pinhole free. LPCVD might have been usable but was not available. Trials with organical materials failed, either because of deposition,patterning, adhesion or removal problems. LPCVD Si_3N_4 proved then to be an excellent material, but was for us not directly accessible and wet etching would have been cumbersome, too. So, we finally grew thermal (steam) SiO_2 to a thickness of over 3 μm and cooled it down very carefully. No warping of the wafers was observed and this thickness was sufficient to etch about 1mm of silicon in KOH at 60° C

For most of the hereinafter described processes wafer of 380μm thickness were used and here 1.5 μm of SiO_2 was sufficient. This oxide could be grown within a reasonable time (growing goes with the root of the time). We used the 60° C fixing, because it showed the smallest surface roughness at an acceptable etch rate for Si and SiO_2. We did not add isopropanol as reported in literature, because this increased the roughness and the anisotropy might even be lost (cf. Fig. 3.2).

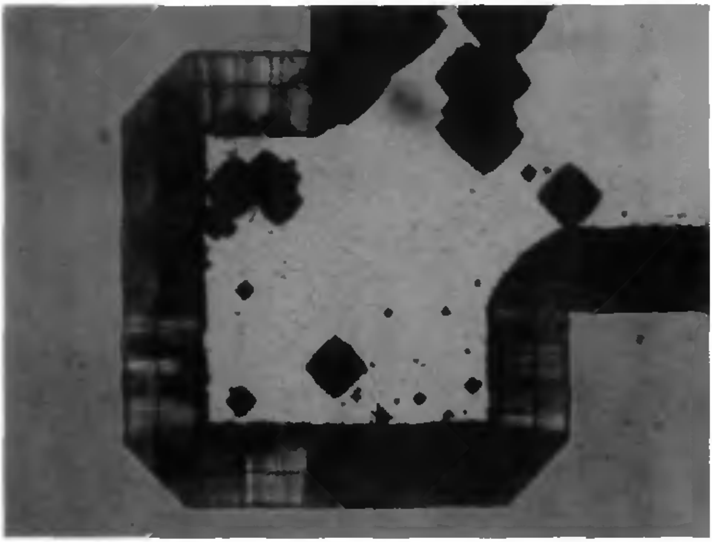

Fig.3.2. Photograph of an etched surface KOH/Isoprapanol

Other alkalines are reported to etch anisotropically, too[10,11]. We did some experiments with NaOH and LiOH. For NaOH some irregularities were observed (pyramids at the etched surface), too. This might have been caused also by impurities and the fact that we did not stirr the solution. With LiOH, although there is evidence of anisotropical etching, the result becomes disastrous as shows Fig.3.3.

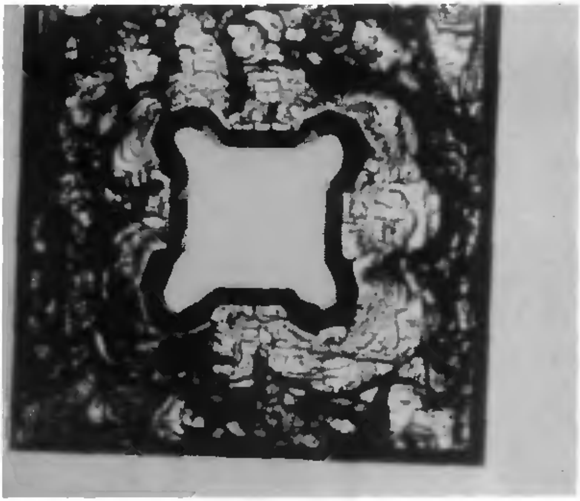

Fig.3.3. Photograph of the surface of the LiOH esaturated) etched silicon.

A comprehensive work on etch rates of different alcalic bases of silica is that of Hooley[12]. All solutions show a maximum of the etch rate far before saturation. Heating the KOH mostly in a water bath and the fact that KOH is hydrophilic, had as a practical consequence that the etch rate of the 40% b.w. KOH increased with the age of the bath, which fact we used reversely to determine the age of the bath. Typically we had 15,5µm/h for a fresh bath and 18µm/h for an old (some days at 60°C). For special cases we used also a directly heated bath, to reduce this aging. But typically this time dependence of the etch rate was not critical, only the ratios of the etch rate in different direction is important and these changed much less.

Kendall[13] presented in 1982 a nice method to determine quite easily the etch rates in different directions, called wagon wheel. We applied it for our KOH, (001) oriented wafers[14] (see Fig.3.4.).

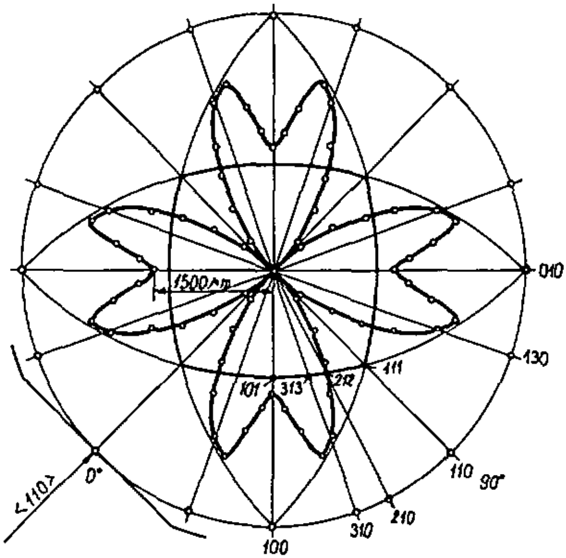

Fig.3.4. Diagram of the different etch rates obtained by the wagon wheel method

For the opening of the masking layer (SiO_2) the usual photolithographic techniques were used. Positive resist AZ 1400 from Shipley as well as negative one HNR 80, 120 from Hunt Chemicals were used. The more viscous one HNR120 was used to perform photolithography on the non-polished side of the wafer. As far as possible we used double side polished wafers, which allowed to use one type of resist. For the exposure a double side mask aligner (Karl Suess MJB 21) was utilized.

When we had to etch from two sides with different etch depth, we avoided a second Photolithographic step on the pre-etched structures by the following procedure (see Fig.3.5): Both sides were covered by photoresist, exposed and developed together. The etching of the mask (SiO_2) was stopped after a pre-calculated time, and the side of with the smaller etch depth (say the backside) was covered completely with photoresist. The front side was then opened completely. After cleaning the wafer (the front side) was etched till the thickness of the left over was double the etch depth of the backside. Only a dip in BHF was needed to open the SiO_2 mask at the backside and etching could be finished in KOH. For equal etch depth from back and front side this procedure of course was not necessary.

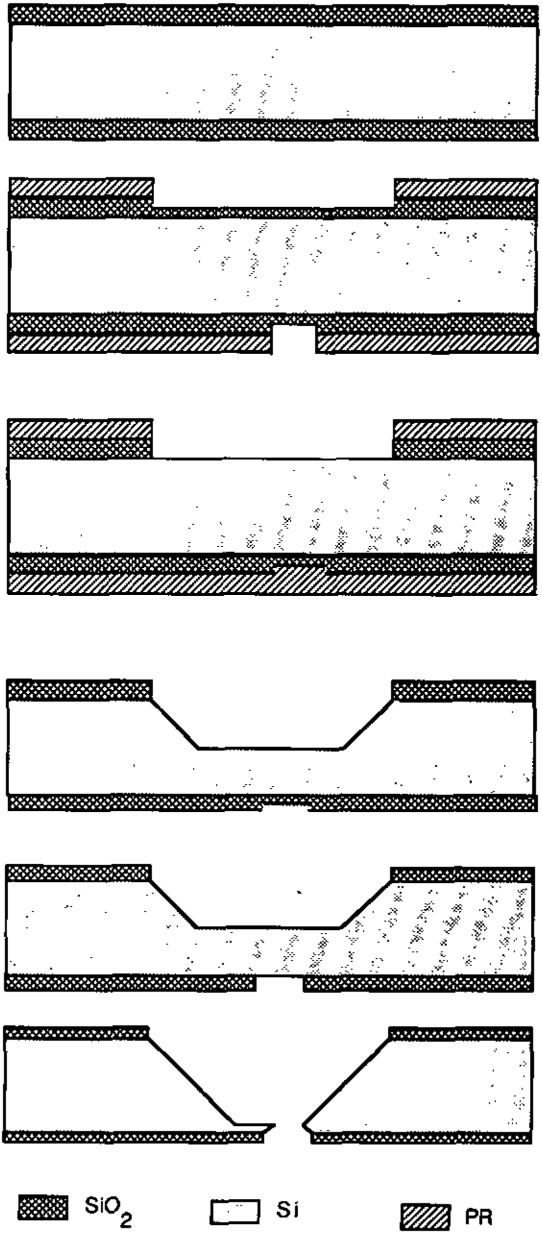

Fig.3.5 Fabrication process

3.3. Simulation program[15]

3.3.I.Introduction

In order to be able to predict easily the three-dimensional shape of etched silicon structures from a two-dimensional mask, we developed a simulation program in the language PASCAL.Our program runs for KOH etching of (100) oriented silicon, but by the same principle etch simulation programs for other etchants and other crystals might be constructed. Such a program represents a complete knowledge on anisotropic etching. It is thus described now whereas the description of the fabrication techniques follows in section 3.4.

PASCAL as a file oriented language suggests to program the same way. So each task ends with a data file which can be easily stored and read by the same or other programs (for example input/output auxiliaries). Thus, a mask file is created, then a model file (records which contain all additional planes) and finally a structure file (real), where the etched structure is represented by a top polygon, a bottom polygon and the connection lines between corresponding comers.

The leading idea of the modelling stems from the observation that in spite of an infinite number of planes in a crystal, in etched structures only a few are relevant: (111),(100) and (311), each with its proper etch rate. Once selected, the planes move during etching in the direction of its normal until either

i) etching is over
ii) it is "eaten" by its neighbor planes (faster etching planes, convex shape)
iii) it disappeared when bounded by slower etching planes (concave shape)

The program identifies the lines of the mask as crystal directions. Because only one specific crystal plane can be revealed by etching, this assignment is unequivocal. Special problems occur at the convex comers, where the fast etching planes are revealed. The program classifies different types of comers and adds the necessary planes. Once the crystal planes to be etched are identified, these planes are moved along their normal vector according to their specific etch rate (see Fig.3.6.). Intersection of the planes in the new position as shown in Fig.3.7. reveals the etched structure.

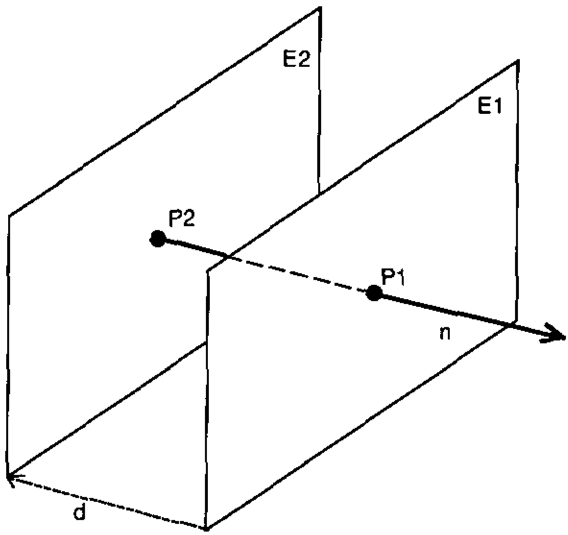

*Fig.3.6. Displacement by a distance d of a plane along its normal **n***

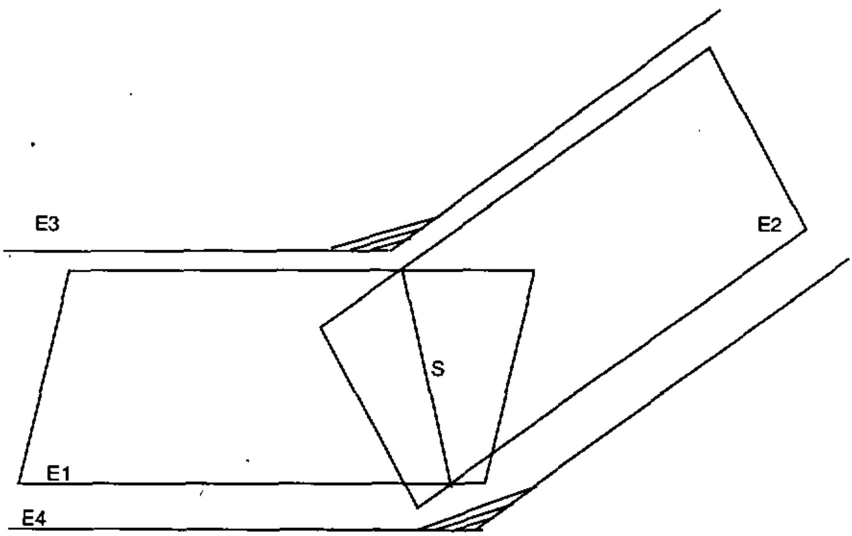

Fig.3.7. Intersection S of two etched planes E1 and E2, the Intersection with the top plane E3 (001) Plane, the surface of the wafer is trivial.The same holds for E4, the bottom of the etched structure

So, the crucial point in modelling as well as in reality is the selection of the planes which is done by alignment. Actually two dimensions allow only to select a set of planes (like 111,112,113, ...) but as said above for nature no ambiguity exists (in this case (111) will be selected.), a question of binding energy of the surface atoms. Concave shapes behave well according to this simple rule. Nevertheless on convex shapes there is a complication, because there the atoms are loosely bound and the fastest etching plane is revealed (311). This phenomena is called underetching. Different authors do not agree on the Miller indices of this plane[16]. This may be caused by the fact, that in KOH a unique dominating plane is revealed but after a certain etch time resulting in the picture that the top of the corner shows a definite plane, but the bottom is composed by large number of planes (cf. Fig.3.11). EDP behaves easier in that respect revealing from the beginning but two planes.

Selection of relevant planes orientation

As can be seen from the discussion above, a mask design makes only sense with rectangular lines(100) planes and lines at 45° (111) planes. In addition the polygons have to be closed. From the sense of rotation of the digitizing the program decides, wether the inside the polygon will be exposed to etch (open oxide) or the outside. This way on each corner there can be decided, wether it is convex or concave, i.e.wether and what (fast etching) planes have to be added. Thus, the model is defined and the shape of the end structure can be simulated by time.

3.3.2.Hardware environment

The System was built up with the following components

Computer (color)	HP 9836C
Plotter (A3)	HP 7475
Graphic tablet	HP 9111A
Harddisk (20 Mbyte)	HP 9153
Printer	Epson, HP

One should be able to correct to mask interactivily and to plot it finally as layout. Moreover the data should be saved on a file. We had an HP-PC- System with plotter, printer, graphic tablet and hard disk. To be able to utilize the program generally, PASCAL was selected as language. This was decisive for the structure of the program, yet the graphic-statement were quite specific to HP.

HP-Pascal is using coded modules for all graphic procedures. These are all in a library. Some supplementary procedure are needed to operate with string-variables. All these module are imported at the beginning of the program.

3.3.3.Performance

The program offers 12 menus to be selected by the graphic tablet.

These are:

1. INPUTMASK

A grid of the possible digitizing point is drawn first (resolution 100μm) and then those other maskes already drawn before and specified in menu 10 are outlined on the screen for reference. All previous drawings of the selected mask level (working level) are destroyed. The program ask then for a type of echo. Only lines of 90° (100 planes) or 45°(111 planes) make sense. The polygons have to be closed. Digitizing clockwise means etching the polygon from outside, counterclockwise from inside.

2. SHOWMASK

Together with a rough grid all masks specified in menu 10 are outlined and the working mask is shown filled (dominant).

3. HARDCOPY

Draws the working mask to the plotter. The polygons are hatched. The scale is as selected in the menu SCALE for format A3. To adjust to millimeter paper P1 can be adjusted before plotting (see manual of the plotter).

4. MOVEOBJECT

First the mask is drawn (as in menu 2.) Then the polygon to be moved can be pointed at by the locater, the polygon is hatched then, and the increment can by typed numerically (integer microns).

5. ERASEOBJECT

Works as 4. but instead of moving the object is removed.

6. ADD_OBJECT

Works as menu 1. but without erasing the existing working mask. Because a supplementary figure is appended at the end of the file, the searching process however starting at the beginning, one can overdraw a wrong figure and erase (or move) it afterwards.

7. CORRECT_OBJECT

Here after having selected the object one is asked line by line (answer TRUE or FALSE) wether this line has to be corrected or not.

8. ETCH

This menu is the central part of the program. It executes the etching procedure as follows.

Starting with the mask the Miller indices of the apparent planes for an orientation of the wafer surface of (001) are determined and can be plotted out (see subroutine MILLER[10]). Concave and convex corners are distinguished, necessary planes are added and finally displaced along the normals of the planes (etching). Only the non etching (111) planes the (100) planes and the fast etching planes (311) are taken into account, because after a certain etching time these are dominant for any starting configuration. Afterwards the planes are intersected which delivers the set of edge points of the etched structure. For the representation all point are projected to a plane but distinguished by different colors. The next but one neighbour planes are not taken into account. This would need matrix calculations because then the points of intersection are no longer necessarily on top or on bottom of the etched structure. For deep etching overlapping may occur, but the figure might by interpreted correctly by just cutting them out.

10. LEVEL TABLE

The program allows working with 16 masks. These can be visualized during input or correcting of the working mask. One mask can be visualized as etched structure, which allows positioning of pads e.g. Because for every mask a file is created (MASK#) it can with the help of the PASCAL FILER copied to any other level to serve e.g. as a staring mask for a modified mask. Moreover these data files can by saved to disks.

11. WORKING_LEVEL

Because all time all data are stored on files on the hard disk one can change the level of working (=selecting another mask as working mask) without special saving. One has only to note, that the table of the masks to be showed outlined is not affected by this procedure.

Note hat the masks are always up to date, but the etched structure (the File STRU# is only actualized by running menu 8 or 9.

12. SCALE

The scale should be selected in between 10 and 100 (because of the resolution). An object can be drawn in another scale than the rest of the mask. Noter however, that a magnification of the scale might move an object out of the screen (it stays however on the file). The resolution stays constant for all scales (100 µm) (Actually 10 units).

3.3.4. Structure of the program

The variables are mostly defined globally in order to reduce the list of parameters. If only part of the program should be used (ETCH e.g.) one has to care that for and add the declaration of variable from the main as far as necessary.

INPUTMASK creates an integer file which is read by ETCH. ETCH itself produces then via the model-file (file of record), where all the planes are stored, the structure-file (File of real), which contains the mesh of the threedimensional etched structure.

Procedures, functions and files are capitals as far as they are not library programs. The menus called from the main represent closed blocks with respect to Input/output procedures (they end all with *display_term*) but not with respect to variables or procedure calls.

3.3.5.Example

Fig 3.8. shows a layout with all possible combinations of adjacent planes. They are labeled by the corresponding Miller indices. Fig. 3.9. shows the result of the simulation program after 100µm deep etching.

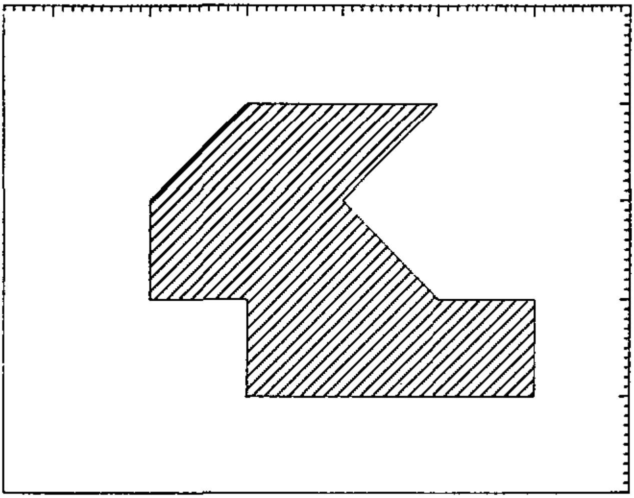

Fig.3.8. Layout of the mask to be etched (100µm per division)

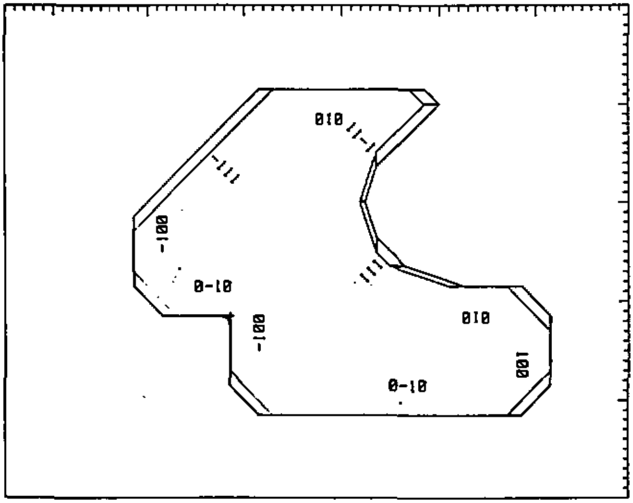

Fig.3.9. The result of the etching program for 100µm etch depth

3.3.6. Concluding remarks.

This program is a minimal structure to represent the etch simulation. Pre- and post processor of existing CAD-tools could improve largely the access and usability of the program. If also over next neighbor planes would be taken into account, a full three-dimensional system of linear equations would arise, because the points would then be no longer necessary on top or bottom. Then another procedure would have to be included which decides, wether the intersection point lies in front of or behind the plane surface.

The etch rate in the <111> direction was assumed to be 0, but this could be easily be taken into account for, because the same model can be used.

3.4. Corner compensated mesa mass

As could have been seen in the section above, fast etching planes are destroying quite rapidly convex corners. To compensate this underetching a special technique was used to get precise mesa structures[17]. Using the fact, that vertical walls formed by (010) and (100) planes can be etched in (001) wafers and that these planes move during etching, (111) planes can be revealed. Stopping the etching when say a $(0\bar{1}0)$ and a (010) meet (i.e. they disappear, see Fig.3.10.) a perfect corner formed by (111) planes is left over. Fig.3.11. shows a uncompensated corner after 200 µm deep etching whereas the corner shown in Fig.3.12. was etched with the "street corner compensation" technique described above.

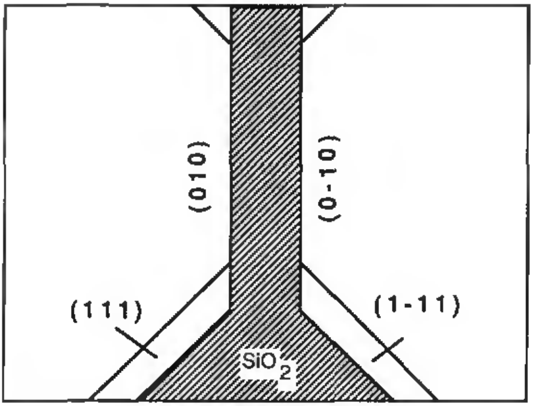

Fig.3.10. "Street" corner compensation mask

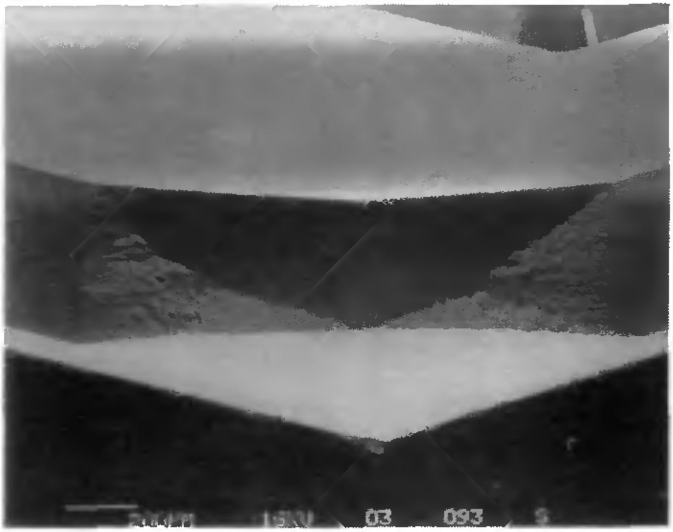

Fig.3.11. SEM Photograph of an uncompensated corner

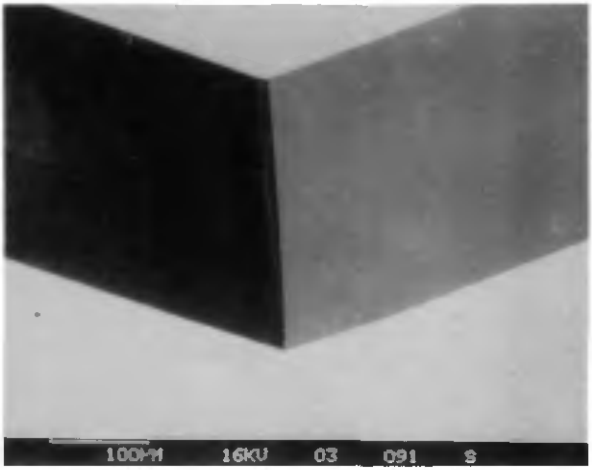

Fig.3.12. SEM Photograph of a compensated corner

3.5. Other fabrication techniques

3.5.1. General

Thin films are sometimes needed to complete the micromachined structure or it may be even the crucial part of the device. Thus, reflecting or absorbing coatings can increase the efficiency of the device. Or because silicon is not piezoelectric it needs special layers like ZnO for the excitation of the resonator or to realize active devices. The transparent oxides with a locally changed index of refraction form waveguides leading to integrated optics. Inert organic layers passivate the surfaces. The thermal oxidation was performed in a Tempress furnace in a humid atmosphere provided by boiling water. The CVD-Silicondioxide (Vapox) was deposited in a self made furnace. The metals were evaporated in a evaporator by an E-gun (Leybold-Heraeus).

3.5.2. Anodic Bonding

The mechanism of anodic bonding is fully described in a IMT internal report[18,19]. We worked at 450°C and 1000V, in order to obtain a good contact of the aluminum strips (chapter 5).

Fig.3.13. Photograph of the anodic bonding set-up

3.5.3. Simultaneous oxidation and diffusion

Some structures were fabricated with a diffusion layer to study the influence of doping on behavior. For that purpose the oxidation at 1100°C was done after deposition of a doped CVD silicon dioxide (see Fig. 3.14.). The diffusion depth was about 6.7μm.

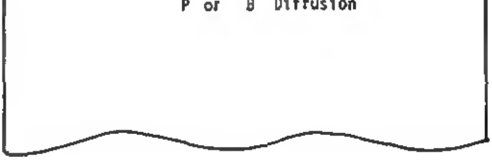

Fig.3.14. Simultaneous oxidation and diffusion

3.6. Discussion

Although the work described in this chapter was the most time consuming it was kept quite short, because laboratory details are not a very attractive subjects or are (meanwhile) become quite common knowledge like masking techniques, e.g. It is however to note, that the corner compensation technique, the vertical etching technique and the simulation program are quite unique tools described here for first time in some detail.

---

1 Greenwood, J.C.; J. Electrochem. Soc. Vol 116, 1325 (1969)

2 Lee, D.B.; Anisotropic etching of silicon, Journal of Applied Physics, Vol. 40, no1. Oct. 1969

3 Weirauch, F. Donald.; Correlation of the anisotropic etching of single-crystal silicon spheres and wafers. Journal of Applied Physics, Vol. 46, No.4, 1975 p. 1478.

4 Bean, Kenneth E.; Anisotropic Etching of Silicon, IEEE Transac. on El Dev. VOL ED-25, no 10, October 1978

5 Mehregany, M., Senturia, S.; Anisotropic etching of silicon in Hydrazine, sensors and actuators, 13, (1988) p. 375-390.

6 Csepregi, L., Hauk, R., Niessl, R. Seidel, H.; Technologie dünngeätzter Siliziumfolien im Hinblick auf monolithisch integrierbare Sensoren, Forschungsbericht BMFT-FB-T 83-089, Fachinformationszentrum, Karlsruhe., Mai 1983

7 Petersen, Kurt, E.; Silicon as a Mechanical Material. Proc. of the IEEE, Vol. 70. no 5. May 1982. p. 420.

8 see ref. 5

9 Buser , R.A., B. Stauffer,B., de Rooij,N.F.; Realization of a mesa array in (001) oriented silicon wafers for tactile sensing applications, Extended Abstractsof the Fall Meeting of the Electrochemical Society , San Diego, CA, Oct.1986, p.879-880.

10 Baryeka, I. et al.; Sodiium Hydroxide Solution Shows Selective Etching of Boron- Doped SiliconJourn. of the Electrochemical Society, Acc. Brief Comm. February 1979. p.345

11 Pugacz-Muraszkiewiccz, I.J.; Detection of Discontinuities in Passivation Layers on Silicon by NaOH Anisortropic Etch. IBM J. Res. Develop., September 1972,

12 Hooley, J.G.; The Kinetics of the Reaction of Silica with Group I Hydroxides. Canadian J. of Chemistry, vol 39, 1961.

13 Kendall, D.L., de Guel G.R., Torres-Jacome, A.; The Wagon Wheel Method applied around the \{01-1] Zone of Silicon, Spring meeting of the El. Chem. Soc. 1982, Abstr. no 132, p. 209.

14 Stauffer, Kayal, IMT internal report

15 Buser, R.A.; Silicon anisotropic etch simulation program, IMT internal report No 253 IC 01/89, 1989.

16 Fast etching plane Miller index

17 see ref. 7.

18 Decroux, M. and Buser R.; Schutzkonstructionen für Siliziumsensoren. IMT rapport interne Nr. 182 EC 01/86, 1986.

19 Schenk, J.R.; Influence de l'anodic bonding sur les caracteristiques d'une strucutre MOS. Travail de diplome, IMT, Université, Neuchâtel. 1984.

Chapter 4
Experimental

4.1. Introduction

4.1.1. Statement of the problem

In this chapter we are going to describe these mountings and measurement systems that have been used to investigate the various types of mechanical vibrating structures. Each chapter will have its own section where supplement modifications and specialities are emphasized.

It was the double purpose of this work, to mount a test stand which allowed to measure the physical parameters of the structures as accurate as possible while keeping in mind set-ups, measurement methods and devices as close to realizable sensor-devices as possible.

In order to end with general results, we had to be able, besides calculations which eliminated the dependance of the resonance frequency on geometric factors, on the experimental part to fix temperature and pressure. Moreover the structure should not be disturbed by attached pieces for exciting and sensing.

The first idea was to excite the structure acoustically but this excitation would have rendered the excitement medium dependent and of course impossible under vacuum conditions. We finally decided to excite by means of the inertia of the system itself, i.e. by displacing the base of the structure (excepting the tuning fork type described in chapter 8). All other exciting methods like

- piezoelectric layers,
- Lorentz forces (excepting when silicon is used directly as conductor)
- thermal (optically or resistive)

would have changed the properties of the device under test or they would not have been strong enough as e.g.

- optical momentum (order of nN per Watt of incident optical power)[1].

For measuring almost the same arguments as for exciting hold with the two exception, that

i) measuring the base movement is not a good technique because we are expecting a low coupling between the structure in resonance and the support for high Q-factor elements, and

ii) optical measurement is, just because of the low interaction cited before, very attractive.

We utilized an interferometer built by Willemin[2] to measure the amplitude and free amplitude decay of our resonators. It has the following features:

- absolute amplitude measurements 6% down to Ångströms
- phase measurements to a precision of 4°
- in plane measurements
- spatial resolution of 30 μm

We built a vacuum chamber, which also supported some over pressure (1 bar) and could thus contain also other gases. The temperature was regulated by thermostated water, flowing through a block of brass. Thus we constructed a quite universal measuring tool, allowing to measure vibrating structures with very small amplitudes under various physical conditions.The whole measurement set-up was placed on a concrete block of 2m x 1m x 0 .1m, a mass of about 600 kg.

The electromagnetic set-up, described in Chap 8, could be positioned into the same chamber, too, and tested that way optically and electrically.

4.1.2. State of the art

For the measurement of the elastic constants, ultrasonic wave velocity measurement method are widely used[3]. Also static deflection method are described in literature. Some papers outside the sensor field deal with resonance methods. The same methods are used to measure damping.

All these methods use special clamping like suspension on thin filaments or attaching of ultrasonic transducers[4]. Because we want to test real devices, the clamping was part of our structures as described in the previous chapter.

4.2. Mounting and Excitation

4.2.1. Excitation set-up

The structures were excited by mounting them on a piezoceramic disk by means of a brass base and a clamping spring. In one series of measurements the structures were also fixed by bee's wax.

The mounted structures were placed on a block of brass, which was fixed itself on a three-dimensional stage. Thus, the laser spot can be positioned on that part of the structure, which has to be measured.

Piezoceramic disks from Philips (PXE42) with a diameter of 38,1 mm and a thickness of 6.35 mm we used. They were mounted in three ways In a first set-up the disk was mounted on a rigid stage and not thermostated. It showed a quite flat frequency spectrum response in the range of interest and thus the resonance frequency of the structure was easily to determine. Fig.4.1.shows the second way, where the ceramic disk lays in between the thermostated block and the structure.

Thermally the disk represents a barrier which slowed down thermal equilibrium settlement. In the third mounting (see Fig.4.2.), where the structure was mounted quite directly to the thermostated block, the piezo disk excited the hole set-up (although in the order of Ångströms) and a variety of resonances were discovered (see section 4.2.3.) becoming thus unadapted to find the resonance frequency at ease. A photograph of the set-up of Fig.4.1. is shown in Fig.4.3.

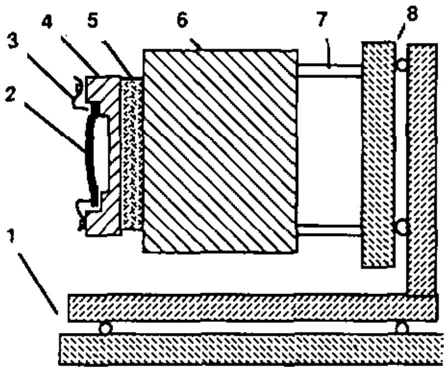

Fig.4.1. Schematic view of the mounting with the piezoelelctric disk on the front-side *1 The x-y-stage, 2 The device under test 3. The clamping spring, 4. The brass base 5 The piezoceramic disk 6 The thermostated brass block 7 The thermal isolation 8 The z-stage*

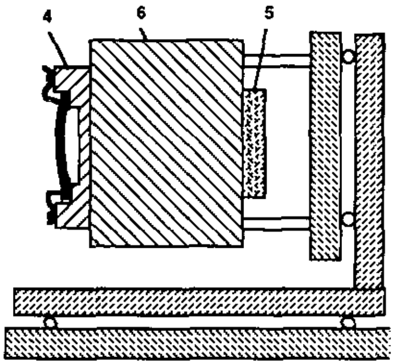

Fig.4.2. Schematic view of the mounting with the piezoelelctric disk on the backside. Legend see Fig.4.1.

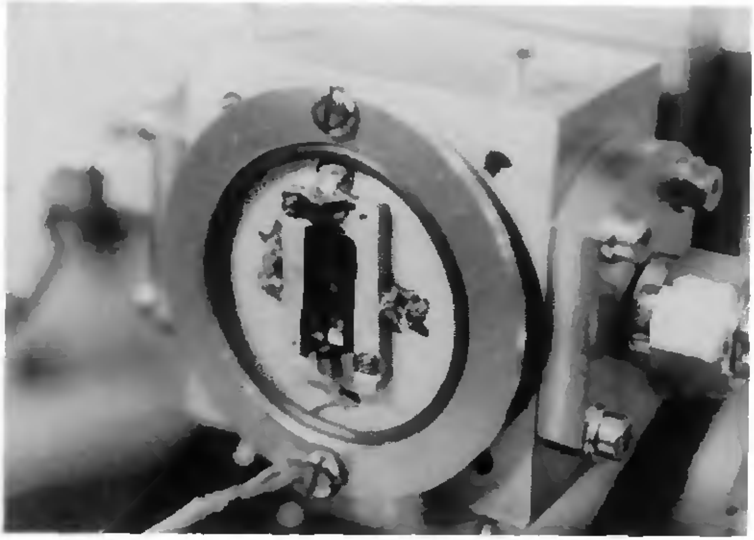

Fig.4.3. Photograph of the piezoelectric disk with the brass fixing part

The electromagnetic set-up is described in chapter 8.

4.2.2. Platform

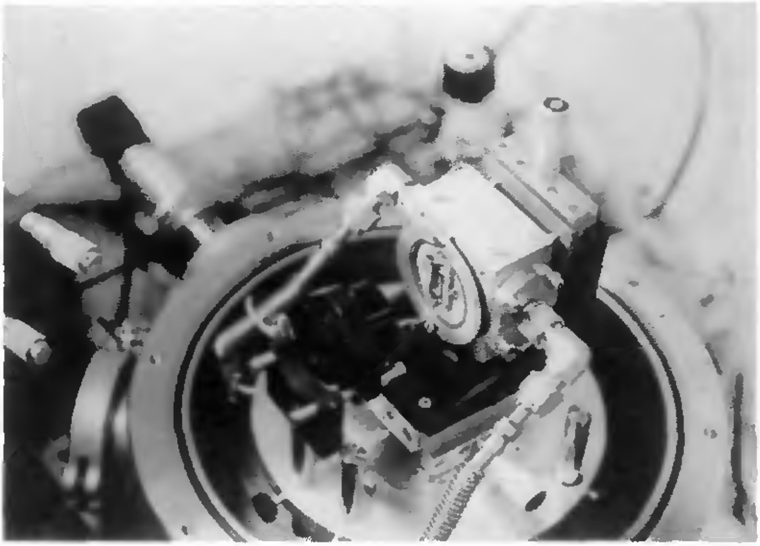

Fig. 4.4. Photograph of the platform

The above assembly was positioned in a vacuum chamber. Four bars fixed at the bottom of the chamber supported a platform, which was adjustable in height (see Fig.4.4.). On that platform, bars can be mounted to support the lenses. The xyz-stage was mounted on the platform in that way that it could be rotated somewhat in order to adjust for the angle of incidence.

4.2.3 The characterization of the excitation system

Fig 4.5. shows the amplitude of elongation of the brassblock versus the applied voltage at 2.8 kHz. In most cases 100mV or 1Å were sufficient for the exitation.

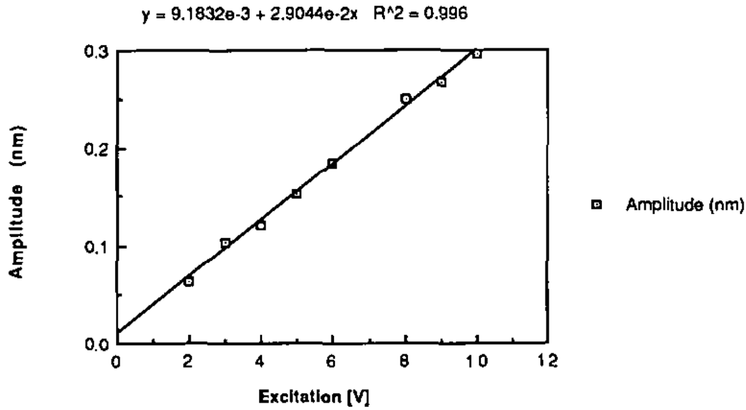

Fig.4.5. The amplitude of the brass block as a function of the applied voltage at 2.8kHz

Fig. 4.6. shows the amplitude of elongation versus the frequency at $3V_{pp}$ of the piezeceramic disk directly. The other set-up (cf Fig.4.2.) shows about the same characteristics, both in frequency and amplitude.

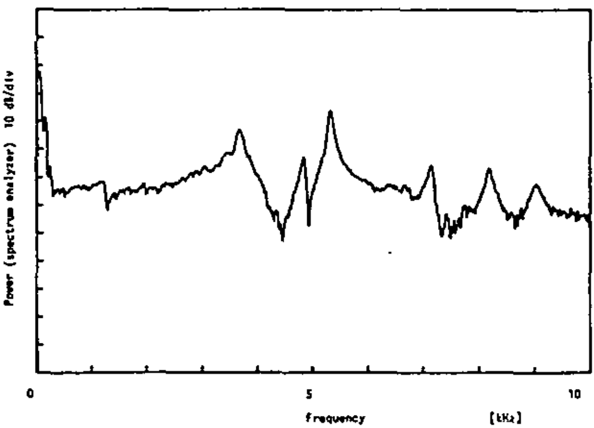

Fig.4.6. The frequency dependence of the amplitude of the piezoceramic disk at $3V_{pp}$.

4.3. The vacuum system

As stated before, we had to construct a chamber which can be evacuated and loaded with different gases up to a pressure of 2 bar.

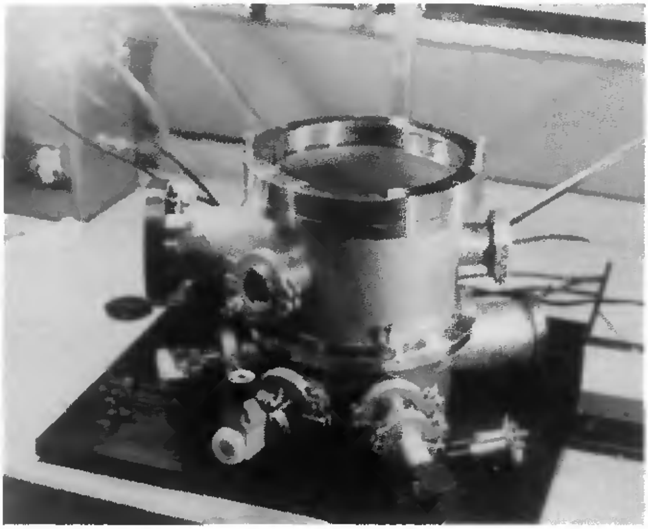

Fig.4.7. Photograph of the vacuum chamber

The vacuum chamber consist of three parts (see Fig 4.7.):

i) the base with all the feed through
- ° a 5 pole electrical
- ° a 12 pole electrical
- ° a gas inlet
- ° vacuum pump exhaust (DN 63 ISO)
- ° a cooling water/N_2 feed-through
- ° a vacuum gage connection

ii) the middle part with four plan-parallel windows (Tempax, Balzers) for the laser beam, positioned at 0°, 45°, 90°, 180°, the one at 45° had a diameter of DN 63 ISO, the others KF 45

iii) The cover which is either a disk of glass or a bell of glass

The glass bell could also be posed directly to the base.The chamber is leakproof in both direction meaning that different gases can be kept in it.

A rotational pump (Alcatel 2004) with liquid nitrogen trap was used. This allows pressures somewhat lower than 10^{-3} mbar.The pressure was measured by a pirani cell. The electronics had a analog output which was digitized by the DVM of the HP Counter. The calibration curve for different gases can thus be stored in the computer. For the over pressure range we used a simple precision manometer (Trigress) of class 0.6

4.4. Thermostating

The temperature of the brass block is controlled by an external thermostat Lauda Compact Thermostat Typ CS-6 using a closed loop flow of water. An external temperature sensor Pt 100 (from Julabo) contacted thermally to the brass block allowed an efficient temperature regulation (Lauda Externregler R22).

For the electromagnetic set-up we utilized a direct electrical heating with a thermocouple element and a regulator (see Chapter 8).

4.5. Measurement method and system

4.5.1. Interferometer

The vibrating amplitude of the resonator was measured by a hetherodyne interferometer of the Mach-Zehnder type, where the beam passed through a window into a vacuum-system (see Fig.4.8.). This measuring set-up allows absolute amplitude measurement in the order of Ångströms. If one wants to measure material properties and not device properties low amplitudes are necessary in order to avoid nonlinear effects, which are difficult to interpret[5]. The amplitudes for all our measurements were lower than 100 nm (cf. the dimension of the structures are typically 10 mm). The noise level is typically 0.1 nm.

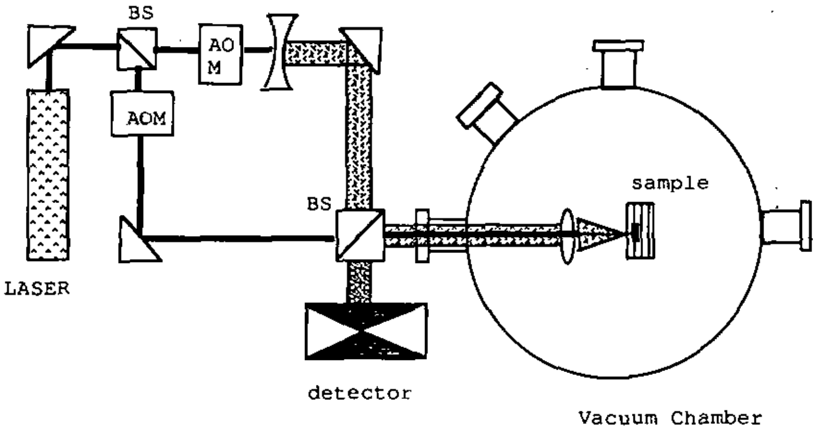

Fig.4.8. The interferometer set-up (BS: Beam splitter, AOM: Acousto-opticmodulator)

No supplementary load such as aluminium layers or treatement such as diffusion of piezoresistors were necessary for measuring, allowing thus to study the influence of those treatments. This interferometric set-up provided us also with a method to determine the mode of the vibration by simply scanning the structure. We used here the interferometer in a direct reflecting mode increasing thus a little bit the sensitivity and facilitating also the adjusting procedure. But the set-up is foreseen to measure also in plane movements as described by Willemin[2].

4.5.2. Absolute amplitude measurement

The detector furnishes a frequency modulated signal.The carrier frequency is given by the difference of the exciting frequencies of the optoacuostic couplers, 40.0 MHz and 40.1 MHz, which gives a carrier frequency of 100 kHz. The spectrum analyzer decomposes this signal to its Fourier coefficients, which can be shown to be the Bessel functions, whose argument contain the amplitude of the measured oscillation. By the principle of the hetherodyne interferometer the carrier (Besselfunction of the 0th order J_o) can be used as a reference for the intensity and the amplitude can be calculated by inverting the Besselfuntion of the first order J_1 divided by the one of the zeroth (notation of Willemin[2]).

$\frac{J_1(\phi_o)}{J_o(\phi_o)} = \sqrt{\frac{P_1}{P_o}}$ with $\phi_o = \beta u_o$, $\beta = \frac{4\pi}{\lambda}\cos\alpha$, α the angle of incidence, $\lambda = 633$ nm the wavelength of the laser beam, u_o the amplitude of the device vibration and P_i the measured power. For small arguments ($\phi_o < 1$), the Bessel function J_1 can be approximated by $J_1(\phi_o) \approx \frac{\phi_o}{2}, J_o(\phi_o) \approx 1$ .This allows a direct calculation of the amplitude.

$u_o \approx \frac{2}{\beta}\sqrt{\frac{P_1}{P_o}}$. For a perpendicular incidence $\beta = 19.852\ \mu m^{-1}$

Thus, an amplitude measurement consists of a measurement of the carrier and that of the side bands. Technically this cannot by done simultaneously in a single channel spectrum analyzer. During the scanning form the carrier frequency to the side band frequency the carrier might have changed. In a manual mode, where we keep the scanner fixed at one frequency and we are looking at the relative change of the amplitude, the accuracy of the measurement depends of course on the stability of the carrier. This is examined in the following paragraph.

The physical limitations of the interferometer are described by Willemin[2]. Having a spectrum analyzer of higher performance at disposition than he had in his original work (HP3585A instead of HP 8553), i.e. with an amplitude resolution of .01 dB instead of 0.5 dB. we could see some more details, mainly the fluctuation of the carrier that he could not resolve. To obtain some insight in the limitation on the accuracy of the amplitude measurement we measured the carrier in the manual mode by connecting the video output to a digitizing oscilloscope (HP 5183T) and performing an FFT (see Fig.4.9.)

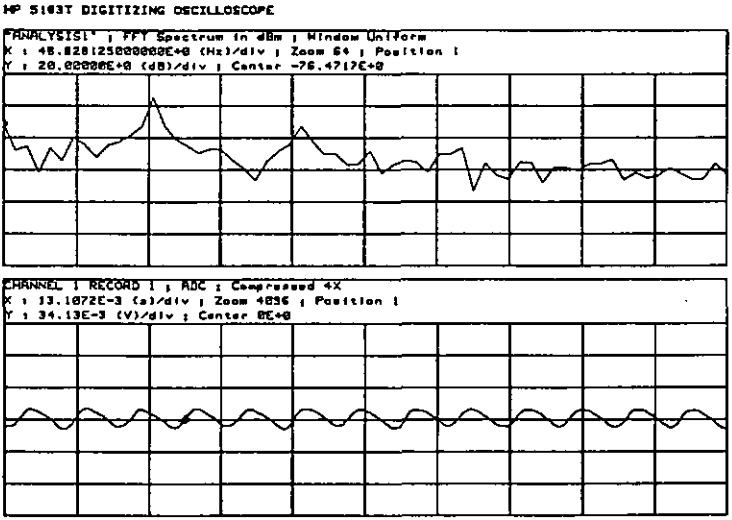

Fig.4.9. The direct signal of the carrier and its Fourier transformed.

The 50 Hz resp. 100 Hz peak may stem either from the Laser, the oscillator of the acoustooptic coupler or be mechanical. A direct measurement of the signal of the (actually quite simple) oscillators showed, that they are sligthly modulated by 50Hz. It could not be decided however, wether the laser transmitted 50 Hz, too, or not because we had no fast intensity measurement intrument at disposition.

Moreover we performed 1000 measurements of absolute amplitude on a long beam accelerometer at resonance. At an amplitude of 26 nm the standard deviation is ±.47nm. This is about a layer of atoms of the silicon crystal. The measurements series took several hours. The result in Fig.4.10. shows an evidence of a drift.

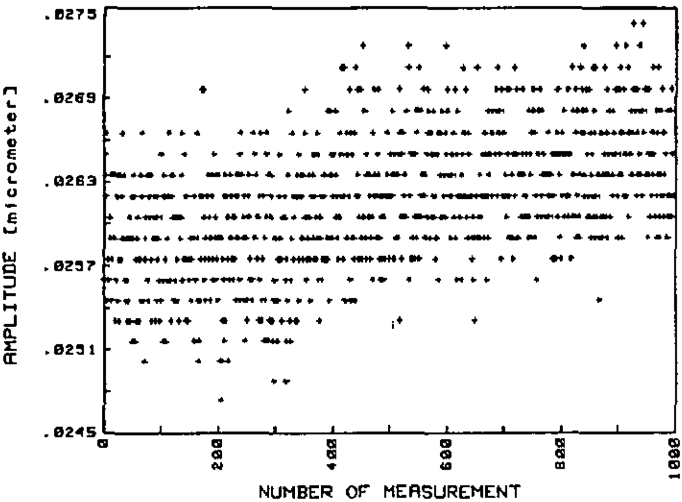

Fig.4.10. Plot of the 1000 amplitude measurements (uncorrected)

To correct for that we performed a linear regression on the data and subtracted then Δy. The corrected values have a mean of 25.74 nm and a standard deviation of ± .41 nm. Fig. 4.11. shows a normal probability plot of the corrected values. The straight line indicates a good fit to a normal distribution.

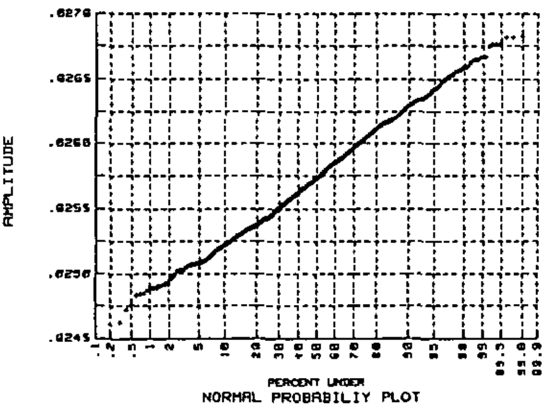

Fig.4.11. Normal probability plot

Then we plotted a histogram (see Fig.4.12) and performed a χ^2-test to check the normality of the measurements. With 11 cells (thus the degree of freedom $v = 8$) we calculated $\chi^2 = 14.21$ which lies below the theroretical value $\chi^2_{.95} = 15.5$. Thus the normality is not too good but acceptable. This can be explained by the fact, that the intensity of the signal is modulated by 100 Hz (2x 50 Hz of the power line) of about .5 dB (this corresponds to an amplitude of about 1 nm) as seen above. Thus the measurements are not fully independent.

Remark: A two channel spectrum analyzer would have allowed to calculate the correlation function and to see this directly.

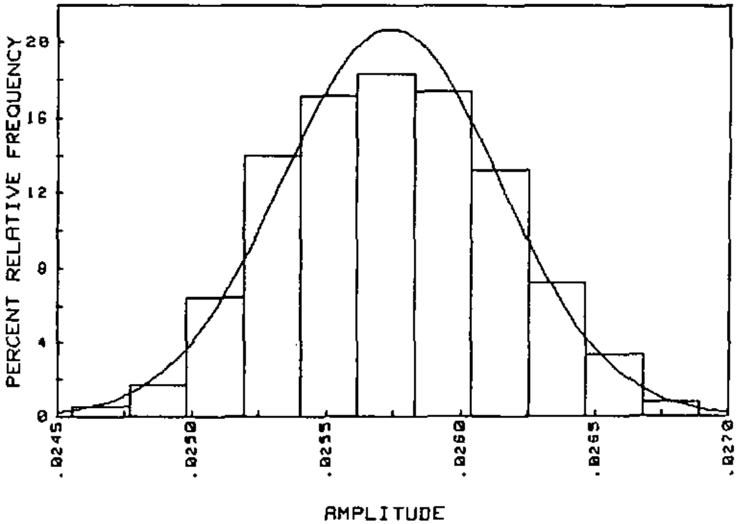

Fig.4.12. Histogram of the measured amplitudes

4.5.3. The measurement of the frequency

The resonance frequency was found by changing the excitation frequency till the amplitude was maximal for a given amplitude of excitation. For the mass beam structures described in chapter 6 (f= 2.4 kHz, Q= 30'000) the frequency can be measured to a precision of 10 mHz (5 ppm) but different clamping of the whole structure causes differences of some Hz. For the high Q elements of chapter 9 the frequency could be adjusted better than 1ppm. Demodulation of the frequency modulated signal would have allowed to measure the frequency by a counter, but this was not available.

4.5.4.The measurement of the Q-factor

For beams of weak bending or weak torsion the total stored energy in the system is proportional to the square of the maximum amplitude and experimentally an exponential decay of the amplitude with time is found (see Fig.4.13. and 4.16.) for all structures at any pressure, a direct consequence of the linearity of the underlying DE. These two facts characterize also a damped harmonic oscillator with a damping force proportional to the velocity. By applying the formalism of the harmonic oscillator the Q-factor can be given by $Q \approx \pi/\Lambda$ (cf [2.65]) with the logarithmic decrement of the amplitude $\Lambda = \ln(A_n/A_{n+1})$ to be measured.

Without demodulation it wouldn't have been easy to measure the Q-factor by recording the square of the amplitude versus frequency and calculating Q by

$$Q = \frac{\omega_r}{\Delta\omega} \qquad [4.1.]$$

$\Delta\omega$ with the width at half maximum $\Delta\omega$ of the resonance peak ω_r

ω_r the resonance frequency

Moreover with the decrement method we could observe the characteristics of the damping.

In a first period of measurements, where we did not have high performance instruments at disposition, we created a periodic signal by applying periodically a step function at the actuator, setting the spectrum analyzer to the resonance frequency and looking at the video output of the analyzer (see Fig.4.15.). Thus by representing both signals on a digitizing oscilloscope we could resolve the problem of syncronisation (see Fig.4.13.).

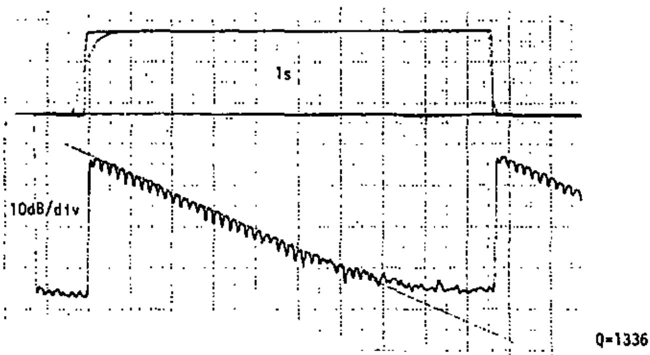

Fig.4.13. The electrical excitation signal at the actuator and the response from the optical system.

But most of the measurements presented here were done with the instruments listed below (see Fig 4.14.), which could be synchronized by a computer.The electronic part of the measurement system consists of

HP 3325 A	Function generator
HP 5335 A	Counter
HP 5183 A	Waveform recorder (digitizing oscilloscope)
HP 3585	Spectrum analyzer
HP 310	PC with a 20Mbyte hard disk

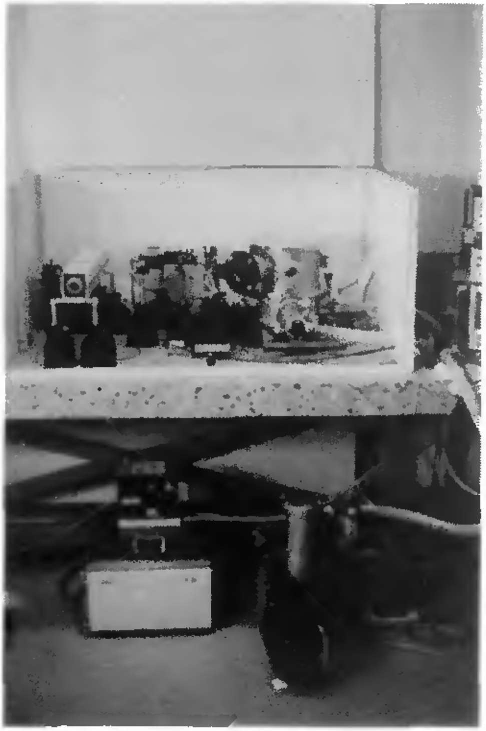

Fig. 4.14. Photograph of the measurement system

The PC controls all these instruments and automatizes thus the measurement cycle (see Fig.4.15.).The function generator excites directly the piezoceramic disk. We applied a sinusoidal waveform at the actuator and stopped it to let the resonator decay freely.

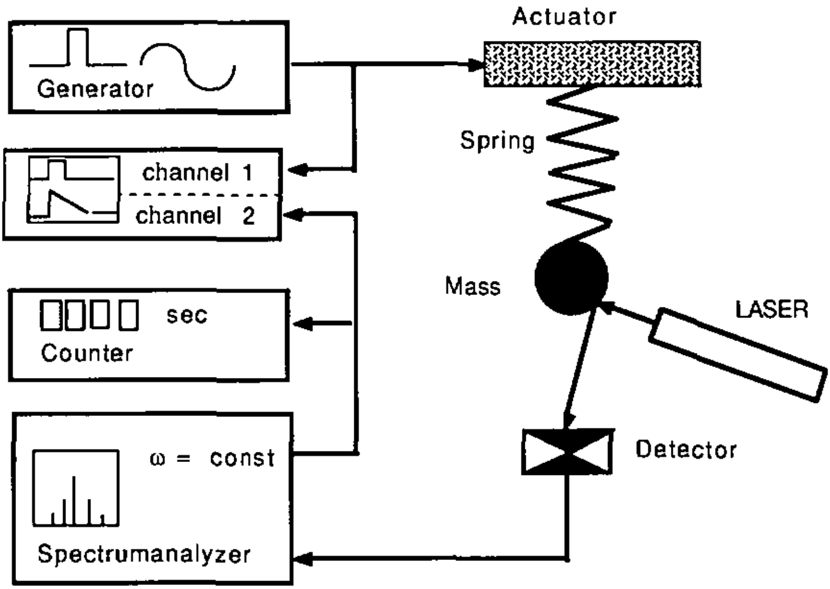

Fig.4.15. Scheme of the measurement system

To find Λ one can measure either the free amplitude decay over a certain period or the time τ for a fixed amplitude decay k. The latter case is easier to perform, because we can set fixed trigger points and perform one time measurement, whereas otherwise we would have to do two amplitude measurements at given time points.

The chosen decay in amplitude k is given by $k = (A_o/A_n) = (A_o/A_1)n = e^{n\Lambda}$. Preselecting k = 10 and *replacing the integer number of periods n by* $m = f\,\tau$, *where* m is the number of periods the oscillation made to decay the predefined decay k and f the resonance frequency we find $\Lambda = 1/m \ln k = 1/m \ln 10$ and finally $Q = \pi f \tau / \ln 10 = 1.36438 f \tau$. τ was typically in the order of seconds.

The decay of the amplitude was stored in the digitizing oscilloscope and a linear regression was performed over about 100 data points. With this method a standard deviation of ±1.5% was found. Moreover it confirms the exponential decay of the amplitude by a regression coefficient in a semilog representation of the amplitude of typically $r^2 = 0.99$ (cf. Fig.4.16.).

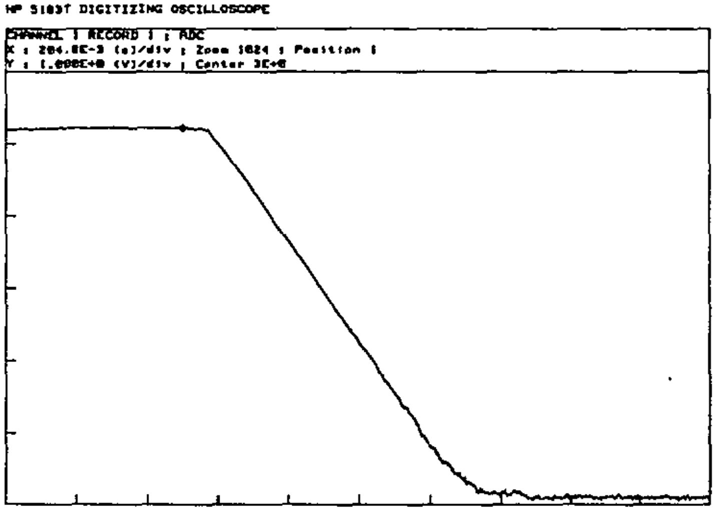

Fig.4.16. The the exponential decay of the square amplitude in a dB scale .

A complete measurement cycle consist in the following steps: After an initialization the computer checks the correct trigger levels of the counter and starts then the measurement cycle, where the exciting frequency is set to zero and the time for a decay of 20 dB of the square of the amplitude is measured by the counter (for checking only). The decay of the amplitude is also stored in the digitizing oscilloscope and a linear regression is performed then by a commercially available Statistics Program, which had to be modified in order that it runs without disturbing the common block of the measuring program that runs the digitizing oscilloscope and transmits the slope to the main program, where the Q-factor is calculated.

For the pressure measurement, a DVM transforms the analog output of the piranicell to a real number which is compared to a calibration curve by the PC. This allows the use of different calibration curve say for different gases.

At unchanged clamping the reproducibility is as follows: Measuring with the counter (direct triggering) shows a standard deviation of ±3%, while recording the whole decay in a waveformrecorder and executing a linear regression on the data the sd reduced to ±1.5% (see Fig.4.17.).

The mean of the counter measurement lies below that of the linear regression because the laser shows energy deviation by preference downwards, and the counter triggers the stop (which lies in the lower region of the curve thus in the more sensitive because of the logarithmic scale) too early and the decay time becomes too short.

The reproducibility of different clamping (meaning that the structure was removed and installed again) is very poor, showing differences up to 20%. Standard deviation over 10 measurements is ±7%.

Fast measurements (high decay rates) would give results with smaller σ. This is confirmed by measurements where for structures with the same Q-factor (same intrinsic stability) those with resonance frequencies ten times higher the standard deviation of the Q-factor also reduces by about a factor ten.

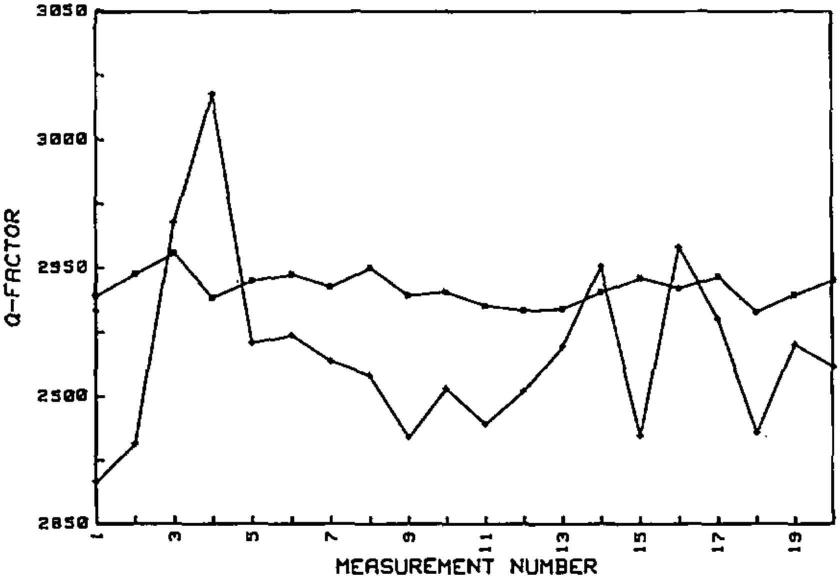

Fig.4.17. Q-factor measured by counter and digitizing oscilloscope

4.6. Discussion

The optical measuring set-up allows the investigation of the influence of additional elements (such as thin films or diffused areas) on the resonant behaviour of a pure silicon structure. Thereby the amplitude might be very small. The vacuum chamber allows measurements in the range of 10^{-6} up to 2 bar. The temperature range is limited by the thermostat and the medium (we only used water), 20°C to 60° in our case, but technically liquid nitrogen and higher temperatures would be possible, too. We have thus a quite universal automated instrument to measure resonance frequencies, modes and Q-factors of miniaturized resonant structures in dependence of surrounding gaseous medium and temperature.

---

1 Culshaw, B., Uttam, D., Nixon, J., Thornton, K., Wright, A.; Micromachined resonant structures. SPIE Vol. 718 Fiber optics and laser sensors IV, 1986 p. 92

2 Willemin, J.F.; Interférometrie hétcrodyne de speckles: Application à la mesure de vibration mécanique microscopique, Ph. D. thesis (1983), University of Neuchâtel, Switzerland.

3 Schreiber, E., Anderson, O.L. and Soga N.; Elastic constants and their Measurement, Mc Graw Hill, New York, 1973

4 Braginsky V.B. Mitrofanov,V.P., Panov, V.I..; Systems with small dissipation . Chicago Press Chicago London 1985.

5 Andres,M.V., Foulds, K.W.H., Tudor, M.J.; Nonlinear vibrations and hysteresis of micromachined silicon resonators designed as frequency-out sensors. Electronics Letters 1987, Vol 23, No 18, p. 952

Chapter 5

Tactile Sensor[1,2]

5.1. Introduction

5.1.1. Statement of the problem

On the VIth Robot Conference, 1982, Harmon[3] presented a study on the needs and potentials of *Automated Tactile Sensing* in the USA. The needs seem to surpass by far the technical availability of such systems. Various prototypes were developed since this analysis [4,5,6, 7,8], all with their specific advantages and disadvantages. We are proposing here a sensor which is manufactured completely out of single crystal silicon with the aim of having a mechanical fast reacting system with very low hysteresis and relatively high resolution. The utilization of silicon technology paves the way for the complete integration of the sensor.

Silicon based pressure and force sensors, piezoresistive as well as capacitive ones, fabricated with IC technology are widely used at present [9,10]. Since it is common in IC technology to produce the devices already in an array form, it is easy to make the array functional as a whole by convenient connection of the single elements.

Silicon force sensors have all in common three constructive elements:

i) a plate as the spring,
ii) an element that transfers the applied force to an appropriate spring deformation (called here force transmitter)
iii) a support to hold the plate.

For two-dimensional tactile sensors partly pressure sensors covered with elastomers as force transmitters partly these elastomers itself were used as construction elements. Elastomers have generally the disadvantage of a large hysteresis[3].

When the contact surface is given, it is possible with pressure sensors to determine the force acting on an element. But if one wants to measure e.g. the distribution of a force of an itself elastic impression or an unknown contact surface the latter one has to be defined from the sensor itself, the force transmitter has to be rigid. Such a concept was proposed by Petersen[11]. He milled mechanically the cams and the single elements were assembled afterwards.

We will present here a new force transmitter, consisting of perfect mesa structures (bosses) with well defined flanks and no corner underetching. This force transmitter is fully etched (no milling) and has a well defined border between the plate and the mesa foot (no undefined set of planes). The special construction of the array allows deep etching but nevertheless small lateral plate dimensions.

5.2. Calculations and design

5.2.1. Introduction

We describe here the realization of a prototype silicon tactile sensor array without having a special application in mind.

5.2.2. Design and etch simulation

On behalf of the corner compensation technique described in chapter 3, we realized with the mask shown in fig. 5.1. a field of bosses (force transmitter mesas). Because the (111)-planes are almost not etched, they are revealed by etching the (001)-planes. When the mask is symmetrical, two (111)-planes which touch at the surface at an angle of 90° are left over after the wall is etched through. Appropriate masking results in an array of cams.

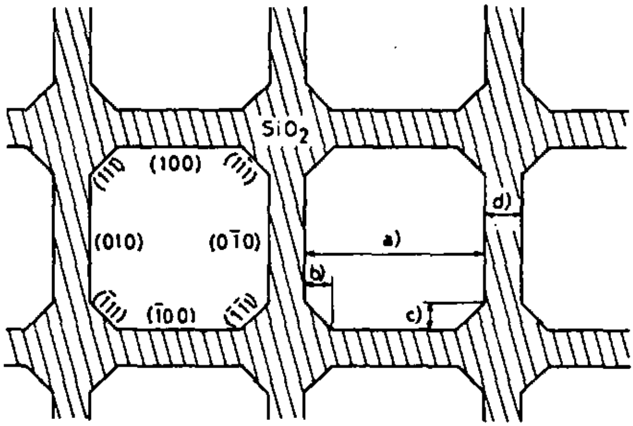

Fig.5.1. Mask with the street corner compensation., a= 2.40mm, b= 0.30mm , c=0.30mm , d= 0.40mm

Two arrays of mesas were etched from both sides of a double sided polished silicon wafer, the upper ones serves as the force transmitters whereas the lower one as the support (spacer mesa, see Fig.5.2.). Underneath the upper bosses electrodes of aluminium are placed which form together with counter-electrodes on the glass plate a capacitance, as is known from pressure sensors.

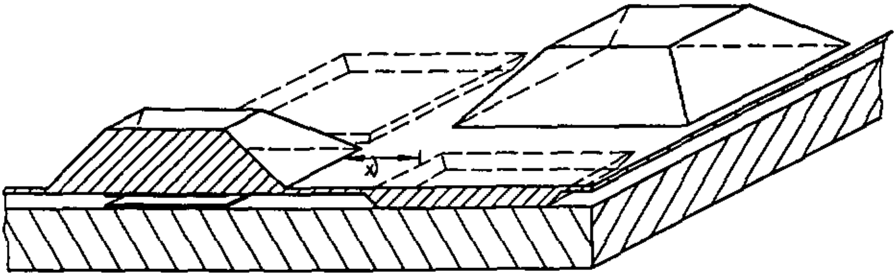

Fig.5.2. Cross section of the tactile sensor

The areas of the electrodes on the glass plate are somewhat smaller than those on the silicon wafer to compensate for adjusting tolerances (see Fig.5.3.a). The glass plate is bonded anodically to the silicon wafer. In order to obtain a single element readout the interconnections of the upper and the lower part of metals pads have to be perpendicular to each other. The lanes cross at the electrodes itself avoiding thus supplementary stray capacities (see Fig.5.3.*a* and *b*)

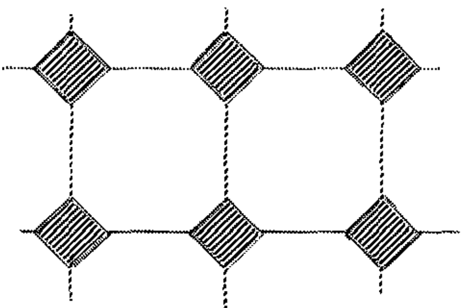

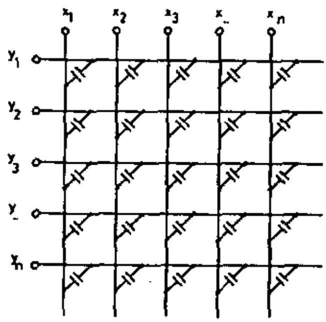

Fig.5.3.a) The layout of the electrodes *5.3.b) The interconnection of the capacitors*

At one border the metal lanes of the silicon plate are lead down over rounded edges (see Fig.5.4).With the anodical bonding of the mesas to the glass plate these lanes are bonded to metal strips on the glass plate. Thus an electrical contacting of the whole device is easily possible.

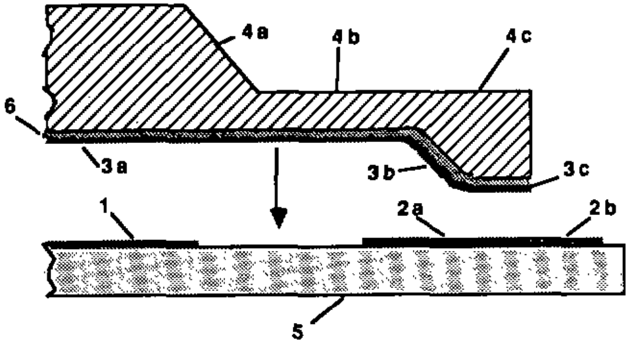

Fig.5.4. Schematic cross section of the Silicon mesas and the glass plate just before Anodic Bonding (arrow) 1 Electrode on the glass, 2a Al lane part to be bonded anodically to the the lane from the silicon electrode 3c). 2b) Wire bonding pad. 3a) Electrode on the silicon. 3b) Al lane on the slope and the rounded edges. 3c) Metallic lane to be bonded anodically to 2a.4a) Force transducer mesa, 4b) Plate 4c) Spacer mesa.5) Glass plate 6) Isolating SiO2

This construction represents a force sensor array with the possibility to vary its sensitivity over a large range by adjusting the surface of the plate determined by the distance x), the thickness of the plate and the distance between the condensator electrodes (see Fig. 5.2.).

Table 5.I. Dimensions of a cell (2,8 mm x 2,8 mm) in µm

Upper boss	
Height:	221
upper side length:	865
bottom side length:	1180
Lower boss	
Height:	7
Side length:	1300
Thickness of the plate:	134
Length of the plate between the two bosses x)	740
Side length of the upper electrode:	990
Side length of the lower electrode:	848
Thickness of the electrodes:	1
Distance between the electrodes:	5

5.2.3. Capacitance

The height of the spacer mesas is 7 μm. With thickness of the aluminium we have thus a distance between the electrodes of 5 μm.This results in a capacitance of

$$C=\frac{\varepsilon_r \varepsilon_0 A}{d}= 1.28pF. \qquad [5.1.]$$

5.2.4. Mechanical stiffness

For a doubly clamped beam of length L with a central load P we have for the displacement[12]

$$w(L/2) = -\frac{PL^3}{192\, EJ_y} \qquad [5.2.]$$

We model an tactile element as a force transducer acting (instead of a particularly clamped plate) on two beams rectangular to each other and clamped at both ends. With the data from table 5.I as

$L = 2{\cdot}740\mu$

$J_y = \frac{b\,h^3}{12}$

b= either 1180μm (beam limited by the upper boss) or 1300μm (beam limited by the lower boss)

h= 134μm

$E= 1.69{\cdot}10^{11}$ Pa

we can calculate with the above formula the eqivalent spring constant

$$k = -2\cdot\frac{L^3}{192\, EJ_y} \qquad [5.3.]$$

This results first the first case in k=8.4 μm/10N

and in the second one in K = 7.6 μm/10N

We measured (see Fig. 5.10.) about 5μm/10N, hence a stiffer behaviour, which is obviuos from the fact that we disregarded quite a large part of the plate in our calculations.

5.3. Fabrication of the structures

5.3.1. Introduction

The principal etching technique is described in chapter 4. As mentioned in section 5.2. we had to perform a photolithography on a wafer which was structured by mesas of about 10 μm height. Moreover we had to guarantee a good step covering (see Fig. 5.4.) of the aluminium layer as well as of the photoresist. Soldering of the two Al layers together by the anodic bonding process was then another novelty.

5.3.2. Fabrication techniques

We succeeded in solving the problems stated above as follows:

i) Photolithographic process at the bottom of a 10µm deep etched well by low spin speed (2000 RPM)

ii) Metallization of the slope and the corner of that slope (see fig 5.4.) rounding of the corner by isotropic etch (scotch)

iii) Photolithogaphic process over the edge high viscosity PR, low spinning speed and rounding of the corners.

iv) Bonding of the aluminium lane to a aluminium lane on the glass plate during anodic bonding By applying relatively high voltages and high temperatures.

5.3.3. Process lists

Material: boron doped Si-wafer (5-7 Ω cm), 3"

<u>Topside process</u>

1.	Wet Oxidation 1.5 µm.
2.	Photolithography (opening the oxid)
3.	KOH (41% b.w.) 60°C in a water bath (PP vessel). 16µm/h. 200µm deep

The result is shown in Fig.5.5.

<u>Backside Process (lift off technique)</u>

4.	Photolithography (opening the oxid)
5.	KOH 35' (10µm)
6.	Remove oxid in buffered HF
7.	Scotch (HNO_3:HF:CH_3COOH:H_2O ≙ 3.5:1:1:.1) 90"
8.	Dehydration bake 200° 20'
9.	Photoresist 1350J (Shipley),500 rpm 5", 2000 rpm 30"
10.	Prebake 85° 10"
11.	Exposure
12.	Development
13.	Deposition Al
14.	Lift off (Acetone)

The result is shown in Fig. 5.6.

Glass plate

1.	Deposition Al
2.	Photolithography

Afterwards the glass plate and the wafer are bonded anodically together

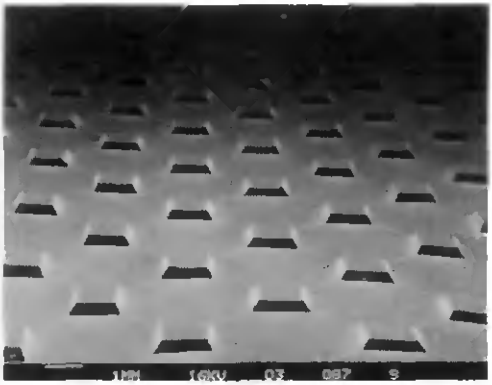

Fig.5.5. Etched array of mesas.

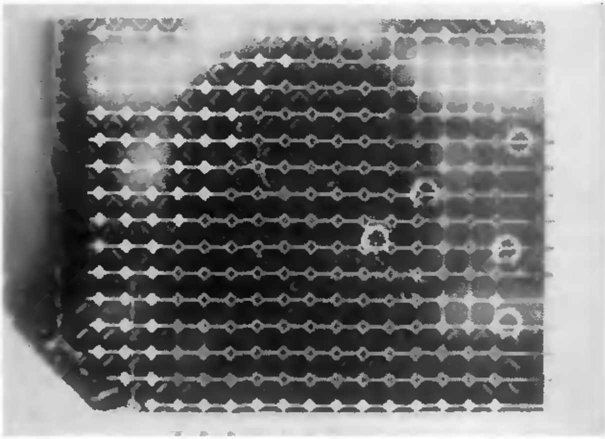

Fig.5.6. The electrodes and the spacer mesas of the tactile sensor.

5.4. Experimental

5.4.1. Introduction

The sensor was characterized by three different approaches. First we measured purely mechanically the spring constant of a single element. Then we measured the capacitance in function of the applied force using precision instruments and finally we showed by means of a simple commercially available electronic circuit that it would be possible to realize a functional sensor with a pre-processed signal output (which was not obvious from the beginning because one has to measure femtofarads!).

5.4.2. Measurement method and system

5.4.2.1. Force measurement

In the direct mechanical measurement the force was measured using a beam with a mounted strain gauge and the displacement by a Carycompar (inductive stylus displacement measure apparatus).

In the electronic set-up the force was applied to a single element via a pickup equipped with a sapphire needle and measured underneath by a digital balance from Mettler

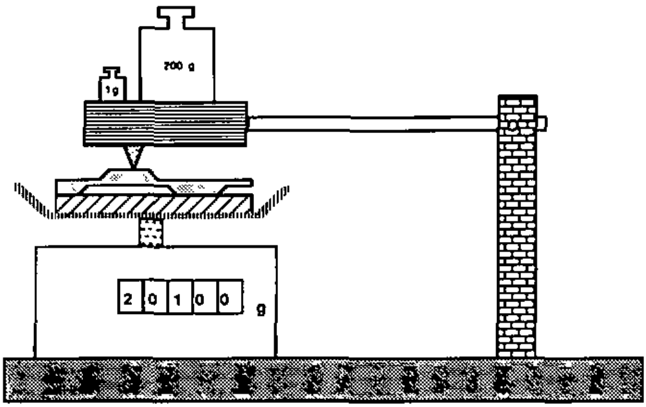

Fig. 5.7 . The force measurement set-up

5.4.2.2. Capacitance measurement

The capacitance was measured by a HP4275A Multi-Frequency LCR Meter at a frequency of 1MHz . Those electrodes which were not measured were hold on the potential of the counterelectrode in order to reduce the stray capacitics.

5.4.3. Oscillator

In order to show the applicability of this device as a sensor we connected in parallel the capacity to measure to that of the time base of a cheap and simple electronic circuit a Voltage/frequency converter IC LF 331) ; thereby the voltage actually to convert was hold constant and all rows and column not addressed were grounded.

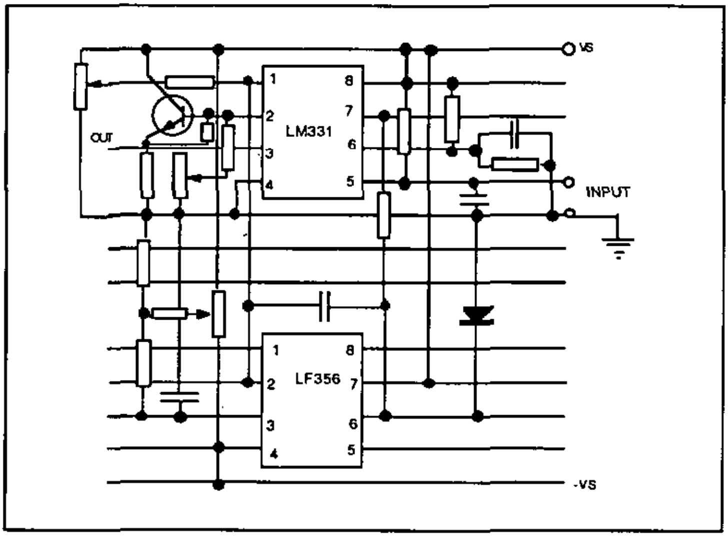

Fig.5.8. The electronic circuitry used for a capacity/frequency conversion[13]

5.5. Results

5.5.1. Introduction

With the selected dimensions an upper limit for the force per element was found to be at about 10 N. Then the upper boss touches the glass plate (the two electrodes touch each other). This is a built in security against overload. Other ranges are easily possible by selecting other dimensions.

5.5.2. Capacity as a function of force

The dependence of capacity on the applied force per element is shown in Fig.5.9. It shows the expected hyperbolic characteristic.

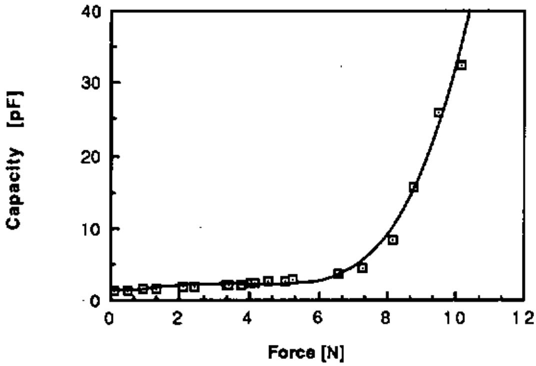

Fig.5.9. The capacityance as a function of the applied force

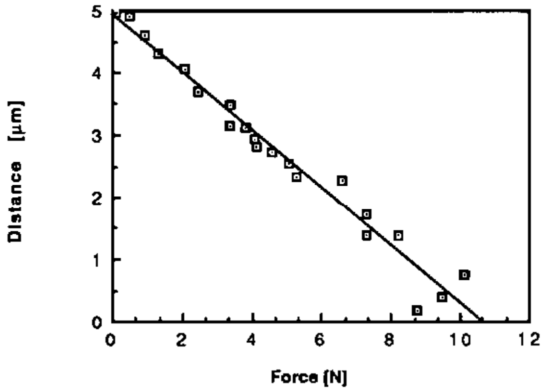

Fig.5.10. The distance between the electrode as a function of applied force

5.5.3. Frequency readout by the electronic circuit

The standard deviation s of a frequency measurement at 54 kHz (Frequency counter HP5335) for 100 measurements and a gatetime of o.1 s is s = ± 1.2 Hz. This corresponds to a resolution of about 3fF, which in the lower part of the force corresponds to about 10 mN.

The addressing can be performed by analog multiplexer as described in literature[14], and a complete readout by utilizing a system available by Burr and Brown[15].

5.6. Discussion

We could show that a monolithic silicon tactile sensor array can be realized. Our prototype showed a resolution of force of 1% with the simple electronic readout and is able to support up to 100 N/cm^2, having a resolution in space of 10 points/cm^2. It is a special advantage of this device to be able to cover a large range of specifications. The reaction on the publication of this prototype showed an unexpected vast field of applications. Possible application fields of such sensors are grippers in robots the measurement of rolling profiles of wheels or medical research.

---

1 Buser, R.A., Stauffer, B., de Rooij, N.F.; Realization of a mesa array in (001) oriented silicon wafers for tactile sensing applications, Fall meeting of the Electrochemical Society , San Diego, CA, Nov 1986.

2 Buser, R.A., de Rooij, N.F.; Monolithisches Kraftsensorfeld, VDI Berichte Nr. 677, 1988 p115, VDI Verlag Düsseldorf.

3 Harmon, Leon D.; Automated Tactile Sensing, Robot VI Conference March 2-4-, 1982 Detroit Michigan. Technical Report, Society of Manufacturing Engineers.P.O Box 930, Dearborn, Michigan 48128.

4 Chun, Kukjin and Wise, Kensall.; A high-performance Tactile Imager Based on a Capacitive Cell. IEEE Trans. on ED, Vol ED-32,No7 July 1985.

5 Sugiyama, Susumu et. al.; High-Resolution Silicon Pressure Imager with Cmos Processing Circuits, 4th Int. Conference on Solid-State Sensors and Actuators, Transducers '87, Tokyo 1987.

6 Regtien,Paul.; Integerated Tactile Imaging Sensor. 4th Int. Conference on Solid-State Sensors and Actuators, Transducers '87, Tokyo 1987.

7 Hillis, D.; A High Resolution Imaging Touch Sensor, The Int. Journal of Robotics Resaerch, Vol.1, No 2, Summer 1982 p.33.

8 Raibert, M.H.; An all digital VLSI tactile array sensor, Proc. Int. Conf. Robotics (Atlanta, GA) pp. 370, Mar. 1984.

9 Clark, S. K., Wise, Kensall, D.Wise.; Pressure Sensitivity in Anisotropically Etched Thin-Diaphragm Pressure Sensors. IEEE Transactions on electron Devices, Vol. ED-26, No 12, December 1979.

10 Tanigawa, H.; Ishihara T, Hirata, M. Suzuki,K.; MOS Integrated Silicon Proessure Sensor. IEEE Trans. on Electron Dev. VOL ED-32 No 7 July 1985.

11 Petersen, Kurt et al.; A Force sensing Chip designed for Robotic and Manufacturing Automation Applications. 3rd Int. Conference on Solid-State Sensors and Actuators, Transducers '85 , Philadelphia, 1985.

12 Szabo, I.; Einführung in die Technische Mechanik, Springer,Berlin, 8th ed.,1984, p.114.

13 Modificated circuit taken from data book. Highstability version.

14 Boie, R.A.; Capacitive impedance readout tactile image sensor, Proc. Int. Conf. Robotics (Atlanta,GA), pp 370-378, Mar. 1984.

15 Nicol, K.; A New Capacitive Transducer System for Measurering Force Distribution Statically and Dynamically, Transducer Tempcon 81 Conference, 10 June 1981.

Chapter 6.

Mass-beam-system

6.1. Introduction

6.1.1. The mass beam system as an accelerometer (static)

Since the first publication on an accelerometer micromachined in silicon by Roylance[1], different groups have realized "their" accelerometer, too (Chen[2], Rudolf[3], Petersen[4], Tsugai[5]). Typically the publications restrict themselves to the pure description of their work, without having a general look of the problem. Only Seidel *et.al.*[6] gives some theoretical considerations for optimal accelerometers but they do not take into account the damping.

One problem all accelerometers, realized till now, have in common is, that the mesa (proof mass) is not well etched at the corners, thus, the mass is not calculable. We achieved to suspend this lack with the help of our corner compensation techniques and were thus able to model the resonance frequency respectively the bending precisely.

6.1.2. The mass beam structure as a resonator (dynamic)

Resonant structures published until now are all quite small compared to those presented in this chapter. The reason is besides miniaturization the context with fiber optics as pointed out in the general introduction (references see chap. 10).

Since we do not want to content ourselves to just realize another structure but to find to what extend silicon resonators might be competitive not only as a cheap mass produced sensor, but also as high precision sensor element, it is very important to be able to describe the structures theoretically. This is the reason, why we used this quite simple and large type of structure to start our dynamical measurements. A theoretical problem however was, to describe this accelerometer type structure, when it vibrates in a damping medium. The solution to this problem is treated in chapter 2, where with the help of modal analysis and a Laplace transformation we could derive an analytical expression for the frequency and the damping. In the present chapter we deduce the optimal dimension for minimized damping for this type of structure.

Investigation were made mainly on the losses characterized by the Q-factor and the pressure dependence of the resonance frequency. Also the influence of various thin films on the Q-factor have been studied.

6.2. Calculations and design

6.2.1. Introduction

The proof mass of the accelerometer was fixed by two beams in order to maintain the surface of the mass perpendicular to the vibration movement (see Fig.6.1.). The simulation program predicts the three-dimensional geometries of etched silicon structures starting from the two-dimensional mask. The corner compensation technique was used to obtain precise mesa structures, of which the mass can be easily calculated (see Chapter 3).The stiff part in the middle has the following advantages:

i) we have an area with no rotation, so a LASER beam is not deflected.
ii) possible heating by the light of the LASER does not influence or at least not immediately the elastic behavior of the system.
iii) higher Q-factor in a damping medium
iv) the modes are better defined (in the limit of a massless beam the system becomes one-dimensional)

Meanwhile other authors have recognized the advantage of a double side clamped structure, Sandmaier *et al* [7], Terry[8], to reduce cross acceleration. Moreover, the publication of Terry recognizes the role of the damping.

6.2.2. Design and etchsimulation

In principle a structure as we are describing here was published by Roylance[1] as an accelerometer. Besides different dimensioning our construction contains a corner compensated rigid mesa mass so that the mass could be calculated accurately. Moreover in our design, the proof mass is supported by two beams. Thus the system gets more stable but as accerelometer less sensitive. Structures with an extremely long cantilever (beam length L) and such with a short one have been fabricated in order to be able to determine the influence of a single geometric parameter (the length) on behavior. For the same reason single beam types as in classical accelerometers have been made also. The beam width b is the same for all structures.The individual structures could bee easily separated on account of the trenches round the structure. A schematic diagram of the structure with the long beam is shown in Fig.6.1. The backside shows no step, so that optical scanning was possible over the clamping. In addition thin films could thus be deposited homogeneously (without a shadowing effect)

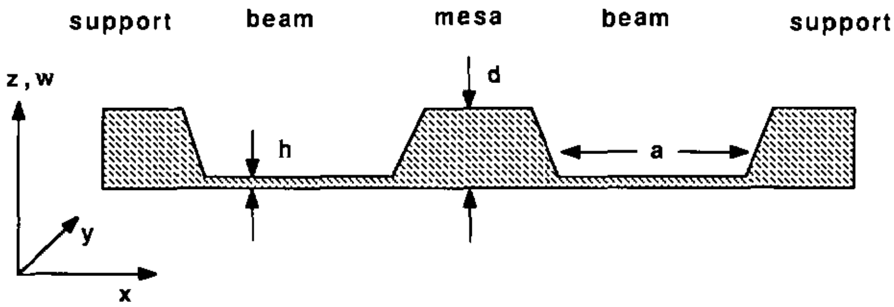

Fig.6.1. Cross section of the mass beam structure

Fig.6.2 shows the mask layout, Fig.6.3. the CAD output and Fig.6.4 is a photograph of the resulting etched silicon structure. The simulation is done for deep etching (300 μm) and reveals the mesa structure and the frame. The shallow etching from backside resulting in the two lateral beams supporting the mesa is not shown in this simulation.

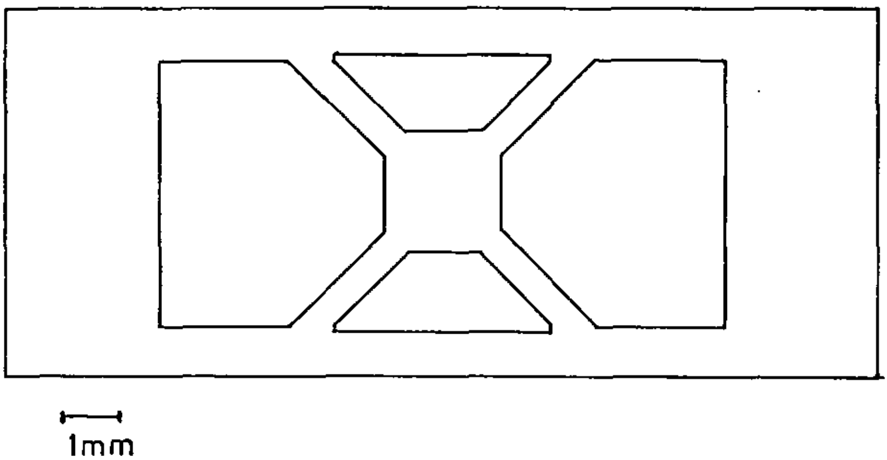

Fig.6.2. Mask layout

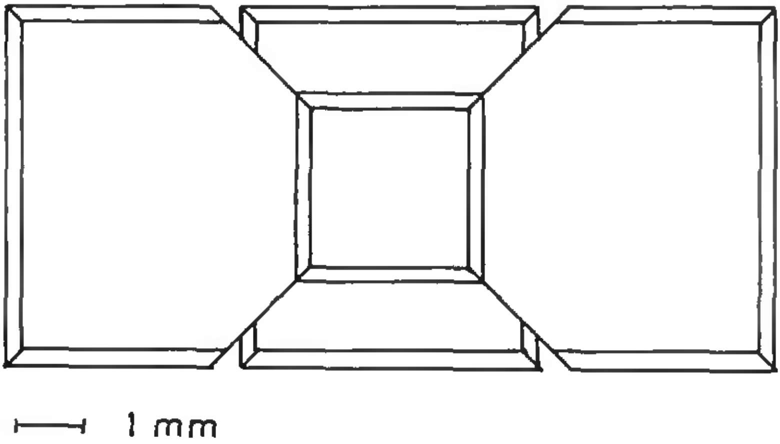

Fig.6.3. The simulated structure

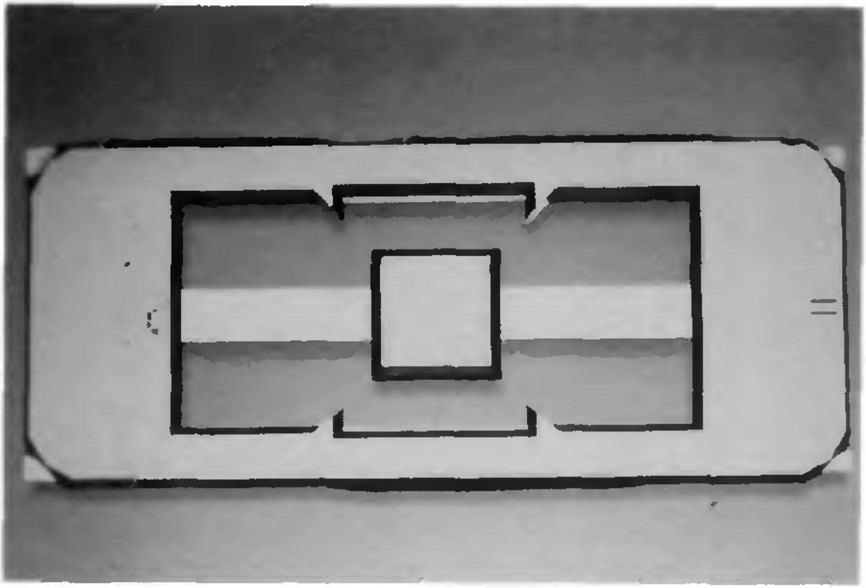

Fig.6.4. Photograph of the realized structure with the long beams

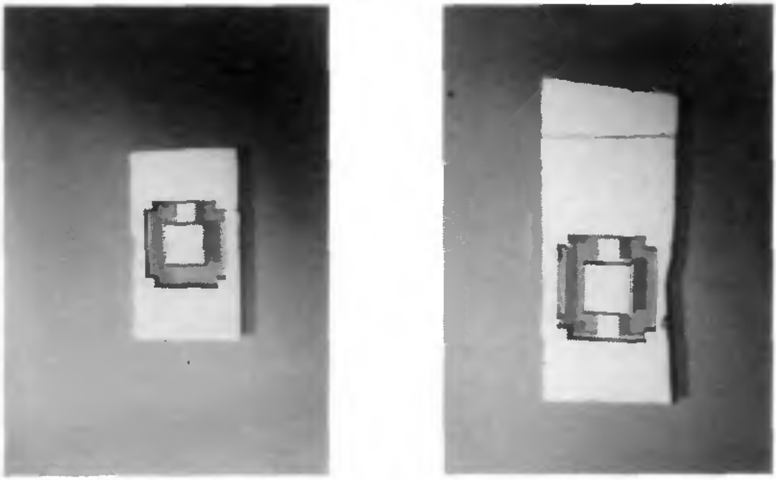

Fig.6.5. Photograph of the structures with one and two short beams (L=1.2mm)

The dimensions of the beam thickness h, the wafer thickness d (which determines the mass of the mesa) and the calculated mass of the mesa are given in Table 6.I.

Table 6.I. Dimensions of the structures with long beams
L= 3.95 mm and b= 1.0 mm for all structures

wafer number	h(μm)	d(μm)	M(mg)
1	64	385	5.43
2	55	382	5.38
3	58	382	5.38
4	54	380	5.35

6.2.3. Calculation of the Mesamass

We are using the formula given in chapter 2.2. The thickness of the mesa and the dimension of the roof of it determine the mass. Because we are etching from two sides we have two mesas, one from top and one from bottom (which are designed to match at their base). All the calculation were done by computer programs. The results are shown in Table I. To check the calculations we weighted a mesa (after having broken them out of beam and frame):

Calculated mass: 5.52 mg
Measured mass 5.4 mg

6.2.4. Calculation of the resonance frequency

As described in section 2.3. the resonance frequency under vacuum conditions was calculated by solving the equations of the transverse vibration of a beam with thc appropriate boundary conditions. This allows to include different boundary conditions properly and also to calculate higher order eigenfrequencies. In the following subsections we are citing but the results of the calculations of chapter 2. For a given mass ratio of beam and proof mass, by the function plotted in in fig. 2.8.one can find the resonance frequencies by the formulas given below, but the values are actually found by computer programs calculating the λ for cach run scparatly.

With the simple formula

$$f=\frac{1}{2\pi}\sqrt{\frac{24\ E'\ J_y}{M\ L^3}} \qquad [2.22]$$

wc calculated the dependence of the resonance frequency of the structure with the long beams on the geometrical dimensions. The results are plotted in the figures 6.6. to 6.8.

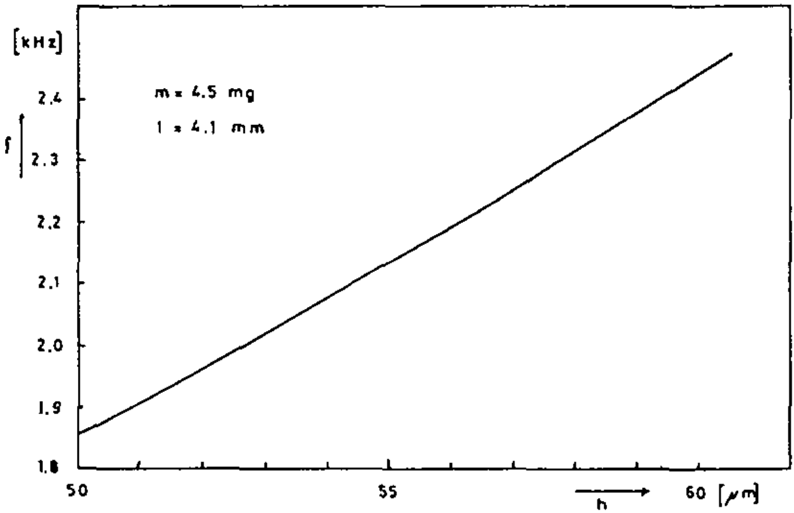

Fig.6.6. Resonance frequency dependence on the thickness of the beam

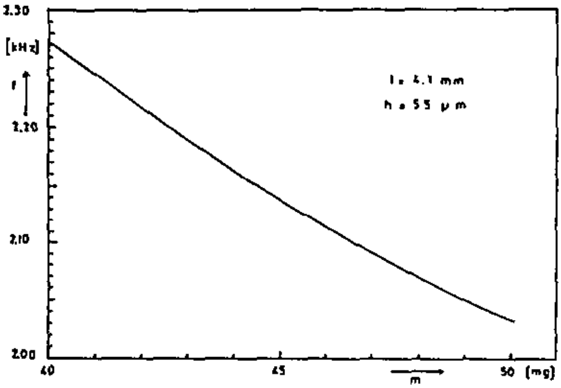

Fig.6.7. Resonance frequency dependence on the mass of the mesa

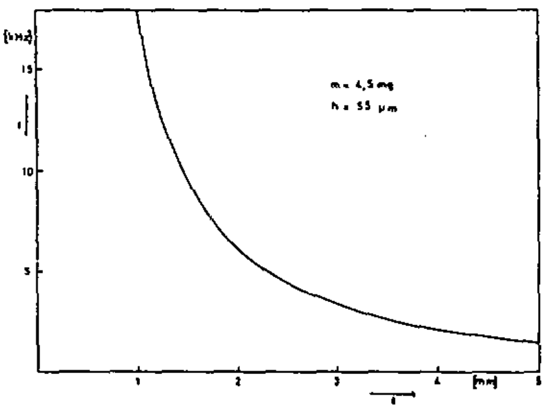

Fig.6.8. Resonance frequency dependence on the length of the beam (one side)

For thc precise calculation we used the formula [2.7]:

$$f = \frac{1}{2\pi}\left(\frac{\lambda}{L}\right)^2\sqrt{\frac{E\ J_y}{\mu}}$$

λ can be found in Fig. 2.8. or calculated with formula [2.25] numerically.

The same formula [2.7] as above applies for structures with one side clamping only and λ can be found again in Fig.2.8. or calculated again numerically by setting the determinant of A [2.31] to zero.

In the torsional mode the following formula applies (see also appendix F)

$$f = \frac{1}{2\pi}\sqrt{\frac{J_1}{\Theta_{bar}\, L}\left(\frac{3\kappa}{3+\kappa}\right)} \qquad [2.42]$$

with κ the ratio of the inertial moments of proof mass and beam.

6.2.5. Damping

6.2.5.1. Resonance frequency in dependence of the gas pressure

Neglecting the dissipation effect on the resonance frequency, we nevertheless have to take into account the supplementary inertial mass of the sourrounding gas (viscous region, in the molecular region the frequency change is very small, see experimental results). This means that the λ for the coresponding (pressure dependent) mass ratio $r_{mass} = \frac{\mu+\chi}{m_d} = \frac{m}{m_d}$ of beam and proof mass has to be calculated or found in Fig.2.8. m and m_d are given by the expressions [2.126] and [2.127] respectively.The resonance frequency can be calculated then by

$$\omega_0 = \left(\frac{\lambda}{L}\right)^2 \sqrt{\frac{E\, J_Y}{\mu+\chi}} \qquad [6.1.]$$

A more accurate picture of the pressure dependence follows from the equation [2.105], which was derived with modal analysis in section 2.4, since it includes also the dissipating term. As we have seen however, this first approximation results in a eigenfrequency which is too high.

$$\Omega = \sqrt{\frac{4\left(m + m_d\, \phi_o^2\right)\left(m\, \omega_1^2\right) - \left(c + c_d\, \phi_o^2\right)^2}{4\left(m + m_d\, \phi_o^2\right)^2}} \qquad [2.105]$$

with m, m_d, c the damping per unit length of the beam and c_d the damping of the proof mass given in the expression [2.124] to [2.127].

6.2.5.2. Damping in the low pressure range (<1 mbar)

With the formulas given in section 2.4. we are able to calculate the pressure dependence of the Q-factor in the low pressure range. As the experiment shows, we can neglect in this region the inertial contribution of the gas (the frequency is constant in this range see section 6.5.).

The Q-factor was calculated to be in the first approximation :

$$Q^2 = \frac{2\left(m + m_d\,\phi_o^2\right)\left(m\,\omega_1^2\right)}{\left(c + c_d\,\phi_o^2\right)^2} - \frac{1}{4} \qquad [2.113]$$

With from section 2.4.4.1.1. the expression needed as follows

$m = \mu = \rho\, b\, h$: Mass per unit length of the beam

$m_d = \rho\, d\, c_1^2$: Mass of the mesa

where c_1 is the side length of the mesa (correct formula for the mass see section 2.2)

$c = \xi_o + \xi$: Damping per unit length of the beam

where ξ_o is the simulated damping in vacuum (internal, clamping) and

$$\xi = 4b\sqrt{\frac{2}{\pi}}\sqrt{\frac{M}{R_oT}}\;p \qquad [2.118]$$

$c_d = \frac{\xi}{b} c_1^2$: air damping of the mesa ($\frac{\xi}{b}$ is the pressure of the air damping see above)

Thus we have

$$Q^2 = \frac{2\left(\mu + \rho_{Si}\, d c_1^2\, \phi_o^2\right)\left(\mu\,\omega_1^2\right)}{\left(\xi_o + \xi + \frac{\xi}{b} c_1^2\, \phi_o^2\right)^2} - \frac{1}{4}$$

$$Q = \sqrt{\frac{2\,\rho_{Si}^2\left(bh + dc_1^2\,\phi_o^2\right)\left(bh\omega_1^2\right)}{\left(\xi_o + \xi\left[1 + \frac{c_1^2}{b}\phi_o^2\right]\right)^2} - \frac{1}{4}} \qquad [6.2]$$

with $\phi_o = \phi_1(r_1) = \frac{1}{\sqrt{L}}\,1.58815$ (see [2.78])

$$\phi_o^2 = \frac{2.5222}{L}$$

$$Q(p) = \sqrt{\frac{2\,\rho_{Si}^2\left(bh + dc_1^2\,\frac{2.5222}{L}\right)\left(bh\omega_1^2\right)}{\left(\xi_o + 4b\sqrt{\frac{2}{\pi}}\sqrt{\frac{M}{R_oT}}\,p\left[1 + \frac{c_1^2}{b}\frac{2.5222}{L}\right]\right)^2} - \frac{1}{4}} \qquad [6.3]$$

With the numerical values as

$$\frac{M}{R_o} = 0.003367 \quad \text{for nitrogen at } T = 300\,\text{K}$$

we can calculate

$$4\sqrt{\frac{2}{\pi}}\sqrt{\frac{M}{R_o T}} = .010692$$

and insert this factor in the equation [6.3]:

$$Q(p) = \sqrt{\frac{2\,\rho_{Si}^2\left(bh + dc_1^2\,\frac{2.5222}{L}\right)\left(bh\omega_1^2\right)}{\left(\xi_o + (.010692)\,bp\left[1 + \frac{c_1^2}{b}\,\frac{2.5222}{L}\right]\right)^2} - \frac{1}{4}} \qquad [6.4]$$

The pressure dependency of the Q-factor was calculated numerically with the above formula for various parameter. The plots are shown in Fig. 6.9. to Fig. 6.12.

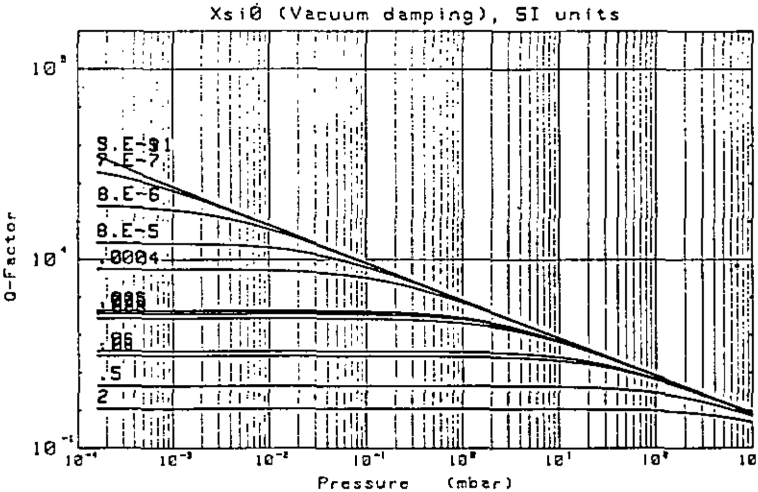

Fig.6.9. Q-factor as a function of pressure with the internal damping ξ_o as parameter, h= 60μm, d=380μm, L=8mm. c_1=2.2mm.

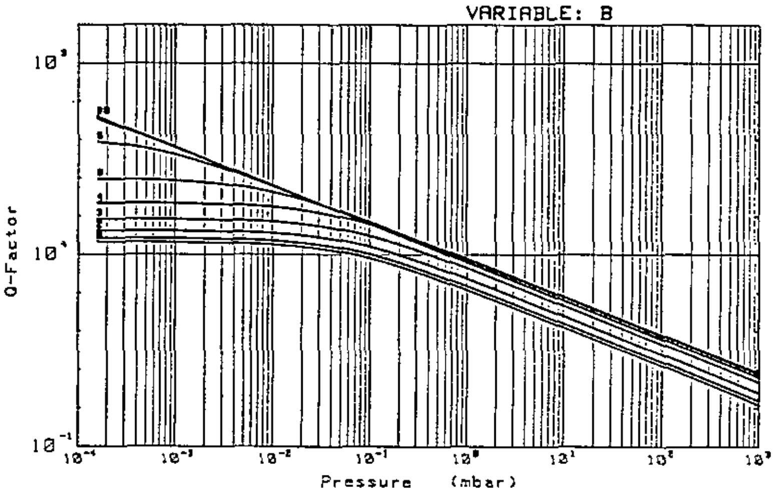

Fig.6.10. Q-factor as a function of pressure with width of the beam b as parameter,h= 60μm, d=380μm, L=8mm, c_1=2.2mm, ξ_o=.0001 kg/s, 0) b =10μm, 1) b =16μm 2) b =39μm, 3) b =160μm, 4) b =1mm, 5) b =10mm.

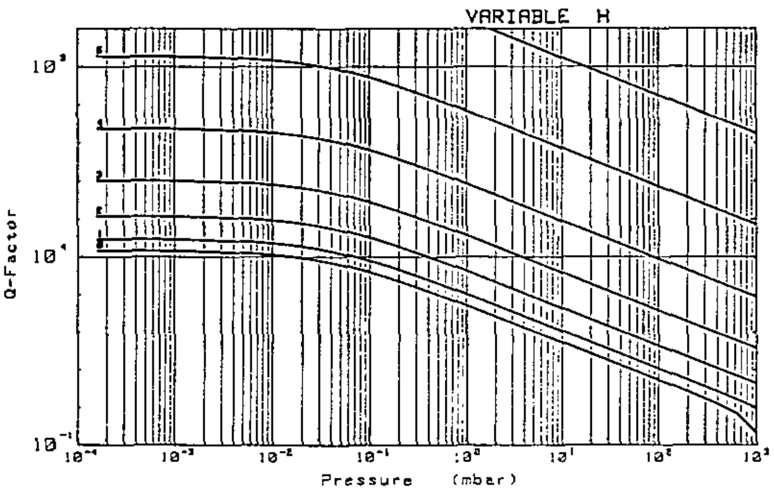

Fig.6.11. Q-factor as a function of pressure with the thickness of the beam h as parameter, b= 1mm, d=380μm, L=8mm, c1=2.2mm, ξ_o=.0001 kg/s, 0) h =10μm,1) h =16μm, 2) h =39μm, 3) h =160μm, 4) h =1mm, 5) h =10mm.

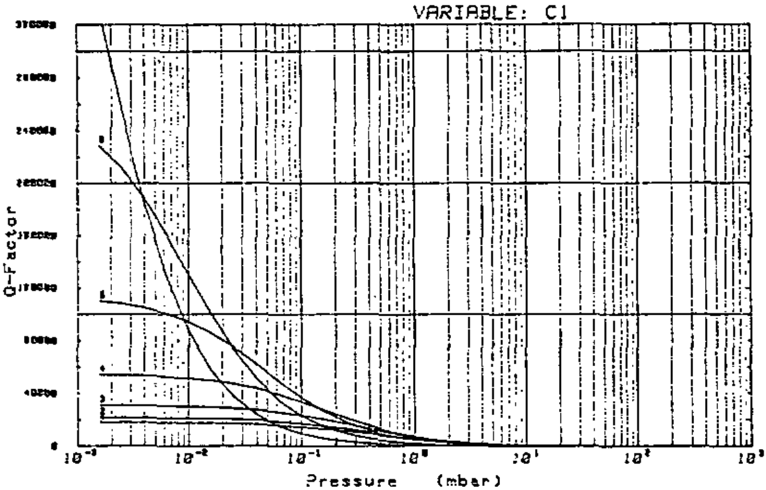

Fig .6.12. Q-factor as a function of pressure with the width of the mesa mass c_1 as parameter. $h=65\mu m$, $b=1mm$, $d=386\mu m$, $L=8mm$, $\xi o=.0001$ kg/s, 0) $c_1=0.2mm$, 1) $c_1=.43mm$, 2) $c_1=.71mm$, 3) $c_1=1.25mm$, 4) $c_1=2.44mm$, 5) $c_1=5.23mm$, 6) $c_1=12.3mm$, 7) $c_1=32.0mm$.

To find the maximum of the Q with respect to the lateral dimension of the middle mass c_1 for example we have to derive the formula for $Q(c_1)$ from above. Because of simplicity we are deriving the square of Q:

$$\frac{\partial Q^2(c_1)}{\partial c_1}=\frac{\partial}{\partial c_1}\frac{\left(\mu+\rho_{Si}\, d_1\, c_1^2\, \phi_0^2\right)\ \left(\mu\ \omega_1^2\right)}{\left(\xi_0+\xi+\frac{\xi}{b}c_1^2\,\phi_0^2\right)^2} \qquad [6.5]$$

This is a equation of the following type:

$$\frac{\partial}{\partial x}\frac{ax^2+d}{(b+cx^2)^2}=\frac{(b+cx^2)^2\,2ax-ax^2\,2(b+cx^2)\,2cx}{(b+cx^2)^4}-\frac{d\,2(b+cx^2)\,2cx}{(b+cx^2)^4} \qquad [6.6]$$

The zeroes of the numerator determine the extrema:

$\Rightarrow (b+cx^2)\,2ax-ax^2\,2.2cx\ -d\,2.2cx\ =0$

$\Rightarrow (b+cx^2)\,a-ax^2\,2c\ -d\,2c=0$

$\Rightarrow ab+ac\,x^2-2acx^2-2cd=0$

$$\Rightarrow \quad + acx^2 + 2cd - ab = 0$$

$$\Rightarrow \quad x^2 = +\frac{b}{c} - 2\frac{d}{a}$$

$$x_{1,2} = \pm\sqrt{\frac{b}{c} - 2\frac{d}{a}} \text{ and } x_3 = 0 \qquad [6.7]$$

with

$a = \rho_{Si} d_1 \phi_o^2 \mu\, \omega_1^2$

$b = \xi_o + \xi$

$c = \frac{\xi}{b}\, \phi_o^2$

$d = \mu^2\, \omega_1^2$

and $x = c_1 >= 0$

we find

$$c_1 = +\sqrt{\frac{\xi_o + \xi}{\frac{\xi}{b}\, \phi_o^2} - 2\,\frac{\mu^2\, \omega_1^2}{\rho_{Si}\, d_1\, \phi_o^2 \mu\, \omega_1^2}}$$

$$c_1 = +\frac{1}{\phi_o}\sqrt{b\left(\frac{\xi_o}{\xi} - \frac{2h}{d_1} + 1\right)} \qquad [6.8]$$

with $$\xi = 4b\sqrt{\frac{2}{\pi}}\sqrt{\frac{M}{R_oT}}\,p \qquad [2.118]$$

$$c_1 = +\frac{1}{\phi_o}\sqrt{\frac{\xi_o}{4\sqrt{\frac{2}{\pi}}\sqrt{\frac{M}{R_oT}}\,p} + b\left(1 - \frac{2h}{d_1}\right)} \qquad [6.9]$$

Thus the optimum of c_1 is pressure but not frequency dependent in that model. The higher the pressure, the smaller the mesa has to be. When the beam is large or thick, the mesa has to be large, too. When the mesa is thick (d_1) , c_1 can become small.

The same calculation could be done, of course, with respect to all the parameters, where the dependency is not obvious. Thus one could derive a design rule for an optimal Q-factor device.

6.2.5.3. Damping in the high pressure range (> 1mbar)

Instead of fromula [2.113] the Q-factor is equivalently defined by the formula (cf. eq [2.65]

$$Q=\frac{\Omega}{2D} \qquad [2.112]$$

with

$$D=\frac{\left(c+c_d\,\phi_o^2\right)}{2\left(m+m_d\,\phi_o^2\right)} \qquad [2.104]$$

and again m, m_d, c the damping per unit length of the beam and c_d the damping of the proof mass are given in the expression [2.124] to [2.127]. Since Ω corresponds to the resonance frequency ω and the methods used in section 2.3. are better than the formalism (in the first approximation) of modal analysis, where Ω stems from, we better use that one. In the experimental part the measured frequency (in vacuo) is used. Examples for the theoretical curves can be found there (see section 6.5.4. and chapter 8, e.g.)

6.2.6. Supplementary layer

6.2.6.1. The resonance frequency in the presence of thin films

For a beam with $H_2=\frac{H_1}{100}$ and $E_2=\frac{E_1}{2}$ (see Fig.2.10.), we find with the help of equation [2.47]. $h_1= 0.5025\,H_1$, e.g. $H_1= 60\ \mu m$ Si and $H_2= 0.6\ \mu m$ Al, Au or SiO_2 the shift of the neutral axis compared to the uncovered beam is 0.152 µm. For the same example we find with equation [2.48] $J_1 = 1.8\ 10^{-17} m^4 + 1.39\ 10^{-21} m^4$, where the first term represents the uncovered beam. The change is thus about 100 ppm and with [2.49] $J_2= 2{,}72\ 10^{-19}\ m^4$, thus about 1% of J_1.

By equation [2.52 b] the resonance frequency of the covered beam f_{cov} is

$$f_{cov}=\frac{1}{2\pi}\left(\frac{\lambda}{L}\right)^2\sqrt{\frac{(E_1J_{y1}+E_2J_{y2})}{\mu}}$$

Here μ is the mass per unit length of the beam including the layer and λ has to be found for the correct mass ratio of beam and proof mass (cf. Fig.2.8) For the example above, λ changes from 1.2315 for the uncovered structure to λ_{cov}=1.2353 and the change in frequency can be calculated to be

$\Delta f = f_{uncov} - f_{cov} = 2286.12 - 2285.9 = 0.22$ [Hz]

or about 100 ppm.

6.2.6.2.The damping by thin films

The explanation for the addittivity of the inverse of the Qs which have to be attributed to different damping processes is given in section 2.4.2.3.:

$$1/Q_{tot} = 1/Q_1 + 1/Q_2 + ... \qquad [2.70]$$

In literature[9] an approach by energy rather than as here by forces can be found. But this supposes that the differential equation is separable in time and space.

6.2.7. Temperature characteristics of the structures

The resonance frequency of a mass and beam system changes for two reasons:

i) change of the dimensions by thermal expansion

ii) change of the modulus of elasticity

Knowing the linear thermal expansion coefficient α we can calculate the temperature coefficient of the modulus of elasticity as a function of the change of the resonance frequency.

To be able to derive an analytical equation we have to start with an analytical representation of the resonance frequency. Thus we are starting with the formula [2.22], introducing the tempeature dependence and taking the square:

$$\omega^2(T) = \frac{E(T)}{s(T)} \quad \text{with } s(T) = \frac{ML^3(T)}{2b(T)h^3(T)} \qquad [6.10]$$

Thus

$$E(T) = s(T)\,\omega^2(T) \qquad [6.11]$$

$$\left.\frac{dE(T)}{dT}\right|_{T_o} = \omega_o^2\frac{ds(T)}{dT} + s_o 2\omega_o\frac{\partial\omega(T)}{\partial T} \qquad [6.12]$$

where the index zero means at temperature T_o

$$\frac{ds(T)}{dT} = \frac{M}{2}\left(\frac{1}{b_o h_o^3}\frac{dL^3(T)}{dT} + L_o^3 \quad \frac{d}{dT}[b^{-1}(T)h^{-3}(T)]\right)$$

$$= \frac{M}{2}\left(\frac{3L_o^2}{b_o h_o^3}\frac{\partial L(T)}{\partial T} + L_o^3\left[(-1)b_o^{-2}h_o^{-3}\frac{\partial b(T)}{\partial T} + (-3)b_o^{-1}h_o^{-4}\frac{\partial h(T)}{\partial T}\right]\right)$$

$$= \frac{ML_o^3}{2b_o h_o^3}\left(3\;\frac{1}{L_o}\frac{\partial L(T)}{\partial T} - \left[b_o^{-1}\frac{\partial b(T)}{\partial T} + 3h_o^{-1}\frac{\partial h(T)}{\partial T}\right]\right) \qquad [6.13]$$

Since α is isotropic (see Appendix I.7), we can write:

$$\alpha = \frac{1}{L_o}\frac{\partial L(T)}{\partial T} = \frac{1}{h_o}\frac{\partial h(T)}{\partial T} = \frac{1}{b_o}\frac{\partial b(T)}{\partial T} \qquad [6.14]$$

Thus all but one α cancels and we can rewrite [6.13]:

$$\frac{ds(T)}{dT} = - s_o\,\alpha \qquad [6.15]$$

and thus [6.15] becomes

$$\frac{dE(T)}{dT} = - \omega_o^2 s_o\,\alpha + 2\,\omega_o^2 s_o \frac{1}{\omega_o}\frac{\partial \omega(T)}{\partial T} \qquad [6.16]$$

With the abbreviation $\beta = \frac{1}{\omega_o}\frac{\partial \omega(T)}{\partial T}$ the temperature coefficient of the modulus of elasticity is finally

$$\left.\frac{dE(T)}{dT}\right|_{T_0} = \omega_o^2 s_o\,(2\beta - \alpha) = E_o\,(2\beta - \alpha) \qquad [6.17]$$

6.3. Fabrication of the structures

Double sided clamped beam structures with a stiff mesa mass in the middle have been fabricated by anisotropical etching of monocrystalline silicon [(100) surface orientation], in a KOH solution of 40% b.w. The structures were etched from both sides with different etch times as indicated in chapter 3.

<u>Processlist</u>

1.	Oxidation 1.5 µm	
2.	Photolithography on both sides	
3.	Etching BHF 10/1 both sides	
4.	Protecting backside (cantilever)	
5.	Etching frontside BHF 10/1	
6.	KOH 60°C 250 µm	
7.	Etching backside silcondioxyd BHF 10/1	
8.	KOH 60°C until through	

We selected a variety of different doped wafers hoping to find some differences in the Q-factor. The measurement showed however that for these kind of structures the influence of the clamping is much larger than one could expect from internal damping (see section 2.4.4.2). Because the wafers were also of different thickness the structures originating from different wafers had different mass distributions and we could thus check the accuracy of our calculations of the resonance frequency.

6.4. Experimental

6.4.1. Mounting and Excitation

In a first series, the structures were glued by bee's wax on a silicon frame and then to the piezoceramic disk. The were measured in air, thus we had no outgasing problems, but mounting and demounting was tedious. All the following measurements were done then by fixing the structures on the piezoceramic disk by means of a brass base and a clamping spring as described in chapter 4. By clamping only one side of the structure's frame, the Q-factor was almost doubled. Fig. 6.13. shows the different clamping systems we used. The third type is shown in Fig. 4.3.

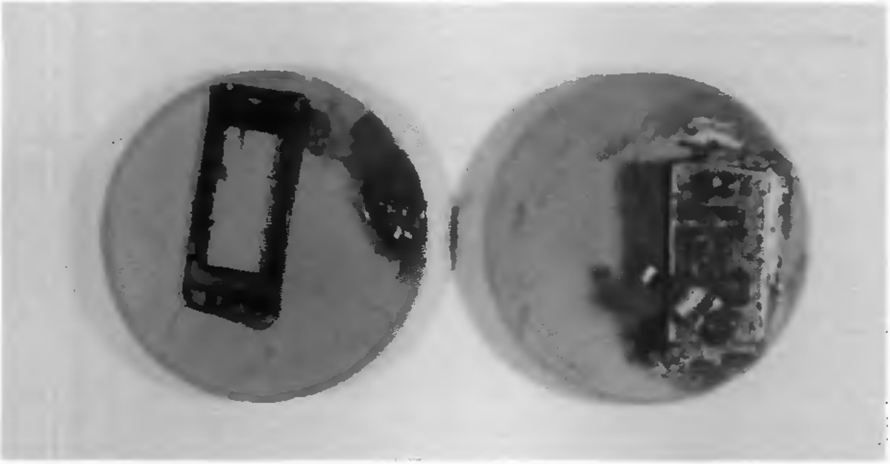

Fig.6.13. Photograph of the mounting by wax we used in the first measuring series and of the single side clamping .

6.4.2. The measurement methods (cf. chapter 4)

6.4.2.1. Absolute amplitude measurement

The amplitude of the resonator was measured by the interferometer. The amplitudes for all our measurements were lower than 100 nm (cf. the dimension of the structure is 10 mm). 1000 measurements at the same condition showed for the long beam accelerometer at resonance at 25.74 nm amplitude a standard deviation of ±.4nm. (see Fig.4.10). This corresponds to about one layer of atoms of the silicon crystal.

6.4.2.2. The measurement of the frequency

The resonance frequency was found by changing the excitation frequency till the amplitude was maximal for a given amplitude of excitation. This allowed to have for all measurements the same order of (small) amplitudes. The frequency can be measured to a precision (in vacuum) of 10 mHz (5 ppm) but different clamping of the hole structure causes differences of some Hz.

6.4.2.3. The measurement of the Q-factor

At unchanged clamping the reproducibility is as follows: Measuring with the counter (direct triggering) shows a standard deviation of ±3%, while recording the whole decay in a waveformrecorder and executing a linear regression on the data the sd reduced to ±1.5%

The reproducibility of different clamping (meaning that the structure was removed and installed again) is very poor, showing differences up to 20%. Standard deviation over 10 measurements is ±7%.

The changes due to thin films of the order of 1000 Å are typically smaller than 10% and thus not detectable with these structures.

6.5. Results

6.5.1.The first series of measurements

A great variety of wafer types were used in the beginning of this study in hope of seeing some significant differences in the damping behaviour. They were characterized by the same interferometer described in chapter 4, but the electronical apparati utilized in that early research stage were much less performant. Thus the spectrum analyzer was the HP8556, as used originally by Willemin, for the excitation a simple Phillips waveform generator, allowing a precicion of 3 digits was used and for the storing a Gould digitizing oscilloscope. A synchronisation (triggering) of these simple apparati was not easily possible. In order to capture the signal we excited the piezoceramic disk periodically (typically 1Hz) by a rectangular waveform. The disadvantage of this method was the small amplitude and we were always close to the noise level (see Fig.4.13y.). Moreover the evaluation of the plots was quite tedious.

All the structures listed in Tables 6.II.&III. were glued by bee's wax on a silicon frame and then to the piezoceramic disk. They were all measured in air.

Table 6.II. Dimensions, resonance frequencies and Q-factor of structures from various types of wafers. () means with oxid 2000Å

Nr	Type	Ωcm	polishing	Wafer [μm]	Beam [μm]	Mass [mg]	Frequency[kHz] theor.	meas.	Q [-]
C2	p	50	one side	381	55	5.52	1.955	(2.02)	(1369)
C5	p	3-5	double	393	67.5	5.73	2.596	2.52	1419
C6	p	3-5	double	386	65.5	5.61	2.508	2.47	1482
C6a	p	3-5	double	387	65	5.63	2.41	(2.52)	(1393)
C8	p	4.25-5.75	one side	383	55			2.02	1424
C8a	p	4.25-5.75	one side					(1.991)	(1403)
C10	n	15-35	one side	384	59	5.57	2.159	2.09	1437

A silicon dioxide layer of about 2000Å increased the frequency with about 20 Hz and reduced the Q-factor by about 50 to 100. A layer of photoresist painted by hand on the structure reduced the Q-factor to about 1000.

Table 6.III. Dimensions, resonance frequencies and Q-factor of structures for various types of dopings. () means with oxid 2000Å

Nr	Type	Ωcm	doping	Wafer [μm]	Beam [μm]	Mass [mg]	Frequency[kHz] theor.	meas.	Q [-]
D1	p	3-5 d	P 6.7 μm	386	65.5	5.61	2.509	(2.56)	(1354)
D3	n	15-35 o	P 6.7 μm	391	62	5.67	2.299	(2.33)	(1232)
D2	p	3-5 d	B 6.5 μm	331	66	4.71	2.68	(2.71)	(1594)
D4	n	15-35 o	B 6.5 μm	312	52	4.40	1.948	(2.12)	(1327)

Table 6.IV. Dimensions, resonance frequencies and Q-factor of various structures and modes. () means with oxid 2000Å

Nr	Description	Wafer [μm]	Beam [μm]	Mass [mg]	Frequency[kHz] theor.	meas.	Q [-]
D4	Torsional mode	312	52	4.40	3.7	(3.91)	(2408)
A	Short bridge	371.5	42	5.37	7.92	9.05	1302
A	Accelerometer (single beam)	368	39	5.3	.888	.898	3000

6.5.2. The modes of the structures

6.5.2.1. Two dimensional distribution of the vibration amplitude

We measured the form of the bent beam by scanning with the yx-stage over the beam. The result is shown in Fig.6.14. The middle part from about 6 to 8 mm should be flat because we are scaniing here over the (rigid) mesa. The end at 13 mm is not zero becuse the frame was here free to move what it actually did(one side clamping of the frame). The plot can be compared to the theoretical curve Fig.2.9. Although we excited here the base and not the beam, it can be shown, that in resonance the same shape results. To be able to detect the difference of a shape with or without mass, the error of the amplitude measurement should be about ten times lower. The same holds for the detection of higher modes of nonstanding waves. Morover we would need for the latter case to know the phase. Thus, no more details could be studied with the present interferometer without investments in stability and demodulation.

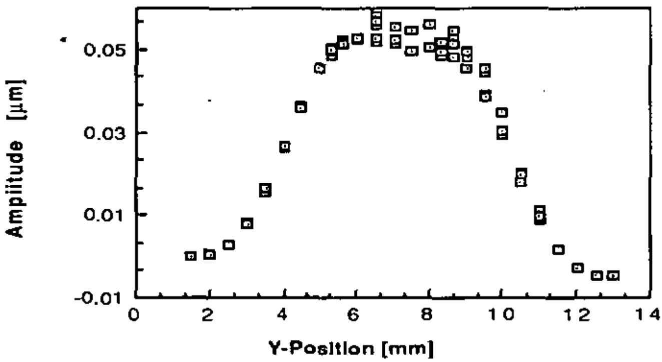

Fig.6.14. The measured function X(x)

6.5.2.2. Comparison of calculated resonance frequencies with measured in vacuo

Results of our numerical calculations are compared with the value calculated by the simple formula as well as with the measured values. Measured and calculated values agree within a few percent (see Table 6.V.).The resonant frequency depends heavily on the beam thickness (cf. Fig.6.5.). The beam thickness of the etched structures shows a variation of about 1µm. This causes an uncertainty of about 100 Hz for the theoretical resonant frequency. The non-ideal boundary conditions (elastic clamping) have only minor influence on frequency. The simple model gives, as does a Rayleigh approximation, a higher eigenfrequency.

Table 6.V. Resonance frequencies (Hz)

Structure Number	Simple model	Rigid clamping	Elastic clamping	Measured values
1	2618	2494.98	2494.95	2485
2	2075	2006.52	2006.50	2024
3	2247	2169.16	2169.14	2128
4	2081	2012.29	2012.27	2008

6.5.3. The influence of a gaseous medium on the resonance frequency

In an atmosphere of gas, several forces act on the resonator, which have to be taken into account in the differential equation describing the transverse vibration of the mass-beam system and the boundary conditions (cf. section 2.4.2.2. and 2.4.4.1.2). Not the damping causes the observed dependence of the frequency on pressure, but the additional mass c of the gas molecules to be accelerated[10,11]. Mass is added to the beam, which changes the differential equation, as well as to the mesa (proof mass), which changes the boundary conditions, but as p_{gas} decreases the effect becomes negligible.

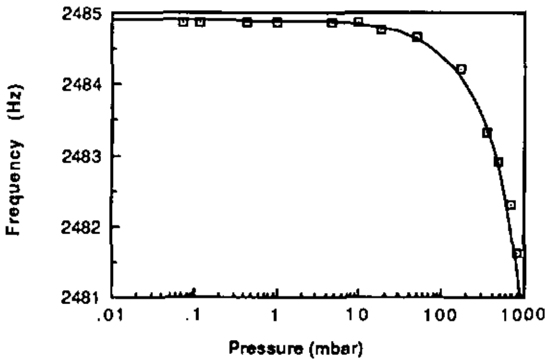

Fig.6.15. Resonance frequency in dependence of nitrogen pressure in semilog plot and interpolated.

The pressure dependence of the resonance frequency of a long beam structure (C6) starts at about 10 mbar (see Fig.6.15.). Simple beam structures as published by other authors[12], show the same strong dependence of the resonant frequency on pressure as ours in the range from 10 to 1000 mbar and almost no dependence below that pressure.

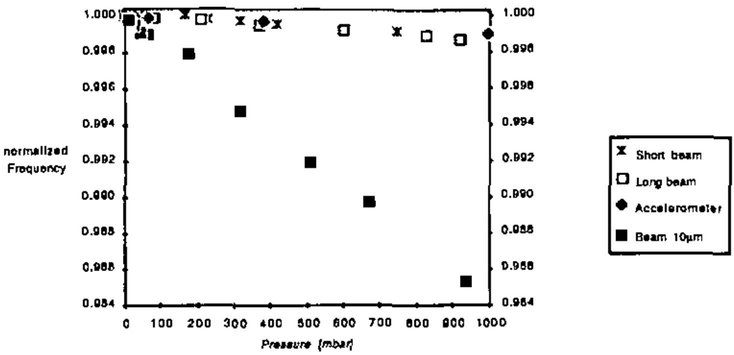

Fig.6.16. Normalized change of the resonance frequency in a linear plot for a) Doubly clamped proof mass, long beam,b) doubly clamped proof mass, short beam, c) simply clamped proof mass short beam (accelerometer), d) simple beam without proof mass, one end free, 10μm thick,

Fig.6.16. shows the normalized change of the resonance frequency in a linear plot for different structures. Those with a proof mass (same dimensions for all) have all about the same slope, whereas that whithout proof mass and a beam thickness of only 10μm shows a ten times stronger dependence of the resonance frequency on pressure. For an application as a pressure sensor this higher sensitivity has to be paid on the other hand by a ten times lower Q-factor (see chapter 10) and thus a ten times lower resolution in frequency. Since low Q-factors mean implication of dissipation effects it would be preferable for stability reasons to select from the two possibilities of equivalent performance the one with the proof mass.

6.5.4 Pressure dependence of the Q-factor

An exponential decay of the amplitude at all pressures was found (see chapter 4, Fig.4.16.), which suggests that damping is proportional to velocity, similar to the model Christen[13] used for a quartz tuning fork (see Chap. 2). The decay of the amplitude was stored in a digitizing oscilloscope and a linear regression was performed over about 100 data points. With this method a standard deviation of ±1.5% was found. The coefficient of the linear regression is $r^2>0.99$. When the signal to noise ratio is very high (>60dB) we observe a rounding at the foot of the slope. There the amplitude is of the order of Ångströms. This means, that the Q-factor is increasing in this region, i.e. the damping mechanism changes.

Different clamping of the frame showed, that the beam mass system is strongly coupled to the frame. Differences up to 20 % of the Q-factor are observed. With 10 times mounting and demounting the structure a standard deviation of ± 7% was found.

The pressure dependence of the Q-factor of a long beam structure (same measurement series as Fig.6.15.) starts at about 0.01 mbar (see Fig.6.17.). Below that pressure only internal friction and the energy loss through the clamping causes dissipation. In the theoretical part we distinguished between a low and a high pressure region. As the simulation plotted in Fig. 6.17., black dots, shows, the transition region is at about 0.1mbar. The only parameter for this calculation was the intrinsic damping $\xi_o = 0.0010214$ kg/s. Although the physical models are rather crude and the mathematical approximation only of first order, theoretical and measured curves are in a rather good harmony, especially in the high pressure region, where no parameter fit was necessary (see Fig.6.18.). Only in the transition region between molecular and viscous damping the theory over estimates the damping. This is obvious from the fact, that we assumed a constant viscosity η, which should actually be corrected for pressures below about 10 mbar. As the theoretical calculations in section 6.2. showed, the pressure dependency in the molecular region should be inversionally proportional, a fact not observed with this structure type. We will see in chapter 9 and 10, that in order to observe that, the intrinsic damping should be about ten times lower.

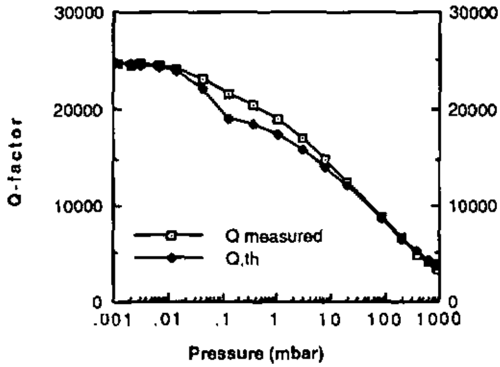

Fig. 6.17. Q-factor in dependence of nitrogen pressure

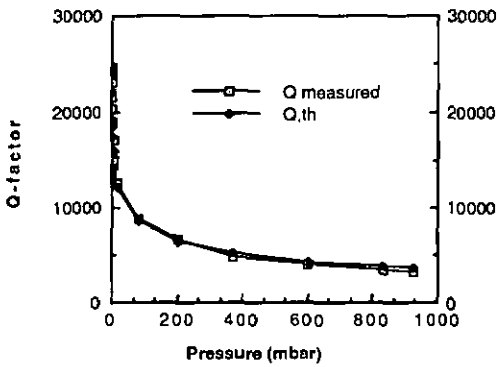

Fig.6.18. The same data as in Fig.6.18. But in a linear scale to show the good agreement of the calculated and the measured Q-factor.

In order to decide, wether the damping characteristics may be caused by the interface between the structure and the brass clamping, we glued a long beam structure by paraffin directly to the brass part (similarly to the mounting we used in the beginning). This experiment showed (see Fig.6.19.), that, although the Q-factor is reduced, the pressure dependence stays the same down to the molecular region as in the case of a spring clamped structure. The theory overestimates the Q-factor in the high pressure region by a constant factor. This cannot be simply attributed to the losses in the paraffin, because we fitted ξ_0 for the vacuum damping. It seems that at higher pressures the frame of the structure is pressed more against the holder, which causes more friction. This may also explain, why this measurement series shows more clearly the two pressure regions.

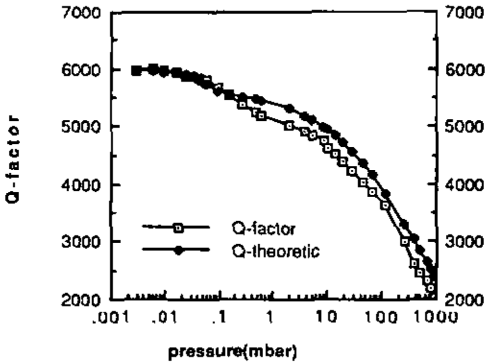

Fig.6.19. The pressure dependence of the Q-factor of a structure glued by wax to the support. and the theoretical curve with the parameters.,b=.001m,h=.0000655m, d=.000386m, L=.0081m, c1=.0022, ξ_0=.00423.

It didn't make much sense to do statistics over different structures, because with differences of up to 20% from mounting the same structure not much could be expected to be seen. To give an impression, however, we give in table 6.VI. the value for three different structures of the same wafer 13C8, all with more or less optimized clamping with respect to high Q-factors in air.

Table 6.VI. Three different structures of the same wafer 13C8

Nr	Freq $_{air}$ [Hz]	Q $_{air}$ [-]	Freq $_{vac}$ [Hz]	Q $_{vac}$ [-]	Wafer [μ]	Beam [μ]
1	2013	3037	2015.8	46752	381	57
2	2020.3	3057	2023.15	50643	382	53.5
3	2015.34	3078	2018.54	46818	382	54.5

We tried also to measure an unseparated array of structures, but the optimum clamping for high Q was different for each structure. Thus we gave up these trials comming to the conclusions, that the clamping has to be much more reproducible for precise studies and that making the clamping itself out of the silicon monolith would be a good approach (see next chapters).

6.5.5. Damping by layers

6.5.5.1. Metals

Metals with a layer thickness in the order of 1μm show a sufficient damping to be seen with these structures. A layer of evaporated aluminium (1μm thick) reduces the quality-factor in vacuum to about 1/6 of its original value.

Table 6.VII. Q-factor with metal layers

	1 bar nitrogen		vacuum	
Layer	without	with	without	with
Aluminum 1μ with oxide 2651Å C5				
Element a)		2225		5750
Element b)		1300		4000
Element c)	3396	2250	35816	5774
Aluminium 2μ C5 El d)		1153		1843
Titan Silver 1μ C8-5 with Oxide		2650	47267	16800
Titan Platinum 1μ C8-6 with Oxide	2978	2846	46000	24395
ZnO 3μ C8-7	3154	2726	29800	16872

Table 6.VIII. Influence of the layer thickness of Aluminium on damping

Element C5 c) with oxide 2651Å

thickness[μ]	1 bar	vacuum	
1	2250	5774	
.66	2468	7975	
.33	2868	13337	
0	3396	35816	

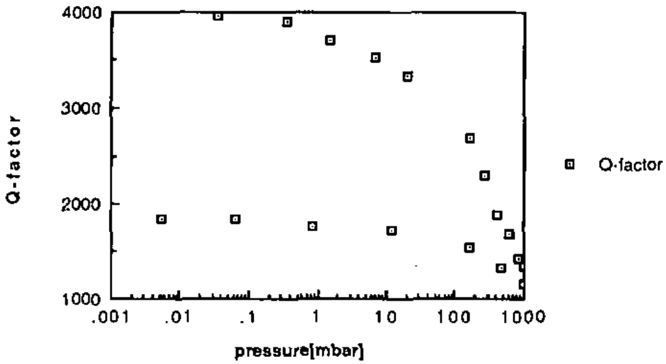

Fig. 6.20. The Q-factor of a doubly clamped mass beam structure covered with 1μm (upper curve) and 2μm (lower curve) of Al as a function of pressure in a semilog plot.

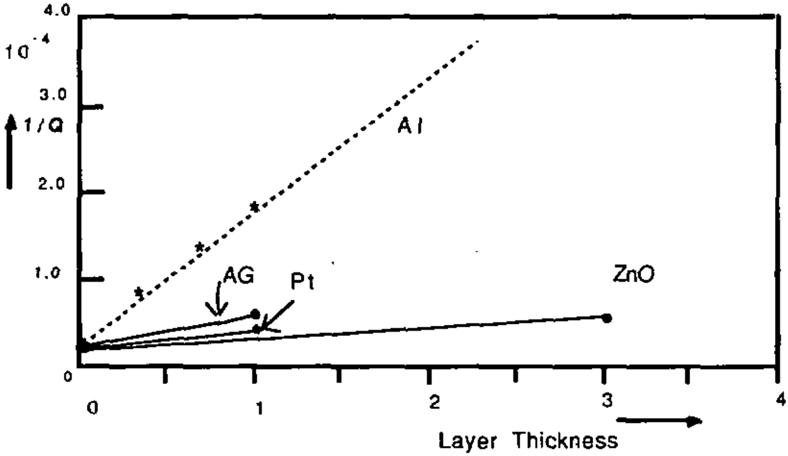

Fig. 6.21. The inverse of the Q-factor as a function of the layer thickness for various materials.

Although some alloys of aluminium are known to have low internal losses, the pure aluminium layer evaporated as a thin film seems to have higher losses than Platinum or silver. This may favorize the use of the latter type of metals in the construction of high Q devices.

6.5.5.2. Oxides

As the example of ZnO in the last section showed, oxides may damp much less than the ductile metals. Thus thin silicondioxide (±2000 Å) did not damp significantly (within the large error bar of 20 % discussed in section 6.5.4.).

Table 6.IX. C6 with a layer of Vapox of 8000Å

Description	Pressure	Frequency	Q-factor	r^2
with 8000 Å Vapox	962 mbar	2466.4Hz	3281	.9984
with 8000 Å Vapox	0.004mbar	2471.07Hz	30528	.9989
Same structure without vapox:	977 mbar	2462.97Hz	3268	.9987
dismounted and mounted again	977mbar	2462.67Hz	3237	.9988
dismounted and mounted again	977 mbar	2463.17 Hz	3200	.9994
	0.003mbar	2466.53Hz	43256	.9964

The conclusion, that the damping of the vapox layer is about 13 000, has to be drawn with care, since the measurement of other C6 structures and no oxides showed typically Qs of 30'000, too. Thus it might be just a special clamping condition that allowed this high Q of 43'000. This examples shows the whole problematic situation of the unreproducible clamping. Nevertheless it can be concluded that even this poor quality oxide near of 1µm thickness damps much less than metals.

6.5.6. Temperature characteristics of the structures

6.5.6.1. Resonance frequency versus temperature

Temperature dependence of the resonance frequency is shown in Fig.6.22. (about 40ppm). The frequency was measured under vacuum conditions.From these data we can extract a value for $\beta = -3.78 \cdot 10^{-5}$/K. The thermal expansion coefficient is $\alpha = 2.3 \cdot 10^{-6}$/K. This results in a temperature coefficient of the modulus of -1.23 10^7 Pa/K at 25 °C or $K_{E<110>}$ = -72ppm/K. An early publication by McSkimin et al.(1951)[14] gives the temperature coefficient of the Elastic constants as

K_{C11}= - 75.3 ppm/K

K_{C12}= - 24.5 ppm/K

K_{C44}= - 55.5 ppm/K

he uses an α of $7.63 \cdot 10^{-6}$, where $2.33 \cdot 10^{-6}$ is the accepted value today (see app.I), whereas Londolt Börnstein cited in "Properties of Silicon"[15] gives

K_{C11}= - 94 ppm/K

K_{C12}= - 98 ppm/K

K_{C44}= - 83ppm/K

Although the value can not be compared directly (matrix calculation see appendix I) they give the indication that our measurement are of the same magnitude as published values

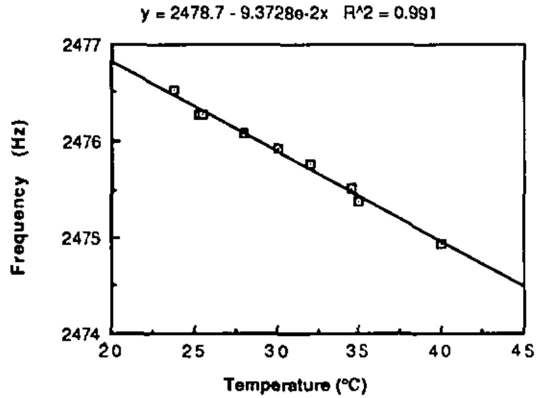

Fig.6.22. The temperature dependence of the resonance frequency

6.5.6.2. Temperature dependence of the Q-factor

As expected, also the Q-factor under vacuum conditions shows (Fig.6.23.) an increase with lower temperatures. As stated at the end of chapter 2 this should be interpretable as a thermally activated jumping or diffusion process described by an Arrhenius equation. This is visualized in Fig. 6.24. From the slope we find a activation energy of 0.055 eV. For saphir a similar value of 0.04 eV is reported in literature[16]. We have here in our measurements a rather unspecified process because frequency and temperature are not adjusted to any specific peak in intemal damping. A jump of an interstitial oxigen atom in a silicon lattice, for example would need 2.5 eV, but would be observable at 1000° C at 100kHz[17].

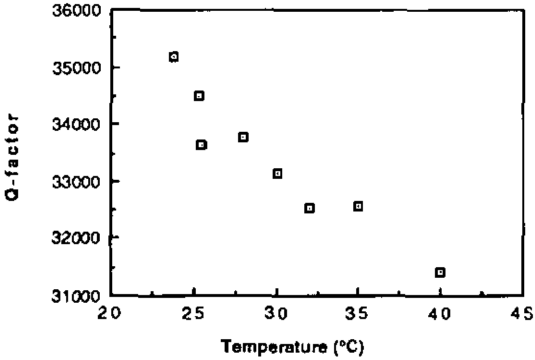

Fig. 6.23. The temperature dependence of the Q factor

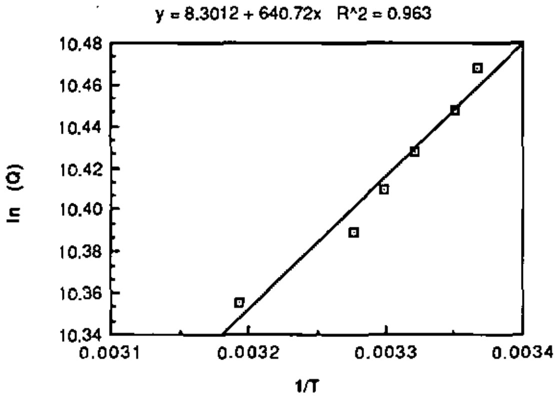

Fig.6.24. An Arrhenius plot of the data of Fig. 6.23.

6.6. Discussion

We examined in this chapter the dynamical behaviour of an accelerometer type structure and thereby especially the dependence on nitrogen damping. Moreover we could derive the temperature dependence of the modulus of elasticity for the crystal direction <110>. The studies of various thin films showed their influence on the Q-factor. As a conclusion we can report, that aluminium seems not to be the best metal as a conductor on mechanical high Q-devices, but platinum e.g. might show a better performance. Oxides of similar thickness seems to damp much less than metals.

The main problem encountered in this chapter is the strong coupling between the vibrating part of the structure and the frame This coupling is much more than one would expect by considering only static deformation. Other type of clamping, especially more reproducible ones could be tried, but the aim is however to develop structures which are not dependent on the clamping at all. This would solve the problems of reproducibility, high Q, packaging and long term stability (depending partly on glue and clamping) of the device at once.

The good agreement between the theoretical calculation and the measurements justifies the calculations done in section 2.4. As we could show theoretically, the elasticity of the clamping had only a minor influence on the resonance frequency. On the damping however the influence was obviously much more pronounced. The elastic waves of the vibration are only partly rejected at the clamping and thus energy flows out , if not rejected later. Thus the conditions of the frame have a feedback to the vibrating part. Ideas of how to reduce this coupling to the clamping are developed in the next chapters.

---

1 Roylance, L.M.; A Miniature integrated circuit accelerometer for biomedical applications. Integrated circuits laboratory, Atansford University, Standford, CA 94305, Technical Report No 4603-2.November 1977.
2 Chen, P. et al.; Integrated Silicon Microbeam PI-FET Acceleromter,IEEE Trans. on El Dev. Vol. ED-29, No 1 Jan 1982 p.27
3 Rudolf.F.; A Micromechanical Capacitive asselcrometer with a two-point inertial mass suspension. Sensors and Actuaturs, 4(1983) p. 191-198.
4 Petersen, K. Shartel. A, Raley. N.; Micromechanical Accelcrometer Integrated with MOS Detection Circuitry, IEEE Trans. on El Dev. Vol. ED-29, No 1 Jan 1982 p.23
5 Tsugai, M. Bessho, M. Semiconductor Accelerometer for Automotive Controls.Transducers '87, 4th Int. Conf. on Solid-state Sensors and Actuators, Tokyo, 1987.
6 Seidel, H., Csepregi, L.; Design optimization for cantilever-type accelerometers, Sensors and Actuators, 6(1984) p.81-92
7 Sandmaier, H., Kühl, K., Obermeier,E.; A silicon based micromechanical accelerometer with cross acceleration sensitivity compensation, Transducers '87, 4th Int. Conf. on Solid-state Sensors and Actuators, Tokyo, 1987.
8 Terry, S.; A Miniature silicon Accelerometer with buit-in Damping, Solid State Scnosr and Actuator Whorkshop, IEEE CAt 88TH0215-4,Technical Digest, Hilton Head, June 6-9, 1988., p.114.
9 Baker, W., Woolam, W., Yound, D.; Air and internal damping of thin cantilever beams. Int J. Mech. Sci, Vol 9 1967, pp 743-766.
10 Kokubun, K.; A bending and stretching mode crystal oscillator as a friction vacuum gauge, Vacuum , Vol 34, No 8-9, 1984. p. 731.
11 Christen, M.; Air and gas damping of quartz tuning forks, Sensors and Actuators, 4(1983) p.555.
12 Kokubun, K. *et al.*; Frequency dependendence of a quartz oscillator on gas pressure, J. Vac.Sci Technol. A3 (6), Nov/Dec. 1985. p.2184.
13 see ref 11.
14 McSkimin, H.J., Bond, W.L.,Buehler, E. Teal, G.K.; Measurement of the Elastic Constants of Silicon Single Crystals and their thermal Coefficients. Phys. Rev. 83. 1080 (1951)
15 see appendix I.
16 Braginsky, V.B. Mitrofanov, V.P. Panov.V.I.; Systems with Small Dissipation, University of Chicago Press, Chicago and London 1985.
17 Nowick, A.S.; Berry, B.S.; Anelastic relaxation in crystalline solids, Academic Press, New York. 1972

Chapter 7
Compensated Structure

7.1. Introduction

As we have seen in Chapter 6, the mass spring system was not decoupled completely from the frame. To achieve this, we are applying an idea, similar to that proposed by Weisbord[1] for structures in quartz, that compensates for the moments and the force at the clamping in a flexural mode. It is possible to compensate at the clamping the forces by the moments, when the clamping itself is a mass distribution with its center of gravity behind the point of the clamping, i.e. not in the clamping structure but somewhere on the beam. Thus the force creates a moment which is of opposite sign to that originating from the stress of the elongated beam. In his proposed realization in quartz the clamping structure can not really turn around the center of mass and it stays somewhat unclear, what all belongs to the mass of the clamping part. We realized a structure in silicon based on the same compensating principle, but with a mounting of the clamping part which allows in principle a rotational movement. So the center of mass is clearly defined. The fixation of the clamping itself is provided by a bar of etched silicon. This means, that an additional momentum of torque has to be taken into account. This momentum however is not free of friction as that caused by the force of the stress. But when the compensation is well done, no actual movement should occur and therefore no loss of energy by friction. However, this reasoning holds only in the case that the clamping structure is a rigid body, which transmits no acoustical waves. This of course, is an idealization.

The major problem for the realization of such a compensation for a structure of exactly the same dimensions as those in chapter 6, was to have the center of mass far enough away from the clamping point. It was in fact impossible to get this realized without having a unwieldy structure with a main danger of vibrating itself in different modes. This would of course deviate too far from the assumption of a rigid body.

7.2. Calculations and design

7.2.1. Calculations

In contrast to the quartz structure of Paros[2], who realized the idea of Weisbord, our suggestion in silicon has its tines not on the plane of vibration, but beside. The principle however stays the same. In order to decouple even more, but renouncing on the possibility of using the structure as a force sensor, we also fixed this inner structure to the main frame by torsional bars at the sides.

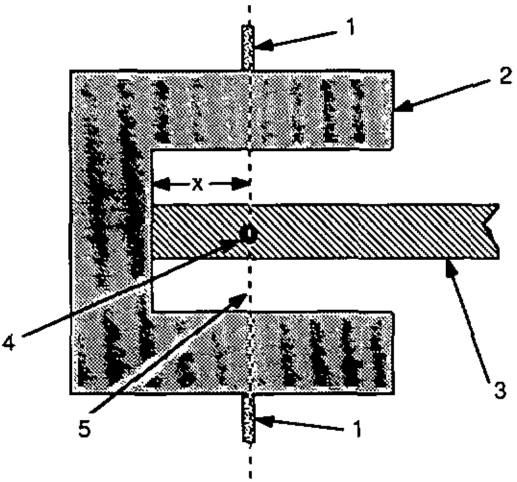

Fig 7.1. Schematic view of the clamping part with 1) the torsional support, 2) the decoupling mass, 3) the vibrating beam, 4) the center of mass of the decoupling mass 5) the imaginary (because it should when well compensated not turn) axes going through 1 and 4.

The equation, which has to be satisfied in order, that the moment M at the clamping is compensated by the force F multiplied by the distance x to the turning point, which is the center of mass is as follows: x F=M or

$x\ EJ_y\ w'''(0,t)=EJ_y\ \ w''(0,t)$

thus for x we find, (because the time dependence is the same for both sides)

$$x=\frac{X''(0)}{X'''(0)}$$

These derivatives are listed in appendix B. We find then that

$$x=\frac{L}{\lambda}\Gamma$$

with Γ from [2.15] and the other parameters as usual.

Thus, after having found where the decoupling mass (see Fig.7.1.) should turn for optimal compensation, we should bring the center of mass of this decoupling mass right on that pivot. Obviously this needs quite a lot of mass on the right side (referring to Fig. 7.1.) of the axis. Since we wanted, in order to be able to compare, to compensate the given mass beam structure described in chapter 6, the decoupling mass was the only design parameter. Only very special, unusable structures would have accomplished this task correctly.

7.2.2. Design and etch simulation

The discussion above shows, that the turning point is preferably close to the clamping , since that way the CM of the decoupling mass doesn't have to overhang too much. Thus for a given length of the beam and thus a given room for the decoupling mass, λ should become large, while Γ should stay small. But Γ is actually a function of λ and thus the problem reduces to find a minimum of the function $f(\lambda) = \frac{\Gamma(\lambda)}{\lambda}$ varying various parameters, which was done numerically.

As said in the introduction, it was not easily possible with silicon, for the mass beam system to move the center of gravity of the U-shaped mass toward the middle of the structure without ending in very unwieldy structures which would eventually develop their own eigen frequencies, because silicon is quite light compared to its strength.

Finally we have renounced trying to bring the center of mass to the correct position, but we placed the suspension (the torsional bars) to the correct position (Fig.7.2.). Another structure was made, where the suspending is positioned at the real center of mass (Fig.7.3.). The third design connected the decoupling structure by thin beams in the longitudinal direction of the structure (Fig.7.4.). This one comes closest to the concept of Weisbord and would allow to apply stretching forces. Because we feared, that this would represent a weak construction we laid a thin membrane between the two decoupling structures. The layouts are shown in Fig.7.2. to Fig.7.4.

Nevertheless a design very close to that discussed in the introduction is possible in silicon, too, as shows a glance to the structures described in chapter 8. Quite similar geometries are possible to realize and thus a similar behaviour can be expected.

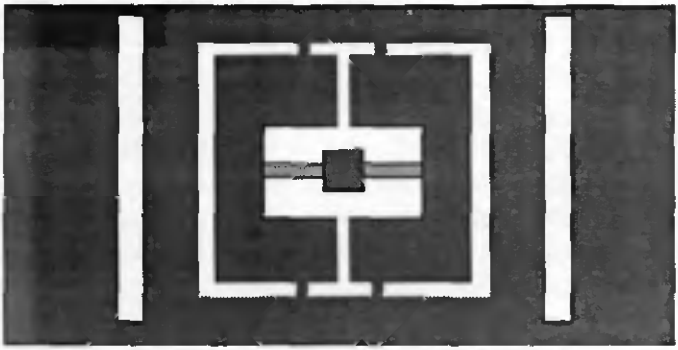

Fig.7.2. The layout of the structure with the torsional suspending at the point where it should turn in order to compensate for force and moment

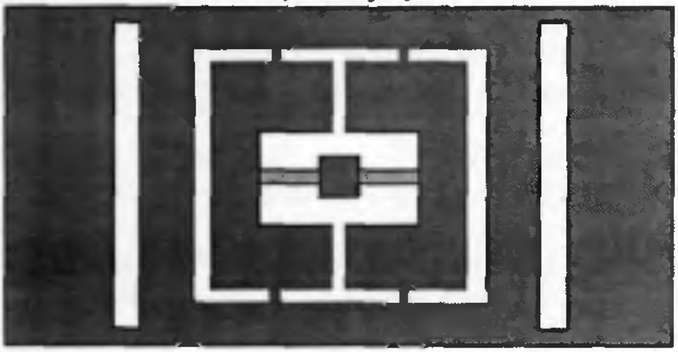

Fig.7.3. The layout of the structure with the torsional suspending at the effective center of mass

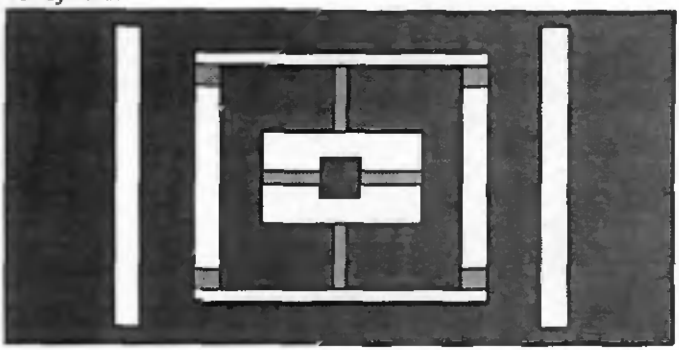

Fig.7.4. The layout of the structure with a band suspending

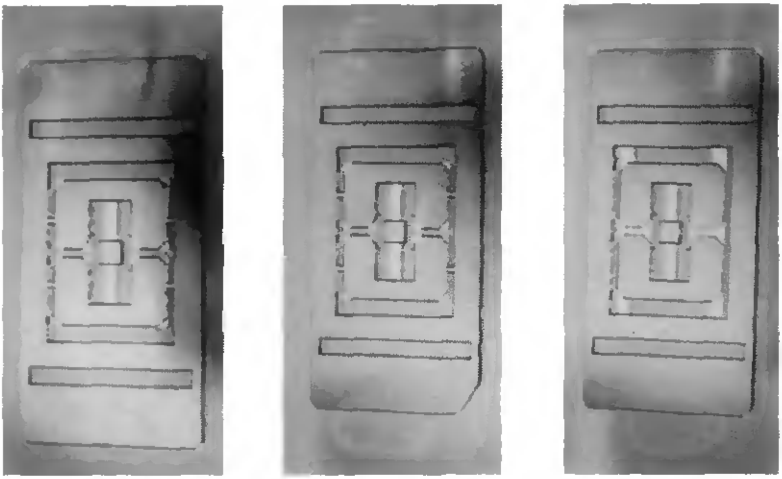

Fig.7.5. Photograph of the structures

7.3. Fabrication of the structures and experimental

The fabrication is exactly the same as the structures of chapter 6. The only particularity might be the large dimension of the complete structures (40mm x 20mm) where it has to be noted, that the resonator itself is exactly the same as described in chapter 6. In one structure we etched the mesa mass in the middle down to the beam thickness, increasing thus the resonance frequency and in another one we thinned the suspension rods to about 50μm.

Experimentally we had to construct a new holder for this structure, where only the most outer part touched. It was made out of brass again and was provided with a hole for a thermocouple. We could thus establish an efficient feedback loop for the thermostat.

7.4. Results

7.4.1. Damping by nitrogen

7.4.1.1. The frequency in dependence of the nitrogen pressure

Fig.7.6. shows the pressure dependence of the resonance frequency in a semilog plot whereas in Fig.7.7. the plot is linear, showing thus the pressure dependence

near atmospheric pressure. Compared to the structures of chapter 6 no particularity is observed.

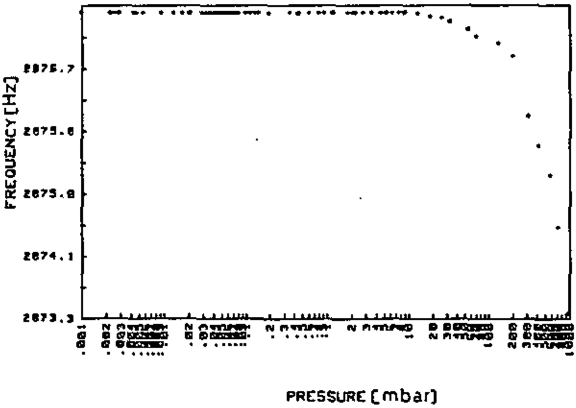

Fig.7.6. Pressure dependence of the resonance frequency for the band suspended structure

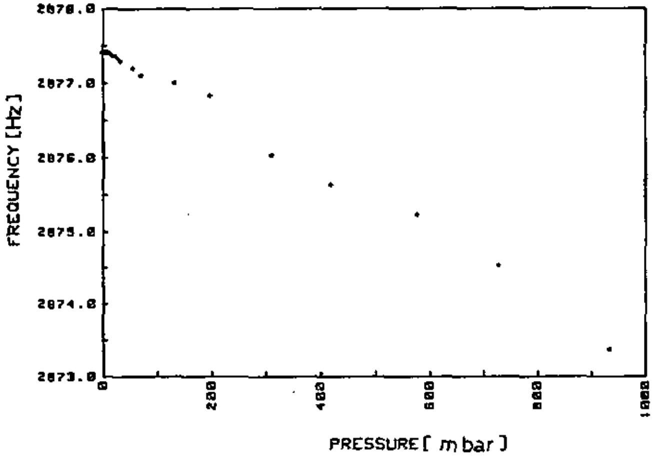

Fig.7.7. Pressure dependence of the resonance frequency for the band suspended structure in a linear scale

The resonance frequencies in vacuo for the structures of Fig.7.2 and of Fig.7.3 are 3097.7 Hz and 2790.5 Hz respectively.

7.4.1.2. The Q-factor in dependence of the nitrogen pressure

For the structure of Fig.7.4. no difference in the behaviour of the pressure dependence of the Q-factor compared to the resonators of chapter 6 was found (see Fig. 7.8.). Just for illustration we represented this data set also in a doubly log-scale (see Fig.7.9.). That way details are lost but the general law can be seen more direct.

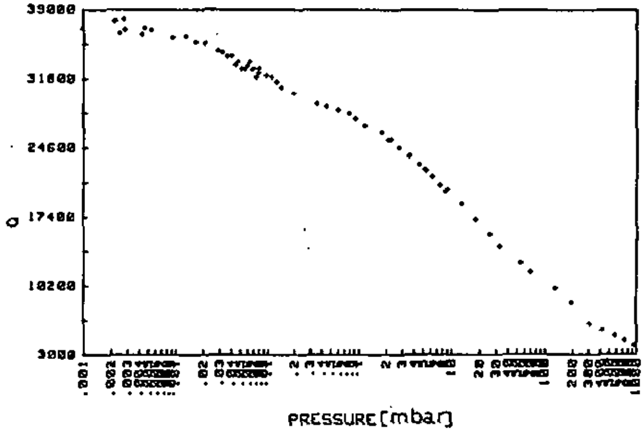

Fig. 7.8. The pressure dependence of the Q-factor for the band suspended structure.

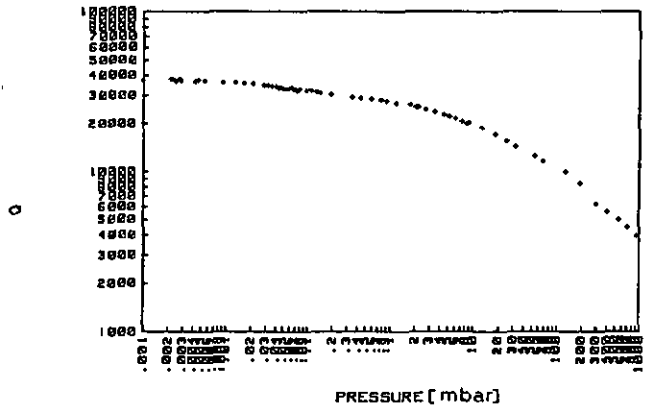

Fig.7.9. The same data as in Fig. 7.8. but in a doubly log-scale.

In spite of the calculation effort for the structures of Fig.7.2. and 7.3. they showed no higher Q-factors than about 7000 in vacuo. The fact, that the structures described in this chapter have no higher Q-factors than the simple ones of chapter 6, shows that the decoupling is a much more serious problem than thought in the beginning. It might be caused by the fact, that the compensation was not perfect.

7.4.2. Structural damping

In order to get more insight on the structural damping mentioned above we measured the two dimensional distribution of the vibration amplitudes of the whole structure.

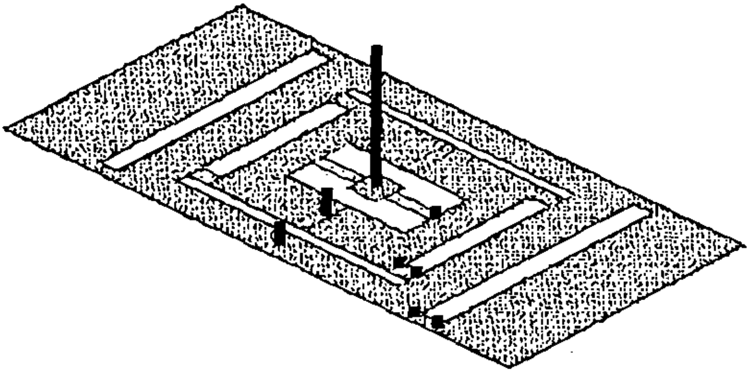

Fig.7.10. The amplitudes at different places of the structure with the flexural beam suspension, when the inner resonator is in resonance and the excitation is constant.

Fig. 7.10. shows the amplitudes (black bars) at different places on the structure of Fig.7.4., when the inner resonator is in resonance (2877.6 Hz) and the excitation is constant. The amplitude of the proof mass is 26nm and the others are to scale.

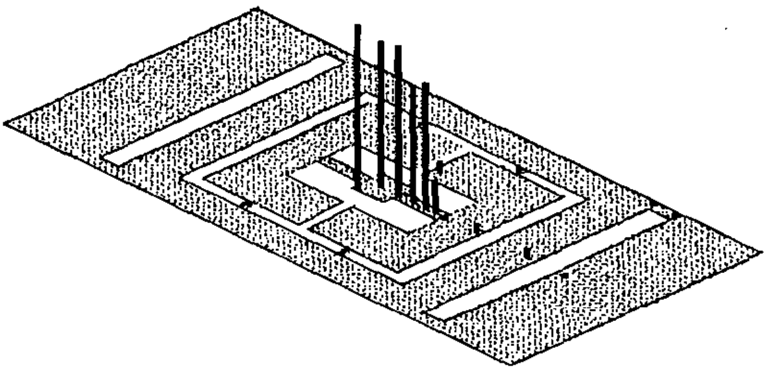

Fig.7.11. The amplitudes at different places of the structure of Fig.7.3.,when the inner resonator is in resonance and the excitation is constant.The largest bar is 34.9nm

The same experimental situation holds for the structure with the turning bar suspensions. Fig.7.11. shows the amplitudes at different places on the structure of Fig.7.3., when the inner resonator is in resonance (2790.5 Hz) and the excitation is constant). One can see, that the decoupling structure is turning but the pivot itself is not completely at rest. This may be caused by the fact that the center of mass is not at the height of the pivot as it should be. If the compensation would be perfect, the decoupling structure should not turn at all.

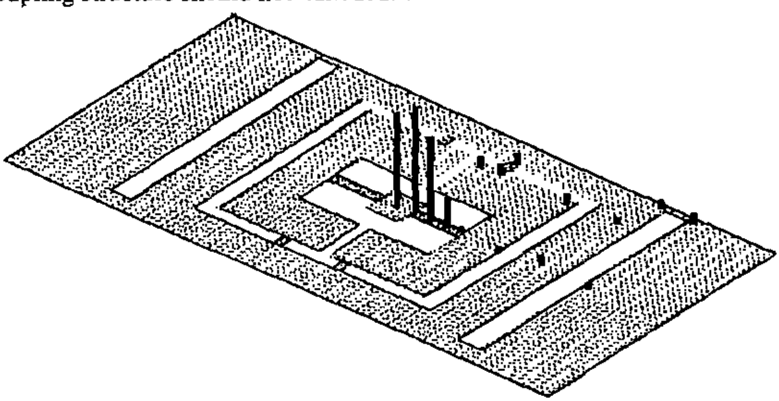

Fig.7.12. The amplitudes at different places of the structure of Fig.7.2.,when the inner resonator is in resonance (3097.7 Hz) and the excitation is constant. The largest bar is 20.9nm

Although Fig 7.12. shows, that at the clamping point of the resonator the amplitude is very small, meaning there is a node at that point, the decpoupling mass moves which brings the whole frame to vibration and the Q-factor is very poor, although decoupled as much as possible.

In order to bring things to the right light one has to mention however, that in comparison the structures of Paros in quartz have no higher Q-factor than we have for the structure Fig.7.4., the only difference is, that he claims to be independent of clamping, what we are not.

These structures are actually too complex to be calculated analytically. A FEM program like ANSYS would do the job and perhaps reveal some interesting details.

From a wave point of view one could say, that at a boundary part of the wave is reflected and part is transmitted. The transmitted one arrives then to another boundary where the same thing happens again. It is known [3] that such a situation represents a filter for acoustic waves being permeable for some frequencies. This could explain the still strong dependence of our structures on the clamping.

7.5. Discussion

Much more care has to be taken to the design of the surrounding frame (eigenfrequency and wave length). It would be worth to try a well compensated structure in silicon, giving up the mass beam design of the inner resonator. By the etching techniques described in chapter 8 it would be actually possible to realize a structure quite similar to that realized in quartz.

---

1 Weisbord, L. Single Beam Force Transducer with Integral Mounting Isolation, US Patent No 3,470,400, Sept 30,1969.

2 *Paros J.M., Precision Digital Pressure Transducer, ISA TRANSACTION, Vol 12, 1973,p173.*

3 Lindsay, R.B. Mechanical Radiation, McGraw-Hill, New York, 1960.p.79

Chapter 8
Tuning Forks in Silicon

8.1. Introduction

In this chapter we are going to present a type of design, which has been successfully applied to quartz devices[1,2,3,4], but never been realized in silicon, namely tuning forks. This type of devices compensates by its antiparallel modes the forces and the moments at the base and may reach therefore high Q-factors. Moreover we propose here an electrodynamical driving and readout set-up, which is original for micromachined sensor, too. The electrodynamical driving principle is known however as excited metallic strings used for force measurements[5]. These structures are therefore complete sensor and might be used as sensors of force, moment, viscosity, gas pressure etc. A test set-up was built, in which the dynamical behaviour of the structures could be measured electrically as well as optically.

8.2. Design and calculations of the tuning forks

8.2.1. Design

Vertical etching in (100) oriented wafers permits the realization of structures with tines similar to that realized in quartz. Compared to the previous structures these described here have an orientation in the <010> direction of the crystal. This allows some comparison to the structures described in the previous chapters with respect to the crystal direction. Different types were realized among them a real tuning fork (see Fig.8.1. and 8.2). But most of the structures were double ended tuning forks, which allow an excitation by the Lorentz force and to apply a force or a moment at the ends of the structure.

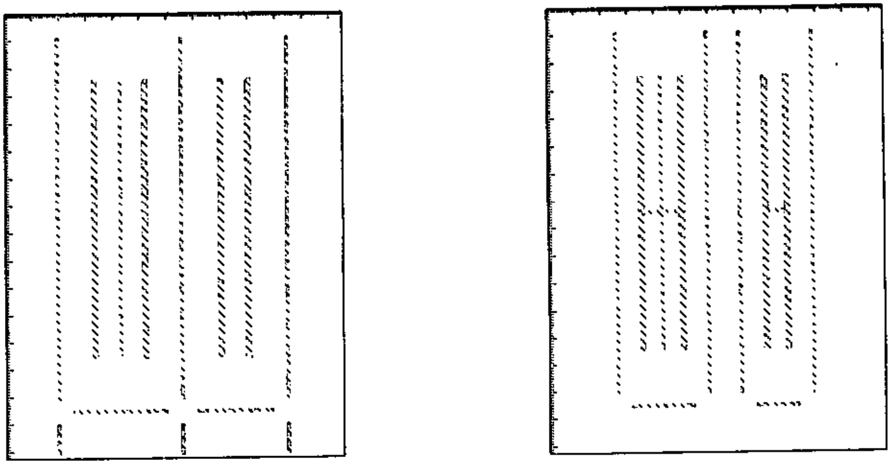

Fig. 8.1.The layout of the structures (100μm per division)

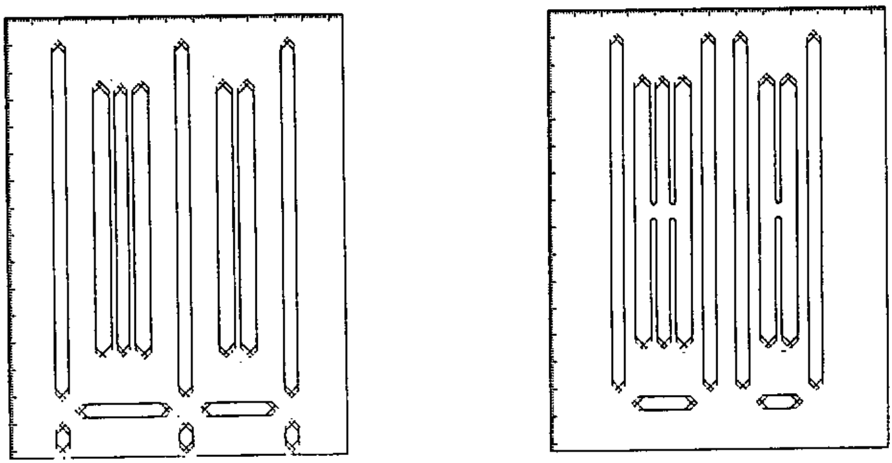

Fig. 8.2. The simulated etched structures (100μm per division)

8.2.4. Resonance frequency

8.2.4.1. Introduction

The experimental situation is sketched in Fig.8.3. On application of a EMF U_{appl} a current I flows in a conductor which is in a induction field **B**. The conductor C_1 feels thus a force **F** (Lorentz force). This is the exciting mechanism. On the other hand an electric field $\mathbf{E}_{ind}$ is induced in a moved or deformed conductor C_1 in a magnetic field. $\mathbf{E}_{ind}$ can be integrated along C_1 to give the induced voltage U_{ind}.

$$U_{ind} = \oint_{C_1} \mathbf{E}_{ind} \cdot ds \qquad [8.1]$$

U_{ind} is opposite the applied voltage (Lenz's rule).

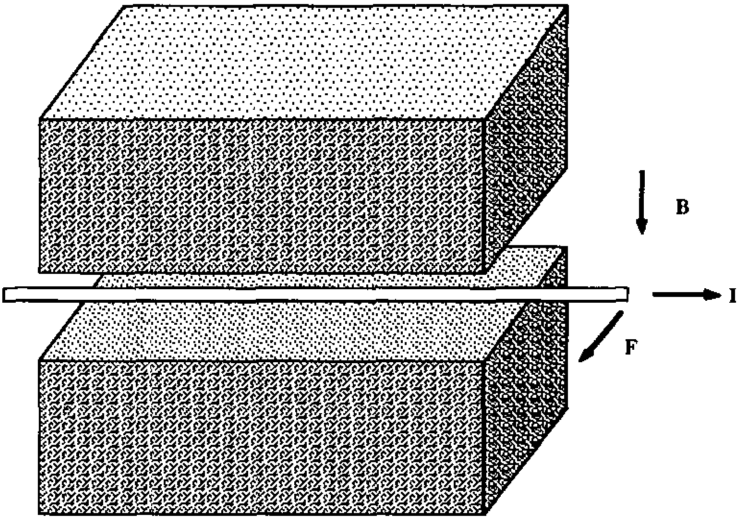

Fig.8.3. The simplified model of a rigid conductor in a magnetic field

Now the conductor C_1 is on a elastic beam. Thus we have to solve a DE of a homogeneous Euler-Bernoulli beam with an external force (cf. Chap.2, [2.73]) :

$$E\,J\,\frac{\partial^4 w(x,t)}{\partial x^4} + c\,\dot{w}(x,t) + m\,\ddot{w}(x,t) = g(x,t) \qquad [8.2]$$

$g(x,t) = I(t)\,\mathbf{B}\cdot\mathbf{l}/l$ the exciting force per unit length stemming from the Lorentz force.

We have to find now an explicit expression for I(t). With **B** the homogeneous and constant magnetic field, the induced electric field

$$\mathbf{E}_{ind} = \mathbf{v} \times \mathbf{B} \qquad [8.3]$$

$$U = U_{appl} - U_{induc} \qquad [8.4]$$

where

$$U_{appl} = U_0 \cos(\omega t) \qquad [8.5]$$

$$U_{induc} = \oint_{C_1} \mathbf{v} \times \mathbf{B} \cdot d\mathbf{s} \qquad [8.6]$$

Neglecting the rotation of the conductor (length l) we can write

$$U_{induc} = B_Z \int_0^l \dot{w}(x,t)\, dx \qquad [8.7]$$

Thus the formula for the resulting current I(t) is:

$$I(t) = \frac{U(t)}{Z(t)} = \frac{U_{appl} - U_{induc}}{i\omega L(t) + R} \qquad [8.8]$$

I is thus actually complex.

$$Z = i\omega L(t) + R \qquad [8.9]$$

L(t) is the time dependent coefficient of self inductance
R is the ohmic resistance of the conductor.

or

$$I(t) = \frac{U_0 \cos(\omega t) - B_Z \int_0^l \dot{w}(x,t)\, dx}{i\omega L(t) + R} \qquad [8.10]$$

We obtain thus the following integrodifferential equation ([8.11])

$$\boxed{E\,J\,\frac{\partial^4 w(x,t)}{\partial x^4} + c\,\dot{w}(x,t) + m\,\ddot{w}(x,t) = B_Z\,\frac{U_0 \cos(\omega t) - B_Z \int_0^l \dot{w}(x,t)\, dx}{i\omega L(t) + R}}$$

The Integral on the right side couples the space with the time and the DE is no longer separable in time and space.

8.2.4.2. Simple model

Instead of applying the formalism of modal analysis, we are calculating a simple model where we replace the bending beam (with a bending path of current) by a rigid thin conductor with the inertial mass of the actual beam m, suspended at two springs with each half of the spring constant k/2 necessary to result in the observed eigenfrequency of the actual system. The true length l, the true resistivity R, negligible selfinduction L are supposed (see Fig.8.3.). Then the DE writes as follows:

$$kx(t) + m\ddot{x}(t) = Bl/R\{\, u_o \cos(\omega t) - \dot{x}(t)\, Bl\} \quad [8.12]$$

or

$$\omega_o^2 x(t) + c\dot{x}(t) + \ddot{x}(t) = A/m \cos(\omega t) \quad [8.13]$$

with

$$c = \frac{(Bl)^2}{Rm} \quad [8.14]$$

$$A = \frac{Blu_o}{R} \quad [8.15]$$

$$\omega_o^2 = k/m \quad [8.16]$$

The solution of the DE is then[6]

$$x(t) = x_o \cos(\omega t + \alpha) \quad [8.17]$$

with

$$x_o = \frac{A}{m\sqrt{(\omega_o^2 - \omega^2)^2 + c^2\omega^2}} \quad [8.18]$$

and

$$\alpha = \arctan\left(\frac{c\omega}{\omega_o^2 - \omega^2}\right) \quad [8.19]$$

8.2.4.3. The Q-factor

An equivalent definition of the Q-factor for a harmonic oscillator as given by [2.65] is the following one:

$$Q = \frac{x_{o\omega_r}}{x_{oo}} \quad [8.20]$$

with the amplitude at (almost) zero frequency x_{oo} and $x_{o\omega_r}$ the amplitude at resonance

With the same notation as above we find

$$x_{oo} = \frac{A}{m\omega_o^2} \quad [8.21]$$

$$x_{o\omega_r} = \frac{A}{mc\sqrt{\omega_o^2 - \frac{c^2}{4}}} \quad [8.22]$$

and the Q-factor is therefore

$$Q = \frac{x_{o\omega_r}}{x_{oo}} = \frac{\dfrac{A}{mc\sqrt{\omega_o^2 - \frac{c^2}{4}}}}{\dfrac{A}{m\omega_o^2}} = \frac{\omega_o^2}{c\sqrt{\omega_o^2 - \frac{c^2}{4}}} \qquad [8.23]$$

When the damping c is low the following approximation holds

$$Q \approx \frac{\omega_o}{c} = \frac{Rm\omega_o}{(Bl)^2} \qquad [8.24]$$

8.2.4.4. The induced voltage at resonance

8.2.4.4.1. Without mechanical damping

At resonance the induced voltage is

$$u_{induc} = -\dot{x}(t)\,Bl \qquad [8.25]$$

with [8.17]

$$\dot{x}(t) = x_{o\omega_o}\omega_o \cos(\omega_o t + \alpha)$$

$$\approx \frac{A}{mc\omega_o}\omega_o \cos(\omega_o t + \alpha) = \frac{A}{mc}\cos(\omega_o t + \alpha)$$

$$= \frac{Blu_o}{Rmc}\cos(\omega_o t + \alpha) = \frac{Blu_o}{Rm\,\frac{(Bl)^2}{Rm}}\cos(\omega_o t + \alpha) = \frac{u_o}{(Bl)}\cos(\omega_o t + \alpha) \qquad [8.26]$$

It follows that

$$u_{induc} = -\dot{x}(t)\,Bl \approx -u_o\cos(\omega_o t + \alpha) \qquad [8.27]$$

Thus at resonance with no mechanical damping we have:

$$\boxed{|u_{induc}| \approx |u_{appl}|} \qquad [8.28]$$

The damping from the electrical circuit alone is only very weak ($Q = 10^6$).This is by far not observed the experiment (see section 8.5.2)

8.2.4.4.2. With mechanical damping

When mechanical damping β is included, the [8.13] has to be extended as follows:

$$\omega_o^2 x(t) + c\dot{x}(t) + \beta\dot{x}(t) + \ddot{x}(t) = A/m \cos(\omega t) \qquad [8.29]$$

with the same abbreviations as in the preceding paragraph.

Because [8.29] is formally equal to [8.13], if only we replace c by c+β, immediately we can write by [8.26] the velocity of the conductor to be

$$\dot{x}(t) = x_{o\omega_o}\omega_o \cos(\omega_o t + \alpha) = \frac{A}{m(c+\beta)\omega_o}\omega_o \cos(\omega_o t + \alpha)$$

$$= \frac{A}{m(c+\beta)}\cos(\omega_o t + \alpha) = \frac{Blu_o}{Rm(c+\beta)}\cos(\omega_o t + \alpha) \qquad [8.30]$$

and thus by [8.25] the induced voltage as

$$u_{induc} = - \dot{x}(t)\, Bl = - \frac{(Bl)^2 u_o}{Rm(c+\beta)} \cos(\omega_0 t + \alpha) \qquad [8.31]$$

When we replace now the expression $(c + \beta)$, which represents actually the damping, by the expression (cf [8.24])

$$(c+\beta) = \frac{\omega_0}{Q}$$

we find then the induced voltage to be

$$u_{induc} = - \frac{(Bl)^2 u_o}{Rm \frac{\omega_0}{Q}} \cos(\omega_0 t + \alpha) = - \frac{Q(Bl)^2 u_o}{Rm\ \omega_0} \cos(\omega_0 t + \alpha) \qquad [8.32]$$

The resonance frequency ω_0 of a simple doubly clamped beam is by [2.7]

$$\omega_0 = \left(\frac{\lambda}{l}\right)^2 \sqrt{\frac{EJ_y}{\rho bh}} = \left(\frac{\lambda}{l}\right)^2 \sqrt{\frac{Ebh^3}{12\rho bh}} = \left(\frac{\lambda}{l}\right)^2 \sqrt{\frac{Eh^2}{12\rho}} \qquad [8.33]$$

with

$\lambda = 4.730$

$\mu = bh\rho$

l the length of the beam

Thus [8.31] can be written as [7]

$$u_{induc} = - \frac{Q(Bl)^2 u_o}{R\ lbh\rho \left(\frac{\lambda}{l}\right)^2 \sqrt{\frac{Eh^2}{12\rho}}} \cos(\omega_0 t + \alpha)$$

$$= - \sqrt{\frac{12}{\lambda^4}} \frac{QB^2 l^3}{Rbh^2 \sqrt{E\rho}} u_o \cos(\omega_0 t + \alpha) = -0.155 \frac{QB^2 l^3}{Rbh^2 \sqrt{E\rho}} u_o \cos(\omega_0 t + \alpha) \qquad [8.34]$$

For a Q-factor of 5000, a resistance of R=8 Ω, a magnetic field strength B of 0.4 Tesla we have thus about 1.3% of the applied voltage induced.

8.3. Fabrication of the structures

8.3.1. Generalities

As designed in section 8.2 we could etch different types of tuning forks,- simply clamped as well as doubly clamped ones,- with the technique for vertical wall etching in (100) oriented silicon. Moreover we succeeded in developing a method for executing a photolithographic process on these etched through devices as described in section 8.3.3.

In order to reduce the lateral etching, the structures were etched simultaneously from both sides with symmetric masks. The two side bars were designed to have a rather stiff frame in which the two inner ones vibrate. Moreover, by clamping in the middle of these two side bars, one could reduce the influence of thermal stress. For the optical measurement, one of these bars was broken out.

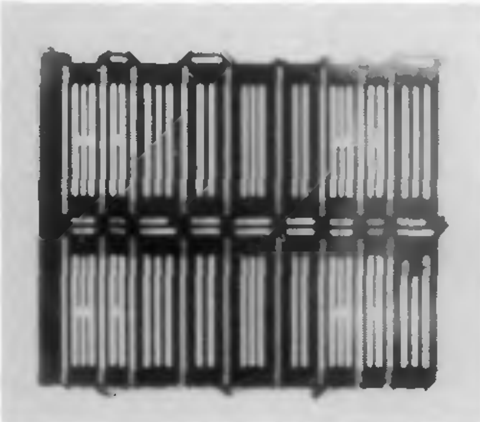

Fig.8.4. The various tuning fork structures after the etching process

Fig.8.5. SEM of a tuning fork

8.3.2. The photolithographic process on a completely etched through wafer

In order to perform the photolithographic steps on the etched wafer after the metallization the latter one is glued to a glass plate by means of a layer of positive photoresist (Shipley). After a short prebake we filled from the backside heated (liquid) paraffin into the holes and let it harden (see process list). In acetone the photoresist is dissolved and the wafers are separated. Thus the holes are closed and a sufficiently plane surface is left to apply a normal photolithographic procedure to the wafer. This procedure can be repeated on the backside to end with a double side metal lane structure (see Fig.8.6.).

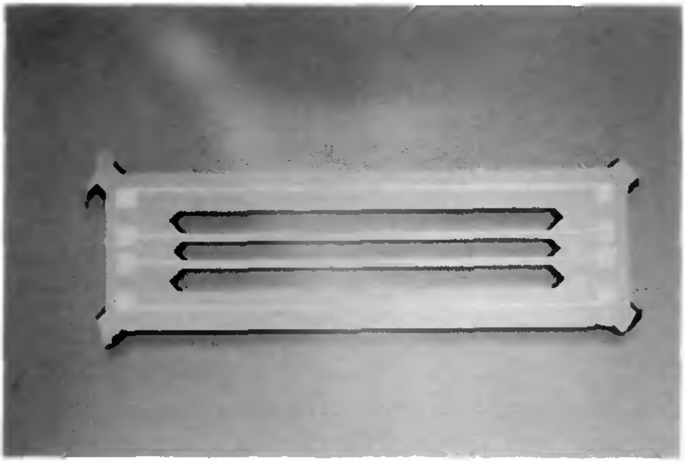

Fig.8.6. Photograph of the tuning fork with metal lanes

8.3.3. Process list

1.	Oxidation	
2.	Double side photolithography	
3.	Buffered HF- etch	
4.	Cleaning HNO_3	
5.	KOH etching	
6.	BHF-etch, to remove the underetched silicondioxid	
7.	Deposition of VAPOX for isolation (both sides)	
8.	Metallization 1μm Al both sides	
9.	Standard cleaning	
10.	Coating AZ 1470, ramp 5, 1500 rpm, 30" on glass substrat	
11.	Glueing wafer to glass	
12.	Prebake 85°C 1'	
13.	Filling backside by paraffin 75°C	
14.	Separation of wafer and glass in acetone 2h	
15.	Cleaning in Isopropanol	
16.	Priming HMDS 15'	
17.	Fixation of the wafer by scotch tape double face	
18.	Coating AZ 1350J, coat all tuning forks before turning $ramp_1$:5 1000rpm 3" $ramp_2$:5 4000rpm 30"	
19.	Prebake 85°C 3'	
20.	Cleaning paraffin by heptan 85°C, no butyle acetate !	
21.	Coating AZ to another wafer ramp 5 1500 rpm 30"	
22.	Glueing (for handling reasons)	
23.	Prebake 85°C	
24.	Exposure > 120 mJ/cm^2	
25.	Developing AZ 351 1:3 and cleaning H_2O	
26.	Hardbake 120°C 30'	
27.	Alu-etch 42 °C 2'	
28.	Separation Acetone, iospropanol, H_2O	
29.	Cleaning HNO_3	

8.4. Experimental

8.4.1. Generalities

A test set-up was built, in which the structures could be excited electrically and measured optically. The set-up allows optical (interferometric measurement) access to the vibrating legs. The whole set-up is placed in the same vacuum jar as described in chapter 4.

8.4.2. Mounting and Excitation

A magnetical circuit is created by means of two legs each with permanent magnet joined by a soft iron yoke (see Fig.8.7.). The device under test is placed in the air gap an supported by a massive brass piece. This piece is equipped with two low voltage (24 V) heating cartridges and a thermoelement. The magnetic induction B was measured to be about 0.4 Tesla, quite homogeneously distributed in the air gap. The set-up is combined with the interferometer (see Chap 4) whose beam has access to the vibrating bars. The first mode was excited by placing the whole structure into the magnetic field, whereas the second mode was excited by placing only half of the structure into the magnetic field.

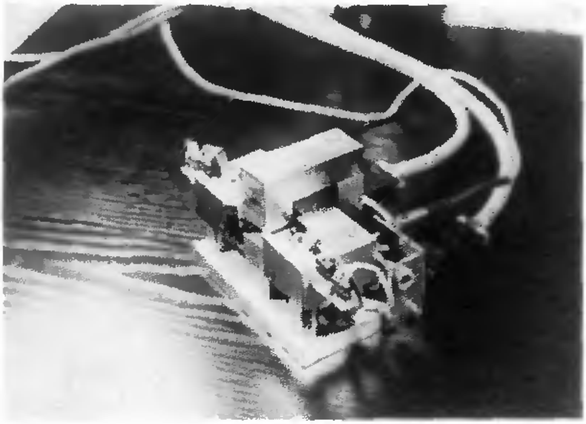

Fig.8.7. Photograph of the electromagnetic set-up

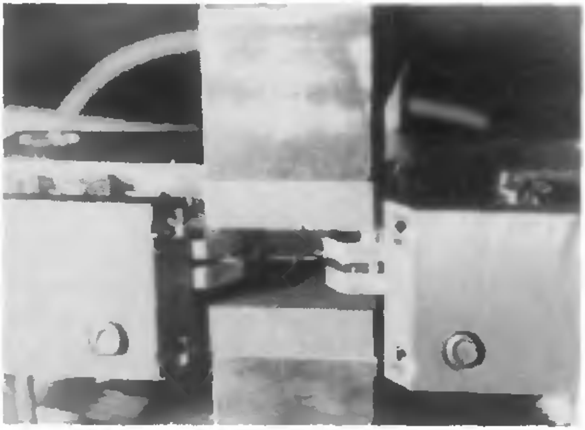

Fig.8.8. Photograph of the structure mounted in the airgap

8.4.3. Measurement method and system

The same interferometer as described in chapter 4 was utilized here.

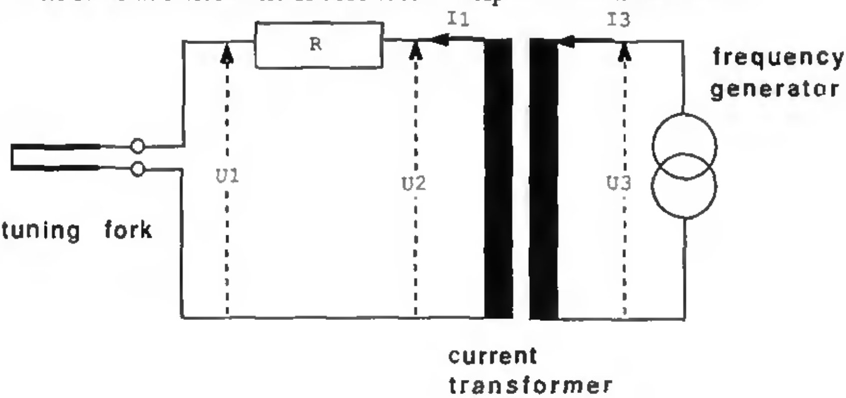

Fig.8.9. The electrical circuit of the tuning fork

By connecting the left side of the metallic lanes of the tuning forks we excite the double ended tuning fork automatically in antiphase. The secondary winding of the current transformer is actually just a wire wound four times around a ring transformer. We achieve thus a decoupling of the tuning forks circuit from the internal characteristics of the frequency generator (or tracking generator when U_2 is measured by the spectrum analyzer).The characteristics of the current transformer is not completely linear but sufficiently smooth over the interesting range of frequency (see Fig.8.10.).

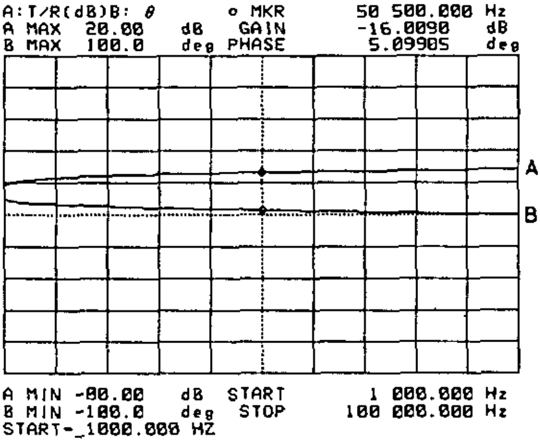

Fig.8.10. The Phase -Gain characteristics of the current transformer

For a free decay measurement the current transformer should actually be switched off completely during the decay period (by a mercury switch[8], e.g.). The calculation in the section 8.2.4.4.2. showed however, that the influence of that current loop is very small. This was confirmed experimentally by the fact that no difference in the decay rate could be observed wether the path for I_1 was open or closed (the induced voltage being but less than one percent of the applied voltage, the power dissipated by the electrical circuit is but some ppm of the mechanical one).The following equation holds then

$$I_1 = \frac{U_2}{R} \qquad [8.35]$$

and the dissipated power is

$$P = \overline{U_2}\ \overline{I_1} = \overline{U_2^2}/R \qquad [8.36]$$

Because the internal DC resistance of the conductors on the tuning forks is not zero as it should ideally be , but in the order of 8.5Ω, U_1 was not zero and could be measured and P was then $P = \overline{U_1^2}/8.5\Omega$ [8.36]

8.5. Results

8.5.1. The calculation of the resonance frequencies

The formulae were developed in chapter 2. The measured structures have a beam width of 376 µm, a beam thickness of 420µm and a beam length of 9.5 mm. Because the clamping is not an abrupt one, the beam length has to be corrected for the calculations of the resonance frequency to an effective length, which was, by fitting the first resonance frequency, found to be 9.85 mm. The second resonance frequency was then calculated to be 91.6 kHz, which matches the measured one to about 1%.

8.5.2. Electrical measurements

An electrical power of typically 10 µW results in an amplitude of about 60 nm at first resonance in air. The stored energy for this amplitude was calculated to be $2*1.13\cdot10^{-10}$ J (see Chapter 2,two doubly clamped beams). Because the Q-factor is the ratio between the total energy stored in the system E_{tot} and the energy ΔE lost in the period $\frac{1}{2\pi f_o}$:

$$Q=\frac{E_{tot}}{\Delta E} \qquad [8.37]$$

we can calculate the mechanical power dissipation

$$P_{mech} = \Delta E\ 2\pi f_o = \frac{2\pi f_o\ E_{tot}}{Q}, \qquad [8.38]$$

which is for a Q-factor of Q=5000 P_{mech} =9.46 10^{-9} W for the whole tuning fork. This means that most of the electrical power delivered into the system (the 10 µW from above) is dissipated electrically (the conducting resistance is 8.5Ω). With the formulae developed in section 8.2.4.) we have calculated that under these conditions about 2.6% of the applied voltage is induced.

The impedance |Z| and the phase ϕ as a function of frequency is shown in Fig.8.11 for the first mode and Fig.8.12 for the second mode, when the tuning fork is placed only half in the magnetic field. It was measured by an impedance meter HP 4194 by a direct impedance measurement in air and in vacuum. The shift of the peaks as well as their broadening when the resonator is in air (curves with the o-marker) is obvious in both cases, but more stringent in the second mode (Fig 8.12.), where a change from 40'000 in vacuo to 6000 in air occurs. The impedance change at resonance (first mode, in air) of about 150mΩ compared to 8.5Ω of total impedance or 1.7%, confirms roughly the calculations (based on a simplified model) from above (the induced voltage appears as an increase of the impedance).

Broad peaks at 17kHz, 22 kHz and at 79 kHz could be observed. Their Q is very low and they may be therefore modes of the frame or the whole structure. The amplitudes at these frequencies could nowhere to be made larger than some nm and optical scanning didn't reveal clearly any nodes.

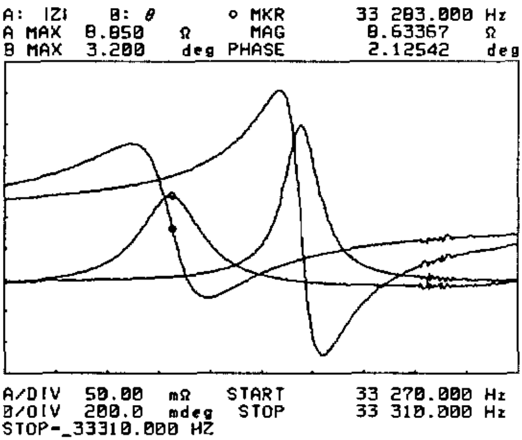

Fig.8.11. The impedance and the phase as a function of frequency for the first mode

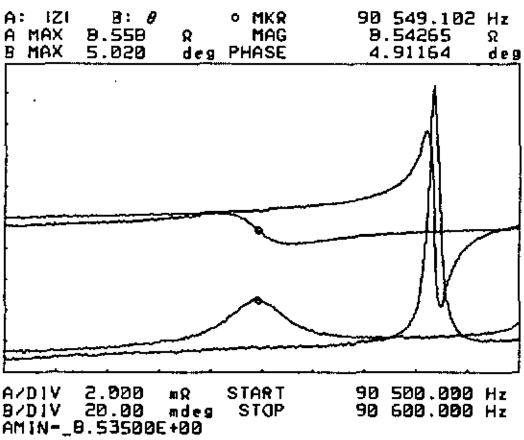

Fig.8.12.The impedance and the phase as a function of frequency for the second mode

8.5.3. The pressure dependence of the resonance frequency

Fig. 8.13. shows the pressure dependence of the resonance frequency of the first mode in a semilog plot whereas in Fig.8.14. the plot is linear, showing thus the pressure dependence near atmospheric pressure.These can be compared directly to measurements on (simple ended) quartz tuning forks[9]:

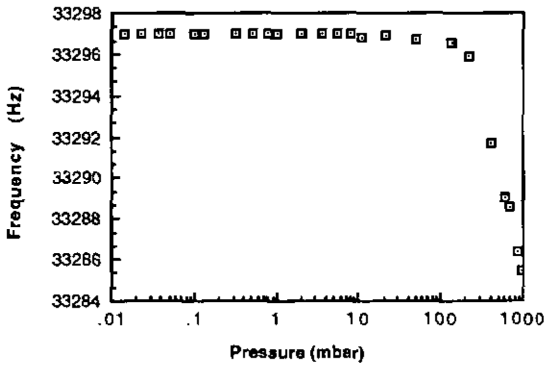

Fig.8.13. Pressure dependence of the resonance frequency of the first mode.

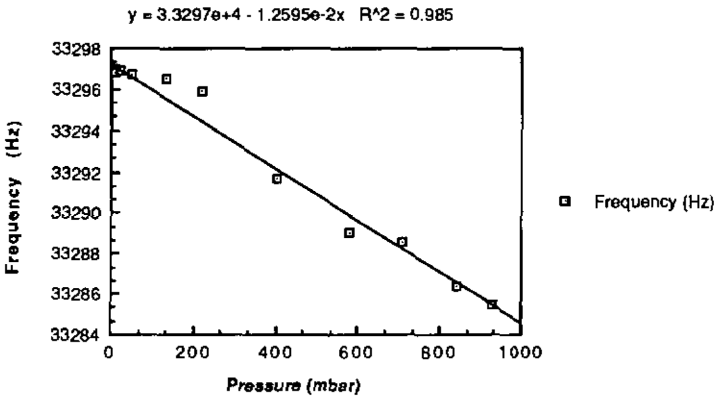

Fig.8.14. Pressure dependence of the resonance frequency of the first mode in a linear scale

Hauden[10] presents a simple clamped tuning fork in quartz with a sensitivity around atmospheric pressure of 1.1 ppm/mbar, where we have in the first mode 0.36 ppm/mbar in the second mode 0.43ppm/mbar in nitrogen. Using the simple formula given by Christen[11] we can calculate a value of 0.37ppm/ mbar.

Fig.8.15. and Fig.8.16. represents the frequency dependence of the second mode in a semilog plot and a linear plot respectively. Both modes show the same characteristics.

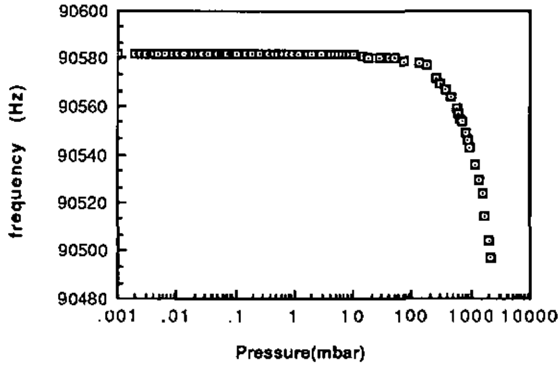

Fig.8.15. Pressure dependence of the resonant frequency of the second mode in semi logarithmic scale

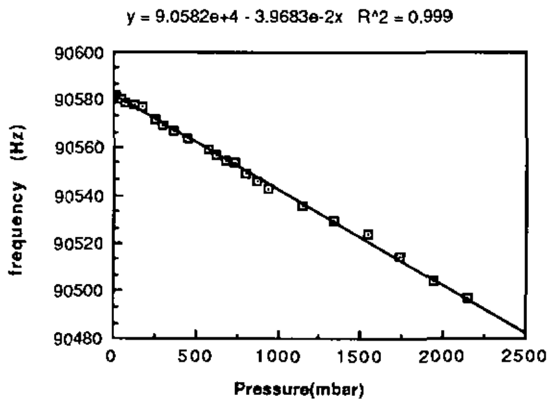

Fig.8.16. Pressure dependence of the resonance frequency of the second mode in a linear scale

8.5.4. The pressure dependence of the damping

Setting in eq [2.113] all discrete masses and discrete dampings to zero, the Q-factor reduces to

$$Q = \frac{\sqrt{8\left(m\,\omega_1\right)^2 - c^2}}{2c} \qquad [8.39]$$

We obtained the theoretical Q-factors as shown in Fig.8.17. for the first mode and in Fig.8.18. for the second mode by taking in the low pressure range the damping as $c = \xi_o + \xi$ from section 2.4.4.1.1. with ξ as the expression [2.118] and ξ_o is the intrinsic damping (empirically: $\xi_o = 0.00757$ kg/s for the first and $\xi_o = 0.00515$ kg/s for the second mode) and in the high pressure range as

$$c = \xi_o + \pi\, b\sqrt{2\eta\omega\rho} + 2\pi\eta, \qquad [2.124]$$

$\eta = 17.2\ 10^{-6}$ Pa s viscosity

$\rho = 1.293$ kg/m^3 density of air

$$m = \mu + \chi = \rho_{Si}\, bh + \frac{\pi\,\rho\, b^2}{2} \qquad [2.126]$$

and the formula $\rho = \frac{p}{RT}$ from section 2.4.4.1.2.

The comparison of the dependence of the Q-factor on the nitrogen pressure of the two modes shows (Fig.8.17. & 8.18.), that the first mode is heavily damped by the clamping. The theory underestimates somewhat the damping. This may be due to an air pumping effect within the two tines[12], which is not taken into account in the calculations.

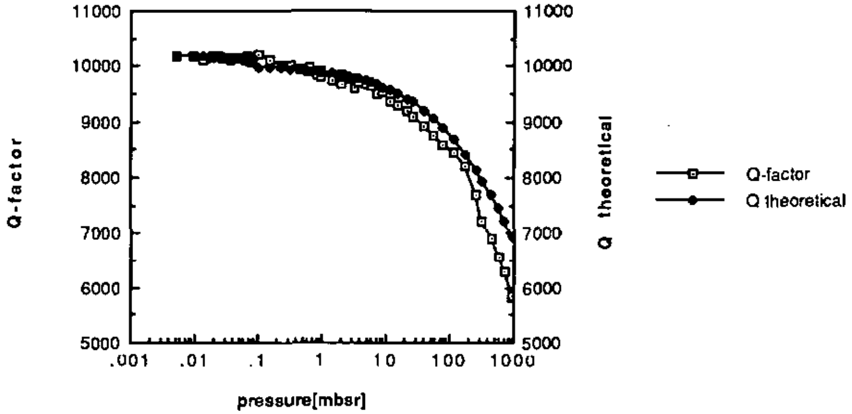

Fig.8.17. Pressure dependence of the Q-factor of the first mode

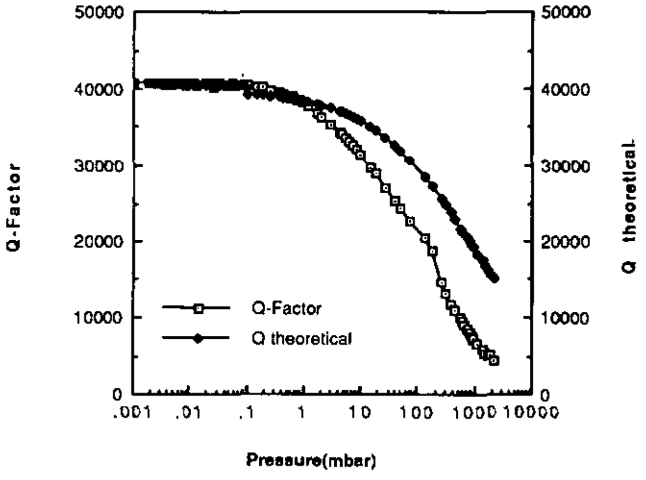

Fig.8.18. Pressure dependence of the Q-factor of the second mode up to 2 bar.

From the formulae [8.39] and [2.124], we can see easily, that the inverse of the Q-factor follows a square root law in the high pressure region (neglecting the fact that the denominator is somewhat pressure dependent):

$$\frac{1}{Q}=\frac{2\left(\xi_o+\pi\, b\sqrt{2\eta\,\omega\rho_{gas}}+2\pi\eta\right)}{\sqrt{8\left(m\,\omega_1\right)^2-c^2}} \qquad [8.40]$$

This is confirmed experimentally as can be seen in Fig 8.19.

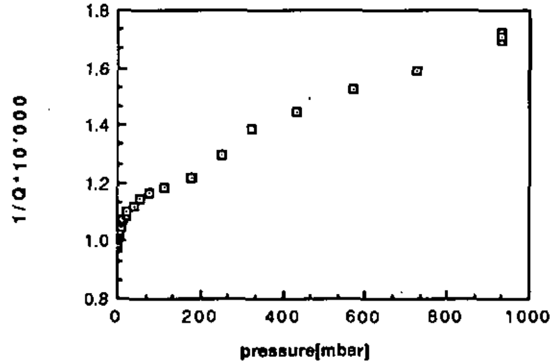

Fig.8.19. Pressure dependence of the inverse of the Q-factor (first mode)

Fig 8.19. is similar to the plot made by Christen[10] for his quartz tuning forks.

8.6. Discussion

Excepting the fact, that the effective length has to be determined empirically, the calculation of the resonance frequency is quite direct, because we have just a simple doubly clamped beam (respectively two of them). Therefore also the modes are classical. Here, we have some energy flow in the mode,too of course, originating from the fact that some energy is flowing out of the system by the clamping. But in contrast to the mass beam structure described in chapter 6, the gas damping, which is much stronger than the damping by the clamping or the internal damping, is here proportional to mass and strength distribution (at least in first approximation). We measured the first and the second mode. This was checked by scanning the laser beam over the beam. Zeros and maxima of the amplitude were found at the appropriate locations.

For these tuning fork structures, too, the decoupling was not that effective enough to show in the low pressure region the theoretically expected 1/p-dependence of the damping. In the high pressure region in the second mode one can observe a light decrease of the pressure dependence above 1 bar, showing that there is a transition from the first to the second (pressure independent) term in the expression for the damping c [2.124] (see above).

Since for this type of structure it was compulsory to have isolating layers as well as metallization, it was not adapted to study the influence of supplementary layers .

Actually we have metal layers on both sides of the tines. This was foreseen to excite the tuning fork symmetrically. But at high Q-factors this is not absolutely necessary and one could use the second one for the measurement, separating this current loop well from the excitation. Backside bonding could be done by anodic bonding as described in chapter 5 (Fig 5.4.).

We have shown, that it is possible to realize tuning forks structures in silicon similar to those reported in quartz and to excite them by electromagnetic forces with a power of typically 20 μW. It might even be possible, to activate the device without the external magnetic field, simply by the magnetic field of the two currents, or even electrostatically.

We showed, that micromachined structures in silicon are competitive with similar quartz structures: Chung[2] finds for his quartz tuning forks, which have similar dimensions as ours in silicon, for the first mode Q=50'000, f= 41 kHz and Q= 75'000, 109.9 kHz for the second one. The second mode of our structure with Q= 40'000, f= 90,6 kHz is thus competitive with the quartz structures. Moreover we found in his publication two interesting statements :"*The quality factor of the crystal operating at higher overtone flexure mode is higher than that operating at fundamental mode. The quality factor of the double-ended tuning fork quartz crystal is much lower than that of the single-ended tuning fork operated in flexure mode at the identical frequency:*" [2]

The tuning forks are a good approach for sure, but still much care has to be taken to the clamping and the tuning of the two tines as shows the case of the first mode. Clayton[13] has investigated this phenomen for double-ended tuning fork in quartz by a finite element analysis program (SAP IV). The next chapter shows a quite unconventional approach to solve the problem of the coupling to the clamping.

1 Ueda,T.et al.; Temperatue Sensor using Quartz tuning Fork Resonator, 40th Annual Frequency Control Symposium, Philadelphia, May 1986, p.224.

2 Chuang, Shih S.; Force sensor using double-ended tuning fork quartz crystals Proc. 38th ann symp. on freq. control, 1983, p. 248

3 Langdon, R.M.; Resonator sensors a review, J. PhysE: Sci. Instrum., Vol 18, 1985, p103, GB.

4 see ref 3.

5 Zulliger, H.R.; Precise measurement of small forces.Sensors and actuators,4(1983) pp-483-495.

6 *Kuchling, H.; Taschenbuch der Physik. Verlag Harri Deutsch, Thun Frankfurt a,M. 1986*

7 Doorenbosh,F.; finds in his internal report Mettler, by another path of calculation a similar formula differing only by the numerical factor (he has .069). This oomes from the fact that he considers also in a way the bending of the conductor.

8 Tough, J.T. McCormick, W.D. and Dash, J.G.. Vibrating wire viscosimeter. Rev. Sci. Instr. 35 (1964) 1345-48.

9 Kokubun,K et al.; Frequency dependence of a quartz oscillator on gas pressure, J. Vac.Sci Technol. A3 (6), Nov/Dec. 1985. p.2184.

10 Hauden,D.; Miniaturized Bulk and Surface Acoustic Wave Quartz Oscillators used as Sensors. IEEE transactions. VOL UFFC-34. No 2. March 1987, p.253.

11 M. Christen, ; Air and gas damping of quartz tuning forks. Sensors and Actuators, 4(1983) p.555.

12 Newell,W.: Miniaturization of Tuning forks. Science Vol.161. Sept. 1968, p.1320.

13 Clayton, L.D., Swanson, S.R., EerNisse, E.P.; Modification of the Double-Ended TuningFork Geometry for Reduced Coupling to Its Surroundings: FInite Element Analysis and Experiments. IEEE Transactions on Ultrsonics, Ferroelelctrics and Frequency COntrol, Vol UFFC-34, No 2, March 1987, p. 243.

Chapter 9
Torsional Structure

9.1. Introduction
9.1.1. Statement of the problem

The vibration in a torsional mode of the mass-beam system described in chapter 6 showed a higher Q-factor than the vibration in a transverse mode. In case of a torsional mode only moments have to be compensated, no forces and the coupling to the frame is thus not that strong. Moreover in weak torsion there is only pure shearing present and no volume change occurs. Thus much less internal damping can be expected. These observations motivated a design of a structure optimized to vibrate in a torsional mode.

The fundamental difference between vibration isolation in common mechanical problems and the conceiving of a high-Q system is that in the later one the isolation may not be achieved by dissipation. The isolation has to be therefore either infinitly rigid, which is mechanically not possible or a high-Q system, too (dynamical absorbers). A single piece structure, the resonant structure as well as the isolation system integrated, as possible with the techniques described here, is the solution of the problem.

The calculation of the transferfunction of a coupled two spring mass system with damping suggested a decoupling of the resonator from the frame by a heavy mass and a low springconstant and turned out to be very successful showing the highest Q-factors ever reported for micromachined silicon resonators (cf.[1,2,3,4]).This was achieved by designing a frame around the resonator which itself can vibrate in a torsional mode, too, but with about 1/10 of the resonators frequency (see Fig.9.1.).

9.1.2. State of the art

Petersen[5] described a structure (Silicon Torsional Mirror) vibrating in a torsional mode. Seeking for an other application than resonator he doesn't indicate the Q-factor. But based on his resonance curve we estimate it to be below 100 in air, due probably to the support ridge he found necessary to stabilize the vibration for a optical application. The dimensions and therefore the resonance frequencies are similar to ours. Kaminsky[6] claims to have structures etched in 110 oriented silicon with $Q=10^5$ at 0°C and $Q=10^8$ at 2K, but neither frequency nor experimental condition are given. Recently Andres[7] presented quite complex shaped structures which vibrate in rather complex modes. The Q-factor ranges from 6300 for a low mode at 85 kHz to 49000 of a high order mode at 400 kHz.

9.2. Calculations and design

9.2.1. Calculations

The torsional resonance frequency of a *simple* rod with an end mass was calculated in section 2.3. [2.42] (for the calculation of a structure as in Fig.9.2. the same formulae apply if one takes only half of the structure):

$$\omega = \sqrt{\frac{G\,J_t}{\Theta_{bar}\,L}\left(\frac{3\kappa}{3+\kappa}\right)} \qquad [2.42]$$

where

$\Theta_{bar} = \Theta L$ inertial moment of the bar

L= length of the torsional bar

$G = \frac{1}{2}(c_{11} - c_{12}) = 5.085\cdot 10^{10}$ Pa, shear modulus in the appropriate crystal direction (see Appendix I)

$\Theta_o = \frac{\rho_{Si}\, b\, d\, a^3}{3}$, moment of inertia of (half) the end mass (see Fig.9.2.) [9.1.]

$\kappa = \frac{\Theta_{bar}}{\Theta_o}$

J_t = Static moment of inertia, which depends on the dimensions and the shape of the cross section of the bar.The bar in our case is actually a prism with a symmetrical but not regular hexagonal cross section. We approximated it by an elliptical cross section of about the same surface (see Fig.9.1.) For an elliptical cross section (including circular) J_t is

$J_t = \frac{\pi\, e^3 f^3}{e^2 + f^2}$, e and f the major and minor axis of the ellipse respectively.

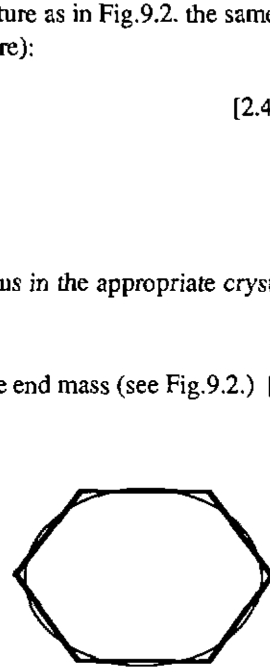

Fig. 9.1. The cross section of the torsional bar, real and elliptic approximation.

The calculation of the resonance frequency of the decoupling structure follows exactly that above. Only the aspect ratio of the torsional bar is different now, and because the wafer thickness and the angles are given, only the width is different.

Similar to the derivation given in section 6.2.7. the temperature dependence of G can be found to be

$$\left.\frac{dG(T)}{dT}\right|_{T_o} = G_o \left\{2\beta - \alpha\right\}, \beta = \frac{1}{\omega_0}\frac{\partial\omega(T)}{\partial T}, \alpha = \frac{1}{L_o}\frac{\partial L(T)}{\partial T} \qquad [9.2]$$

To describe the damping one can either use the theory developed in chapter 2.4. for the mass beam system or one can assume a relatively strong damped vane at the end of a rod by neglecting the inner dynamics of the rod. The damping coefficient D of the vane in the low pressure region can be calculated as[8]

$$D = \frac{\Delta p}{u} 2 \int_0^a y^2 dA \qquad [9.3]$$

with

$$\frac{\Delta p}{u} = 4\sqrt{\frac{T}{2\pi}}\, p\sqrt{\frac{M}{R_o\, T}} \qquad [2.116]$$

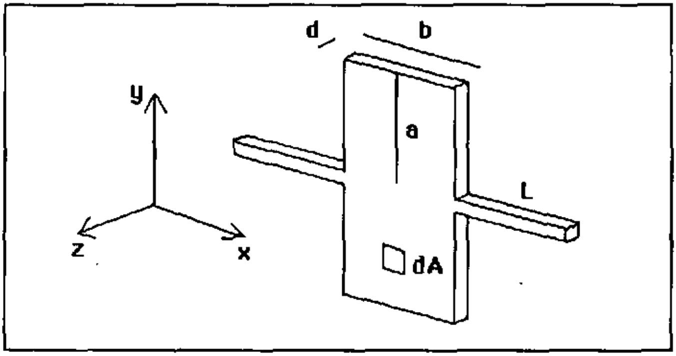

Fig.9.2. Scheme of the vane with the torsion bars , L= 2mm , a= 2mm, b= 2mm and d= 0.372mm

For a rectangular vane (see Fig.9.2.) with the dimension in direction of the axis of b and perpendicularly to the axis 2a

$$\int_0^a y^2 dA = \frac{b\, a^3}{3} \qquad [9.4]$$

$$D = 4\sqrt{\frac{T}{2\pi}}\, p\sqrt{\frac{M}{R_o\, T}}\, 2\, \frac{b\, a^3}{3} = \frac{8}{3}\sqrt{\frac{T}{2\pi}}\, p\sqrt{\frac{M}{R_o\, T}}\, b\, a^3 \qquad [9.5]$$

The logarithmic decrement is

$$\Lambda = \frac{\pi D}{\omega\, \Theta_o} \qquad [9.6]$$

and Q therefore

$$\boxed{Q\ (p) = \frac{\omega\ \Theta_o}{D} = \frac{3\sqrt{2\pi}}{8}\ \frac{\omega\ \Theta_o}{p\ b\ a^3}\sqrt{\frac{R_o\ T}{M}}} \qquad [9.7]$$

The pressure dependence of the Q-factor is thus similar to that found for the other devices, only the proportionality constant is different.

With Θ_o from [9.1] inserted in eq. [9.7] we find

$$Q\,(p) = \frac{3\sqrt{2\pi}}{8}\ \frac{\omega\ \frac{2}{3}\rho_{Si}\ b\ d\ a^3}{p\ b\ a^3}\sqrt{\frac{R_o\ T}{M}} = \frac{\sqrt{2\pi}}{4}\ \frac{\omega\ \rho_{Si}\ d}{p}\sqrt{\frac{R_o\ T}{M}} \qquad [9.8]$$

and with Q_o as the pressure independent Q-factor (by the additivity of the reciprocals) for the total Q-factor for the low pressure region.

$$Q_{tot} = \frac{Q\ (p)\ Q_o}{Q\ (p) + Q_o} \qquad [9.9]$$

9.2.2. Design and etch simulation

In order to decouple the resonator from the clamping we designed a frame around the resonator which itself can vibrate in a torsional mode, too. The aim of the design was to have a high ratio of the resonance frequency between the resonator and the frame. This signifies for the frame large masses (inertial moment) and low spring constants i.e. thin bars. The brittleness of the resulting structure set the limits empirically for save handling. Moreover too thin suspension bars would favour transverse mode as stated by Petersen[5]. Starting from a reasonable resonance frequency for the inner resonator the rest was more or less given. The decoupling frame might also be designed with two halves, allowing thus e.g. to exert a force on the axes. We maintained the same outer frame as in the structures described in chapter 7 to facilitate comparison by having the same clamping.

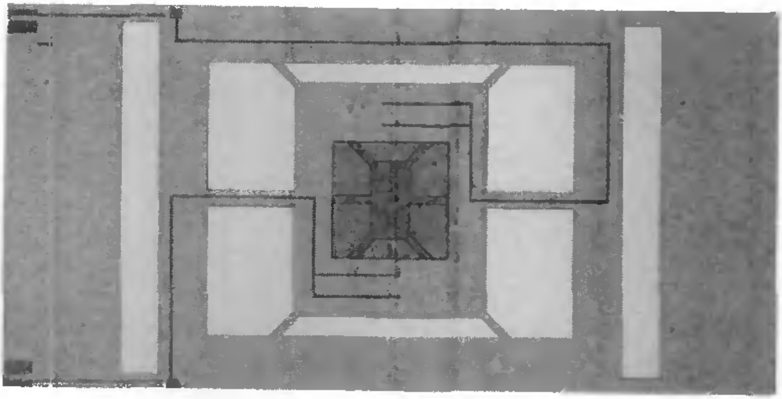

Fig.9.3. The design of the torsional structure with a decoupling frame

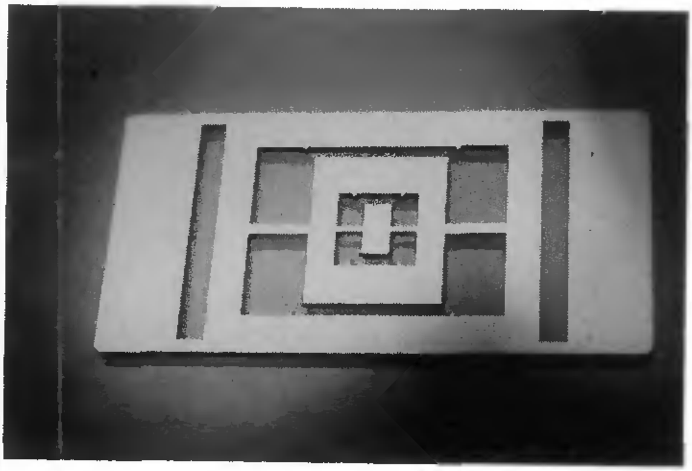

Fig.9.4. A Photograph of the decoupled torsional structure. The total length of the structure is 40mm and the width 20mm

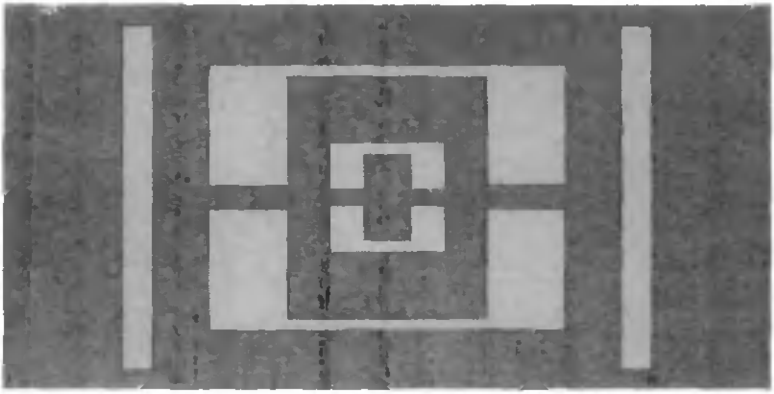

Fig.9.5. The design for another crystal orientation of a torsional structure with a decoupling frame.

9.3. Fabrication of the structures

The fabrication of these structures follows the procedure of those described in chapter 8, thus etching from both sides simultaneously in KOH. Fig. 9.6. shows a schematic cross section of a possible construction for an electrostatical excitation and measuring. After the metal mask (applied with the same technology as described in chapter 8) the resonator in the middle has to be etched down some microns to have space to oscillate. Then a glass plate with two electrodes,- say one for exciting and one for measuring,- can be bonded anodically to the decoupling part. By using the silicon directly as counter-electrode, no supplementary layers have to be deposited on the torsion bar, leaving thus the Q-factor unaffected.

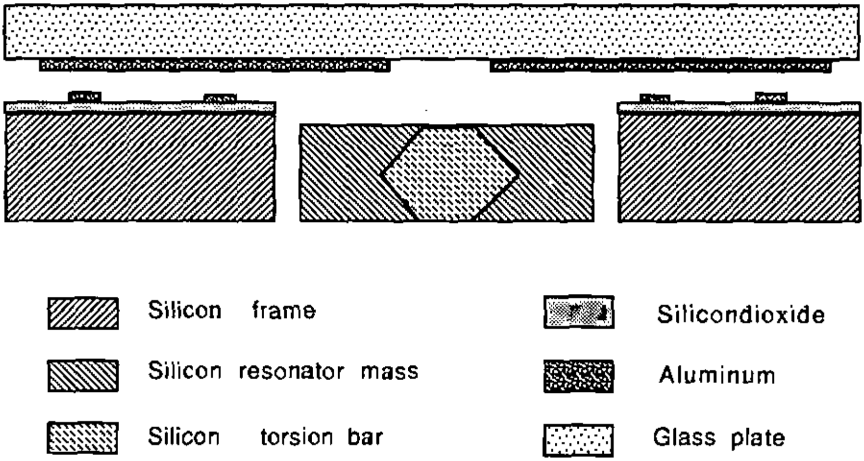

Fig 9.6. A possible construction for an electrostatical excitation and measuring

9.4. Experimental

Although actually a torsional excitation would be needed, experimentally a transverse excitation was sufficient. Thus the same setup could be used as described in chapter 7. The laser beam was set far from the central axis in order to have large amplitude. Nothing new was added to the hardware of the measurement system, but because of the high Q-factor observed with this structure the measurements had to be carried out much more carefully. Especially the temperature had to be very stable: The temperature gradient of these structures was 1.2 Hz/ K. Experimentally 10 mHz could be resolved in vacuum meaning that differences in the order of 0.01 K affect still the amplitude.

9.5. Results

9.5.1. Damping by nitrogen

9.5.1.1. Resonance frequency versus gas pressure (nitrogen)

We calculated a resonance frequency of 22.5 kHz and measured one of 23,9kHz in vacuo. The pressure dependence of the resonance frequency by the additional mass of the surrounding gas starts at about 10 mbar (see Fig.9.7.) and varies above that pressure linearly with pressure with a slope of 0.7 ppm/mbar(see Fig.9.8.).

This is simular to that observed for the mass beam structures of chapter 6 (cf. Fig.6.16).

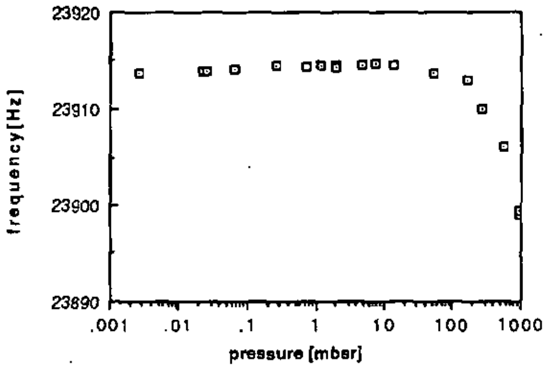

Fig.9.7.Resonance frequency in dependence of nitrogen pressure in semilog plot

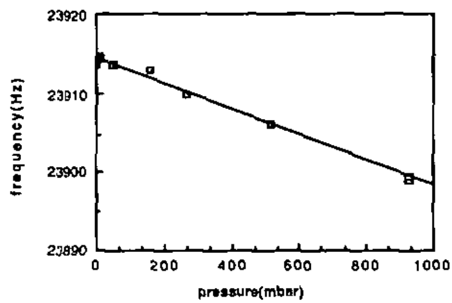

Fig.9.8. Pressure dependence of the resonance frequency in a linear scale

9.5.1.2. Pressure dependance of the Q-factor

The pressure dependance of the Q-factor starts at about .01 mbar (see Fig.9.9.) and flatens out in the viscous region above 100mbar. The theoretical Q-factor was calculated with the help of Eq. [9.9]. The experimental behaviour is well characterized even until higher pressures, although no viscous damping is included in the model. Especially the strong dependence of the Q-factor in the region around 0.1 mbar determined by the molecular damping not seen with the structures in chapter 6 is now well revealed.

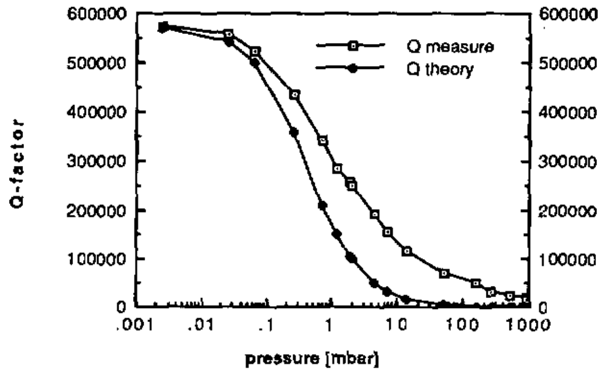

Fig.9.9. Q-factor in dependence of nitrogen pressure in a semilog plot.

9.5.2. Damping by layers

A layer of 8000Å of SiO_2 on both sides of the structure reduces the Q-factor to about 500'000, whereas a one side covering with .05µm of Ti and 1µm of Ag reduces the Q-factor to about 200'000 and the resonance frequency to 23'710 Hz.

9.5.3. Temperature characteristics of the structures

9.5.3.1. Resonance frequency versus temperature

Temperature dependence of the resonant frequency is shown in Fig.9.10. The frequency was measured under vacuum conditions and 20 minutes was given for each point to stabilize. For β (see Eq.[9.2]) we get a value of $\beta = - 5.01 \cdot 10^{-5}$/K . This results in a temperature coefficient of the shear modulus of $5.21 \cdot 10^{6}$ Pa/K at 25 °C or about 100.3 ppm/K (cf. $K_{G[110]}$ = -91.5 ppm/K of appendix I).

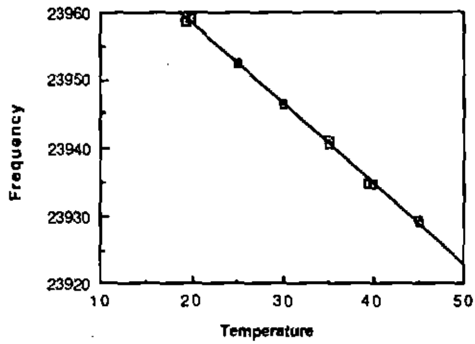

Fig.9.10. The temperature dependence of the resonance frequency

9.5.3.2 Temperature dependence of the Q-factor

As observed already for the structures of chapter 6-, also the Q-factor under vacuum conditions shows (Fig.9.11.) an increase with lower temperatures. It is interesting to note, that lowering the temperature to about 19°C increased the Q-factor to 640 000. The encircled points in Fig.9.11. were measured after the others but during the same measurement cycle. The trend toward higher Qs just by waiting may indicate a kind of relaxation. The temperature alone is stabilized much faster as shows a comparison with Fig.9.10., where the corresponding frequencies are plotted. This phenomena is investigated in next paragraph.

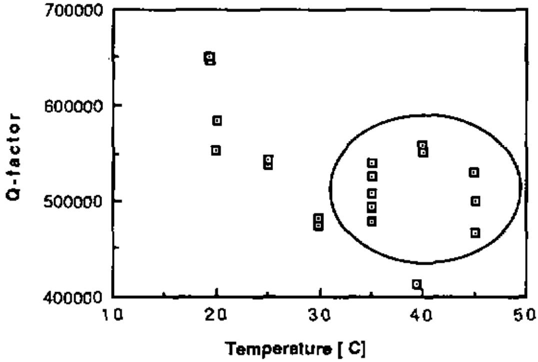

Fig.9.11. The temperature dependence of the Q-factor

As in chapter 6 we made an Arrhenius plot (see Fig.9.12.). From the slope we find a activation energy of 0.156 eV. thus about three times higher than for the structures of chapter 6. We were working here at a frequency of 23 kHz and here, too, the activation process is rather unspecified.

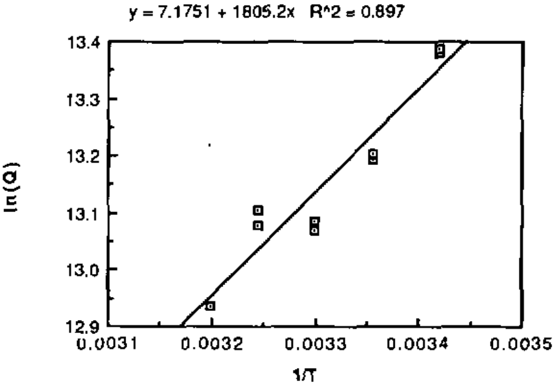

Fig.9.12.-An Arrhenius plot of the O-factor without the encircled points in Fig.9.11.

9.5.4. Drift

As mentioned above we observed that the Q-factor shifted much stronger than the frequency, when the support of the structure was set to a certain temperature in vacuo. This fact is confirmed in a long term experiment, where the support was set to a temperature of 35°C (itself stable after about 15' thanks to the external temperature feedback of the thermostat) and measurements have been carried out during 4 hours. We found (see Fig.9.13.), that not only the Q-factor, but also -to a lower extend of only 6 ppm/h -, the frequency shifts during at least four hours. The pressure was kept in the range from .8 to 1 mbar, where no dependence of the resonance frequency on the pressure should occur (cf. Fig. 9.7.). The first four measurements of Fig. 9.14. showed a correlation between pressure and Q-factor, but no longer the last two ones. Hence other effects than pressure fluctuations are responsible for that drift. It could be a temperature phenomenon, but sure not a direct one, because a rise of the temperature would decrease the resonance frequency (see Fig.9.10.) as well as the Q-factor (see Fig. 9.11.), where here both increase. Supposing that the outer frame is hotter than the resonator (in the experiment we started from a temperature of 24°C) then there would be an axial stress on the inner resonator increasing the frequency, which would be released in time, when the resonator approaches the applied temperature. Since no such release is observed within 4 hours (at 1 mbar we have still a contribution of the convection to the heat transfer) we suppose that an outgasing (or at least migration) of e.g. H_2O, H or O_2 may take place which by loss or redistribution of mass would explain the phenomenon.

It has to be noted that the increase in frequency is only observable because of the high Q-factor of the device.

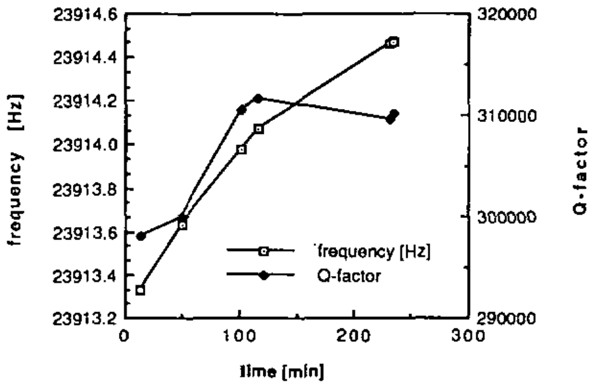

Fig.9.13 Drift of the resonance frequency and the Q-factor

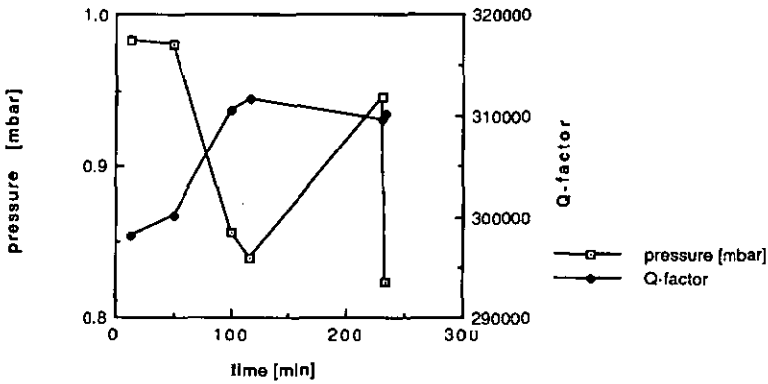

Fig.9.14. Correlation between pressure and Q-factor

Another measurement series (see Fig.9.15.), where we left the same device as above 12 hours under vacuum at room temperature and heated then to 35°C and where we took care to switch the laser light on only for the measurement about 1 minute, showed by having the same characteristics as Fig.9.13., that it is rather the temperature that makes the effect and not the vacuum.

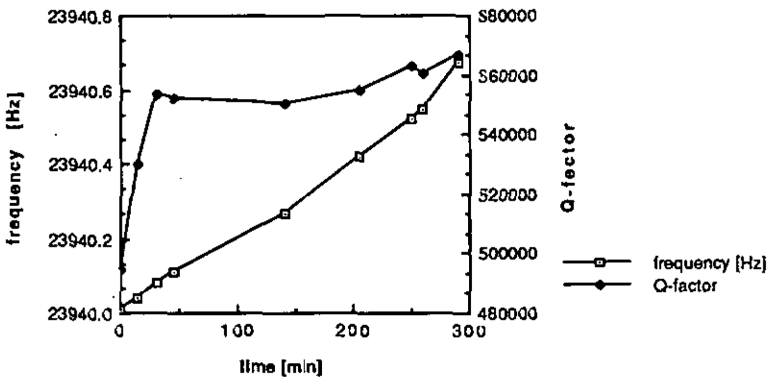

Fig.9.15. Another drift measurement series of the same device

9.6. Discussion

Although the torsional movement is somewhat more complicated to calculate, especially when the cross section is not circular or elliptical, but hexagonal, the movement itself is very simple, because the torsion angle can be assumed to be constant over the bar and the paddle to be rigid. Thus, also for the damping the situation simplifies because one can assume to have only a rigid vane, which is damped. It is however still a problem to model correctly the damping of a torsional accelereted movement of a plate of the dimension of the acoustical wavelength.

On this structure the theoretically expecpted inverse proportionality of the pressure dependence of the Q-factor could be observed, which was not the case with the devices of the previous chapters.

The low damping of silver, observed already with the structure of chapter 6 is confirmed by the measurements made with this structure and oxide damping could now be measured.

The decoupled torsional structure showed at a resonance frequency of 22 kHz Q-factors in the order of 600'000 in vacuum at room temperature. By equation [4.1.] we find a witdth of the resonance peak at half maximum of 0.24 Hz. Experimentally we could adjust the frequency to a precision of about 10mHz. Thus a resolution less than one ppm of the frequency is possible. Having a Q of about 15000 at air pressure such a structure is still a high precion sensor under this condition (e.g. as a pressure or absorption sensor). Since the intrinsic damping of this structure comes close to the physical limits (in contrast to the mechanical of the clamping) it may be suited for studies on internal damping mechanisms with the advantage compared to conventional ultrasonics measurement techniques that no transducer has to be attached to the structure.

---

1 J. G. Smith et al.; Resonant Diaphragm pressure measurement system with ZnO on Si Excitation, Sensor and Actuators, 4 (1983) p. 565.

2 J. C. Greenwood; Etched Silicon Vibrating Sensor, J. Phys. E: Sci Instrum., Vol 17, 1984, p. 650.

3 Wölfelschneider,H. Kist,R. Knoll.G. Ramakrishnan,S. Höfflin,H., Benecke, W., Csepregi, L. Heuberger, A., Seidel,H..; Optically excited and interrogated micromechanical silicon cantilever structure. SPIE Vol. 798. Fiber optic sensors II (1987) p.61

4 Kaminsky, G.; Micromachining of silicon mechanical structures, J.Vac. Sci. Technol. B 3(4), Jul/Aug 1985 p.1015

5 Petersen, Kurt, E.; Silicon as a Mechanical Material. Proc. of the IEEE, Vol. 70. no 5. May 1982. p. 420.

6 Kaminsky, G. Micromachining of silicon mechanical structuresm J.Vac. Sci. Technol. B 3(4), Jul/Aug 1985 p.1015.

7 Andres, M.V., Foulds, K.W.H., Tudor, J. M.; Senisitivity and Mode Spectrum of a Frequency-output Silicon Pressure Sensor, Sensors and Actuators, 15 (1988) p.417-426

8 Christian, R.G.;The Theory of oscillating-vane vacuum gauges, Vacuum 16, no 4,175 (1966)

Chapter 10
Small Structures for Optical Excitation

10.1. Introduction

We are closing this work with a rather speculative chapter, opening a window to another high-tech world. The structures described in the previous chapters were all quite large. The measurement of a small thin (10μm) beam structures described in chapter 6 without proof mass has shown a higher sensitivity to the surrounding medium than the ones with the proof mass and the thick beam. For the application as a density sensor such small structures are thus more appropriate. Although having lower Q-factors in air these structures may need less energy to be excited e.g. by a thermooptical effect. Hence the combination of fibre optics with micromachined structures seems to be a promising way to get micropackaged sensors.

Giallorenzi[1] gives an overview of the different sensors possible with fiber optics. Fluitman[2] classifies optical waveguide sensors into intrinsic ones, where the waveguide play an essential role and extrinsic ones, where the modulation of the light is done outside the waveguide. In this chapter we are going to present some possibilities that silicon technology offers to realize such extrinsic fiber sensors with silicon. The fiber serves then just as a waveguide.

Membranes, cantilever beams, or bridges are suitable mechanical structures with movable surfaces to modulate the light. Static deflection might be detected by measuring the intensity of the reflected light. But the dynamic operating and measuring of such structures is more attracting. The change of the resonance frequencies of these devices may be detected as intensity or phase modulated light by fiber optics. Thus, the information is directly frequency coded, an interesting feature from the view of data transfer. These sensors allow also a special multiplexing by just designing different resonance frequency for different sensors[3].

The idea of not only measuring microdisplacements but also inducing them by light attracts an increasing interest. Photon pressure, charge carriers creation (in semiconductors) and heating (by the induced temperature gradient and the therefrom resulting different thermal dilatation) are described as being the cause of induced mechanical stress by light[4] Only the last two effects contribute substantially to mechanical deformation. Silica, having a thermal expansion coefficient of a quarter of silicon[4] allows to realize a certain bimetallic effect, when the temperature gradient in silicon alone is not high enough to induce enough stress.

One of the first author who published on the mechanical excitation by an optical beam was E. Dieulesaint in 1981[5]. He describes a circular membrane of silicon of about 10 μm thickness and a diameter of some millimeters. One side of the membrane was blackened in order to absorb more light, which originates either from a LASER or a diode. The resonance frequencies of his structures are in the range of some kHz and the Q-factor in the order of ten.

Beam like structures excited optically are reported by other authors[6]. Structures with lateral dimensions of typically 1 mm and a thickness of typically 5μm to 10μm need an optical power in the range of .5 mW for excitation. The disadvantage of these small structures lies in their high sensitivity to air damping resulting in low Q-factors in the range of 100.

Even silica beams may be suitable materials for optically activated resonators[7]. With a thickness of about 1 μm and lateral dimension in the range of 100 μm they need only around 10 μW of optical power for activation, but published ones show very low Q-factors (order of 50), too [8].

By using a Fabry-Perot interferometer a direct feedback of the modulated light can keep the structure in resonance[9] and no additional electronic circuitry is necessary to provide this.

Lammerink[10] has published on a shutter like device. Here an etched pyramid on a membrane cuts more or less the light beam going from one fiber to another.

10.2. The structures

Three types of structures were investigated in this chapters in order to obtain an impression of the possible miniaturization and the obtainable Q-factors. The first structure was just the beam of the beam mass system of chapter 6, whose frequency dependence on pressure was already discussed there. Next to mention are the row of paddles of different shapes They were designed by Mr. Müller from the Corporate Research ABB (former BBC). We etched them by common etching techniques as thin as 5 μm (see Fig.10.1.). The processing corresponds exactly to that discribed in chapter 3 with the speciality of having beam a thickness of 5 and 10 μm and the thickness of the proof mass same as the beam. They have the small dimensions needed for optical activation.

For an application as Atomc Force Microscope (AFM) cantilever we realized an array of silica (wet thermal grown silicon dioxide) beams (see Fig.10.2.). The thickness is 1.5.μm for all beams, the length varies from 100μm to 220μm and the width are 20μm and 40μm. They are fabricated by etching anisotropically from the basckside until a few microns membrane and reoxidized then to the cantilevers thickness. After a photolithographic procedure the wafer is etched from both sides until all silicon is removed under the silica beams. A thin layer of gold is evaporated then to the beam actually for the AFM application but it helps also to reflect the laser beam.

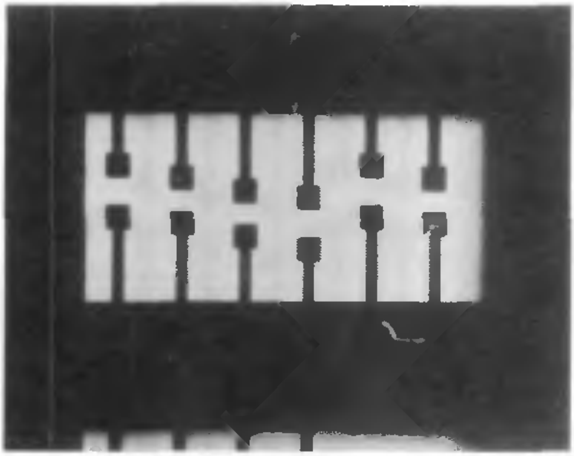

Fig.10.1. Photograph of a row of microfabricated paddles with a thickness of 10μm and a length of about 1mm.

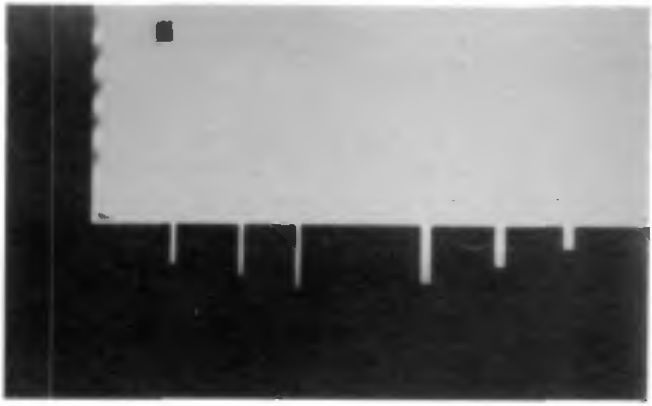

Fig.10.2. Photograph of a silicon dioxide cantilever covered from backside by a layer of gold.

10.3. Results

10.3.1. The frequency dependence on nitrogen pressure

The characteristics of the frequency dependence on pressure for the paddle structure with dimesions of 200µmx1100µm for the beam and 400µmx400µm for the paddle is similar to all those reported in the previous chapters (see Fig. 10.3.). With a drop to .994 in the normal frequency plot of Fig. 6.16. it lies inbetween mass beam structures and the simple cantilever.

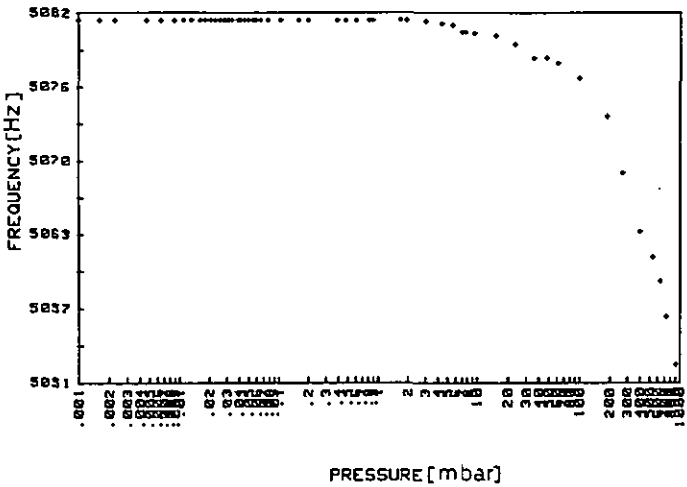

Fig.10.3. Frequency in dependence of the nitrogen pressure of a paddles structure

10.3.2. Q-factor in dependence of the nitrogen pressure

The pressure dependence of the Q-factor of the simple cantilever beam of 10µm thickness shows a slight beginning of the molecular determinent damping at about .4 mbar, although it is represented in a doubly log-plot (Fig.10.4.). Much more pronounced is this characteristics in the plot of the paddle type structure described above (see Fig.10.5). The steep stright line indicates the 1/p law expected for the molecular region (see section 2.4.), whereas the flat one indicates the$1/\sqrt{p}$ law expected for the higher viscosity region. The relatively elevated Q-factor of 200000 is quite unique, not only compared to other publications but also to the same row. Other paddles had Q-factors ranging from 6000 over any value to typically 20000. It seems that the clamping is particularly well adapted to this specific vibration mode.

The silica beam of 140x40x1.5μm, covered by 500Å Au, had a measured resonance frequency of 65'890 Hz and showed a Q-factor in air of about 800.

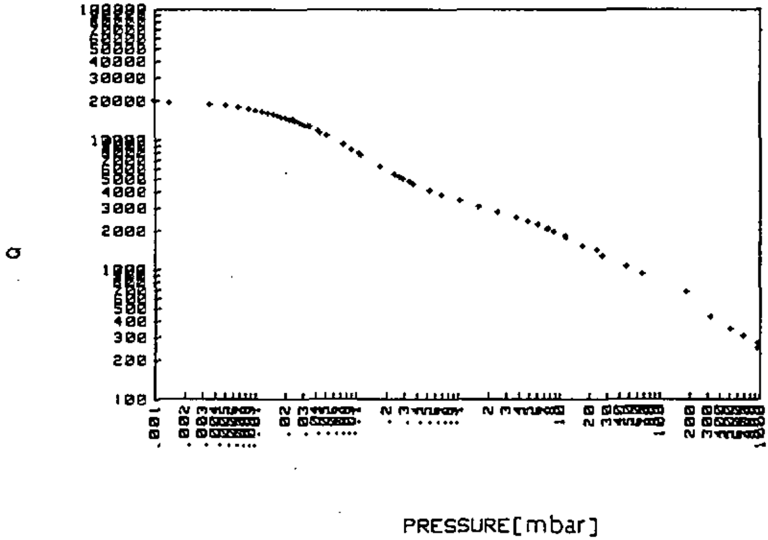

Fig.10.4. Q-factor in dependence of the nitrogen pressure of a silicon beam structure

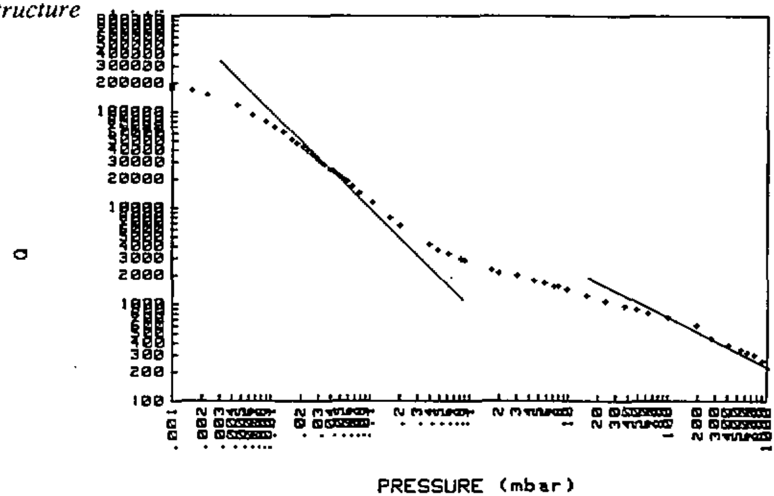

Fig.10.5. Q-factor in dependence of the nitrogen pressure of a paddles structure

10.4. Packaging of fibers together with silicon resonators

When the fiber functions as a waveguide it has to end more or less perpendicularly to the reflecting surface. Vibrating devices are typically fabricated in planar technology resulting in a set-up as shown in Fig.10.6., ending

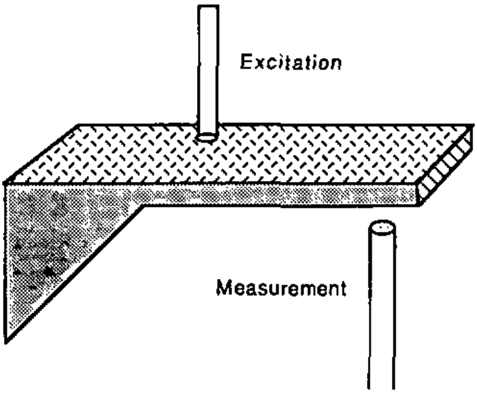

Fig.10.6. Typical set-up of a resonator energized and measured by Fiber-Optics.

in a considerable packaging problem. Fig.10.7. shows, how by using a meanwhile common used technique to attach fibers by etching anisotropically V-grooves into silicon and the techniques of underetching of high doped regions a planar integration of the fiber is possible. The walls of the grooves are crystal planes (111) and therefore well defined and highly accurate to fabricate. The transverse (111) plane functions here as a mirror. Although this plane is not 45 degrees inclined (but 54.7 degrees), it might be sufficient for the excitation of the beam.

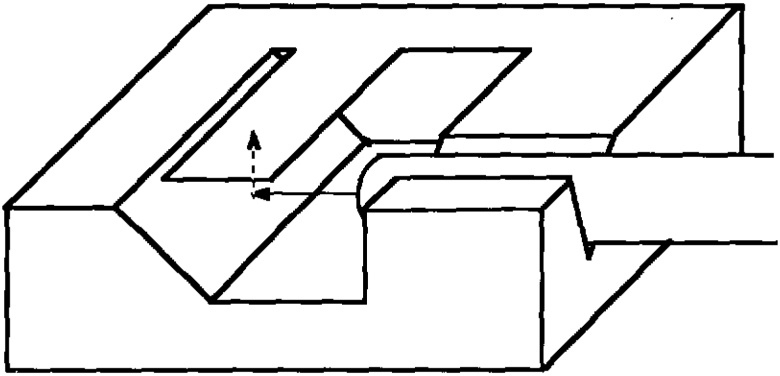

Fig.10.7. Etched mirror with a cantilever and a fiber in a etched V-groove

The fact that vertical walls in (100) wafers can be etched allows to realize a device sketched in Fig.10.8., where the beam vibrates in the plane of the chip surface. The two fibers are here aligned perfectly to 45 degrees.

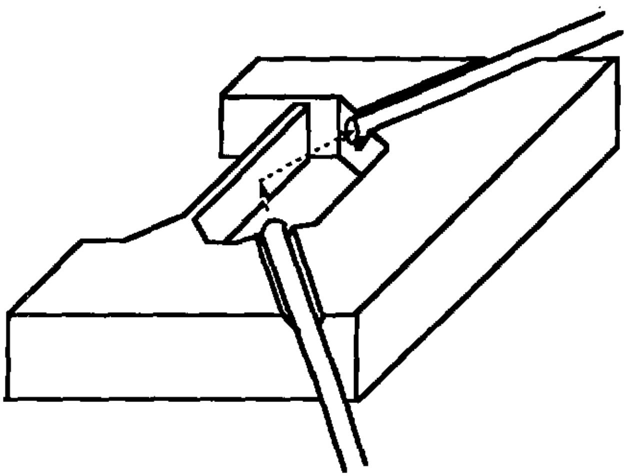

Fig.10.8. Beam with vertical walls vibrating horizontally, activated and/or measured via fibers embedded in V-grooves.

When transmission of light is the changing parameter of the sensor a device as sketched in Fig.10.9. may be constructed. A glass top cover bonded anodically to the silicon support closes the cavity and completes thus the double fiber tip sensor.

That way, the construction of a device as proposed by Poalo Dario[11] for example could thus be much simplified. The crystal planes itself guarantee for a precise adjustment.

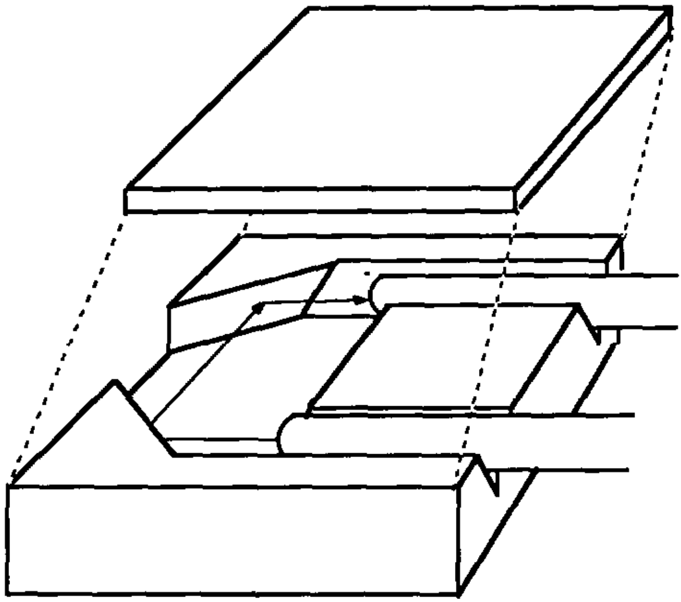

Fig.10.9. Two etched vertical mirrors, being 45 degree rotated with respect to the V-grooves of the fibers. On the left side there is a opening where either gas, liquid or even a solid shutter can be introduced in the optical path. A glass plate can be bonded anodically to the silicon block.

10.5. Discussion

The structures described in this chapter have the small dimensions needed for optical activation and show the expected[12] low Q-factor of about 200 in atmospheric pressure, but some achieved a Q of 20000 or even 200000 in vacuo. Therefore here again it is confirmed, that it is not the silicon itself which limits the Q-factor but the structural damping i.e. the clamping. The resonance frequencies of our paddle structures lies in the lower kHz range.

Only the aspect of silicon technology and micromachined structures was discussed here. But the combination with the silicon's electronic possibilities opens a vast field for sensor applications. Silicon is well known as light detector and is therefore also the ideal link between optics and electronics. By integrating a photovoltaic cell one can even generate electrical power locally at the end of a fiber in order to run an electronic circuitry or a piezoelectric actuator.

The synthesis of fiber optics and silicon technology,- these two different but independently well developed technologies,- seems to have a high innovation potential. Reducing the dimensions of the resonator, - easy to perform by the technology described above -, to fit directly to the fiber tip might be the ultimate step to have a minlaturized and micropackaged fiber optical sensor[13].

---

1 Giallorenzi,Th. G. et al.; Optical Fiber.Sensor Technology. IEEE J. of quantum Electronics, Vol. QE-18, No 4, April 1982, p.626.
2 Fluitman, J. and Popma, Th.; Optical waveguide sensors. Sensors and Actuators, 10(1986), p.25.
3 Dakin J.P.; Multiplexed and distributed optical fibre sensor systems. J. Phys. E:Sci. Instrument. 20. (1987) p. 954.
4 Culshaw ,B.; Silicon in Optics. SPIE Vol. 798 Fiber Optic Sensors II (1987) p. 346.
5 Dieulesaint, E. Royer, D., Bonnefoy, C.; Mechanical excitation of a membrane by an optical beam. IEEE Proc. of the Ultrasonics Symposium, 1981 New York, p. 802.
6 Wölfelschneider, H., Kist,R., Knoll.,G., Ramakrishnan, S., Höfflin, H., Benecke,W., Csepregi, L., Heuberger, A., Seidel, H.; Optically excited and interrogated micromechanical silicon cantilever structure. SPIE Vol. 798. Fiber optic sensors II (1987) p.61
7 Venkatesh, S., Novak S.; Micromechanical resonators in fiber-optic systems. Optics letters. Vol. 12. No 2. 1987,p. 129.
8 Stokes, N.A.D., Fatah, R.M.A., Venkatesh, S.; Selfexcited vibrations of optical microresonators, Electronics Letters, 23rd June. 1988, Vol. 24, No 13, p.777
9 Langdon, R.M. Dowe, D.L. ; Photoacoustic oscillator sensors. SPIE Vol 798 Fiber Optic Sensors II (1987) p. 86.
10 Lammerink, T.S.J., Gerristson S.J.; Fiber-optic sensors based on resonating mechanical structures. SPIE vol 798 Fiber optic Sensors II (1987) p.67.
11 Dario, P., Femi, D., Vivaldi F.; Fiber-optic catheter-tip sensor based on the photoelastic Effect. Sensors and Actuators, 12(1987) p. 35.
12 Andres, M.V., Foulds,K.W.H., Tudor, M.J.; Optical activation of a silicon vibrating sensor. Electronics Letters vol 22 No 21 (1986) p. 1097.
13 Johnsson, L. and Hök, B.; Multimode fibre optic accelerometers, Proc. 2nd Int. Conf. on fiber Sensors, Stuttgart, Sept. 1984. p. 67.

Chapter 11
Conclusions

Resonant structures of single crystal silicon were investigated in view of their potential use as basic elements for various sensors for the measurements of forces, torques, mass or a change of the modulus of elasticity (e.g. temperature). We have presented structures etched in monocrystalline silicon which show a high Q-factor allowing a frequency resolution in the order of ppm. Thus silicon monocrystalline structures are good candidates for high resolution sensors. Moreover a measurement system was described that allows to characterize structures vibrating with very small amplitudes (order of Å). The influence of the variables pressure and temperature on the resonance frequency and the Q-factor have been studied and the temperature coefficient of the modulus of elasticity has been extracted.

In the theoretical part (chapter 2), we achieved to formulate the general solution for the transient behaviour of a beam in a flexural or torsional mode with an arbitrary mechanical impedance somewhere on the beam. These results may be helpful in other fields, too.

Experimentally an exponential decay of the amplitude for all structures at all pressures was found. Thus, linear equations may well describe the systems. Only at very low amplitudes (below 1Å) the decay characteristics changed. The various models of the physical nature of the gaseous damping reported in literature were reviewed and applied to our structures showing in spite of the quite simplified assumptions a rather good agreement without a lot of fitting parameters.

We developed a special corner compensation method to obtain perfect mesas by anisotropic etching, which could thus be calculated precisely. The etch simulation program turned out to be a very helpful design tool by reducing the amount of calculations and the possible mistakes in the layout by inexperienced micromachiners. Thus, it was meanwhile applied to design micromachined valves[1], microphones and accelerometers. In a next version of the program, the next but one neighbor and hidden planes should be taken into consideration, too, although the programming task may be considerable depending on the modules at disposition from the computer software (like matrix calculations, hidden line processing). Pre- and post processing were not developed very far, since powerful software packages are on the market for these tasks. It is the aim of the author, to develop the necessary interfaces in order to use the VTI mask layout program from VLSI Technology as preprocessor and to use the output file of our simulation program as input file for the ANSYS FEM-program from Swanson Inc. to model the mechanical behaviour of the designed structure. Together with the automatized measurements this should deliver the tool for an efficient control of design and performance of microstructures.

The simple analysis in chapter 6 showed a strong dependence of the resonance frequency on fabrication tolerances. A tolerance of 1μm for 10 to 100μm structures is actually unacceptable. But this is about the limit of conventional IC technology. Etch stop techniques may improve somewhat the thickness tolerances to .5 μm but the thickness of the layers of this technology is limited to typically 20μm and thus the tolerance stays still at 2%. Submicron technology for the (relatively large) mechanical structures is thus the new challenge for micromachiners.

Although the interferometer is a very sensitive instrument concerning the amplitude, the error of the absolute measurement, which is in the range of some percent due to instabilities in the interferometer, is not very satisfying (c.f. Fig. 6.19.). This could be easily improved by using oscillators of higher stability and less noise for the acoustooptic modulators or directly a two beam laser. Also the mechanical fixation of the optical parts could be improved and the use of a two channel spectrum analyzer would allow to measure the carrier and the side band simultaneously, as described in section 4.6.1.

A demodulation of the signal would allow a frequency measurement by a counter and replace our indirect method with the excitation. The method described by Willemin for demodulation with a Revox Tuner demands oscillators with other frequencies in order to have a carrier at about 87 MHz. The oscillators at disposition showed higher noise. Moreover, the Low Frequency range is limited to about 20 kHz. We made just one measurement with this setup to check the sine wave form of our resonators (mass beam structure).

During the measurement cycles the resonance frequency had to be adjusted manually at the generator. Here, too, the measurements could be speeded up with demodulation by a direct frequency measurement. Also the pressure was adjusted manually. A simple electronic interface together with electromagnetic valves might allow to automatize the measurement cycle completely.

It would be interesting, to measure the Q-factor at liquid nitrogen temperature, especially that of the high-Q-structure of chapter 9 in order to reveal more physical details of internal damping. The feed through and the brass block are suited for such a measurement, it would be only necessary to evacuate one side of the cooling pipe system in order to suck the liquid nitrogen in through the pipes.

Experimentally a great variety of devices were presented. First of all as a static device a tactile sensor array was realized with truncated pyramid shaped force transmitters. Thus, upon application of force on this mesas the capacitance underneath is changed and thus the resonance frequency of a properly connected oscillating circuitry (chapter 5). Publications in application oriented journals found wide echo for this device.

Next to mention are the mass-beam systems were the mass is a perfect geometrical body and thus calculable. This mass is doubly supported and exerts thus no torsional movement (as it would, if only simply supported). On these type of structures most of the studies are done (chapter 6). The damping by various thin films is a general result.

A special compensation of the forces at the clamping for mass beam systems was obtained with another design, which is presented in chapter 7.

We achieved to realize tuning fork structures in silicon. These were provided with metallic lanes so that they could be excited and measured electromagnetically (chapter 8).

A decoupled torsional structure showed Q-factors in the order of 600 000 in vacuo at room temperature and allows thus a resolution of some ppm of the frequency. With this structure it could be proved, that competitive devices for sensor applications (compared to quartz e.g.) are possible in silicon (chapter 9).

We finally realized an array of paddle type devices with dimensions in the order of µm, which can be excited optically (chapter 10), showing much higher Q-factors than typically reported for such devices.

The temperature will always be a problem with silicon devices, because no crystal cut of zero α can be found, since a cubic crystal behaves with respect to α like an isotropic body (cf. appendix I). Creating internal stress to compensate the effect of the thermal expansion by bonding silicon of different orientations together (e.g. a silicon resonator on a silicon frame) might be an idea.

In conclusion for high Q-factor devices aluminum on bending parts should be avoided, use rather Pt or Ag. Oxides are less critical. Rotational structures show generally higher Q-factors than flexural ones. Special attention has to be paid to the isolation from clamping; a statical analysis of stress distribution is not sufficient because we are dealing with elastic waves.

A large field of study was treated here ranging from masking materials research and application optimization for photoresists over the construction of a measuring system and computer simulations to physical modelling and functional analysis. It is obvious that none of these subjects could be treated exhaustively but we hope, that with the study presented here, we could give a contribution to the knowledge of the possibilities and the limitations of sensors, especially resonators, micromachined in silicon.

1 Krebs, Philippe; Evaluation d'une microvanne electrostatique et Realisation d'un Prototype en Silicium. Travail de Diplome Université de Neuchâtel, Inst. de Microtechnique, 1988.

Appendix A

Literature review of mass-beam systems

Hereafter we summarize an overview over the literature on mass beam systems (see table A.1) in view of the contribution for solving the problem of finding the eigenfrequencies and eigenmodes of continuous systems with discrete masses and with proportional and non proportional (discrete damping). The expression proportional damping is used in the sense of distributed damping in continuous systems. The black points means only the main emphasis of the corresponding article, because sometimes the methods can be applied to other situations (other boundary condition e.g.). Especially modal analysis methods developed actually for discrete systems (finite dimensions) can also be applied to continuous ones (infinite dimensions) although it is sometimes difficult to give a mathematical expression for the error (Wahle[60]). The problem of discrete damping however is by nature only apparent in continuous systems (solved by the introduction of delta functions). Non-proportional damping in the sense of non being proportional to mass and stiffness distribution is also present in discrete systems (solved by special matrix transformations or in continuous systems also by integral transformations). The modal analysis is a technique very well adapted to be solved by numerical methods and the search for special analytical solution became in the last ten years less attention. Looking through the tables below one sees immediately that in spite of the large number of publications on that subject (although not in the context of sensors) only few treat the problem as a whole. Herman[34] e.g., performs two Laplace transformations, one with respect to time and one with respect to space. He gives an expression for the backtransformed solution, but the complex frequencies have to be found numerically. Jacquot[43] starts then by modal analysis and a Fourier transformation for the time part a path we completed with the present work by doing a Laplace transformation and executing the backtransformations combining thus the method of Herman and Jacquot. Our aim was to find an analytical expression for the Q-factor in order to be able to include physical expressions for the damping.

Reference list (chronologically)

1. McBride, E.J.; The free lateral vibrations of a cantilever beam with a terminal dashpot. Journal of applied mechanics. Vol 10: A168 to A-172. September 1942.

2. Young,O.; Vibration of a beam with concentrated Mass Spring and Oashpot. Transactions of ASME, Ser. E.: Journal of applied Mechanics, Vol 15, 1948, pp. 65-72.

3. Mindlin, R.D: and Goodman, L.E.; Beam Vibrations with time dependent Boundary conditions. Journal of applied mechanics, Vol. 17:377-380. December 1950.

4. Ayre, R.S., Jacobson , L.S. Hsu C.S;1952. Procceedings of the First U.S. National congress of Applied mechanics. N.Y. ASME, *Transverse vibration on one and two span beams under the actionof a moving load.*

5. Young. D.;1952. Procceedings of the First U.S. National congress of Applied mechanics. N.Y. ASME. Theory of dynamic vibration absorbers for beams.

6. Morgan, G.W.; Some Remarks on a class of Eigenvalue Problems with Special Boundary conditions. Quart. Appl. Math. 11, p 157-165, (1953)

7. Velestos A.S., Newmark , N.M; 1954 Procceedings of the second U.S. National congress of Applied mechanics. N.Y. ASME, A simple approximation for the fundamental frequencies of two span and three span continous beams.and Determination of the natural frequencies of continous beams on flexible supports.

8. Hagel, W.C., Clark, J.W.; The specific damping energy of fixed-fixed beam specimens. J. Apll. Mechanics. vol. 24, 1957, p. 426-430.

9. Foss, K.A.; Co-ordinates which uncouple the equation of motion of damped linear Systems. Journ. Of. Appl. Mech. Sept. 1958, pp. 361-364.

10. Yen, T.C. and Kao,S.; Vibration of beam mass Systems with Timedependent boundary Conditions.;Journal of Applied Mechanics, Vol 26, No 3 Trans. ASME, Vol. 81, Series E. Sept. 1959. pp. 353-356.

11. Caughey, T.K.; Classical normal modes in damped linear Dynamic systems. Journal of applied Mechanics. Vol. 27: 269-271. June 1960

12. Caughey, T.K. and O'Kelly, M.E.J.; Effect of damping on the natural frequencies of linear Dynamic systems.Journal of the accoustical society of america. Vol. 33: 1458.1461. November 1961

13. Maltbaek, J.C.; The influence of a concentrated Mass on the free vibrations of a uniform Beam.Int. Jour. Mech. Sci., Pergamon Press Ltd. vol 3 1961, pp. 197-218.

14. Rodden, W.P., Whittier, J.S.; Damping of shaker-excited beams calculated solely from amplitude measurements.. *J. Acuost. Soc. Am. , vol 34, 1962, 4, p. 469-471.*

15. Chen. Y.; 1963, Journal of applied Mechanics 30. p. 310.-311. On the vibration of beams or rods carrying a concentrated mass.

16. Pan, H.H.; Some Applications of symbolic functions on beam problems. Journal of the Franklin Institute. Vol. 275: 303-313. April 1963.

17. Baker, W.E.; 1964. Journal of applied Mechanics 31, 335-337. Vibration frequencies for uniform beams with central masses.

18. Hess, M.S.; Vibration Frequencies for a uniform Beam with central mass and Elastic Supports. Journal of Applied Mechanics, Vol 31, No 3 Trans. ASME, Vol. 86, Series E. Sept. 1964 pp. 556-557.

19. Neubert, V.H. Dynamic Absorbers Applied to a bar that has Solid damping, Journ. of the Acostical Soc. of America, Vol. 36. no 4. April 1964, pp. 673-680.

20. Caughey, T.K. and O'Kelly, M.E.J., Classical normal modes in damped linear dynamic systems. Journal of applied mechanics. Vol. 32: 583-588. September 1965.

21. Pan, H.H.;Transverse vibration of an Euler beam carrying a System of heavy bodies.;Journal of Applied Mechanics, Vol 32, No 2 Trans. ASME, Vol. 87, Series E.June 1965 ,pp. 434-437

22. Adkins, R.L.; Effect of tuned vicoelastic dampers on response and damping of a clamped clamped beam. Air Force Materials Lab. Report AFML-TR-66-100. WPAFB 1966.

23. Cobble, M.H. Fang.P.C.; Finite transform solution of the damped cantilever beam Equation having Distributed Elastic, Support and the wall Edge elasticity restrained against rotation. Journ. of Sound and vibration. 6(2): 1966,p187.198.

24. Cobble. M.H.; Finite-Transform Solution of the Damped, Clamped -clamped Beam Having Distributed Load and Elastic Support. J. Aucoust. Soc. Amer. 40 p. 1529-1533, (1966).

25. Maybee, J.S.; Normal and Quasi- Normal modes in damped linear dynamic systems.Journal of applied mechanics. Vol. 33: 413-416. June 1966.

26. Morgenthaler, G.W., Normal mode Vibrations for some Damped n. degree of freedom nonlinear systems. Journ. of Appl. Mechaniocs. Vol. 33: 877-880. December 1966.

27. Snowdon, J.C.; Vibration of cantilever Beams to which Dynamic Absorbers are attached.Journ, of the Acostical Soc. of America, Vol. 39, no 5, 1966, pp. 878-886.

28. Weissenburger, J.T., The effect of Local Modification on the Eingenvalues and Eigenvectors of Linear Systems.; D.Sc. dissertation, 1966, Sever Inst., Washington Univ. St. Louis, Mo.

29. Jeyapalan, R.K. and Richards, E.J.; Radiation efficiencies af beams in flexural vibration, J. Sound Vibration, 67 (1979) 55-67.

30. Meirovitch, L.; 1967. Analytical methods in vibration. New York: Macmillan and Co. Inc.

31. Seireg, A. and Howard, L.; An approximate normal mode method for damped lumped parameter systems. Jorn. of Engineering for Industry. pp 597.604. November. 1967.

32. Weissenburger, J.T.; 1968. Journal of applied Mechanics 35. p. 327-332. Effect of local modifications on vibration characcristics of linear systems.

33. Crandall, S.H.; The role of Damping in vibration Theory. Journal of Sound and vibration. Vol. 11: No 1: 3-18. 1970.

34. Herman, H. and Pappas, M.; Vibrations of disspative composite lumped distributed systems. Journal of the Aceoustical Society of America. Vol. 47: 1: Pt.2: 211.219. January 1970.

35. Jacquot, R.G. and Soedel,W.; 1970 Journal of the Acoustical Society of America. 47, p. 1354-1358. Vibrations of elastic surface systems carrying dynamic elements.

36. Kerlin, R.L.; Snowdon, J.C.; Driving point impedance of cantilever beams. Comparision of measurement and Theorie. J. Acoust. Soc. Am. , vol 47. 1970, 1, p 220-228

37. Mead, D.J.; The Existence of Normal modes of linear systems with arbitrary damping. Paper no 5. C5. Proceedings of Symposium on Structural Dynamics. Loughborogh, England. March. 1970.

38. Milne, R.D.; A constructive Theory of lineary Damping. Paper no c4 . Proceedings of Symposium on Structural Dynamics. Loughborogh, England. March. 1970.

39. Dowell, E.H.; 1971 Journal of Applied Mechanics. 38, pp. 595-600 Free vibration of a linear structure with arbitrary support conditions.

40. Pomazal, R.J. and Snyder, V.W.; 1971 American Institute of Aeronautics Journal 9. p 2216-2221. Local modifications of damped linear systems.

41. Chun, K.R.; 1972 Journal of applied Mechanics 39. p 1154-1155. Free vibrations of a beam with one end spring-hinged and the other free.

42. Dowell, E.H.; 1972 Journal of Applied Mechanics. 39, pp. 727-732.;Free vibration of an arbitrary structure in terms of component modes.

43. Jacquot, R.G. and Gibson, J.D.; 1972. Journal of sound and vibration. 23, p. 237-244. The effects of discrete masses and elastic supports on continous beam natural frequencies.

44. Tompson, W.T. and Carvani, P.; Forced Normal mode vibration of Visocolastic Systems. Jour. of. Appl. Mechanics. Vol 39., 2: 625-627. June 1972

45. *Willmert, K.D., Fox, R.L.; Optimum design of a linear multidegree of freedom shock isolation system.* Journ. of Eng. for Ind., May 1972, 465-471.

46. Goel, R.P.; 1973. Journal of applied Mechanics 38, 821-822. Vibration of a beam carrying a concentrated mass.

47. Hallquist, J. and Snyder, W.V.; 1973 Journal of applied Mechanics 40. p 312-313. Linear damped vibratory structures with arbitrary support coditions.

48. Lee, T.W.; 1973 Journal of applied Mechanics 38. p. 813.815 Vibration frequencies for a uniform beam with one end spring-hinged and carrying a mass at the other free end.

49. Raghavan, K.S. and Sundararajan, V.; Vibrations of an Euler BEam with a system. of discete Masses Springs and dashpot. Journal of aircraft. Vol.10 no. 3: 190-192, March 1973.

50. Van de Vegte,J. Hladun, A.R.; Design of optimal passive beam vibration Controls by optimal contral techniques, Journal of dynamic Systems, Measurements and control. Transaction of the ASME December 1973, p 427-434.

51. Farshad, M.; Variations of eigenvalue and eigenfunctions in continuum Mechanics. AIAA J. Vol 12, No 4 1974,, pp. 560-561

52. Gupta, K.K.; Eigenproploem solution of damped strucutral systems. International journal of numerical methods engineering, 8, pp 877-911. 1974

53. Jacquot, R.G.; 1974, Journal of Sound and vibration 32, 459-466. The vibration of regularly supported elstic surface systems subject to additional point constraints.

54. Adkins, R.L.; Modal Analysis of liner non-conservative system.Air Force Materials Lab. Report AFML-TR-75-2, 1975.

55. Howell, L.J.; 1975 American Institute of Aeronautics and astronautics 13, p. 685-687. Effects of constraint modification on random vibration of damped linear structures.

56. Laura, P.A.A., Maurizi, M.J. and Pombo, J.L.; 1975 Journal of sound and Vibration 41, p. 397-405. A note on the dynamic analysis of an elastically restrained free beam with a mass at the free end.

57. Jacquot, R.G.; The forced vibration of simply modified damped elastic surface systems. Journ. of Sound and Vibr. 48(2), 1976, pp. 195-201.

58. Hirai, I. and Kashiwaki, M.; Derivatives of Eigenvectors of locally modified structures. Int. J. Num Meth Eng. Vol. 11, 1977 pp. 1769-1773.

59. *Hsiao, M.H., Haug, E.J., Arora, J.S.; A state space method for optimal design of vibration isolators, Journ.* Mech. Design. Vol 101, april 1979, 309-314

60 Wahle, M.; Beitrag zur passiven Kontrolle schwach gedämpfter elastischer Strukturen mittels dynamischer Schwingungsdämpfer. Dissertation TH Aachen, Aachen 1984.

61. Kaneko,T.; Relations between elastic constants and flexural resonant frequencies of a beam. J. Non-Cryst Solids, 95-6 (dec) P2, 87 p. 993.

62. Sandmaier, H., Kühl, K., Obermeier, E.; A silicon based micromechanical accelerometer with cross acceleration sensitivity compensation, Transducers '87, 4th Int. Conf. on Solid-state Sensors and Actuators, Tokyo, 1987.

63. Present work

Table A.I. Literature overview of mass beam systems

	01	02	03	04	05	06	07	08	09	10	11	12	13	14	15	16	17	18	19	20	21	22	23	24	25	26	27	28	29	30	31	32	33	34	35	
numerical method																														●						
discrete system									●		●	●								●					●	●				●	●		●			
steady state		●			●														●								●						●			
continouus system	●	●	●	●	●	●	●			●			●		●	●	●	●	●		●		●	●			●		●	●		●		●	●	
clamped-clamped beam								●					●						●																	
proportional Damping																							●	●					●	●			●			
discrete masses, springs		●		●	●		●		●	●			●			●	●	●	●		●				●	●	●			●	●	●		●	●	
discrete damping		●			●				●										●						●	●	●			●	●			●		
transient vibration																																		●		
eigenfrequencies																																		●		
eigenmodes																																		●		
elastic clamping			●													●		●					●	●												
dissipative clamping	●		●																																	
nonlinear system																										●										

	36	37	38	39	40	41	42	43	44	45	46	47	48	49	50	51	52	53	54	55	56	57	58	59	60	61	62	63
numerical method															●	●	●						●	●	●	●		
discrete system					●				●	●																		
steady state	●																					●			●			
continouus system				●		●	●	●			●	●	●	●	●		●	●		●	●	●	●			●		●
clamped-clamped beam																											●	●
proportional damping												●					●					●			●			●
discrete masses, springs					●			●			●		●	●	●			●		●	●	●			●		●	●
discrete damping					●				●	●				●						●		●			●			●
transient vibration																									●			●
eigenfrequencies						●	●	●					●					●			●					●	●	●
eigenmodes							●														●		●					●
elastic clamping	●			●		●	●	●				●																○
dissipative clamping	●			●																								○
nonlinear system																								●				

Appendix B

Boundary conditions for simple beam and rigid clamping

The boundary conditions for that case were :

I: $w(0,t) = 0$

II: $w'(0,t) = 0$

III: $w(L,t) = 0$ [2.9]

IV: $w'(L,t) = 0$

The derivatives of the space solution [2.8] are as follows:

$$X'(x) = -C_1 \frac{\lambda}{L} \sin\frac{\lambda}{L}x + C_2\frac{\lambda}{L} \cos\frac{\lambda}{L}x + C_3\frac{\lambda}{L} \cosh \frac{\lambda}{L}x + C_4 \frac{\lambda}{L}\sinh \frac{\lambda}{L}x$$

$$X''(x) = -C_1 \left(\frac{\lambda}{L}\right)^2 \cos\frac{\lambda}{L}x - C_2\left(\frac{\lambda}{L}\right)^2 \sin\frac{\lambda}{L}x + C_3\left(\frac{\lambda}{L}\right)^2 \sinh \frac{\lambda}{L}x + C_4 \left(\frac{\lambda}{L}\right)^2\cosh \frac{\lambda}{L}x$$

$$X'''(x) = C_1 \left(\frac{\lambda}{L}\right)^3 \sin\frac{\lambda}{L}x - C_2\left(\frac{\lambda}{L}\right)^3 \cos\frac{\lambda}{L}x + C_3\left(\frac{\lambda}{L}\right)^3 \cosh \frac{\lambda}{L}x + C_4 \left(\frac{\lambda}{L}\right)^3\sinh \frac{\lambda}{L}x$$

$$X''''(x) = C_1 \left(\frac{\lambda}{L}\right)^4 \cos\frac{\lambda}{L}x + C_2\left(\frac{\lambda}{L}\right)^4 \sin\frac{\lambda}{L}x + C_3\left(\frac{\lambda}{L}\right)^4 \sinh \frac{\lambda}{L}x + C_4 \left(\frac{\lambda}{L}\right)^4\cosh \frac{\lambda}{L}x$$

From the boundary condition [2.9] I it follows:

$$X(0) = C_1 \cos\frac{\lambda}{L}0 + C_2 \sin\frac{\lambda}{L}0 + C_3 \sinh \frac{\lambda}{L}0 + C_4 \cosh \frac{\lambda}{L}0 = 0$$

$$\Rightarrow \boxed{C_1 + C_4 = 0}$$

From the boundary condition [2.9] II it follows:

$$X'(0) = -C_1 \frac{\lambda}{L} \sin\frac{\lambda}{L}0 + C_2\frac{\lambda}{L} \cos\frac{\lambda}{L}0 + C_3\frac{\lambda}{L} \cosh \frac{\lambda}{L}0 + C_4 \frac{\lambda}{L}\sinh \frac{\lambda}{L}0 = 0$$

$$\Rightarrow \boxed{C_2 + C_3 = 0}$$

From the boundary condition [2.9] III it follows:

$$X(L) = C_1 \cos\frac{\lambda}{L}L + C_2 \sin\frac{\lambda}{L}L + C_3 \sinh \frac{\lambda}{L}L + C_4 \cosh \frac{\lambda}{L}L = 0$$

$$\Rightarrow C_1 \cos\lambda + C_2 \sin \lambda + C_3 \sinh \lambda + C_4 \cosh \lambda = 0$$

and with the results from I & II:

$$\Rightarrow C_1 \cos\lambda + C_2 \sin \lambda - C_2 \sinh \lambda - C_1 \cosh \lambda = 0$$

$$\Rightarrow \boxed{C_1 (\cos\lambda - \cosh \lambda) + C_2 (\sin \lambda - \sinh \lambda) = 0}$$

From the boundary condition [2.9] IV it follows:

$$X'(L) = -C_1\frac{\lambda}{L}\sin\frac{\lambda}{L}L + C_2\frac{\lambda}{L}\cos\frac{\lambda}{L}L + C_3\frac{\lambda}{L}\cosh\frac{\lambda}{L}L + C_4\frac{\lambda}{L}\sinh\frac{\lambda}{L}L = 0$$

$\Rightarrow\ -C_1\sin\lambda + C_2\cos\lambda + C_3\cosh\lambda + C_4\sinh\lambda = 0$

and with the results from I & II:

$\Rightarrow\ -C_1\sin\lambda + C_2\cos\lambda - C_2\cosh\lambda - C_1\sinh\lambda = 0$

$\Rightarrow \boxed{-C_1(\sin\lambda + \sinh\lambda) + C_2(\cos\lambda - \cosh\lambda) = 0}$

The two last framed equations are equivalent with eq. [2.10].

Appendix C

Boundary conditions in the case of a simple beam with elastic clamping

If the clamping is elastic, the four boundary conditions of a mass-beam system as shown in Fig.2.1. b) were as follows ([2.17]):

$$
\begin{array}{lll}
\text{I} & w(0,t) & = c_F\ |F(0)| = c_F\, EJ_y\, |w'''(0,t)| \\
\text{II} & w'(0,t) & = c_M\, |M(0)| = c_M\, EJ_y\ |w''(0,t)| \\
\text{III} & w(L,t) & = c_F\ |F(L)| = c_F\, EJ_y\, |w'''(L,t)| \\
\text{IV} & w'(L,t) & = c_M\, |M(L)| = c_M\, EJ_y\ |w''(L,t)|
\end{array}
\qquad [2.17]
$$

Here F is the transverse force and M is the momentum . c_F and c_M are constants of the elastic resistance against F and M. c_F was calculated for a elastic beam with a linearly decreasing cross section as encountered at anisotropically etched silicon The clamping constant c_F was calculated for the symmetrical case (see Fig. 2.3.). By setting $h_b = 0$ the formula given by Szabo[1] reduces to $c_F = \frac{18\,L^3}{Ebd^3}$ and because the relation between L and d is given by $d = L\sqrt{2}$ (fixed for an anisotropically etched clamping) the constant is finally:

$$c_F = \frac{4.5\sqrt{2}}{Eb}$$

whereas c_M was taken from the simulation program SENSIM[14] ($c_M = 1\cdot10^{-6}\ N^{-1}$)

With the abbreviations [2.18],[2.19] the first boundary condition I is:

$$X(0) = C_1 \cos\frac{\lambda}{L}0 + C_2 \sin\frac{\lambda}{L}0 + C_3 \sinh\frac{\lambda}{L}0 + C_4 \cosh\frac{\lambda}{L}0 =$$

$$c_F\, EJ_y \left(C_1 \left(\frac{\lambda}{L}\right)^3 \sin\frac{\lambda}{L}0 - C_2 \left(\frac{\lambda}{L}\right)^3 \cos\frac{\lambda}{L}0 + C_3 \left(\frac{\lambda}{L}\right)^3 \cosh\frac{\lambda}{L}0 + C_4 \left(\frac{\lambda}{L}\right)^3 \sinh\frac{\lambda}{L}0 \right)$$

$$\Rightarrow C_1 + C_4 = c_F\, EJ_y \left(-C_2 \left(\frac{\lambda}{L}\right)^3 + C_3 \left(\frac{\lambda}{L}\right)^3 \right) = c_F\, EJ_y \left(\frac{\lambda}{L}\right)^3 (-C_2 + C_3)$$

$$\Rightarrow C_1 + C_4 = \alpha\,(-C_2 + C_3) \Rightarrow C_1 + C_4 + \alpha C_2 - \alpha C_3 = 0$$

$$\Rightarrow \boxed{C_1 + \alpha C_2 - \alpha C_3 + C_4 = 0}$$

similarly for the other boundary conditions:

so **II**

---

1 Szabo, I.; Einführung in die Technische Mechanik, Springer,Berlin, 8th ed.,1984, p.173

$$C_2\frac{\lambda}{L} + C_3\frac{\lambda}{L} = c_M EJ_y\left(C_1 \left(\frac{\lambda}{L}\right)^2 + C_4 \left(\frac{\lambda}{L}\right)^2\right)$$

$$\Rightarrow C_2 + C_3 = \beta (C_1 + C_4) \Rightarrow C_2 + C_3 - \beta C_1 - \beta C_4 = 0$$

$$\Rightarrow \boxed{-\beta C_1 + C_2 + C_3 - \beta C_4 = 0}$$

and III

$$C_1 \cos\lambda + C_2 \sin\lambda + C_3 \sinh\lambda + C_4 \cosh\lambda =$$

$$c_F EJ_y\left(C_1 \left(\frac{\lambda}{L}\right)^3 \sin\frac{\lambda}{L}L - C_2 \left(\frac{\lambda}{L}\right)^3 \cos\frac{\lambda}{L}L + C_3 \left(\frac{\lambda}{L}\right)^3 \cosh\frac{\lambda}{L}L + C_4 \left(\frac{\lambda}{L}\right)^3 \sinh\frac{\lambda}{L}L\right)$$

$$= c_F EJ_y\left(C_1\left(\frac{\lambda}{L}\right)^3 \sin\lambda - C_2 \left(\frac{\lambda}{L}\right)^3 \cos\lambda + C_3 \left(\frac{\lambda}{L}\right)^3 \cosh\lambda + C_4 \left(\frac{\lambda}{L}\right)^3 \sinh\lambda\right)$$

$$= c_F EJ_y \left(\frac{\lambda}{L}\right)^3 \left(C_1 \sin\lambda - C_2 \cos\lambda + C_3 \cosh\lambda + C_4 \sinh\lambda\right)$$

$$\Rightarrow$$

$$C_1 \cos\lambda + C_2 \sin\lambda + C_3 \sinh\lambda + C_4 \cosh\lambda$$
$$= \alpha \left(C_1 \sin\lambda - C_2 \cos\lambda + C_3 \cosh\lambda + C_4 \sinh\lambda\right)$$

$$\Rightarrow$$

$$C_1 \cos\lambda + C_2 \sin\lambda + C_3 \sinh\lambda + C_4 \cosh\lambda$$
$$- (C_1 \alpha \sin\lambda - C_2 \alpha \cos\lambda + C_3 \alpha \cosh\lambda + C_4 \alpha \sinh\lambda) = 0$$

$$\Rightarrow$$

$$C_1 \cos\lambda - C_1 \alpha \sin\lambda + C_2 \sin\lambda + C_2 \alpha \cos\lambda + C_3 \sinh\lambda - C_3 \alpha \cosh\lambda + C_4 \cosh\lambda - C_4 \alpha \sinh\lambda = 0$$

$$\Rightarrow$$

$$\boxed{C_1(\cos\lambda - \alpha \sin\lambda) + C_2(\sin\lambda + \alpha \cos\lambda) + C_3(\sinh\lambda - \alpha \cosh\lambda) + C_4(\cosh\lambda - \alpha \sinh\lambda) = 0}$$

and IV

$$-C_1\frac{\lambda}{L} \sin\lambda + C_2\frac{\lambda}{L} \cos\lambda + C_3\frac{\lambda}{L} \cosh\lambda + C_4 \frac{\lambda}{L}\sinh\lambda =$$

$$c_M EJ_y\left(- C_1 \left(\frac{\lambda}{L}\right)^2 \cos\lambda - C_2 \left(\frac{\lambda}{L}\right)^2 \sin\lambda + C_3 \left(\frac{\lambda}{L}\right)^2 \sinh\lambda + C_4 \left(\frac{\lambda}{L}\right)^2 \cosh\lambda\right)$$

$$\Rightarrow$$

$$- C_1 \sin\lambda + C_2 \cos\lambda + C_3 \cosh\lambda + C_4 \sinh\lambda =$$
$$\beta\left(- C_1 \cos\lambda - C_2 \sin\lambda + C_3 \sinh\lambda + C_4 \cosh\lambda\right)$$

$$\Rightarrow$$

$- C_1 \sin\lambda + C_2 \cos\lambda + C_3\cosh\lambda + C_4 \sinh\lambda - (- C_1 \beta\cos\lambda - C_2 \beta\sin\lambda + C_3\beta \sinh\lambda + C_4\beta\cosh\lambda) = 0$

$\Rightarrow$

$- C_1\sin\lambda + C_1\beta\cos\lambda + C_2\cos\lambda + C_2\beta\sin\lambda + C_3\cosh\lambda - C_3\beta \sinh\lambda + C_4 \sinh\lambda - C_4\beta\cosh\lambda = 0$

$\Rightarrow$

$$\boxed{C_1(-\sin\lambda+\beta\cos\lambda)+C_2(\cos\lambda+\beta\sin\lambda)+C_3(\cosh\lambda-\beta\sinh\lambda)+C_4(\sinh\lambda-\beta\cosh\lambda)= 0}$$

Thus $\mathbf{A}\cdot \mathbf{C} = \mathbf{0}$ with ([2.20] and [2.21]):

$$\mathbf{A} = \begin{pmatrix} 1 & \alpha & -\alpha & 1 \\ -\beta & 1 & 1 & -\beta \\ (\cos\lambda-\alpha\sin\lambda) & (\sin\lambda+\alpha\cos\lambda) & (\sinh\lambda-\alpha\cosh\lambda) & (\cosh\lambda-\alpha \sinh\lambda) \\ (-\sin\lambda+\beta\cos\lambda) & (\cos\lambda+\beta\sin\lambda) & (\cosh\lambda-\beta\sinh\lambda) & (\sinh\lambda-\beta\cosh\lambda) \end{pmatrix}$$

$$\mathbf{C} = \begin{pmatrix} C_1 \\ C_2 \\ C_3 \\ C_4 \end{pmatrix}$$

q.e.d.

Appendix D

Boundary condition for a mass beam system: Rigid clamping

For unelastic clamping we have at the side of the frame the same conditions as in Appendix 2.3.A , thus:

I: $\boxed{C_1 + C_4 = 0}$

II: $\boxed{C_2 + C_3 = 0}$

For the boundary condition at the side of the mass we deduce from [2.23]:

$$\text{III: } C_1\left(\frac{\lambda}{L}\right)^3 \sin\frac{\lambda}{L}L - C_2\left(\frac{\lambda}{L}\right)^3 \cos\frac{\lambda}{L}L + C_3\left(\frac{\lambda}{L}\right)^3 \cosh\frac{\lambda}{L}L + C_4\left(\frac{\lambda}{L}\right)^3 \sinh\frac{\lambda}{L}L =$$

$$-\frac{M}{2\mu}\{C_1\left(\frac{\lambda}{L}\right)^4 \cos\frac{\lambda}{L}L + C_2\left(\frac{\lambda}{L}\right)^4 \sin\frac{\lambda}{L}L + C_3\left(\frac{\lambda}{L}\right)^4 \sinh\frac{\lambda}{L}L + C_4\left(\frac{\lambda}{L}\right)^4 \cosh\frac{\lambda}{L}L\}$$

$\Rightarrow$

$$C_1\sin\lambda - C_2\cos\lambda + C_3\cosh\lambda + C_4\sinh\lambda =$$
$$-\frac{M\lambda}{2\mu L}\{C_1\cos\lambda + C_2\sin\lambda + C_3\sinh\lambda + C_4\cosh\lambda\}$$

using I and II we have:

$$C_1\sin\lambda - C_2\cos\lambda - C_2\cosh\lambda - C_1\sinh\lambda =$$
$$-\frac{M\lambda}{2\mu L}\{C_1\cos\lambda + C_2\sin\lambda - C_2\sinh\lambda - C_1\cosh\lambda\}$$

$\Rightarrow$

$$C_1\left(\sin\lambda + \frac{M\lambda}{2\mu L}\cos\lambda - \sinh\lambda - \frac{M\lambda}{2\mu L}\cosh\lambda\right)$$
$$+C_2\left(\frac{M\lambda}{2\mu L}\sin\lambda - \frac{M\lambda}{2\mu L}\sinh\lambda - \cos\lambda - \cosh\lambda\right) = 0$$

and IV (from below [2.23]):

$$-C_1\frac{\lambda}{L}\sin\lambda + C_2\frac{\lambda}{L}\cos\lambda + C_3\frac{\lambda}{L}\cosh\lambda + C_4\frac{\lambda}{L}\sinh\lambda = 0$$

using I and II:

$$\text{IV: } -C_1\frac{\lambda}{L}\sin\lambda - C_1\frac{\lambda}{L}\sinh\lambda + C_2\frac{\lambda}{L}\cos\lambda - C_2\frac{\lambda}{L}\cosh\lambda = 0$$

$$\Rightarrow \boxed{C_1(-\sin\lambda - \sinh\lambda) + C_2\left(\cos\lambda - \cosh\lambda\right) = 0}$$

as in the simple case.

and again $\mathbf{A}\cdot\mathbf{C} = \mathbf{0}$ with ([2.24]):

$$\mathbf{A} := \begin{pmatrix} (\sin\lambda-\sinh\lambda)-\frac{M\lambda}{2\mu L}(\cosh\lambda-\cos\lambda) & -(\cos\lambda+\cosh\lambda)-\frac{M\lambda}{2\mu L}(\sinh\lambda-\sin\lambda) \\ -(\sin\lambda+\sinh\lambda) & (\cos\lambda-\cosh\lambda) \end{pmatrix}$$

$$\mathbf{C} := \begin{pmatrix} C_1 \\ C_2 \end{pmatrix}$$

has a non trivial solution $\Leftrightarrow \det \mathbf{A} = 0$

$\Leftrightarrow$

$$(\cos\lambda-\cosh\lambda)(\sin\lambda-\sinh\lambda)-\frac{M\lambda}{2\mu L}(\cosh\lambda-\cos\lambda)(\cos\lambda-\cosh\lambda)-(\cos\lambda+\cosh\lambda)$$

$$(\sin\lambda+\sinh\lambda) - \frac{M\lambda}{2\mu L}(\sinh\lambda-\sin\lambda)(\sin\lambda+\sinh\lambda) = 0$$

$\Rightarrow$

$$2(\cos\lambda\sinh\lambda+\cosh\lambda\sin\lambda) +$$

$$\frac{M\lambda}{2\mu L}\Big((\cosh\lambda-\cos\lambda)(\cos\lambda-\cosh\lambda)+(\sinh\lambda-\sin\lambda)(\sin\lambda+\sinh\lambda)\Big)=0$$

$\Rightarrow$

$$2(\cos\lambda\sinh\lambda+\cosh\lambda\sin\lambda) +$$

$$\frac{M\lambda}{2\mu L}\{\cosh\lambda(\cos\lambda-\cosh\lambda)-\cos\lambda(\cos\lambda-\cosh\lambda)+\sinh\lambda(\sin\lambda+\sinh\lambda)-$$

$$-\sin\lambda(\sin\lambda+\sinh\lambda)\}=0$$

$\Rightarrow$

$$2(\cos\lambda\sinh\lambda+\cosh\lambda\sin\lambda)+\frac{M\lambda}{2\mu L}\{\cosh\lambda\cos\lambda-\cosh\lambda\cosh\lambda-$$

$$\cos\lambda\cos\lambda+\cos\lambda\cosh\lambda+\sinh\lambda\sin\lambda+\sinh\lambda\sinh\lambda-\sin\lambda\sin\lambda-\sin\lambda\sinh\lambda\}=0$$

$$\Rightarrow 2(\cos\lambda\sinh\lambda+\cosh\lambda\sin\lambda) +\frac{M\lambda}{2\mu L}\{-1-1+2\cos\lambda\cosh\lambda\}=0$$

$$\Rightarrow 2(\cos\lambda\sinh\lambda+\cosh\lambda\sin\lambda) -\frac{M\lambda}{\mu L}\{1-\cos\lambda\cosh\lambda\}=0$$

$$\Rightarrow \boxed{\frac{\mu L}{M} = \frac{\lambda}{2}\,\frac{\{1-\cos\lambda\cosh\lambda\}}{(\cos\lambda\sinh\lambda+\cosh\lambda\sin\lambda)}} \qquad [2.25]$$

When the clamping is elastic at the side of the frame these conditions change and we have for the system of boundary conditions ([2.26]):

I	$w(0,t)$	$= c_F \lvert F(0)\rvert$	$= c_F EJ_y \lvert w'''(0,t)\rvert$
II	$w'(0,t)$	$= c_M \lvert M(0)\rvert$	$= c_M EJ_y \lvert w''(0,t)\rvert$
III	$F(L)$	$= EJ_y\ w'''(L,t)$	$= -\frac{M}{2}\ddot{w} = -\frac{M}{2}\left(\frac{EJ_y}{\mu}w''''(L,t)\right)$
IV:	$w'(a,t)$	$= 0$	

where M is the total mass of the mesa.

The first two boundary condition are the same as in Appendix 2.3.B and can be directly taken from there:

$$\text{I} \Rightarrow \boxed{C_1 + \alpha C_2 - \alpha C_3 + C_4 = 0}$$

$$\textbf{II} \Rightarrow \boxed{-\beta C_1 + C_2 + C_3 - \beta C_4 = 0}$$

The boundary conditions III and IV are the same as above and are thus

III:

$$C_1\sin\lambda - C_2\cos\lambda + C_3\cosh\lambda + C_4\sinh\lambda$$

$$\frac{M\lambda}{2\mu L}\{C_1\cos\lambda + C_2\sin\lambda + C_3\sinh\lambda + C_4\cosh\lambda\} = 0$$

$$C_1(\sin\lambda + \frac{M\lambda}{2\mu l}\cos\lambda) - C_2(\cos\lambda + \frac{M\lambda}{2\mu L}\sin\lambda)$$

$$+ C_3(\cosh\lambda + \frac{M\lambda}{2\mu L}\sinh\lambda) + C_4(\sinh\lambda + \frac{M\lambda}{2\mu L}\cosh\lambda) = 0$$

and IV:

$$-C_1\sin\lambda + C_2\cos\lambda + C_3\cosh\lambda + C_4\sinh\lambda = 0$$

The four equation form again a system of linear homogeneus equations **A** $\cdot$ **C** = **0** with ([2.28])

$$\mathbf{A} := \begin{pmatrix} 1 & \alpha & -\alpha & 1 \\ -\beta & 1 & 1 & -\beta \\ (\sin\lambda + \frac{M\lambda}{2\mu L}\cos\lambda) & -(\cos\lambda + \frac{M\lambda}{2\mu L}\sin\lambda) & (\cosh\lambda + \frac{M\lambda}{2\mu L}\sinh\lambda) & (\sinh\lambda + \frac{M\lambda}{2\mu L}\cosh\lambda) \\ -\sin\lambda & \cos\lambda & \cosh\lambda & \sinh\lambda \end{pmatrix}$$

q.e.d.

<u>Calculation of Γ of a mass beam system in the case of rigid clamping:</u>

$$A = \begin{pmatrix} (\sin\lambda-\sinh\lambda)-\frac{M\lambda}{2\mu L}(\cosh\lambda-\cos\lambda) & -(\cos\lambda+\cosh\lambda)-\frac{M\lambda}{2\mu L}(\sinh\lambda-\sin\lambda) \\ -(\sin\lambda+\sinh\lambda) & (\cos\lambda-\cosh\lambda) \end{pmatrix}$$

[2.24]

because the two equations respresented by **A** are by definition linearly dependent we can select either of the two rows the find the ratio of the two coeficicnts C_1 and C_2. Thus we find from the last row $\Gamma := \frac{(\sin\lambda + \sinh\lambda)}{(\cos\lambda-\cosh\lambda)}$ as in the case of a simple beam (only the λ s are different of course).

Appendix E

Boundary conditions for the case of a simply supported mass

In the case of a simply supported mass, the mass rotates and we have instead of equation of [2.26] IV [2]:

$$\text{IV:} \qquad M(L) = EJ_y\, w''(L,t) = \Theta_o \frac{\partial^2 w'(L,t)}{\partial t^2} \qquad [2.29]$$

Θ_o = the inertial moment of the proof mass.

Noting, that the second derivative with respect to time correspond to a multiplication by ω^2 and with the abbreviation :

$$\gamma = \frac{\Theta_o\, \omega^2}{EJ_y} \qquad [2.30]$$

we can write the boundary condition IV as

$X''(L) = \gamma X'(L)$

$\Leftrightarrow$

$$-C_1\left(\frac{\lambda}{L}\right)^2 \cos\frac{\lambda}{L}L - C_2\left(\frac{\lambda}{L}\right)^2 \sin\frac{\lambda}{L}L + C_3\left(\frac{\lambda}{L}\right)^2 \sinh\frac{\lambda}{L}L + C_4\left(\frac{\lambda}{L}\right)^2 \cosh\frac{\lambda}{L}L$$
$$=\gamma\left(-C_1\frac{\lambda}{L}\sin\frac{\lambda}{L}L + C_2\frac{\lambda}{L}\cos\frac{\lambda}{L}L + C_3\frac{\lambda}{L}\cosh\frac{\lambda}{L}L + C_4\frac{\lambda}{L}\sinh\frac{\lambda}{L}L\right)$$

$\Leftrightarrow$

$$-C_1\left(\frac{\lambda}{L}\right)\cos\lambda - C_2\left(\frac{\lambda}{L}\right)\sin\lambda + C_3\left(\frac{\lambda}{L}\right)\sinh\lambda + C_4\left(\frac{\lambda}{L}\right)\cosh\lambda$$
$$=\gamma\left(-C_1\sin\lambda + C_2\cos\lambda + C_3\cosh\lambda + C_4\sinh\lambda\right)$$

$\Leftrightarrow$

$$-C_1\left(\frac{\lambda}{L}\right)\cos\lambda - C_2\left(\frac{\lambda}{L}\right)\sin\lambda + C_3\left(\frac{\lambda}{L}\right)\sinh\lambda + C_4\left(\frac{\lambda}{L}\right)\cosh\lambda$$
$$+ C_1\gamma\sin\lambda - C_2\gamma\cos\lambda - C_3\gamma\cosh\lambda - C_4\gamma\sinh\lambda = 0$$

$\Leftrightarrow$

$$+ C_1\left(\gamma\sin\lambda - \left(\frac{\lambda}{L}\right)\cos\lambda\right) - C_2\left(\left(\frac{\lambda}{L}\right)\sin\lambda - \gamma\cos\lambda\right)$$

2 Lee, T.W.; 1973 Journal of applied Mechanics 38. p. 813.815 Vibration frequencies for a uniform beam with one end spring-hinged and carrying a mass at the other free end.

$$- C_3\left(\gamma\cosh\lambda + \left(\frac{\lambda}{L}\right)\sinh\lambda\right) + C_4\left(\left(\frac{\lambda}{L}\right)\cosh\lambda - \gamma\sinh\lambda\right) = 0$$

Thus by replacing the last row in the matrix for the doubly supported mass with elastic clamping and taking the full proof mass instead of the half as in the doubly supported mass we have ([2.31])

$$A = \begin{pmatrix} 1 & \alpha & -\alpha & 1 \\ -\beta & 1 & 1 & -\beta \\ (\sin\lambda + \frac{M\lambda}{\mu L}\cos\lambda) & -(\cos\lambda + \frac{M\lambda}{\mu L}\sin\lambda) & (\cosh\lambda + \frac{M\lambda}{\mu L}\sinh\lambda) & (\sinh\lambda + \frac{M\lambda}{\mu L}\cosh\lambda) \\ \left(\gamma\sin\lambda - \frac{\lambda}{L}\cos\lambda\right) & \left(\gamma\cos\lambda - \frac{\lambda}{L}\sin\lambda\right) & -\left(\gamma\cosh\lambda + \frac{\lambda}{L}\sinh\lambda\right) & \left(\frac{\lambda}{L}\cosh\lambda - \gamma\sinh\lambda\right) \end{pmatrix}$$

<u>The calculation of Γ in the case of rigid clamping:</u>

In this ($\alpha,\beta = 0$) case [2.31] becomes a 2x2 matrix:

$$A := \begin{pmatrix} \left(\sin\lambda + \frac{M\lambda}{\mu L}\cos\lambda - \sinh\lambda - \frac{M\lambda}{\mu L}\cosh\lambda\right) & \left(-\cos\lambda - \frac{M\lambda}{\mu L}\sin\lambda - \cosh\lambda - \frac{M\lambda}{\mu L}\sinh\lambda\right) \\ \left(\gamma\sin\lambda - \frac{\lambda}{L}\cos\lambda - \frac{\lambda}{L}\cosh\lambda + \gamma\sinh\lambda\right) & \left(\gamma\cos\lambda - \frac{\lambda}{L}\sin\lambda + \gamma\cosh\lambda + \frac{\lambda}{L}\sinh\lambda\right) \end{pmatrix}$$

and thus

$$\Gamma = \frac{A_{11}}{A_{12}} = \frac{A_{21}}{A_{22}}$$

$$= \frac{\left(\sin\lambda + \frac{M\lambda}{\mu L}\cos\lambda - \sinh\lambda - \frac{M\lambda}{\mu L}\cosh\lambda\right)}{\left(-\cos\lambda - \frac{M\lambda}{\mu L}\sin\lambda - \cosh\lambda - \frac{M\lambda}{\mu L}\sinh\lambda\right)} = \frac{\left(\gamma\sin\lambda - \frac{\lambda}{L}\cos\lambda - \frac{\lambda}{L}\cosh\lambda + \gamma\sinh\lambda\right)}{\left(\gamma\cos\lambda - \frac{\lambda}{L}\sin\lambda + \gamma\cosh\lambda + \frac{\lambda}{L}\sinh\lambda\right)} \quad [2.59]$$

Appendix F

The resonance frequency of the mass beam system in case of a torsional mode

The torsional eigenfrequency of a mass beam system was calculated in section 2.3. to be:

$$\boxed{f_1 = \frac{1}{2\pi}\sqrt{\frac{J_t}{\Theta_{bar}\, L}\left(\frac{3\kappa}{3+\kappa}\right)}}$$

[2.42]

This is aequivalent to

$$\omega = \sqrt{\frac{3}{L(3\Theta_o + L\Theta)}\, G\, J_t}$$

Fig. A.1. Figure of the mass beam system to be calculated

The static torsional moment of inertia for a rectangular beam is [3]

$$J_t = \frac{5}{18} h^3 b \qquad [2.43]$$

The dynamical moment of inertia of a parallelepiped with respect to its CM is

$$\Theta = \frac{\rho}{12}\, b\, h\, (b^2 + h^2)$$

3 Szabo, I.; Höhere Technische Mechanik, Springer, Berlin, 5th ed., 1977, p. 283

With the theorem of Steiner with s as the distance between CM and the axes of rotation the dynamical moment of inertia becomes

$$\Theta_0 = \Theta_{CM} + Ms^2 = M\left(\left(\frac{c^2+d^2}{12}\right) + \left(\frac{d}{2}-\frac{h}{2}\right)^2\right) = \rho\, c\, d\, a\left(\left(\frac{c^2+d^2}{12}\right) + \left(\frac{d}{2}-\frac{h}{2}\right)^2\right)$$

Thus the torsional resonance frequency can be written as

$$\omega = \sqrt{\frac{3}{L\left(3\rho\; c\; d\; a\left(\left(\frac{c^2+d^2}{12}\right) + \left(\frac{d}{2}-\frac{h}{2}\right)^2\right) + L\frac{\rho}{12} b\; h\; (b^2+h^2)\right)} G\, \frac{5}{18} h^3 b}$$

$$\omega = \sqrt{\frac{5G\; h^3 b}{16\left(3\rho\; c\; d\; a\left(\left(\frac{c^2+d^2}{12}\right) + \left(\frac{d}{2}-\frac{h}{2}\right)^2\right) + l\frac{\rho}{12} b\; h\; (b^2+h^2)\right)}}$$

$$\omega = \sqrt{\frac{5G\; h^3 b}{L\; \rho\left(3\; c\; d\; a\left(\left(\frac{c^2+d^2}{2}\right) + \frac{3}{2}(d-h)^2\right) + \frac{L}{2} b\; h\; (b^2+h^2)\right)}}$$

thus for our mass beam system we have:

$$\boxed{\omega = \sqrt{\frac{10\; G\; h^3 b}{L\; \rho\,(3cda(c^2+d^2+3(d-h)^2)+Lbh(b^2+h^2))}}}$$

Appendix G

The energy of a mass-beam system

The amplitude is known (measured) in the middle of the beam. [2.14] together with [2.15] and [2.16] defines then the deformation of the beam. The elastic energy in the beam is generally

$$U = \frac{EJ}{2}\int_0^l X''^2 dx \qquad [2.53]$$

From appendix B we have for the second derivative of a beam with homogeneus boundary conditions at at least one side

$$X''(x) = -\left(\frac{\lambda}{L}\right)^2 C_1\left((\cos\frac{\lambda}{L}x + \cosh\frac{\lambda}{L}x) + \Gamma\ (\sin\frac{\lambda}{L}x + \sinh\frac{\lambda}{L}x)\right)$$

Thus $X''^2(x) = \left(\frac{\lambda}{L}\right)^4 C_1^2 A^2$ with the abbreviation

$$A = \left((\cos\frac{\lambda}{L}x + \cosh\frac{\lambda}{L}x) + \Gamma\ (\sin\frac{\lambda}{L}x + \sinh\frac{\lambda}{L}x)\right)$$

Thus we have to calculate the following integral

$$\int_0^L X''^2 dx = \int_0^L \left(\frac{\lambda}{L}\right)^4 C_1^2 A^2 = \left(\frac{\lambda}{L}\right)^4 C_1^2 \int_0^L A^2$$

Where

$$A^2 = (\cos\frac{\lambda}{L}x + \cosh\frac{\Lambda}{L}x)^2 + 2\left((\cos\frac{\lambda}{L}x + \cosh\frac{\lambda}{L}x)\ \Gamma(\sin\frac{\lambda}{L}x + \sinh\frac{\lambda}{L}x)\right) +$$
$$\Gamma^2(\sin\frac{\lambda}{L}x + \sinh\frac{\lambda}{L}x)^2$$

$$= (\cos\frac{\lambda}{L}x)^2 + (\cosh\frac{\lambda}{L}x)^2 + 2(\cos\frac{\lambda}{L}x)(\cosh\frac{\lambda}{L}x)$$
$$+2\Gamma\left((\cos\frac{\lambda}{L}x)(\sin\frac{\lambda}{L}x) + (\cosh\frac{\lambda}{L}x)(\sin\frac{\lambda}{L}x) + (\cos\frac{\lambda}{L}x)(\sinh\frac{\lambda}{L}x) + (\cosh\frac{\lambda}{L}x)\ (\sinh\frac{\lambda}{L}x)\right) +$$
$$\Gamma^2\left((\sin\frac{\lambda}{L}x)^2 + 2(\sin\frac{\lambda}{L}x)(\sinh\frac{\lambda}{L}x) + (\sinh\frac{\lambda}{L}x)^2\right)$$

To calcultate this rather long-winded integral we are utilizing the following table (G.l) where on the left side we have written the term to be integreted and at the rigth side we wrote the undefinit integral. The coeficients are not repeted but a Paranthese of the type { starts and ends } the terms to whose the factor has to be added. This technique allows to gather after to calculation all the terms and to produce one singular formula.

Table G.I Integrand and Integral

nr	A^2	$\int A^2$
1.	$(\cos\frac{\lambda}{L}x)^2$	$\frac{1}{2}x + \frac{L}{4\lambda}\sin 2\frac{\lambda}{L}x$
2.	$+(\cosh\frac{\lambda}{L}x)^2$	$+\frac{1}{2}x + \frac{L}{2\lambda}(\cosh\frac{\lambda}{L}x)(\sinh\frac{\lambda}{L}x)$
3.	$+2(\cos\frac{\lambda}{L}x)(\cosh\frac{\lambda}{L}x)$	$+2\frac{L}{2\lambda}[(\cos\frac{\lambda}{L}x)(\sinh\frac{\lambda}{L}x)+(\cosh\frac{\lambda}{L}x)(\sin\frac{\lambda}{L}x)]$
4.	$+2\Gamma\{(\cos\frac{\lambda}{L}x)(\sin\frac{\lambda}{L}x)$	$+2\Gamma\{\frac{1}{2\lambda}(\sin\frac{\lambda}{L}x)^2$
5.	$+(\cosh\frac{\lambda}{L}x)(\sin\frac{\lambda}{L}x)$	$+\frac{L}{2\lambda}[(\sin\frac{\lambda}{L}x)(\sinh\frac{\lambda}{L}x) - (\cos\frac{\lambda}{L}x)(\cosh\frac{\lambda}{L}x)]$
6.	$+(\cos\frac{\lambda}{L}x)(\sinh\frac{\lambda}{L}x)$	$+\frac{L}{2\lambda}[(\sin\frac{\lambda}{L}x)(\sinh\frac{\lambda}{L}x) + (\cos\frac{\lambda}{L}x)(\cosh\frac{\lambda}{L}x)]$
7.	$+(\cosh\frac{\lambda}{L}x)(\sinh\frac{\lambda}{L}x)\}$	$+\frac{1}{2\lambda}(\sinh\frac{\lambda}{L}x)^2]$
8.	$+\Gamma^2\{(\sin\frac{\lambda}{L}x)^2$	$+\Gamma^2\{\frac{1}{2}x - \frac{L}{4\lambda}\sin 2\frac{\lambda}{L}x$
9.	$+2(\sin\frac{\lambda}{L}x)(\sinh\frac{\lambda}{L}x)$	$+2\frac{L}{2\lambda}[(\cosh\frac{\lambda}{L}x)(\sin\frac{\lambda}{L}x) - (\cos\frac{\lambda}{L}x)(\sinh\frac{\lambda}{L}x)]$
10.	$(\sinh\frac{\lambda}{L}x)^2\}$	$+\frac{L}{2\lambda}(\cosh\frac{\lambda}{L}x)(\sinh\frac{\lambda}{L}x) - \frac{1}{2}x\}$

Table G.II. Integral at the boundaries

nr	at x= 0	at x= L
1.	0	$\frac{L}{2}+\frac{L}{4\lambda}\sin 2\lambda$
2.	0	$+\frac{L}{2}+\frac{L}{2\lambda}(\cosh\lambda)(\sinh\lambda)$
3.	0	$+\frac{L}{\lambda}[(\cos\lambda)(\sinh\lambda)+(\cosh\lambda)(\sin\lambda)]$
4.	0	$+2\Gamma\{\frac{L}{2\lambda}(\sin\lambda)^2$
5.	$+\frac{L}{2\lambda}[-1]$	$+\frac{L}{2\lambda}[(\sin\lambda)(\sinh\lambda)-(\cos\lambda)(\cosh\lambda)]$
6.	$+\frac{L}{2\lambda}[1]$	$+\frac{L}{2\lambda}[(\sin\lambda)(\sinh\lambda)+(\cos\lambda)(\cosh\lambda)]$
7.	0	$+\frac{L}{2\lambda}(\sinh\lambda)^2\}$
8.	0	$+\Gamma^2\{\frac{L}{2}-\frac{L}{4\lambda}\sin 2\lambda$
9.	0	$+\frac{L}{\lambda}[(\cosh\lambda)(\sin\lambda)-(\cos\lambda)(\sinh\lambda)]$
10.	0	$+\frac{L}{2\lambda}(\cosh\lambda)(\sinh\lambda)-\frac{L}{2}\}$

The only two terms which are nonzero in the first column of table G.II. cancels so we have to sum only over the second column. Thus the value of the definite integral $\int_0^1 A^2$ equals the following expression

$$\boxed{\begin{aligned}&\frac{L}{2}+\frac{L}{4\lambda}\sin 2\lambda+\frac{L}{2}+\frac{L}{2\lambda}(\cosh\lambda)(\sinh\lambda)+\frac{L}{\lambda}[(\cos\lambda)(\sinh\lambda)+(\cosh\lambda)(\sin\lambda)]\\&+2\Gamma\{\frac{L}{2\lambda}(\sin\lambda)^2+\frac{L}{2\lambda}[(\sin\lambda)(\sinh\lambda)-(\cos\lambda)(\cosh\lambda)]+\\&+\frac{L}{2\lambda}[(\sin\lambda)(\sinh\lambda)+(\cos\lambda)(\cosh\lambda)]+\frac{L}{2\lambda}(\sinh\lambda)^2\}+\\&+\Gamma^2\{\frac{L}{2}-\frac{L}{4\lambda}\sin 2\lambda+\frac{L}{\lambda}[(\cosh\lambda)(\sin\lambda)-(\cos\lambda)(\sinh\lambda)]+\frac{L}{2\lambda}(\cosh\lambda)(\sinh\lambda)-\frac{L}{2}\}\end{aligned}}$$

which can be simplified to :

$$\boxed{\begin{aligned}&L+\frac{L}{4\lambda}\sin 2\lambda+\frac{L}{2\lambda}(\cosh\lambda)(\sinh\lambda)+\frac{L}{\lambda}[(\cos\lambda)(\sinh\lambda)+(\cosh\lambda)(\sin\lambda)]\\&+\frac{\Gamma L}{\lambda}\{(\sin\lambda)+(\sinh\lambda)\}^2+\\&+\frac{\Gamma^2 L}{\lambda}\{-\frac{1}{4}\sin 2\lambda+(\cosh\lambda)(\sin\lambda)-(\cos\lambda)(\sinh\lambda)+\frac{1}{2}(\cosh\lambda)(\sinh\lambda)\}\end{aligned}}$$

or

$$\boxed{\begin{aligned}&L+\frac{\Gamma L}{\lambda}\{(\sin\lambda)+(\sinh\lambda)\}^2+\\&\frac{L}{\lambda}\{[\frac{1}{4}\sin 2\lambda+(\cos\lambda)(\sinh\lambda)](1-\Gamma^2)+(\cosh\lambda)(\sin\lambda)(1+\Gamma^2)+(\Gamma^2+1)\frac{1}{2}(\cosh\lambda)(\sinh\lambda)\}\end{aligned}}$$

and finally [2.58]:

$$\boxed{L(1+\frac{\Gamma}{\lambda}[\sin\lambda+\sinh\lambda]^2+\frac{L}{\lambda}\{[\frac{\sin\lambda}{2}+\sinh\lambda]\cos\lambda(1-\Gamma^2)+(1+\Gamma^2)\cosh\lambda[(\sin\lambda+\frac{\sinh\lambda}{2}]\})}$$

q.e.d.

Appendix H

Proof that W(r,s) can be represented as a fraction of two polynominals

The calculations in section 2.4. delivered the following expression for the explicit solution in the Laplace space (variable s):

$$\boxed{W(r,s) = -\sum_i^{\infty} Y_i \chi_i \phi_i(r) + Z(s) \frac{\sum_i^{\infty} Y_i \chi_i \phi_i(r_1)}{1 + Z(s) \sum_i^{\infty} Y_i \phi_i^2(r_1)} \sum_k^{\infty} Y_k \; \phi_k(r_1) \, \phi_k(r)} \qquad [2.95]$$

For the back transformation we have to bring it into a form of a fraction of two polynoms, because then standard transfromations are known. We replace first the abreviated functions of s by its explicit form . Then we write the expression for W as a sum of two terms.

$W = A + B$

with

$$A := -\sum_i^{\infty} Y_i \chi_i \phi_i(r)$$

as a rather simple term containing mainly the initial conditions

and

$$B = +Z(s) \frac{\sum_i^{\infty} Y_i \chi_i \phi_i(r_1)}{1 + Z(s) \sum_i^{\infty} Y_i \phi_i^2(r_1)} \sum_k^{\infty} Y_k \phi_k(r) \, \phi_k(r_1)$$

which has to be worked out further:

$$B = + Z(s) \frac{\displaystyle\sum_{i}^{\infty} \frac{\chi_i \, \phi_i(r_1)}{\psi_i}}{1 + Z(s) \displaystyle\sum_{i}^{\infty} \frac{\phi_i^2(r_1)}{\psi_i}} \sum_{k}^{\infty} \frac{\phi_k(r) \, \phi_k(r_1)}{\psi_k}$$

$$B = + Z(s) \frac{\displaystyle\sum_{i}^{\infty} \frac{\chi_i \, \phi_i(r_1)}{\psi_i} \sum_{k}^{\infty} \frac{\phi_k(r) \, \phi_k(r_1)}{\psi_k}}{1 + Z(s) \displaystyle\sum_{i}^{\infty} \frac{\phi_i^2(r_1)}{\psi_i}}$$

$$B = + Z(s) \frac{\displaystyle\sum_{(i,k)}^{\infty} \frac{\chi_i \;\; \phi_i(r_1)}{\psi_i} \; \frac{\phi_k(r) \;\; \phi_k(r_1)}{\psi_k}}{1 + \; Z(s) \displaystyle\sum_{i}^{\infty} \frac{\phi_i^2(r_1)}{\psi_i}}$$

$$B = + Z(s) \frac{\displaystyle\sum_{(i,k)}^{\infty} \frac{\chi_i \;\; \phi_i(r_1)}{\psi_i} \; \frac{\phi_k(r) \;\; \phi_k(r_1)}{\psi_k} \; \frac{\displaystyle\prod_{(j,h)}^{\infty} \psi_j \;\; \psi_h}{\displaystyle\prod_{(j,h)}^{\infty} \psi_j \;\; \psi_h}}{1 + \; Z(s) \displaystyle\sum_{i}^{\infty} \frac{\phi_i^2(r_1)}{\psi_i} \; \frac{\displaystyle\prod_{k}^{\infty} \psi_k}{\displaystyle\prod_{k}^{\infty} \psi_k}}$$

$$B = \frac{\dfrac{Z(s)}{\prod\limits_{(j,h)}^{\infty}\psi_j\ \psi_h}\sum\limits_{(i,k)}^{\infty}\chi_i\ \phi_i(r_1)\phi_k(r)\ \phi_k(r_1)\psi_k\prod\limits_{(j\neq i,h\neq k)}^{\infty}\psi_j\ \psi_h}{1+\dfrac{Z(s)}{\prod\limits_{k}^{\infty}\psi_k}\sum\limits_{i}^{\infty}\phi_i^2(r_1)\prod\limits_{k\neq i}^{\infty}\psi_k}$$

$$\boxed{B = \frac{Z(s)\sum\limits_{(i,k)}^{\infty}\chi_i\ \phi_i(r_1)\,\phi_k(r_1)\,\phi_k(r)\prod\limits_{(j\neq i,h\neq k)}^{\infty}\psi_j\ \psi_h}{\prod\limits_{(i,k)}^{\infty}\psi_i\ \psi_k+Z(s)\prod\limits_{k}^{\infty}\psi_k\sum\limits_{i}^{\infty}\chi_i\ \phi_i^2(r_1)\prod\limits_{j\neq i}^{\infty}\psi_j}}$$

Thus we have for B a fraction of two polynoms in s which can in priciple be transformad back to the original space.

Appendix I

Some Properties of Silicon

The data given herafter are taken mostly from Properties of silicon[1]

1.General theory of elasticity[2]

The general relation between stress ${}^2\sigma$ and strain ${}^2\varepsilon$ are in the linear approximation as follows (Hook's law):

$${}^2\varepsilon = {}^4S:{}^2\sigma$$

$${}^2\sigma = {}^4C:{}^2\varepsilon$$

where ${}^4S$ is called the tensor of the modulus of elasticity and ${}^4C$ the tensor of the compliance Between ${}^4S$ and ${}^4C$ the following equation holds

$${}^4S:{}^4C = {}^4\mathbf{1}$$

Because the coefficients are not all independet one uses normally a simplified notation defined as follows

$$C_{ijkl} = c_{\mu\nu}, \qquad \mu,\nu = \begin{cases} i\ k & i\ k = j\ l \\ 9-(i+j) & \\ & i\ k \neq j\ l \\ 9-(k+l) & \end{cases}$$

$$S_{ijkl} = \frac{s_{\mu\nu}}{(2-\delta_{ij})\,(2-\delta_{kl})} \qquad \delta_{mn} = \begin{cases} 1 & m = n \\ 0 & m \neq n \end{cases}$$

$$\varepsilon_{ij} = \frac{\varepsilon_\lambda}{2-\delta_{ij}} \qquad (i, j = 1, 2, 3)$$

$$\sigma_{ij} = \sigma_\lambda \qquad (i, j = 1, 2, 3;\ \lambda = 1, 2, \ldots, 6)$$

For a crystal with a cubic symmetry this reduces further to

$$s_{\mu\nu} = \begin{pmatrix} s_{11} & s_{12} & s_{12} & 0 & 0 & 0 \\ s_{12} & s_{11} & s_{12} & 0 & 0 & 0 \\ s_{12} & s_{12} & s_{11} & 0 & 0 & 0 \\ 0 & 0 & 0 & s_{44} & 0 & 0 \\ 0 & 0 & 0 & 0 & s_{44} & 0 \\ 0 & 0 & 0 & 0 & 0 & s_{44} \end{pmatrix}$$

for Si

$s_{11} = \ 0.7691 \cdot 10^{-11}\ \mathrm{Pa}^{-1}$

$s_{12} = -0.2142 \cdot 10^{-11}\ \mathrm{Pa}^{-1}$
$s_{44} = 1.2577 \cdot 10^{-11}\ \mathrm{Pa}^{-1}$
and

$$c_{\mu\nu} = \begin{pmatrix} c_{11} & c_{12} & c_{12} & 0 & 0 & 0 \\ c_{12} & c_{11} & c_{12} & 0 & 0 & 0 \\ c_{12} & c_{12} & c_{11} & 0 & 0 & 0 \\ 0 & 0 & 0 & c_{44} & 0 & 0 \\ 0 & 0 & 0 & 0 & c_{44} & 0 \\ 0 & 0 & 0 & 0 & 0 & c_{44} \end{pmatrix}$$

For Si

$c_{11} = 1.6564 \cdot 10^{11}\ \mathrm{Pa}$
$c_{12} = 0.6394 \cdot 10^{11}\ \mathrm{Pa}$
$c_{44} = 0.7951 \cdot 10^{11}\ \mathrm{Pa}$
Where modulus and complience coeffients are related by

$$c_{11} + 2c_{12} = \frac{1}{s_{11} + 2s_{12}}$$

$$c_{11} - c_{12} = \frac{1}{s_{11} - s_{12}}$$

$$c_{44} = \frac{1}{s_{44}}$$

therefore for the other matrix elements:

$$c_{12} = \frac{1}{3}\left(\frac{1}{s_{11} + 2s_{12}} - \frac{1}{s_{11} - s_{12}} \right)$$

$$c_{11} = \frac{1}{s_{11} - s_{12}} - \frac{1}{3}\left(\frac{1}{s_{11} + 2s_{12}} - \frac{1}{s_{11} - s_{12}} \right)$$

and vice versa

$$s_{44} = \frac{1}{c_{44}}$$

$$s_{12} = \frac{1}{3}\left(\frac{1}{c_{11} + 2c_{12}} - \frac{1}{c_{11} - c_{12}} \right)$$

$$s_{11} = \frac{1}{c_{11} - c_{12}} - \frac{1}{3}\left(\frac{1}{c_{11} + 2c_{12}} - \frac{1}{c_{11} - c_{12}} \right) = \frac{1}{3}\left(\frac{4}{c_{11} - c_{12}} - \frac{1}{c_{11} + 2c_{12}} \right)$$

2.Measure for the anisotropy

$$A=\frac{2c_{44}}{c_{11}-c_{12}}$$

$A_{Si}=1.564$

$A_{Al}=1.2$

$A_{Fe}=2.3$

3.Modulus of elasticity

For all crystall symmetries

$$\frac{1}{E}=s_{11}-2\left(s_{11}-s_{12}-\frac{s_{44}}{2}\right)\frac{k^2l^2+l^2h^2+h^2k^2}{(h^2+k^2+l^2)^2}$$

thus for the [100] direction

$$\frac{1}{E}=s_{11}$$

$$\boxed{E=1.300\cdot10^{11}\ \mathrm{Pa}}$$

and for the [110] direction

$$\frac{1}{E}=s_{11}-\frac{1}{2}\left(s_{11}-s_{12}-\frac{s_{44}}{2}\right)$$

$$\boxed{E=1.6896\cdot10^{11}\ \mathrm{Pa}}$$

4.Shear modulus

For (001) surface and [001] or [011] direction of shear force

$$\frac{1}{G}=s_{44}$$

$$\boxed{G=0.7951\cdot10^{11}\ \mathrm{Pa}}$$

and for (110) surface and [1-10] direction of shear force

$$\frac{1}{G}=2(s_{11}-s_{12}),\ G=\frac{1}{2}(c_{11}-c_{12})$$

$$\boxed{G=0.5085\cdot10^{11}\ \mathrm{Pa}}$$

5.Poisson's ratio

$$\nu = -\frac{s_{\mu\nu}\,(\mathbf{ww})_\lambda(\mathbf{nn})_\mu}{s_{\xi\pi}\,(\mathbf{nn})_\xi(\mathbf{nn})_\pi}$$

with $(\lambda,\mu,\xi,\pi = 1,\ldots,6)$ and

$$(\mathbf{nn})_\lambda = n_i n_j, \qquad \lambda = \begin{cases} i & i = j \\ 9-(i+j) & i \neq j \end{cases}$$

$(i,j = 1, 2, 3)$

Thus

$$(\mathbf{nn})_\lambda = \begin{pmatrix} n_1^2 \\ n_2^2 \\ n_3^2 \\ n_2n_3 \\ n_3n_1 \\ n_1n_2 \end{pmatrix} \qquad (\mathbf{ww})_\lambda = \begin{pmatrix} w_1^2 \\ w_2^2 \\ w_3^2 \\ w_2w_3 \\ w_3w_1 \\ w_1w_2 \end{pmatrix}$$

Thus we have for the numerator:

$$\begin{pmatrix} s_{11} & s_{12} & s_{12} & 0 & 0 & 0 \\ s_{12} & s_{11} & s_{12} & 0 & 0 & 0 \\ s_{12} & s_{12} & s_{11} & 0 & 0 & 0 \\ 0 & 0 & 0 & s_{44} & 0 & 0 \\ 0 & 0 & 0 & 0 & s_{44} & 0 \\ 0 & 0 & 0 & 0 & 0 & s_{44} \end{pmatrix} \begin{pmatrix} w_1^2 \\ w_2^2 \\ w_3^2 \\ w_2w_3 \\ w_3w_1 \\ w_1w_2 \end{pmatrix} \begin{pmatrix} n_1^2 \\ n_2^2 \\ n_3^2 \\ n_2n_3 \\ n_3n_1 \\ n_1n_2 \end{pmatrix}$$

$$\begin{pmatrix} s_{11} \\ s_{12} \\ s_{12} \\ 0 \\ 0 \\ 0 \end{pmatrix} \begin{pmatrix} w_1^2 \\ w_2^2 \\ w_3^2 \\ w_2w_3 \\ w_3w_1 \\ w_1w_2 \end{pmatrix} \begin{pmatrix} s_{12} \\ s_{11} \\ s_{12} \\ 0 \\ 0 \\ 0 \end{pmatrix} \begin{pmatrix} w_1^2 \\ w_2^2 \\ w_3^2 \\ w_2w_3 \\ w_3w_1 \\ w_1w_2 \end{pmatrix} \begin{pmatrix} s_{12} \\ s_{12} \\ s_{11} \\ 0 \\ 0 \\ 0 \end{pmatrix} \begin{pmatrix} w_1^2 \\ w_2^2 \\ w_3^2 \\ w_2w_3 \\ w_3w_1 \\ w_1w_2 \end{pmatrix}$$

$$\begin{pmatrix}0\\0\\0\\s_{44}\\0\\0\end{pmatrix}\begin{pmatrix}w_1^2\\w_2^2\\w_3^2\\w_2w_3\\w_3w_1\\w_1w_2\end{pmatrix}\begin{pmatrix}0\\0\\0\\0\\s_{44}\\0\end{pmatrix}\begin{pmatrix}w_1^2\\w_2^2\\w_3^2\\w_2w_3\\w_3w_1\\w_1w_2\end{pmatrix}\begin{pmatrix}0\\0\\0\\0\\0\\s_{44}\end{pmatrix}\begin{pmatrix}w_1^2\\w_2^2\\w_3^2\\w_2w_3\\w_3w_1\\w_1w_2\end{pmatrix}$$

$$\begin{pmatrix}(w_1^2s_{11}+w_2^2s_{12}+w_3^2s_{12})\\ w_1^2s_{12}+w_2^2s_{11}+w_3^2s_{12}\\ w_1^2s_{12}+w_2^2s_{12}+w_3^2s_{11}\\ w_2w_3\ s_{44}\\ w_3w_1s_{44}\\ w_1w_2\ s_{44}\end{pmatrix}\begin{pmatrix}n_1^2\\n_2^2\\n_3^2\\n_2n_3\\n_3n_1\\n_1n_2\end{pmatrix}$$

$$(w_1^2s_{11}+w_2^2s_{12}+w_3^2s_{12})n_1^2+(w_1^2s_{12}+w_2^2s_{11}+w_3^2s_{12})n_2^2+(w_1^2s_{12}+w_2^2s_{12}+w_3^2s_{11})n_3^2+$$

$$s_{44}(w_2w_3n_2n_3+ w_3w_1n_3n_1+ w_1w_2n_1n_2)$$

$$s_{11}w_1^2n_1^2+w_2^2n_1^2s_{12}+w_3^2n_1^2s_{12}+w_1^2n_2^2s_{12}+w_2^2n_2^2s_{11}+w_3^2n_2^2s_{12}+w_1^2n_3^2s_{12}+w_2^2n_3^2s_{12}+w_3^2n_3^2s_{11}+$$

$$s_{44}(w_2w_3n_2n_3+ w_3w_1n_3n_1+ w_1w_2n_1n_2)$$

$$s_{11}\left(w_1^2n_1^2+w_2^2n_2^2+w_3^2n_3^2\right)+s_{12}\left(w_2^2n_1^2+w_3^2n_1^2+w_1^2n_2^2+w_3^2n_2^2+w_1^2n_3^2+w_2^2n_3^2\right)+$$
$$s_{44}\left(w_2w_3n_2n_3+ w_3w_1n_3n_1+ w_1w_2n_1n_2\right)$$

and similar for the denominator:

$$\begin{pmatrix} s_{11} & s_{12} & s_{12} & 0 & 0 & 0 \\ s_{12} & s_{11} & s_{12} & 0 & 0 & 0 \\ s_{12} & s_{12} & s_{11} & 0 & 0 & 0 \\ 0 & 0 & 0 & s_{44} & 0 & 0 \\ 0 & 0 & 0 & 0 & s_{44} & 0 \\ 0 & 0 & 0 & 0 & 0 & s_{44} \end{pmatrix} \begin{pmatrix} n_1^2 \\ n_2^2 \\ n_3^2 \\ n_2n_3 \\ n_3n_1 \\ n_1n_2 \end{pmatrix} \begin{pmatrix} n_1^2 \\ n_2^2 \\ n_3^2 \\ n_2n_3 \\ n_3n_1 \\ n_1n_2 \end{pmatrix}$$

$$s_{11}\left(n_1^2n_1^2+n_2^2n_2^2+n_3^2n_3^2\right)+s_{12}\left(n_2^2n_1^2+n_3^2n_1^2+n_1^2n_2^2+n_3^2n_2^2+n_1^2n_3^2+n_2^2n_3^2\right)+$$
$$s_{44}(n_2n_3n_2n_3+ n_3n_1n_3n_1+ n_1n_2n_1n_2)$$

Thus for $n = \begin{pmatrix} 0 \\ 0 \\ 1 \end{pmatrix}$ traction and $w= \begin{pmatrix} 1 \\ 0 \\ 0 \end{pmatrix}$ direction of contraction

$$\nu = - \frac{s_{11}(0)+s_{12}\left(0+0+0+0+w_1^2n_3^2+0\right)+s_{44}(000n_3+ 0w_1n_30+ w_1000)}{s_{11}\left(0+0+n_3^2n_3^2\right)+s_{12}\left(0+n_3^20+00+n_3^20+0n_3^2+0n_3^2\right)+s_{44}(0n_30n_3+ n_30n_30+ 0000)}$$

$$\boxed{\nu = - \frac{s_{12}}{s_{11}} = .2785}$$

and for $n = \frac{1}{\sqrt{2}}\begin{pmatrix} 1 \\ 1 \\ 0 \end{pmatrix}$ surface and $w= \frac{1}{\sqrt{2}}\begin{pmatrix} -1 \\ 1 \\ 0 \end{pmatrix}$ direction of contraction

numcrator

$$s_{11}\left(\frac{1}{4}+\frac{1}{4}+0\right)+s_{12}\left(\frac{1}{4}+0+\frac{1}{4}+0+0+0\right)+s_{44}\left(0+ 0- \frac{1}{4}\right)=\frac{s_{11}}{2}+\frac{s_{12}}{8}-\frac{s_{44}}{4}$$
$$=\frac{1}{2}\left(s_{11}+ s_{12} -\frac{s_{44}}{2}\right)$$

denominator

$$s_{11}\left(n_1^2n_1^2+n_2^2n_2^2+n_3^2n_3^2\right)+s_{12}\left(n_2^2n_1^2+n_3^2n_1^2+n_1^2n_2^2+n_3^2n_2^2+n_1^2n_3^2+n_2^2n_3^2\right)+$$
$$s_{44}(n_2n_3n_2n_3+ n_3n_1n_3n_1+ n_1n_2n_1n_2)$$

$$= \frac{1}{2}\left(s_{11}+ s_{12} +\frac{s_{44}}{2}\right)$$

$$\nu = -\frac{s_{11} + s_{12} - \frac{s_{44}}{2}}{s_{11} + s_{12} + \frac{s_{44}}{2}} = 0.06247$$

A graphical representaion of all these engeneering constants in dependence of the crystall direction is given by Wortman[3].

6.The thermal expansion coefficients

${}^2\alpha = \alpha_{ij}$ Coefficients of the linear thermal expansion

${}^2\varepsilon = {}^4S:{}^2\sigma + {}^2\alpha\,\Delta T$

For a cubic crystal the thermal behaviour becomes isotropic

$\alpha_{ij} = \alpha\delta_{ij}$

For silicon[1] :

T [K]	α [10^{-6}/K]
260 K	2.223
280 K	2.432
300 K	2.616
400 K	3.253

α has a minimum at 80 K: $\alpha = -.472 \cdot 10^{-6}$/K and is zero near 120K.

7.The temperature coefficient of the Elastic constants and doping dependence

An early publication by McSkimin et al.(1951)[4] gives the temperature coefficient of the Elastic constants as

$K_{C11} = -75.3$ ppm/K

$K_{C12} = -24.5$ ppm/K

$K_{C44} = -55.5$ ppm/K

he uses an α of $7.63 \cdot 10^{-6}$, where $2.33 \cdot 10^{-6}$ is the accepted value today (see I.6.), whereas Londolt Börnstein cited in "Properties of Silicon"[1] gives

$K_{C11} = -94$ ppm/K

$K_{C12} = -98$ ppm/K

$K_{C44} = -83$ppm/K

As an example we are calculating with the values from above the temperature dependence of the shear modulus G of a (110) surface and [1-10] direction of shear force. We found $G = \frac{1}{2}(c_{11}-c_{12})$ (= $0.5085 \cdot 10^{11}$ Pa) and thus we have

$$\frac{dG}{dT} = \frac{1}{2}\left(\frac{\partial c_{11}}{\partial T} - \frac{\partial c_{12}}{\partial T}\right) = \frac{1}{2}(c_{11}K_{C11} - c_{12}K_{C12}) = \frac{1}{2}\left(-1.557 \cdot 10^{7} + 6.266 \cdot 10^{6}\right)$$

Pa/K= $- 4.652 \cdot 10^{6}$ Pa/K

or $K_{G[110]} = -91.5$ ppm/K

Heavy p doping decreases the constants of elasticity by about 1-1.5%

Specific heat of Si at room temperature

$C = .678$ J/gK

and the Debeye temperature

$\theta = 646$ K

1 Properties of Silicon, emis Datareviews No.4.. INSPEC, London New York, 1988. ISBN 085296 475 7.

2 Pauffler, P.; Physikalische Kristallographie. VCH Verlagsgesellschaft, D-6940 Weinheim. 1986. ISBN 3-527-26454-X

3 Wortman,J.J. and Evans, R.A.; Young's Modulus, Shear Modulus, and Poisson's Ratio in Silicon and Germanium. Journal of Applied Physisc, Vol 36, Number 1 Jan, 1965 p.153.

4 McSkimin, H.J., Bond, W.L.,Buehler, E. Teal, G.K.; Measurement of the Elastic Constants of Silicon single crystals and their thermal Coefficients. Phys. Rev. 83. 1080 (1951)

Summary

This work is thought to present different possibilities for the fabrication of mechanical sensors, which emerges from the technique of anisotropic etching in monocrystalline silicon. In particular the resonance frequency and the Q-factor were measured in function of gas pressure and temperature. The experimental data were compared with the theoretically calculated values.

Resonant structures of single crystal silicon have been investigated in view of their potential use as basic elements for various sensor applications, like pressure, viscosity, temperature or adsorbed molecules, as is already well known with quartz resonators. Special emphasis was laid on a certain optimization of vibrating structures. Starting from relatively simple lumped mass-beam systems the structures have been improved with respect to the clamping. By modelling and extensive calculations optimal structures could be designed. The calculations are resumed in chapter 2.

In chapter 3 we are starting with the description of an etch simulation program, which allows a fast testing of two-dimensional etching masks. For a given shape a certain back calculation from the wanted three-dimensional dimension to the necessary two dimensional mask is possible.The fabrication technique of the structures is described then in the rest of the chapter 3.

The various devices were tested in a for that very purpose constructed chamber, which allowed a pressure up to 2 bar and a vacuum down to 10^{-3} mbar. The temperature was controlled by a thermostated brass block. The elongation was measured optically by an interferometer (chapter 4). The excitation and the electronic part of the measurement setup is described in this chapter, too, as far as it relates to most of the structures under test.

Experimentally a great variety of devices have been realized and measured. First of all as a statical device a tactile sensor array was realized with truncated pyramid shaped force transmitters (called mesas, cams or bosses), where we applied a specially developed corner compensation method. Thus, upon application of force on this mesas the capacity underneath is changed and thus the resonance frequency of a properly connected oscillating circuitry (chapter 5).

It is the purpose of this work to study whether resonant silicon devices can be realized with a frequency resolution in the order of ppm to develop sensors with a similar resolution. To this end high Q-factor resonators are needed. Some investigations on external damping factors like clamping, medium and supplementary thin films of silicon resonators have been carried out in this work. One type of resonators consists of a mass-beam system, where the mass is a perfect geometrical body and thus calculable. This mass was doubly supported

and exerted thus no torsional movement (as it would, if only simply supported). On these type of structures most of the studies were done (chapter 6).

A special compensation of the forces at the clamping for mass beam systems was obtained with another design, which is presented in chapter 7.

We achieved to realize tuning fork structures in silicon. These were provided with metallic lanes so that they could be excited in a magnetic field (chapter 8).

A decoupled torsional structure showed Q-factors in the order of 600 000 in vacuo at room temperature and thus a resolution of some ppm of the frequency (chapter 9). With this structure it could be proved, that competitive devices for sensor applications (compared to quartz e.g.) are possible in silicon.

The above mentioned structures have all dimensions in the order of cm. Thus, we finally realized an array of paddle type devices with dimensions in the order of mm, which can be excited optically. The combination of fibre optics with micromachined structures seems to be a promising way to get micropackaged sensors (chapter 10).

CURRICULUM VITAE

Name	BUSER
First names	Rudolf Alfred
Date of Birth	24.5.1956 in Balsthal /SO
Native place	Bättwil /SO
Primary school	Domach/S0 (5 years)
Secondary school	Realgymnasium, Basel (8 years)
Final examination	Type B, 1976
University of Basel	1 semester, Physics/Mathematics
Basic military training	1976
Fed. Inst. of Technology	ETH, Zürich 1976-1982
	during that time
	- International Student Exchange: SHELL, KSEPL, research, Rijswijk, Holland.
	- part-time employment with Prof. Melchior for the development of a H_2 -sensor
Diploma in physics	ETH, Zürich, 1982
	optional subjects:
	Technical physics:
	Semiconductor devices: Prof. Melchior
	Semester work: H_2 - Sensor
	Diploma: Optoeletronical switch
	Solid state physics:
	Electron scattering with PD Y. Baer
	Neutron scattering with PD A. Furrer
Teaching in Physics	1982-1983
	Kantonsschule Aarau (1 year)
	Kantonsschule Frauenfeld (1/2 year)
Tearhing diploma	Ausweis für das höhere Lehramt , ETH, Zürich, 1985

Since fall 1983 assistent at IMT, Université de Neuchâtel, group Microelectronics and Microfabricated Transducers with Prof. N. de Rooij. During that time as assistent essentially the following studies were undertaken:

- Realization of silicon structures for mechanical applications, what needed the elaboration of a process for very deep etching.
- Development of a masking method for the etching of glass.
- Investigation on the influence of the "Anodic bonding" on CMOS-Parameters.
- Study on metallic thin films, adherence and interdiffusion.
- Development of a miniaturized planar three electrode structure for the application as a glucose sensor (see reference N.F. de Rooij).
- Development of a tactile sensor (out of projects).
- Realization of silicon dioxid cantilevers for the application as Atomic Force Microscope (see references)
- Development of a method for the analysis of Al_2O_3 films by TEM
- Direction of an industrial training course in microelectronics (FSRM)

During the same period, I built up a laboratory on industrial level for the fabrication of integrated sensors.

- Since mai 86: Investigations on the dynamical behaviour of mechanical silicon structures (resonators). These studies are part of the present dissertation .

Since part of the above projects were carried out under industrial contracts, the corresponding reports are confidential and not published. Exceptions are as follows:

- R.A. Buser und N. F. de Rooij, Siliziumsensoren , Sonderpublikation der VDI-Zeitschrift, Hard and Soft. Herausgeber: Raymond Shah, Sensoren 86/87, VDI-Verlag.

- R.A. Buser , B. Stauffer, N.F. de Rooij, Realization of a mesa array in (001) oriented silicon wafers for tactile sensing applications, Extended Abstracts of the Fall Meeting of the Electrochemical Society, San Diego, Cal. October 19-24, 1986.

- Ch. Arnoux, R.A. Buser, M. Decroux, and N.F. de Rooij, Analysis of the structure and drift of Al_2O_3 layers used as pH-Sensitive material for pH-ISFETS, 4th International Conference on Solidstate Sensors and Actuators, Transducers 87, Tokyo, 1987.

- R.A.Buser und N.F. de Rooij, Monolithisches Kraftsensorfeld, VDI Berichte Nr. 677, 1988 p. 115, Tagung Bad Nauheim, 14-16- März

- R.A. Buser, and N.F. de Rooij, Silicon Microetching and FOS: Properties, Compatibility and Synthesis of Transducers, Proccedings of the Sixth European Fibre

optic Communications and Local Area NEtworks Exposition, held June 29-July 1, 1988, pp.223, RAI Amsterdam, NL.

- Rudolf Buser und Nico de Rooij, Mikromechanik, Zeitschrift HARD AND SOFT, VDI, Berlin, Fachbeilage Mikroperipherik, Oktober 1988, pp I-II.

- R.A. Buser, N.F. de Rooij, Resonant silicon structures, Sensors and Actuators, Vol 17. No 1/2 pp. 145-153. Full abstract of Eurosensors II.

- R.A. Buser , N.F. de Rooij, Tuning forks in Silicon, Proceedinggs of the IEEE Micro Electro Mechanical Systems Workshop, Feb. 19-22, 1989, Salt LAke City, Utah, USA.p. 94.

- Rudolf A. Buser, Monocrystalline Silicon Resonators,Seminarband AMA Seminar Mikromechanik, Heidelberg, 14,15 März 1989. p. 193

- R.A. Buser, Very high Q-factor Resonators in Monocrystalline Silicon, accepted for the 5th international conference on Solid state Sensors and Actuators & Eurosensors III, Transducers '89, Montreux, CH.

- G.A. Racine, R.A.Buser, N.F. de Rooij, Low Temperature Operating Silicon Bolometers for Nuclear Radiation Detection.accepted for the 5th international conference on Solid state Sensors and Actuators & Eurosensors III, Transducers '89, Montreux, CH.

Participation on international conferences:

- Fall meeting of the Electrochemical Society, San Diego, California, 1986
- 4th Int. Conf. on Solidstate Sensors and Actuators, Tokyo, Japan, 1987
- VDI Tagung Bad Nauheim, Sensoren Technologie und Anwendung,14-16- März, 1988
- Sixth European Fibre optic Communications and Local Area Networks Exposition, held June 29-July 1, 1988, pp.223, RAI Amsterdam, NL
- Second European Frequency and Time Forum EFTF 88, 16-18 March 88, Neuchâtel, CH
- Eurosensors II , 4th symposium on sensors & actuators , Twente, NL
- IEEE Micro Electro Mechanical Systems Workshop, Feb. 19-22, 1989, Salt LAke City, Utah, USA.
- AMA Seminar Mikromechanik, Heidelberg, 14,15 März 1989.

Performances:

- ITG- Frühjahrstagung 1989,Sensortechnik, Stein am Rhein, 21. 22. März 1989
  Titel : Mikromechnische und chemische Sensoren

Further education:

- "Workshop on Micromachining and Micropackaging of Transducers", Case Western Reserve University, Cleveland, Nov. 7 to 9, 1984.
- Stage de perfectionnement à l'Institut National Polytechnique, Grenoble
  "Utilisation des méthodes d'impédance pour l'étude des réactions électrochimiques", Grenoble , 15-18 Avril 1985.

References:

- A. Heuberger, Mikromechanik, Springer Verlag 1989, p. 346. (Tactile)
- Zeitschrift techno tip, Vogel Verlag , D-8700 Würzburg. Nr 11, 1988. pp. 18 ff. (Tactile)
-Chang, S.C. and Hicks,D. Mesa Structure Formation using Potassium Hydroxide and Ethylene Diamine Based Etchants. Solid-State Sensor and Actuator, Technical digest of the IEEE Workshop, Hilton Head Island, S.C. June 6-9 1988. p.102. (corner compensation)
- N.F. de Rooij , Trends in electrode technology, In " Presurgial Evaluation of Epileptics", Wieser/ Elger, Eds. Springer Verlag, Berlin, p.112 (1987) (Planar three-electrode system, Clark cell)
- Heinzelmann, H. Meyer, E. Güntherodt, H.J. Local step structure of the AgBr(100) and (111) surfaces studied by atomic force microscopy, to be published in Surface Science. (SiO_2 cantilever)